Multi-scale study of massive star forming region NGC 6334I/F

JM Vorster

orcid.org/0000-0001-9572-2425

Dissertation accepted in partial fulfilment of the requirements for the degree *Master of Science in Astrophysical Sciences* at the North-West University

Supervisor:	Prof JO Chibueze
Co-supervisor:	Prof DJ van der Walt

Graduation May 2023

28570057

Acknowledgements

I firstly want to thank my Creator for giving me the grace to study the complex world that He has made. Then I want to thank my wife Iida for her love and support throughout this journey. I also want to thank my wide group of family and friends. Thank you for all the meaningful conversations during this time. With regard to the research, I firstly would like to thank my main supervisor, James Chibueze. He has guided and supported me well during these two years, and I have learned much from him. I also thank my co-supervisor, Johan van der Walt, for all the scientific and non-scientific conversations. I thank the faculty members and other students at the Department of Physics at the North-West University for their kindness and friendship. I thank the Radio Astronomy Group at the NWU, the M2O maser collaboration as well as the KaVA Star Formation Large Program working group for inspiring me to do science well. Specifically, I wish to thank Tomoya Hirota, Ross Burns, Gordon Macleod and Crystal Brogan for supplying data that were used in this work. Lastly, I thank the National Research Foundation for funding this research (UID: 134192).

Abstract

This thesis reports an observational multi-scale study of the high-mass star-forming region NGC6334I/F on scales ranging from 10 000 AU down to 1 AU. In 2015, NGC6334I-MM1B started a period of high accretion analogous to FU Orionis bursts in low-mass stars. This thesis aimed to examine the effects of the burst on the water and methanol masers in the region. Archival 2016.9 5 cm continuum with the Jansky Very Large Array (JVLA) and archival 2015.6 1.3 mm continuum with the Atacama Large Millimetre/Submillimetre Array (ALMA) were used in combination with seven epochs of 22 GHz Very Long Baseline Interferometry (VLBI) observations of water masers with VLBI Exploration for Radio Astrometry (VERA) between 2014 and 2016 and 2019.6 JVLA observations of 6.7 GHz methanol masers in NGC6334I. Water masers were detected in CM2-W2, MM1-W1, UCHII-W1, UCHII-W2 and UCHII-W3. The variability of water masers in CM2-W2 and MM1-W1 showed systematic trends indicating that the variability is associated with the recent accretion burst. UCHII-W1 and UCHII-W2 showed high velocity ($v > 50$ km s^{-1}) proper motions associated with the N-S jet identified in previous studies. UCHII-W3 also showed high velocity ($v \sim 150$ km s^{-1}) proper motions associated with the NW-SE jet. An upper limit on the outflow force of the NW-SE jet was estimated so that $\dot{P} < 33.6 \times 10^{-3} M_{\odot}$ yr^{-1} km s^{-1}. Methanol masers were also detected in MM1, MM2 and MM3-UCHII. A likely calibration error was identified in the flux scaling of the methanol maser observations, but the positions and radial velocities of the observations were found to be reliable. MM1 contained masers likely tracing rotating gas entrained by the N-S or NW-SE jet, as the masers are co-spatial with an outflow cavity, and high-velocity proper motions from previous work. MM2 contained two associations with a symmetric "wing" formation and MM3-UCHII had multiple maser associations along the edge of the UCHII region NGC63334F. Water masers tracing shocked environments and methanol masers tracing hot environments gave insight into the dynamic and complex star formation in the region.

Keywords: masers - stars: formation - ISM: clouds - radio lines: ISM - techniques: interferometric - sources: NGC6334I

Contents

List of Figures

List of Tables

Abbreviations

Name	Abbreviation
Interstellar medium	ISM
Giant molecular cloud	GMC
Star-forming region	SFR
High-mass star-forming region	HMSFR
Young stellar object	YSO
Low-mass young stellar object	LMYSO
High-mass young stellar object	HMYSO
Massive dense core	MDC
High-mass star formation	HMSF
Ionized hydrogen	HII
Ultra-compact HII region	UCHII
Herbig-Haro object	HH
Very long baseline interferometry	VLBI
VLBI Exploration for Radio Astrometry	VERA
Atacama Large (Sub)Millimetre Array	ALMA
Korean VLBI Network and VERA	KaVA
Karl Jansky Very Large Array	JVLA
Hartebeeshoek Radio Astronomical Observatory	HartRAO
Sub-millimetre Array	SMA
Common Astronomy Software Applications	CASA
Astronomical Image Processing System	AIPS
Spectral energy distribution	SED
Full-width at half-maximum	FWHM
System equivalent flux density	SEFD
Root mean squared	RMS
Point spread function	PSF
Signal to noise ratio	SNR
Fast fourier transform	FFT
Ultraviolet	UV
Near-infrared	NIR
Millimetre source	MM
Centimetre source	CM
Microwave amplification by stimulated emission of radiation	Maser
Magnetohydodynamic	MHD
Magnetorotational instability	MRI
Gravitational instability	GI

Physical Constants

Constant	Symbol		Value
The speed of light	c	=	2.99792458×10^{8} m s^{-1}
Planck's constant	h	=	$6.62607015 \times 10^{-34}$ Joule s
The gravitational constant	G	=	$6.67430(15) \times 10^{-11}$ m^{3} kg^{-1} s^{-2}
Boltzmann's constant	k	=	$1.3806493 \times 10^{-23}$ Joule K^{-1}
Elementary charge	e	=	$1.602176634 \times 10^{-19}$ Coulomb
Electron mass	m_{e}	=	$9.1093837015(28) \times 10^{-31}$ kg
Proton mass	m_{p}	=	$1.67262192369(51) \times 10^{-27}$ kg
Neutron mass	m_{n}	=	$1.67492749804(95) \times 10^{-27}$ kg
Stefan-Boltzmann constant	σ_{SB}	=	$5.670374419 \times 10^{-8}$ W m^{-2} K^{-4}
Rydberg constant	R_{∞}	=	$10973731.568160(21)$ m^{-1}

Physical Constants

Constant	Symbol		Value
Astronomical unit	AU	=	149597870700 m
Parsec	pc	=	$3.08567758128 \times 10^{16}$ m
Solar mass	$M_\odot$	=	1.98841×10^{30} kg
Solar luminosity	$L_\odot$	=	3.939×10^{26} W

Chapter 1

Introduction

1.1 Scientific Context

Astrophysics is the science of giving an accurate, consistent and precise account of the physical universe: Accurate, as the statements in astronomy aim for truth and are based on observations of the physical world. Consistent, as the various sub-fields of astrophysics aim to be logically coherent in themselves and between one another. Precise, as astronomers are trying to give numerical values of physical parameters within as narrow a margin for error as possible. When Isaac Newton started to apply physical laws that govern the earth to the observations of space, modern astrophysics was born. In a very real sense, astrophysics is the science of the entire physical universe: It's evolution from its initial state, it's current state, and it's final destiny.

Cosmic, galactic and stellar evolution is where the origin of the structures seen in the modern universe is studied. Cosmological evolution studies changes in the galaxy at the largest (> 500 Mpc) scales (Ellis et al., 2012). Galactic evolution studies the origin and time dependence of galaxies and galaxy clusters (Conselice, 2014). Stellar evolution studies the origin and time evolution of stars.

Star formation can be seen as an intersection between galactic and stellar evolution. Stars affect the environments around them, and their environments affect their formation. Star formation studies can be grouped into primordial, extra-galactic and galactic star formation studies. Primordial star formation examine the very first stars that may have formed (Bromm et al., 2002; Hirano et al., 2015). Extra-galactic star formation studies looks at star formation outside of our galaxy (e.g., Leroy et al., 2021). The benefits of these studies are that you could look at star formation at different stages of cosmic evolution, with the caveat that spatial resolution is highly limited due to the large distances of the other galaxies. On the other hand, galactic star formation studies look at star forming regions (SFRs) within our own galaxy. These studies can take various forms, either as large surveys (e.g., Brunthaler et al., 2021), or studies of individual SFRs. Large surveys can support helpful generalizations, while single SFR studies can give precise in-depth information on the physical processes at work in SFRs. The conclusions from these observational studies can be used to test mathematical models.

A sub-field of star formation which has been predominantly observation-driven in recent years has been high-mass star formation (HMSF), for $M_* > 8M_\odot$ (Zinnecker and Yorke, 2007; Tigé et al., 2017). High-mass young stellar objects (HMYSOs) are difficult to study observationally, because they form in deeply embedded environments with high extinction in most wavelengths, are often relatively far away > 1 kpc, and have short formation times $\sim 10^5$ yrs (Sabatini et al., 2021). On the other hand, the

short lifetimes of HMYSOs have a benefit as some time dependent processes can take place on human timescales. The recent accretion bursts in the high-mass SFRs (HMSFRs) S255IR-NIRS3 (Caratti o Garatti et al., 2017), G358.93-0.03-MM1 (Burns et al., 2020) and NGC6334I-MM1 (Hunter et al., 2017) have shown that HMYSOs also undergo episodic accretion like low-mass stars. These accretion bursts are analogous to FU Orionis and EXor events (Audard et al., 2014). The timescales of the accretion bursts in HMYSOs range between 0.75 yr for G358.93−0.03 (Stecklum et al., 2021), $2 - 2.5$ yrs for S255IR-NIRS3 (Caratti o Garatti et al., 2017) and $40 - 130$ yrs for NGC6334I (Hunter et al., 2021). Some of these events have really short timescales, and can be easily missed without a coordinated observational effort.

Tracers such as infrared (Caratti o Garatti et al., 2017), millimetre (Hunter et al., 2017), and maser emission by various molecule populations (MacLeod et al., 2018) have been found to change dramatically during accretion bursts. The maser monitoring organization M2O (Burns et al., 2022) has been founded to identify and study these accretion events with long-term single-dish monitoring of masers in HMSFRs. Once a maser has been found to flare, follow-up continuum and spectral line observations with connected arrays and Very Long Baseline Interferometry (VLBI) arrays aim to study the regions in detail.

The accretion bursting source NGC6334I, at $d = 1.3 \pm 0.09$ kpc, is known to consist of nine millimetre clumps (Brogan et al., 2016), with the largest millimetre clump hosting multiple cores and outflows (Brogan et al., 2016; Chibueze et al., 2021). In January 2015, various maser species in the region flared significantly (MacLeod et al., 2018), and the region had an increase in millimetre flux by a factor of 4.0±0.3 (Hunter et al., 2017). Spectral energy distributions (SEDs) constructed with millimetre and infrared images indicated that the accretion bursting source in NGC6334I was a $6.7 M_{\odot}$ protostar, which had an increased accretion rate of $\geq 0.0023 M_{\odot}$ yr^{-1} (Hunter et al., 2021). Further, the first detection of 6.7 GHz methanol masers in the accretion bursting source MM1 was after the onset of the accretion burst (Hunter et al., 2018). Some of the outflows are also known to harbour 22 GHz water masers (Brogan et al., 2018; Chibueze et al., 2021). The region is quite complicated, and warrants investigation as a HMSFR that recently underwent an accretion burst. Further, the time dependent nature of the region gives a unique opportunity to better understand some of the maser species in this region.

1.2 Aims and Objectives

The primary aim of this thesis is to measure the effect of the accretion burst in NGC6334I on the 22 GHz water masers in the region directly before and at the onset of the burst. Water masers are used as a tracer for protostellar outflows (Chibueze et al., 2012) and distance measurements (VERA Collaboration et al., 2020). It is known that water masers are variable in flux density over time in general (Felli et al., 2007) and during accretion bursts (MacLeod et al., 2018). The secondary aim of this thesis is to observe the post-burst methanol masers in the region to see if there are significant changes between 2016.9 (Hunter et al., 2018) and 2019.6 (the dataset in this thesis). Methanol masers are known to be associated with HMSFR (Minier et al., 2003) and accretion bursts in HMYSOs (Burns et al., 2020).

These aims are addressed in the following ways. Seven epochs of 22 GHz water masers in epochs spanning between 2014 (before the burst) and 2016 (after the onset of the burst) were observed with the VLBI array VERA. The water maser positions, radial velocities and intensities were used to measure variability in NGC6334I. Further, the VLBI water maser observations were used for calculating proper

motions before and during the accretion burst. Methanol maser observations with the JVLA on 2019.6 was done, and were calibrated and imaged to see if there had been changes three years after the onset of the burst. The maser observations were supplemented with archival continuum images. An archival ALMA 1.3 mm dust continuum image by Brogan et al. (2016) and an archival JVLA 5 cm continuum image from Hunter et al. (2018) were used to give additional context to the maser observations.

1.3 Chapter Outline

Chapter 2 - Star Formation

Chapter 2 serves as a literature review for this work. The main topics of review are star formation and episodic accretion. Star formation in general is discussed, followed by HMSF and the tracers that are used to study SFRs, such as free-free, synchrotron, dust, gas and maser emission. Special emphasis is placed on the maser species that are studied in this work: 22 GHz water masers and 6.7 GHz methanol masers. The second half of the review concerns episodic accretion. First episodic accretion in low-mass stars is introduced, and then accretion bursts in high-mass young stellar objects. Two well-studied accretion bursting HMYSOs S255IR-NIRS3, G358.93-0.03-MM1 are discussed in detail, followed by an introduction to NGC6334I.

Chapter 3 Method

Chapter 3 discusses the techniques used in this work. The first half of the chapter is an introduction into single-dish telescopes as well as interferometry theory, calibration and imaging. The second half of the chapter describes the four datasets used in this thesis, the instruments used to gather the data and details on the data reduction methods.

Chapter 4 - Results

Chapter 4 reports the main results for this work. First the 1.3 mm and 5 cm continuum images are described. The positions and radial velocities of water masers by the multi-epoch 2014-2016 VERA observations are described. The second half of the chapter introduces the spot and spectral methods of proper motion calculations and the proper motions before and during the burst of the water masers derived by these methods. The differences between these methods are outlined. Then the positions and radial velocities of 2019 JLVA 6.7 GHz methanol are described.

Chapter 5 - Discussion

Chapter 5 serves as the scientific discussion for this work. The main topic of discussion is the 22 GHz water maser observations with VERA. Variability of water masers in NGC6334I is discussed in light of the accretion burst. The proper motions calculated in this thesis are compared to previous work on the same source, followed by a discussion on whether water maser proper motions are a reliable tracer of gas motion. Outflow parameters such as dynamic timescales, outflow force, driving source luminosity and mass are calculated. The final section of the discussion critically examines the 6.7 GHz methanol maser observations with the JVLA reported in this thesis, and compares the result to previous work.

Chapter 6 - Conclusion

Chapter 6 answers the scientific aims of this thesis, and concludes the work after possible future work is outlined.

Chapter 2

Star Formation

2.1 Introduction

This chapter offers a review of star formation and episodic accretion. Firstly, star formation is briefly introduced, followed by an in-depth discussion of the tracers used to study SFRs: Astrophysical masers, free-free emission, synchrotron radiation, dust emission and thermal gas. HMSF studies are introduced, as well as a portion of the current understanding of the science. The accretion-ejection link is explored in the context of star formation, followed by a review of episodic accretion in low-mass protostars. Recent theory and observational developments in episodic accretion in high-mass protostars are introduced in detail, as well as the specific observations done over the last few years. Lastly, the SFR presented in this thesis, NGC6334I, is introduced.

2.2 What is Star Formation?

Star formation is the process through which interstellar gas and dust collapse into stars that undergo nuclear fusion in their cores. Studies in star formation attempt to understand the different physical processes at work in SFRs (SFRs). This entails all the processes of gas in a giant molecular cloud (GMC) with a density of $50 - 1000$ particles cm^{-3} and a temperature of $10-50$K, (Mathis, 1990; Bloemhof, 1993), turning into a star with an interior density of 1×10^{25} particles cm^{-3} and a temperature of 10^8 K. A full description of star formation should consider the inclusion of gravity, magnetic fields, rotation, thermal pressure, turbulence, neutral and ionized matter, cosmic rays, shocks, interstellar chemistry and many types of radiative emission and absorption processes (Schulz, 2012; Yamamoto, 2017). Needless to say, it is a complicated affair. Star formation can be grouped into a study of low-mass ($M_* \leq 3M_\odot$), intermediate mass ($3M_\odot \leq M_* \leq 8M_\odot$) and high-mass ($M_* \geq 8M_\odot$) stars.

2.3 Observing Star Formation

Electromagnetic radiation is the chief carrier of information about the processes in SFRs. The different emission processes inside the SFRs determine the positions, frequencies and flux densities of the radiation measured by our telescopes. The main processes of emission in SFRs are briefly described in the following sections. The main focus is on masers, as they are the main tracer used in this thesis. Maser emission, produced by the population inversion of molecules in specific quantum rotational states, also provides information on SFRs. Qualitative information can be gained from the existence, morphology and brightness of specific maser species, such as water, methanol and hydroxyl, as these molecules only undergo population inversion in specific physical circumstances. Further, masers can be used to trace kinematics (Burns et al., 2015), measure distances to objects (Chibueze et al., 2014), measure

magnetic fields (Green et al., 2015) and can even be a low cost observable for significant change in the SFR (MacLeod et al., 2018). Astrophysical masers are described in Section 2.3.2.

The other emission mechanisms are also briefly discussed for completeness, as some of the works cited in this thesis make use of these tracers. Centimetre emission from free-free emission traces the existence and morphology of HII regions, which are ionized. The existence of HII regions indicates that the high-mass young stellar object (HMYSO) in question has already started nuclear fusion in its core, so that it can release UV radiation to ionize the surrounding region (Churchwell, 2002). Free-free emission is described in Section 2.3.3. Synchrotron emission, produced by the motion of free electrons around magnetic field lines, can also be a tracer of strong magnetic fields produced near the young stellar object's poles. Synchrotron emission is described in Section 2.3.4. Millimetre dust emission can provide helpful high angular resolution continuum images of the dust temperature distribution, column density and cloud mass. Many molecules such as SiO, CO and CS have spectral line emission in the millimetre regime that can act as outflow tracers. This combination of chemical tracers of complex molecules and tracers of outflows, makes millimetre spectral line observations very powerful to probe HMYSOs, even if the HMYSO itself cannot be seen. Dust emission is described in Section 2.3.5 and gas emission is described in Section 2.3.6. Before the discussion on masers begin, the basics of radiative transfer is introduced.

2.3.1 Basic Radiative Transfer

Radiation travelling through space is affected by what it encounters. More often than not, the radiation received by astronomical instruments has been affected by various effects that have changed the original emitted radiation. The quantification of the effects that change the intensity and frequency of emission is termed radiative transfer. This presentation is based on Wilson et al. (2013), and an advanced discussion is given by Chandrasekhar (1960).

The specific intensity I_ν (units of W m^{-2} Hz^{-1} sterad^{-1}, or Jy beam^{-1}) is a foundational quantity in astronomy. A basic theorem of intensity is that it is conserved over distance in a vacuum. The flux F_ν is the integral of I_ν over an angle Ω in the sky. The equation of radiative transfer quantifies how intensity changes over distance due to intervening matter:

$$\frac{dI_\nu}{ds} = \epsilon_\nu - \kappa_\nu I_\nu \tag{2.1}$$

with ds the infinitesimal distance, ϵ_ν the specific emissivity (units of W m^{-3} Hz^{-1} sterad^{-1}) and κ_ν the absorption coefficient (units of m^{-1}). ϵ_ν is a measure of how much radiation the material in question releases, and κ_ν is a measure of how much radiation is absorbed as a function of distance. If Equation 2.1 is divided by κ_ν, the term $S_\nu = \epsilon_\nu/\kappa_\nu$ is termed the source function. This term measures the intensity of photons absorbed and emitted by the medium. A formal solution for Equation 2.1 is given by Chandrasekhar (1960):

$$I_\nu(s) = I_\nu(0)e^{-\tau(s,0)} + \int_0^s S_\nu(s')e^{-\tau(s,s')}\kappa_\nu ds' \tag{2.2}$$

with $\tau(s, s')$ the optical depth. It is given by:

$$\tau(s, s') = \int_{s'}^{s} \kappa_\nu ds \tag{2.3}$$

The formal solution should not be seen as explicitly solving Equation 2.1, as the details of the emission and absorption are complicated, depending on the specific radiative processes at work.

τ is a measure of the absorption of radiation through a medium. It can be seen as the total absorption, which reduces the intensity by a factor $e^{-\tau}$. A medium is termed optically thin if $\tau \ll 1$, i.e., close to transparent, and optically thick if $\tau \gg 1$, i.e., opaque to radiation.

2.3.2 Maser Emission

This section discusses microwave amplification by stimulated emission of radiation (MASER) emission, which serves as the main astrophysical tracer used in this study. Masers form in physical conditions that induce a larger population of molecules in a specific higher energy state u than in a specific lower energy state l. The transition $u \rightarrow l$ is termed the masing transition. This state of population inversion causes the gas to have a negative τ_ν, where ν is the frequency of the masing transition. $\tau_\nu < 0$ causes a gas to amplify incident radiation at ν. The masers are identified by molecule and the masing transition, e.g., 22 GHz H_2O or 6.7 GHz CH_3OH masers. If there is sufficient velocity coherence of the molecules along a path so that their line profiles overlap, there will be a significant amplification of radiation along the path. Pumping, in masers, is defined as any physical process that produces population inversion in a population of molecules.

The basis of maser calculations is the rate equations governing the populations of the maser states, and the equation of radiative transfer, which governs the intensity of the radiation along the path length. A simple form of the equations for a two-level system is given by Goldreich and Keeley (1972), and the following discussion is based on their analysis. This model assumes that l is above the ground state. The radiative transfer equation can be written as:

$$\frac{dI_\nu}{dz} = \frac{h\nu}{4\pi}\phi_\nu[(N_\mathrm{u} - N_\mathrm{l})BI_\nu + N_\mathrm{u}A] \tag{2.4}$$

with I_ν the intensity of light with frequency ν, dz the infinitesimal length along the maser amplification path, Planck's constant h, the frequency dependent line response function ϕ_ν (assuming the function is the same for emission and absorption), the number density of the molecules in the upper and lower levels N_u and N_l respectively. A and B are the Einstein coefficients for emission and absorption respectively. The change in the level populations can then be written as:

$$\begin{aligned} \frac{dN_\mathrm{u}}{dt} &= -(N_\mathrm{u} - N_\mathrm{l})BJ - N_\mathrm{u}A + R_2(N - N_\mathrm{lu}) - \Gamma N_\mathrm{u} \\ \frac{dN_\mathrm{l}}{dt} &= (N_\mathrm{u} - N_\mathrm{l})BJ + N_\mathrm{u}A + R_1(N - N_\mathrm{lu}) - \Gamma N_\mathrm{l} \end{aligned} \tag{2.5}$$

with $J = \int_0^\infty J_\nu \phi_\nu d\nu$ the flux density of radiation within the linewidth of the molecules, where $J_\nu = \frac{1}{4\pi}\int I_\nu d\Omega$ is the specific flux density. R_l and R_u are the pump rates for the molecules to the lower and upper states respectively. The pump rates (R_l or R_u) are determined by all processes that can take a molecule from another level to the masing level (l or u). These processes can include collisional (de)excitation, spontaneous or stimulated emission from an upper level or absorption of a lower level. Γ is the inverse lifetime of the maser states, assuming it is equal for both states. Γ is a sum of all the processes that can take a molecule out of u or l. These processes include spontaneous emission, stimulated emission, absorption or collisional (de)excitation to a non-masing level. In more general models, Γ is different for u and l. N is the number density of the molecules in all energy states and $N_\mathrm{lu} = N_\mathrm{l} + N_\mathrm{u}$ is the number density of the two energy levels involved in the masing action.

These equations are a simplification that assumes that the absorption and emission line profiles are equal. Further, all the transitions away from states u and l to non-masing states are described with only one factor Γ. There is still information about the nature of masers from this simplified model.

Equation 2.4 shows that the radiation is amplified along the path length as long as $N_u - N_l > 0$ (i.e., population inversion is the case). Another insight from Equation 2.4 is the ϕ_ν factor, which indicates that the molecules' line profiles must overlap for maser action. This indicates the need for velocity coherence, where enough molecules along the path must have similar velocities for overlap in ϕ_ν. Two important terms in the rate equations are the pump rates $R_2(N - N_{lu})$ and the stimulated emission $-(N_u - N_l)BJ$ terms. The pump rate term is a measure of how many molecules come from the non-masing states into the masing states. For population inversion, $R_2(N - N_{lu})$ must either dominate the first equation of 2.5, which would be called the unsaturated case, or be close to the stimulated emission term $-(N_u - N_l)BJ$, which is the saturated case. Another way to have population inversion, is if the pump rate to the lower level is negligible and the $-\Gamma N_l$ dominates the second equation of 2.5. The specifics of these mechanisms for different molecules are briefly discussed in sections below.

There are physical differences between saturated and unsaturated masers. Unsaturated masers have pumps rates higher than the rates of downward stimulated emission. This causes an increase in I_ν that is exponential along the path length. Saturation, on the other hand occurs when the pump rate and stimulated emission rates are equal, and then the increase in I_ν only scales linearly with path length (Goldreich and Keeley, 1972). This should be taken into consideration when interpreting maser variability in observations. An unsaturated maser might flare dramatically due to relatively modest changes in the background radiation, while a flare in a saturated maser is an indication of changes in the pumping environment. Unfortunately, from an observational standpoint, it is difficult to judge whether or not a maser is saturated (Lankhaar and Vlemmings, 2019; Gray et al., 2020).

A "pumping mechanism" is a description of the steps through a molecule's energy levels through a combination of absorption, stimulated and spontaneous emission and collisional (de)excitation to produce population inversion in a population of molecules. The effectivity of a pumping mechanism is a function of internal and external parameters. The external parameters are the hydrogen gas kinetic temperature and density, the abundance of the masing molecule and the dust temperature. The internal parameters, which are fixed for any particular molecule, are the collisional coefficients of the molecule with H_2, and the Einstein coefficients of the energy states. A single molecule may have many physically realisable maser states, each with different external parameter requirements. A masing transition is "collisionally pumped" if the H_2O molecules are excited to upper energy levels by H_2 and if the radiative de-excitations dominate the collisional de-excitations (Kylafis and Norman, 1991). On the other hand, a maser transition is "radiatively pumped" if the molecule is excited to the upper levels by continuum radiation at a higher temperature than the gas kinetic temperature (Cragg et al., 1992). These two categories are not mutually exclusive, but gives a helpful (if not overly simplified) framework to interpret the observation of certain maser transitions.

The most important astrophysical masers are hydroxyl (OH), methanol (CH_3OH) and water (H_2O). A multitude of other astrophysical masers have also been detected, such as silicon monoxide (SiO), formaldehyde (H_2CO), and many others (Gray, 2012). The environments where masers have been detected in the Milky Way are SFRs and late type stars. Extragalactic "megamasers" have also been found in OH and H_2O (Elitzur, 1992). Extragalactic masers and late-type-star masers are not considered in this work. The following sections describe H_2O, and CH_3OH masers.

Water Masers

Water (H_2O) is the molecule associated with a maser transition at 22.23508 GHz. It has the highest brightness temperature features ($T_b \sim 10^{11} - 10^{14}$ K, Elitzur et al., 1989) and is quite abundant, with an estimated $1000 - 1500$ sources in the Milky Way (Walsh et al., 2011). The water molecule's

rotational energy level tree is divided into two modes, dependent on the relative spins of the H nuclei, para-H_2O (if the spins are aligned) and ortho-H_2O (if the spins are opposite) (Gray, 2012). Other than the 22 GHz transition, Gray et al. (2016) list 26 water maser transitions that are predicted or have been observed in the frequency range $\sim 67 - 906$ GHz and are observable with ALMA. They also list 10 maser transitions in the frequency range $\sim 1269 - 1901$ GHz that are observable with SOFIA. This shows that there is still a great deal of study to be done in water masers. As this work is primarily concerned with 22 GHz water masers, the other water maser transitions are not discussed in this review.

The first detection of 22 GHz water masers was by Cheung et al. (1969) towards Sgr B2, the Orion Nebula and W49. The first theoretical treatment of this maser transition was by de Jong (1973). He calculated the optical depths, gains on the background radiation and path lengths for 22 GHz water masers under certain assumptions of H_2 densities and H_2O molecule abundances. From a theoretical standpoint, a physical picture has emerged on the origin of 22 GHz water maser emission. Elitzur et al. (1989) show that 22 GHz water maser emission may arise in shock fronts; and are typically termed as collisionally pumped. They differentiate two types of shocks. Magnetohydrodynamic (MHD) C-shocks ($v_s \leq 40 - 50$ km s^{-1}) and higher shock velocity J-shocks, where $v_s \geq 40 - 50$ km s^{-1} and MHD effects are negligible. They describe a physical picture for water masers from J-shocks. In their picture, elaborated upon by Hollenbach et al. (2013), shock fronts with sheetlike geometries have regions with long enough path lengths of coherent velocities so that masing action can occur. J-shocks in clouds with densities $n_0 \sim 10^7$ cm^{-3} and temperatures $> 10^4$ K dissociate the molecules as the shock front propagates through the clouds. Some time after the shock front has passed, the material cools down and H_2 reforms on dust grains, are released and have high kinetic energies. Water is also formed in high abundances behind these shock fronts (Elitzur, 1979), and the hot H_2 excites the water molecules to high enough energy levels to induce population inversion for the 22 GHz transition.

The astrophysical applications of 22 GHz water masers in SFRs should be mentioned, although a more in-depth discussion of some topics appear in later chapters. Observationally, 22 GHz water masers are bright, spatially compact and highly time-variable in flux density. The shock nature of 22 GHz water masers has led some to use the proper motions of water masers as a tracer for gas motion (e.g., Burns et al., 2016; Torrelles et al., 2001). These studies utilize multi-epoch VLBI observations of water masers to calculate water maser proper motions.

Methanol Masers

The most common maser transitions for methanol (CH_3OH) are at 6.7 GHz and 12.2 GHz. There are many other transitions that have been observed, and some of them are listed in Cragg et al. (1992) and Gray (2012). More maser transitions have been detected recently in the accretion burst in G358.93-0.03-MM1 (see Section 2.7.1). One of the first groups to report methanol masers were Batrla et al. (1987). They report multiple masers with flux densities > 1000 Jy associated with UCHII regions. Menten (1991) reports the first detection of 6.7 GHz methanol masers from the $5_1 - 6_0 A^+$ transition. Later it was shown by Minier et al. (2003) that 6.7 GHz methanol masers are solely associated with high-mass SFRs. The current consensus is that 6.7 GHz methanol masers are radiatively pumped (Cragg et al., 2002), with flux densities dependent on the intensity of the circumstellar radiation field. This dependence on radiation fields, as well as its exclusive association with high-mass SFRs, have made 6.7 GHz methanol masers an important observable for studies in episodic accretion of HMYSOs. The maser monitoring organization M2O[1] uses long-term single-dish monitoring of 6.7 GHz methanol

[1] www.masermonitoring.com

masers to to try to identify episodic accretion events, also known as "accretion bursts" (Burns et al., 2022).

Successive mathematical modelling of 6.7 GHz methanol masers has shown that 2.7 K seed photons from the cosmic microwave background can be amplified to produce bright maser emission. VLBI observations by Menten et al. (1992) found that 6.7 GHz methanol masers can have brightness temperatures more than 3×10^{12} K. Sobolev et al. (1997) explain these high brightness temperatures with a Large Velocity Gradient model and found the maser brightness to be positively affected by higher dust temperature (if $T_{\rm dust} > 150$ K), higher hydrogen densities (upto $n_{\rm H_2} = 10^{7.5}$ particles cm^{-3}) and methanol abundances ($X_{\rm M} = n_{\rm CH_3OH}/n_{\rm H_2}$), peaking at 10^{-5}. Collisions were found to negatively affect the 6.7 GHz methanol maser gain (for $T_{\rm k} > 20$ K). They considered three possible explanations for the physical environments of 6.7 GHz methanol masers. The first is clumps with cylindrical dimensions, longest in the line of sight, affected by the passage of shocks. The second is protostellar disks, and the third is velocity coherent paths in a turbulent medium. Further modelling by Cragg et al. (2002) and Cragg et al. (2005) show qualitatively similar results as the simulations by Sobolev et al. (1997), with methanol masers found in a wide parameter space. 6.7 GHz methanol masers were associated with fractional methanol abundances in the range $10^{-7.5} < X_{\rm M} < 10^{-5}$, densities $10^5 < n_{\rm H_2} < 10^9$ cm^{-3} and normalized column densities $10^{10.7} < N_{\rm M}/\Delta V < 10^{13.3}$ cm^{-3} s, with $N_{\rm M}$ the methanol column density and ΔV the line width.

The requirements stated above implies that 6.7 GHz methanol masers have to form in regions with strong radiation fields, and the right conditions for the formation of enough CH_3OH. Minier et al. (2003); Breen et al. (2013) found observationally that 6.7 GHz methanol masers are exclusively associated with high-mass SFRs. Norris et al. (1998) hypothesize that 6.7 GHz methanol masers could be associated with protostellar disks. Minier et al. (2000) found that Keplerian fits to methanol masers infer central masses smaller than one solar mass, which is inconsistent with masses derived from other tracers. This indicates that either 6.7 GHz methanol masers do not trace the entire disk, or are not exclusively associated with disks. This result shows that a simple Keplerian interpretation of methanol masers need support from other tracers as well. De Buizer (2003) searched for outflow tracers perpendicular to linear structures of methanol masers, and found outflow perpendicular to only two of the 28 sources observed. VLBI proper motions measurements of IRAS 20126+4104 by Moscadelli et al. (2011) found 6.7 GHz methanol masers to be associated both with a protostellar disk and outflow. This further supports the idea that there are multiple kinds of regions in which methanol masers can form.

2.3.3 Free-free Emission

Free-free emission (or thermal bremsstrahlung) is radiation emitted by charged particles deflected by surrounding charged particles. An example of a source of free-free emission in SFRs is HII regions. The basis for free-free emission is the Larmor formula for non-relativistic charged particles (Griffiths, 2017):

$$P = \frac{\mu_0 q^2 a^2}{6\pi c} \tag{2.6}$$

with P the total power radiated (in Watts), μ_0 is the permeability of free space, q the charge of the particle in Coulomb, a the magnitude of the particle's acceleration and c the speed of light in a vacuum. When a charged particle experiences an acceleration due to the proximity of another charged particle, the charged particle radiates some of its kinetic energy into electromagnetic waves. The energy radiated is proportional to the change in the kinetic energy of the particle. For in-depth treatments of free-free emission, the reader is referred to Rybicki and Lightman (1986) and Longair (2011).

2.3.4 Synchrotron Emission

Synchrotron radiation is emitted from a relativistic electron gyrating around a magnetic field. Synchrotron radiation is an important example of non-thermal emission, produced by non-Maxwellian particle populations (contrary to thermal radiation such as free-free emission and blackbody radiation). The synchrotron spectrum is obtained by starting with the relativistic energy loss rate (Longair, 2011):

$$-\left(\frac{dE}{dt}\right)_{\text{rad}} = \frac{q^2\gamma^2}{6\pi\epsilon_0 c^3}[|a_\perp|^2 + \gamma^2|a_\parallel|^2] \tag{2.7}$$

with $\gamma = 1/\sqrt{1-\beta^2}$ the Lorentz factor, $\beta = v/c$, with v the particle speed. $a_\perp$ is the acceleration perpendicular to the direction of motion of the particle and $a_\parallel$ is the parallel acceleration. The energy loss equation is combined with the Lorentz force law to calculate the acceleration terms:

$$\vec{F} = m\vec{a} = q(\vec{v} \times \vec{B}) \tag{2.8}$$

If an electron population with a power law in the form:

$$N(E) = N_0 E^{-p} \tag{2.9}$$

is considered, with $N(E)$ the population of electrons with a specific energy, N_0 a normalization constant and p the power law index. By adding the synchrotron spectral of all of these electrons, one can show that the spectrum of the synchrotron emission has the following behaviour (Rybicki and Lightman, 1986): For the optically thick region $I_\nu \propto \nu^{5/2}$ and for the optically thin region $I_\nu \propto \nu^{-(p-1)/2}$. The turnover of the spectrum is at the critical frequency ν_c given by (Longair, 2011):

$$\nu_c = \left(\frac{3}{2}\right)\gamma^2 \frac{eB}{2\pi m_e} \tag{2.10}$$

Lastly, the synchrotron spectrum has a cutoff due to energy losses at high frequencies.

2.3.5 Dust Emission

Interstellar dust is an object of study in its own right, and a tracer of physical conditions in the ISM. The absorption of photo-ionizing radiation by dust reduces the ionization fraction of molecular clouds. This, in turn, can reduce the magnetic forces supporting the molecular cloud from gravitational collapse (Shu et al., 1987). The shape, composition, size and porosity of dust grains are still topics of active study. Helpful reviews on this topic are those by Draine (2003) and Williams (2005). Linear polarization measurements of starlight extinction indicate that a substantial population of dust grains have an asymmetric shape (Williams, 2005). Specific absorption features due to dust extinction has helped researchers to narrow down the possible composition of dust grains. Absorption features such as the 9.7 μm feature indicate that dust grains are primarily amorphous sillicon, amorphous carbon and polycyclic aromatic hydrocarbons (PAHs, large carbon chain molecules) (Draine, 2003; Compiègne et al., 2011). Dust particles have sizes ranging from micrometres down to nanometres in size, with a power law size distribution with a slope of -3.5 (Mathis et al., 1977). The ability of dust particles to absorb stellar radiation and to re-radiate the radiation in the infrared, aids gravitational collapse in molecular clouds, which leads to increased star formation efficiency (Draine, 2003). Cooling by dust radiation reduces the pressure that hinders gravitational collapse.

It has been found that the spectral features of dust are complicated for wavelengths $\lambda < 50$ μm due to the chemical composition of the dust grains, but for longer wavelengths $\lambda > 50$ μm, the spectral

features can be reasonably approximated with a greybody approximation (Draine, 2003). The greybody function is given by (Gordon, 1987):

$$F_\nu = \Omega B_\nu(T_d)(1 - e^{-\tau(\nu)}) \tag{2.11}$$

with F_ν the specific flux, Ω the solid angle subtended of the source, $B_\nu(T_d)$ the Planck black body distribution, T_d the dust temperature and τ the optical depth modelled as:

$$\tau_= \left(\frac{\nu}{\nu_c}\right)^\beta \tag{2.12}$$

with ν_c the frequency where $\tau = 1$ and β a power-law index. Further, in the optically thin frequency range, the dust mass M_d can be approximated by (Gordon, 1987):

$$M_d = \frac{F_\nu D^2}{B_\nu(T_d)}\left[\frac{4a\rho}{3Q(\nu)}\right] \tag{2.13}$$

with D the distance to the source, a the radius of the grains, ρ the grain density, $Q(\nu)$ the grain emissivity. Equations 2.11 and 2.13 are useful ways to approximate the dust temperatures and the dust mass given the assumptions of a single dust temperature and a simple dust model. This model is one of the simplest models used to interpret dust emission. Significantly more complex models exist taking into account photons scattering off of dust, photoelectric heating of dust, ice on the dust grains, dust surface chemistry, complex shapes and porosity and photo-dissociation of dust above certain temperatures.

2.3.6 Spectral Line Emission

Spectral line emission by interstellar gas plays a number of roles in the ISM and star formation studies: Interstellar gas is an object of study itself (in the field of astrochemistry), a component of cooling in the ISM, and a probe of physical conditions in astrophysics. The main constituent of interstellar molecular gas is H_2, with CO the second most abundant molecule with a fractional abundance $n_{CO}/n_{H_2} \sim 10^{-4}$ (Winnewisser and Herbst, 1993). Interstellar molecules form in various environments, but the most important consideration is the abundance of atoms that serve as molecular constituents, sufficient temperature to form molecules, and lack of photo-dissociating radiation (typically radiation from stars). Molecular clouds are sites with abundant molecules, as the molecular clouds are typically opaque to destructive stellar radiation due to dust grains with high extinction in the visible and UV bands (Williams, 2005). A large number of atoms and molecules have been detected due to mm and sub-mm observations of their rotational transitions. Figure 2.1 shows the physical conditions in which various molecules emit line emission. Note that the y-axis is inverted, with low densities at the top. The low to mid J CO rotational emission traces low densities (10^2 cm^{-3} $< n_{H_2} < 10^5$ cm^{-3}) and temperatures (10 K$< T_k <$ 300 K) while molecules like NH_3, CS and HCN trace higher densities with $n_{H_2} > 10^5$ cm^{-3}. The critical density n_{crit} is the density at which the rate of collisional excitation to a specific energy level is equal to the rate of radiative de-excitation. For a two-level approximation the critical density is given by (Winnewisser and Herbst, 1993):

$$n_{crit} = \frac{A_{ul}}{\langle \sigma_{ul} v \rangle} \tag{2.14}$$

with A_{ul} the Einstein coefficient for the transition $u \rightarrow l$, with u the upper level and l the lower level. σ_{ul} is the collisional cross-section of the transition and v the particle velocity. The angle brackets indicate averaging over the velocity distribution. n_{crit} is a lower bound of n_{H_2} for emission of the specific line radiation in question. The presence of molecular lines gives a measure of the existence

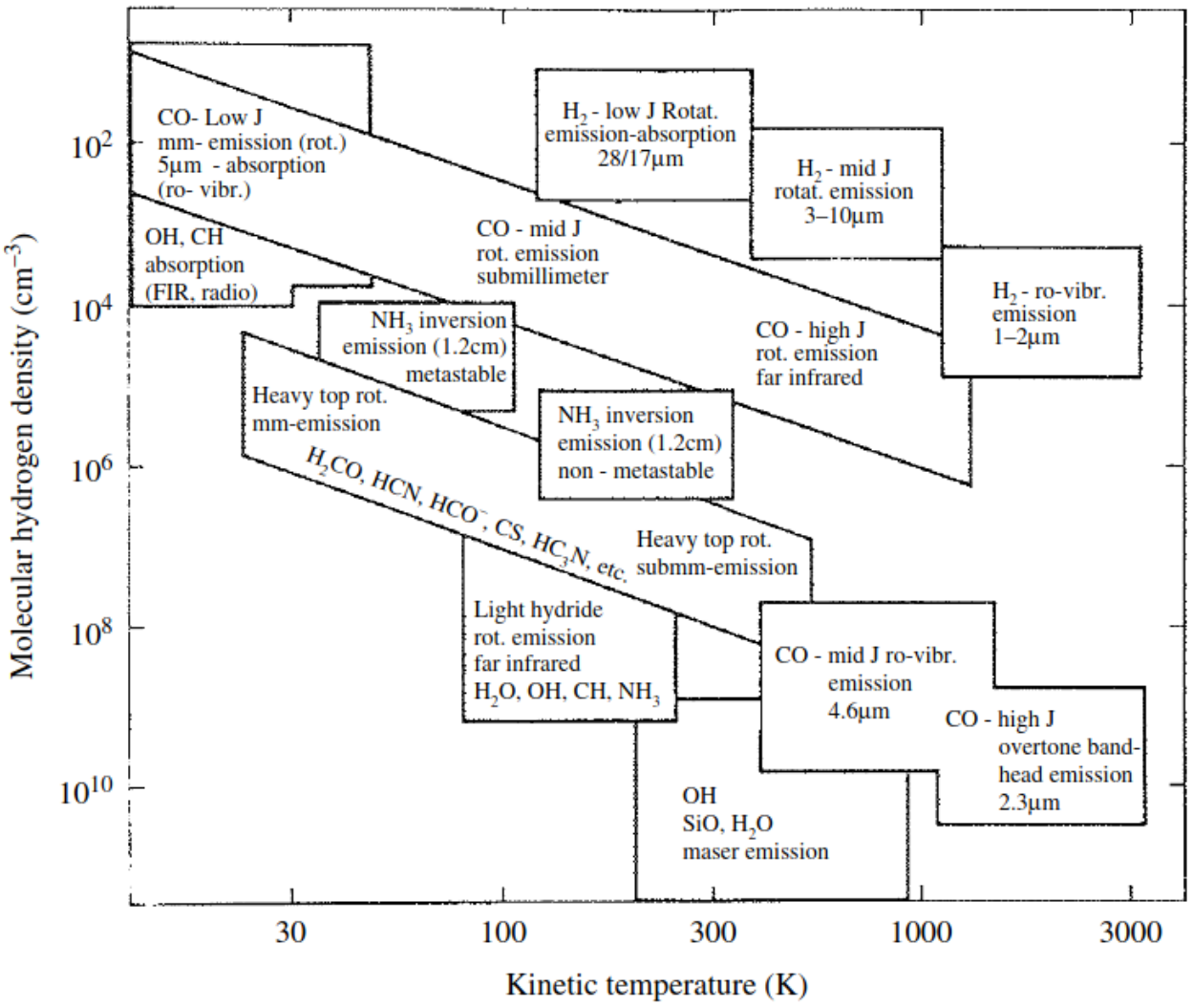

Figure 2.1: Figure illustrating the physical conditions traced by various molecular lines. Figure taken from Lada and Kylafis (1991). The x-axis is the range of kinetic temperatures for which the emission might be visible, and the y-axis is hydrogen densities which allow the emission. Note that this figure is approximate, and only intended to give order of magnitude estimates.

of the molecules that emit these lines, as well as constraints on the density and kinetic temperatures. Further, the intensity of line radiation can be used to accurately constrain n_{H_2}, while the line velocity information, such as linewidths, can give important information on the kinematics of the region in question.

2.4 Large Scale Star Formation

After significant theoretical and observational efforts, a standard picture for the formation of low-mass stars has emerged. Star formation happens predominantly in GMCs, which have masses of $10^{5-6} M_\odot$, diameters of ∼45 pc and average densities of approximately 50 particles cm^{-3} (Blitz, 1993; Williams and McKee, 1997). Carbon monoxide (CO) mappings of the Milky Way have shown that GMCs are almost exclusively found in the galactic spiral arms (Digel et al., 1996; Heyer and Terebey, 1998). GMCs contains many clumps, where clumps are denser bound regions inside the GMCs where stellar clusters may form. Clumps have been found to be either gravitationally bound, or pressure bound by the interclump medium, and the most massive clumps are those in which stars form (Williams et al., 1995). Clumps, in turn, may consists of many prestellar cores, where cores are even more dense gravitationally bound regions ($n \sim 10^5$ cm^{-3}, Benson and Myers, 1989) from which individual stars form. The precise mechanisms behind the origin of high-mass ($> 8 M_\odot$) stars is still a topic of intense study.

The two main paradigms of HMSF diverge on the nature of mass transfer within SFRs. The monolithic hierarchical collapse theory states that the mass of the final stellar cluster can be found exclusively in the original clump, and that there is not significant mass transfer between clumps in GMCs (e.g., Krumholz et al., 2005). On the other hand, there are two sub-paradigms that posit that there is significant mass transfer in a GMC. The competitive accretion model posits that mass moves over time to the centre of a gravitational potential well in the GMC, and that the most massive stars form in the places of highest potential due to the "infall" of gas (Bonnell et al., 2001; Bonnell and Bate, 2006). The inertial-inflow model is a second paradigm which also states that there is mass transfer over a large scale, but that the cause of the mass transfer is turbulent "inflow" due to multiple sources of feedback in the GMC over time, such as supernovae, protostellar jets and HII regions (Padoan et al., 2020). Observationally, the monolithic collapse theory implies the existence of starless massive dense cores (MDCs), which contain all the required mass for HMSF. Tigé et al. (2017) searched for MDCs in NGC6334 and found that the cores they identified likely grow in mass over time, and do not have the mass required for monolithic collapse. These theories concern star formation at the largest scale, but there are also open questions regarding the small-scale process close to the protostar. The next section discusses the concept of gravitational collapse, and then continues to disk and jet systems.

2.5 Mass gain and Feedback in Pre-Stellar Cores

2.5.1 Gravitational Collapse

The foundational mechanism for star formation is gravitational collapse. Gravitational collapse is when the self-gravity of a clump of gas and dust is stronger than the outward supporting forces, such as thermal or magnetic pressure. The precise details of the gravitational collapse is a function of the forces involved and the initial conditions. A short overview of the simplest cases of gravitational collapse will be elaborated from Schulz (2005), before the discussion continues to jet and disk systems.

The simplest case of gravitational collapse is that of a spherically symmetric isothermal sphere (also known as Bonner-Ebert spheres) with a constant initial density $\bar{\rho}$ (Ebert, 1955; Bonnor, 1956).

Jeans (1902) showed that a gas with a mass larger than the Jeans mass, $M_{\rm J}$, will undergo gravitational collapse. $M_{\rm J}$ is given by:

$$M_{\rm J} = \frac{4}{3}\pi R_{\rm J}^3 \bar{\rho} \tag{2.15}$$

with $R_{\rm J} = \frac{1}{2}\lambda_{\rm J}$, where $\lambda_{\rm J}$ is the Jeans length. For an isothermal sphere, $\lambda_{\rm J}$ is given by:

$$\lambda_{\rm J} = \left(\frac{15 k_{\rm B} T}{4\pi G m_{\rm p} \bar{\mu} n}\right)^{\frac{1}{2}} \tag{2.16}$$

with $k_{\rm B}$, Boltzmann's constant, T the temperature of the cloud, $m_{\rm p}$ the proton mass, $\bar{\mu}$ the mean molecular mass, and G the gravitational constant and n the number density of the gas. This shows that in the simplest case, the mass required for gravitational collapse is determined by temperature, density and molecular composition. The Jeans mass is proportional to the gas temperature, with $M_{\rm J} \propto T^{3/2}$, which means that hot gas is less prone to collapse, and as the cloud heats up as it contracts, the expression for $M_{\rm J}$ implies that cooling is important for star formation. The Jeans mass is also dependent on the gas density and mean molecular mass, with $M_{\rm J} \propto n^{-1/2}$ and $M_{\rm J} \propto \bar{\mu}^{-3/2}$, which indicates that higher density gas and gas with higher metallicity is more prone to gravitational collapse. The Jeans mass is a helpful quantity to estimate the conditions under which a particular core will undergo gravitational collapse.

Once gravitational collapse starts, the core goes through multiple stages. With simplified numerical simulations, Larson (1969) identified these stages of protostellar collapse. Initially the gas in the core is in free fall, driven only by gravitation. After a while, a hydrostatic core forms, which is pressure supported and opaque to radiation. Then the core transitions into an accretion phase where material falls from the outer regions onto the hydrostatic core. When the core is massive enough, it enters the main sequence and continues its evolution. The simulation by Larson (1969) was for a spherically symmetric non-rotating cloudlet, and therefore missed the formation of protostellar disks and jets.

2.5.2 Jet and Disk Systems

Recent observational and theoretical efforts have shown the existence of accretion disk-outflow systems in protostellar cores of all masses (Frank et al., 2014). This section aims to describe an emerging picture of disk-outflow systems in star formation. Figure 2.2 from Frank et al. (2014) shows our current understanding of accretion disk-outflow systems in low-mass SFRs. The left panel represents some mechanisms involved in accretion and the disk on scales between 0.01 and 100 AU. The middle panel represents the processes within the jet on scales between 100 and 5000 AU. The right panel represents the idea that feedback from protostellar outflows affects the star forming region on a larger (> 1 pc) scale. It is not yet clear which particular physical processes in low-mass SFRs are also found in high-mass SFRs. Most, if not all, YSOs of all mass ranges are accompanied by accretion driven outflows.

These outflows can be of two kinds. The first is high-velocity collimated (narrow-angle) jets with velocities ranging $v \sim 100 - 1000$ km s^{-1} that are believed to be focused by MHD processes. It was first proposed by Kwan and Tademaru (1988) that toroidal magnetic fields generated by currents in the protostellar disk might serve to collimate material from stellar and disk winds to form high-velocity jets. The other kind of outflow is low-velocity wide-angle molecular outflows with velocities $v \sim 1 - 30$ km s^{-1}. Molecular outflows are seen to consist of material from the protostellar envelope swept up either by the shock of the high-velocity jet, winds from the disk or from a much slower wide-angle component of the jet.

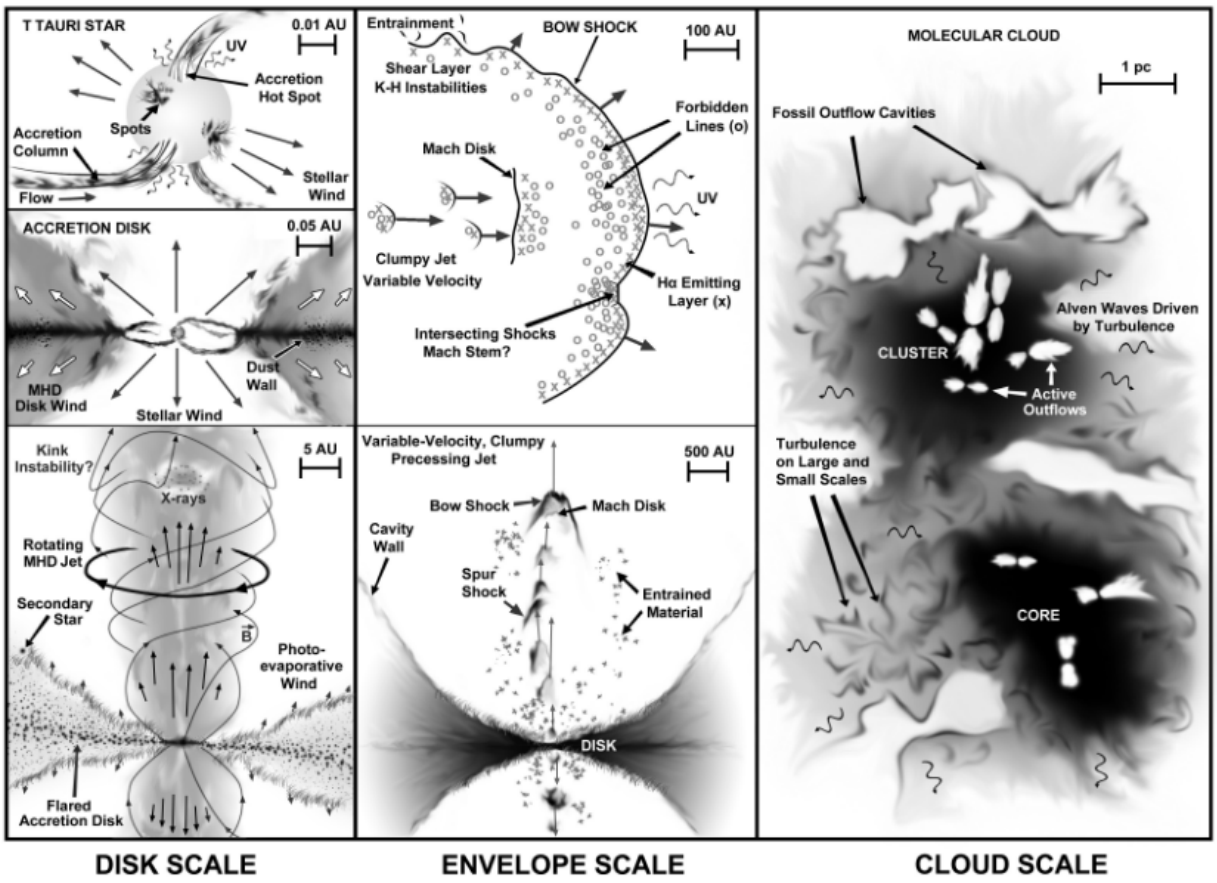

Figure 2.2: A schematic view of jets and outflows in low-mass SFRs. The figure is taken from Frank et al. (2014). This figure is discussed in Section 2.5 Note that the length scales are different for each panel.

This combination of collimated jet paired with a wide-angle outflow has been observed in both low-mass and high-mass YSOs (Arce and Sargent, 2006; Torrelles et al., 2011). It is important to note that jets are not continuous lines of material, but a series of non-homogeneous clumps of material with slightly different physical conditions. It is observed as a single jet due to angular resolution or sensitivity constraints in observing instruments.

Both kinds of outflows have important roles in both increasing star formation efficiency $\eta_{\rm SF}$ on a disk and envelope scale ($\sim$1 $-$ 500 AU) and suppressing $\eta_{\rm SF}$ on cloud scales ($\sim$ 1 pc) (Frank et al., 2014). On disk and envelope scale, rotating jets and outflows serve to extract angular momentum from the protostellar disk, which allows material from the accretion disk to fall onto the star (Frank et al., 2014). An excellent example of this in low-mass protostars is the Herbig-Haro (HH) object HH212 (Lee et al., 2017). On the other hand, ALMA observations of the high-mass young stellar object Orion Source I have shown a velocity gradient perpendicular to the outflow direction. The ejection of angular momentum by outflows has been observed to be important for HMYSOs as well (Hirota et al., 2017).

These jets and outflows open up a cavity in the protostellar envelope through which material and radiation can easily escape. The cavity grows over time as more material is swept up (Frank et al., 2014). The cavities benefit star formation by opening low optical depth paths for radiation and hot material to escape, aiding gravitational collapse (Arce and Sargent, 2006). On the other hand, simulations of protostellar collapse without magnetic fields found that star formation efficiency was significantly hindered by outflows for both low-mass (Hansen et al., 2012) and high-mass (Wang et al., 2010) stars, as outflows can disrupt infalling material on parsec scales. This has an especially great impact for HMYSOs, which might source their mass from large-scale mass inflow.

There is a link between accretion and ejection for star formation studies. Ejection provides a mechanism for releasing gravitational potential energy from the protostellar core, aiding gravitational collapse and mass gain. For HMSF studies, pinning down the precise line between accretion and ejection may be a tool for understanding the embedded central environment of HMYSOs. It has been found some protostars of all masses gain much of their mass in relatively short periods of high accretion rates, relative to the formation time (Audard et al., 2014; Caratti o Garatti et al., 2017; Meyer et al., 2017). These two processes are also intimately related, as some material accreted during accretion bursts are ejected in high-velocity jets or low-velocity outflows.

2.6 Episodic Accretion in Low-Mass YSOs

In 1936, the star FU Orionis underwent a massive flare in its optical brightness. The origin of the flare was later identified as a large increase in mass accretion from an accretion disk of a T Tauri star, a low-mass protostar (Herbig, 1977; Hartmann and Kenyon, 1985). This phenomenon was subsequently observed in multiple T Tauri stars. Figure 2.3 shows the light curves of 5 such bursting sources. From Figure 2.3 it is clear that the bursts observed had different rise times and duration. Some bursts are observed to repeat. Some sources had longer burst and rise times (such as V1057 Cyg, V1647 Ori and HBC 722) while others showed faster rise times and multiple bursts in a relatively short time (such as EX Lup and V2492 Cyg). This has led to the classification of two kinds of bursts: FU Orionis bursts (or FUors), which are typically longer and more luminous, and EXors, which are shorter, more frequent and less bright (Audard et al., 2014).

During outbursts, FUors can have large bolometric luminosities of $100-300 L_{\odot}$, as well as accretion rates between 10^{-6} and $10^{-4} M_{\odot}$ yr^{-1} (Audard et al., 2014). Their bursts can last between a few years

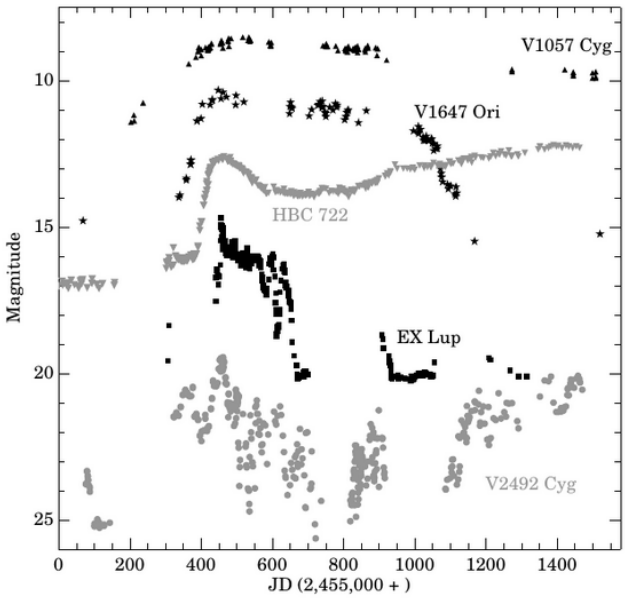

Figure 2.3: Time series for various FU Orionis and EXOr bursting sources. Figure from Audard et al. (2014).

and a few hundred years, with variability of the light curve at time scales much smaller than the burst time. EXors, on the other hand, lack the spectral features of FUors, with bolometric luminosities in the order of $1 \sim 10 L_{\odot}$. Their burst accretion rates are also much lower, ranging between 10^{-8} and $10^{-6} M_{\odot}$ yr^{-1} and with their bursts lasting for about $1 - 2$ years, with sub-bursting variability of $30 - 60$ days (Audard et al., 2014). These differing characteristics indicate different mechanisms for the burst. FUors are thought to occur when more material falls into the protostellar disk from the circumstellar envelope. This leads to a buildup of material in the disk, which falls on to the protostar at some regularity determined by the disk and accretion processes. On the other hand EXors are thought to be caused by instabilities in the protostellar disk, which in turn lead to a variable accretion rate. The mechanisms that cause accretion bursts in low-mass protostars are candidates to explain bursts in high-mass protostars as well. Therefore, the mechanisms proposed for FUors and EXors are briefly enumerated.

Audard et al. (2014) enumerate four possible burst mechanisms. These mechanisms can be internal to the disk, or caused by external bodies. The four mechanisms proposed are thermal instabilities, magnetorotational instabilities (MRI) combined with gravitational instabilities (GI), disk fragmentation and external triggers. Each of these mechanisms predict different rise times, burst lifetime, accretion rates and bolometric luminosities. To understand these mechanisms, the basics of accretion in accretion disks must be understood. Angular momentum conservation in accretion disks implies that gas can only accrete onto the protostar if the gas loses angular momentum. The most frequently proposed mechanism for angular momentum loss is angular momentum transfer due to viscosity in the accretion disk. Viscosity in the accretion disk material causes friction between different annuli of the disk, which allows angular momentum to be transferred from the inner disk close to the star, to the outer disk. If the inner regions of the accretion disk have sufficiently low angular velocity Ω, the material can fall onto the accretion column, and finally the protostar. The consequence of the above argument is that disk viscosity ν is a fundamental parameter determining the accretion rate. The viscosity is difficult to model from first principles, but a helpful expression for viscosity can be found

in Audard et al. (2014):

$$\nu = \alpha \frac{c_s}{\Omega} \propto \frac{\alpha T}{\Omega} \tag{2.17}$$

with c_s the sound speed of the disk, α the viscosity parameter, encoding all the complicated physics of the viscosity and T the temperature of the disk.

The first possible burst mechanism, called a *thermal instability*, occurs when there is a temperature runaway, which in turn increases ν and finally the accretion rate $\dot{M}$. This can happen when the disk is close to the hydrogen ionization temperature $T \sim 5000$ K, which causes the opacity, κ, of the disk to be very sensitive to temperature, where $\kappa \sim T^{10}$. This leads to a disk that traps radiation very well due to its high opacity, and this behaviour only ends once the disk is fully ionized at $T \sim 10^5$ K (when the majority of the photons have energies $h\nu > 13.6$ eV, Audard et al., 2014). Thermal instabilities can either be triggered in the inside disk, or can be caused by an external trigger. It was shown by Clarke and Syer (1996) that sufficiently massive protoplanetary companions of T Tauri stars are possible triggers of the fast bursts observed in FU Orionis and V1057 Cyg. This would cause periodic bursts with a fast (< 1 yr) rise time.

The second mechanism that may explain episodic accretion is *MRI combined with a GI*. It was found by Hawley et al. (1995) that accretion disks with weak magnetic fields and angular velocity increase outward ($d\Omega^2/dr > 0$) generate turbulence in the accretion disks which significantly increases disk effective viscosity and therefore $\dot{M}$. For more information on MRI + GI bursts, see Audard et al. (2014) and the references therein.

The third possible cause of episodic accretion is *disk fragmentation*. Fragmentation in protoplanetary disks occur when the disk's Toomre parameter Q (Toomre, 1964) is below unity. Q is given by:

$$Q = \frac{c_s \kappa}{\pi G \Sigma} \approx \frac{c_s \Omega}{\pi G \Sigma} \tag{2.18}$$

with Σ the disk surface density. When the cooling timescale of the disk is significantly longer than the dynamic timescale of the disk, spiral structures tend to form. On the other hand, for short cooling timescales, the disk fragments into distinct clumps. These fragmented clumps then lose angular momentum due to gravitational interaction with the circumstellar disk, and finally are accreted by the protostar (Machida et al., 2011). As the disk fragments can have various rotation rates, masses and sizes, the accretion bursts driven by disk fragmentation have different accretion rates, rise times and durations. For low-mass YSOs (LMYSOs) it has been shown that for rotating collapsing cores in the thin disk approximation, accretion bursts due to disk fragmentation will happen often during the protostar's formation time (Vorobyov and Basu, 2006). It was also found that bursts were more regular in cores with more rotation in terms of gravitational potential or larger initial core mass will undergo bursts more often. On the other hand, frozen in magnetic fields were found to lower the critical Q value (i.e., making it more difficult for gravitational instabilities to form), which would reduce burst activity. The role disk fragmentation plays in HMYSOs has been examined repeatedly in recent years, and is discussed in Section 2.7.

The final mechanism for accretion bursts in LMYSOs is *external triggers due to binary system or N-body interactions*. It was shown by Bonnell and Bastien (1992) that binary systems of LMYSOs can undergo accretion bursts due to tidal interactions of the disk-star systems. They found that a binary system with an unequal mass ratio can induce an accretion burst in the lower mass companion either through spiral arm formations in the disk (which increase accretion rates due to gravitational torques) or if the star-disk systems pass through each other, essentially increasing the YSOs mass reservoir for a

short period of time. Binary systems will undergo accretion bursts at the orbital period of the system. An important caveat to this model is that there must be a high-mass ratio between the YSOs, which limits this mechanism to star formation clusters containing more high-mass stars. This might indicate this mechanism is important for inducing FU Orionis bursts in LMYSOs in high-mass SFRs. The second external trigger is bursts due to gravitational interactions in a star-forming cluster. Pfalzner et al. (2008) simulated mass loss and gain of star-disk systems in a dense star-forming cluster. They found that in the inner regions (within 0.2 pc of cluster centre) of dense SFRs (such as the Orion nebula cluster) high-mass stars $M_* > 5\ M_\odot$ can add up to 10% of their disk mass due to close encounters with other YSOs. In the next section, the processes found recently to cause episodic accretion in high-mass protostars will be discussed, as well as many confirmed accretion bursts up to the time of writing.

2.7 Accretion Bursts in HMYSOs

2.7.1 Observations

In the last few years, there have been confirmed observations of accretion bursts in a few high-mass SFRs. A few tracers are used to identify and test accretion bursts. Long-term single-dish maser monitoring has been found to be an easy way of identifying accretion bursts, as high cadence (an observation around every 15 days) can give short notice of a maser flare, prompting follow-up observations (Burns et al., 2022). Follow-up observations can include observations in multiple infrared bands, millimetre or centimetre observations. Multi-band infrared observations have a dual use. They can confirm or deny an accretion burst, as infrared flaring is typically associated with an accretion burst.

Millimetre observations can trace the dust envelope of the protostar as well as molecular outflows produced by episodic ejections, allowing an ejection history (and therefore accretion history) to be constructed of past events. Dust and molecular line observations can be used to identify the envelope mass, temperature, density and chemical composition or changes in these parameters if previous observations have been done. Lastly, centimetre observations can see free-free emission by ultra-compact HII (UCHII) regions around the protostar, which is a direct measurement of the protostar's ionizing flux. Interferometric observations of various maser species are also possible in both millimetre and centimetre domains, with each maser species and transition tracing different physical circumstances. This section reviews most confirmed accretion bursts in high-mass SFRs. NGC6334I-MM1 is reviewed separately in Section 2.8.

S255 IR-NIRS 3

S255IR is an embedded protostellar cluster, invisible in optical wavebands, but bright in infrared (Howard et al., 1997). The region has an estimated mass of $300 - 400\ M_\odot$ and bolometric luminosity of $\sim 2 \times 10^4\ L_\odot$ (Zinchenko et al., 2015). The region also harbours 6.7 GHz CH_3OH masers (Longmore et al., 2006), which is one indication that it is a region of HMSF (Minier et al., 2003). The HMYSO S255IR NIRS-3 (hereafter NIRS-3) is located at a distance of $1.78^{+0.12}_{-0.11}$ kpc from the Sun according to parallax measurements of bright H_2O masers (Burns et al., 2016). NIRS-3 harbors a $\sim 20 M_\odot$ protostar, as well as a rotating disk traced in thermal molecular line emission and a large-scale molecular outflow seen in CO (3-2) (Zinchenko et al., 2015). VLBI observations of H_2O masers have also revealed a bow-shock type structure moving away from the central YSO (Burns et al., 2016).

Fujisawa et al. (2015) reported a CH_3OH maser flare in NIRS-3, and follow-up observations were done by Caratti o Garatti et al. (2017) using the Panoramic Near Infrared Camera (PANIC). They observed the region in 1.65μm (H-band) and 2.16μm (K-band) and found a brightening of ~ 3.5 mag

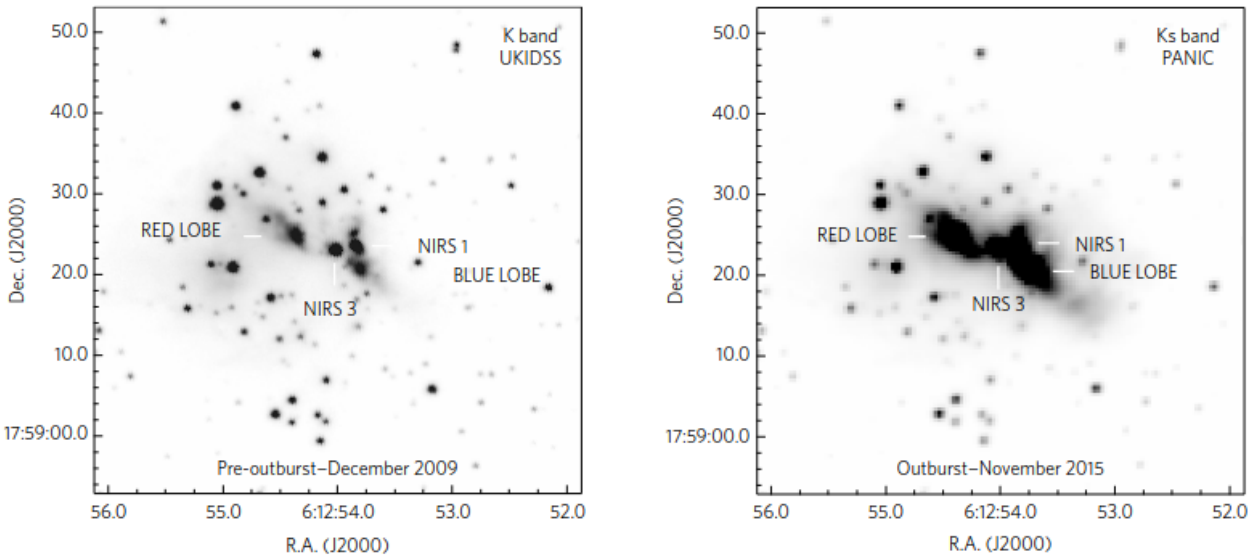

Figure 2.4: Left: K band observations of S255IR-NIRS3 at 2009, before the burst in the region. Right: Ks band observations on 2015, showing the change in infrared radiation in the region due to the burst. Figure from Caratti o Garatti et al. (2017).

and ~ 2.5 mag respectively compared to archival data from 2009. Figure 2.4 shows the infrared images before and after the burst of NIRS 3. It shows a clear brightening of the centre of NIRS 3 as well as the "red lobe" and "blue lobe" associated with bipolar outflows (Zinchenko et al., 2015). Caratti o Garatti et al. (2017) also did spectroscopic observations in K band using SINFONI/VLT of NIRS-3 in 2016 and compared it to previous observations in 2007. New emission lines were excited, specifically Na I and He I, which are associated with accretion bursts in LMYSOs (Audard et al., 2014). Further, compiling data from various wavelengths, they found the peak of the Spectral Energy Distribution (SED) to have moved significantly to longer (redder) wavelengths (Caratti o Garatti et al., 2017, 18 μm to 60μm, Figure 3 of). This is consistent with the prediction of Meyer et al. (2019a) for accretion bursts in HMYSOs. They calculated an accretion bolometric luminosity of $\Delta L_{\rm acc} = 1.6^{+0.4}_{-0.3} \times 10^5 L_\odot$ by comparing the bolometric luminosities calculated from the SEDs before and during the burst. They calculated a mass gain of $\sim 3.4 \times 10^{-3} M_\odot$ from the burst. They concluded this event to be an accretion burst in a HMYSO caused by material falling onto the star due to disk fragmentation.

Many other observations were conducted during and after the accretion burst. Moscadelli et al. (2017) observed 6.7 GHz CH_3OH masers in the region with the European VLBI Network and the JVLA. VLBI imaging showed that new bright CH_3OH masers were excited ~ 700 AU (projected distance) from the 5 GHz continuum peak, one old masing region disappeared and one region remained unchanged. The change in the methanol maser peak implies a linear speed of around 0.02c. They concluded that the change in the masers could not be due to physical gas motion, but was a propagation of pumping conditions for the 6.7 GHz methanol masers. Uchiyama et al. (2020) did long-term IR K_s band observations of NIRS-3 and constructed a time series of the IR radiation from November 2015 to March 2019. They found that the IR luminosity dropped quite sharply in the four years after the burst, even dropping 0.3 mag below the pre-burst magnitude in 2019. Finally, Hirota et al. (2021) did single-dish and VLBI 22 GHz H_2O maser observations of NIRS-3 over seven epochs in 2017. They calculated water maser proper motions, and found them not to be significantly different than the pre-burst proper motions found by Burns et al. (2016), which is consistent with the picture that water masers are collisionally pumped and would therefore only flare after mechanical energy has been

injected from the burst into the bow shocks at the tip of the outflow. This would take more than 60 years. They also found mild variability in the water masers through the observing time, and attributed it to the change in the radiative environment due to the accretion burst.

G358.93-0.03-MM1

G358.93-00.03 (hereafter G358) was detected in 2006 in a 6.7 GHz methanol maser multibeam survey (Caswell et al., 2010). The detection of 6.7 GHz methanol masers marked G358 as a region of HMSF (Minier et al., 2003). In 2018, Sugiyama et al. (2019) detected a flare in the 6.7 GHz methanol masers, which prompted follow-up observations with multiple instruments by members of the maser monitoring organization M2O[2]. Note that before the 2018 flare, the region was not well studied. Follow-up observations during and before the flare proved to be remarkably productive. MacLeod et al. (2019) conducted search observations with HartRAO of multiple CH_3OH, OH, H_2CO and H_2O maser transitions. They detected four new maser transitions in G358, with two of the transitions reported for the first time in any SFR. Three of the observed transitions were found to flare contemporaneously, and quickly. They found 22 GHz water masers to flare with a factor of ~ 45. They also observed the region in near-infrared (NIR) with the Gamma-ray Burst Optical/Near-infrared Detector, and did not find a NIR flare in the region.

Brogan et al. (2019) observed the source for the first time with (sub)millimetre interferometers ALMA and SMA. They discovered 8 cores (MM1...MM8) with ALMA 0.89 mm emission. They did not find any variation in the sub(mm) flux during two epochs of observation after the burst. Further, they used their ALMA and Sub-millimetre Array (SMA) data, combined with other (sub)millimetre and IR data to calculate a bolometric luminosity of $5700 - 22000 L_\odot$ for the whole G358 region. They also discovered 14 new CH_3OH maser lines in the frequency range of 199 to 361 GHz. The maser positions traced an elliptical pattern around G358-MM1 (later confirmed to be the bursting source).

Chen et al. (2020a,b) discovered maser lines in $^{13}CH_3OH$ (isotopic methanol), HDO (water, with one deuterium molecule) and HNCO. Interestingly, these maser lines disappeared within a month after they appeared, but the group confirmed that these maser species traced spiral arms around a core. They hypothesized that the spiral arms were caused by gravitational instabilities and are tracing inward accretion flow onto the HMYSO. Another methanol maser study reported three torsionally excited CH_3OH maser lines (Breen et al., 2019). VLBI observations with the Long Baseline Array of 6.7 GHz CH_3OH masers by Burns et al. (2020) found that during the burst, the masers in G358-MM1 were destroyed and re-exicited at very high speeds $\geq 4\%$ of the speed of light. The authors did not attribute the propagation of the masers to actual gas motions, rather they interpreted it as a propagation of radiative conditions where the radiatively pumped Class II methanol masers can exist. It was later confirmed with far infrared observations with SOFIA that G358 did in fact undergo an accretion burst (Stecklum et al., 2021). They found that the SED for the source changed significantly between their observation with SOFIA and previous observations with the Herschel Space Telescope. They concluded that the G358 burst was much fainter and shorter than the bursts in NGC6334I and S255IR-NIRS3.

M17 MIR and G323.46−0.08

At time of writing, there had been one more confirmed accretion burst (M17 MIR) and a possible but unconfirmed accretion bursting source (G323.460.08) in the literature. M17 MIR is a region that has

[2] www.masermonitoring.com

Table 11
Key Parameters of Six MYSOs with Accretion Bursts

Name	d (kpc)	$L^{\rm pre}$ (10^3 $L_\odot$)	$L^{\rm burst}$ (10^3 $L_\odot$)	$L^{\rm post}$ (10^3 $L_\odot$)	$\Delta F_{\rm IR}$	$\Delta F_{\rm mm}$	Δt (yr)	Maser Flaring	Note
V723 Car	2.5		···	4	∼10	···	5	···	$K \gtrsim 12.9$
S255IR–NIRS3	1.8	29	160	···	$\gtrsim$10	2	2	CH_3OH, H_2O	$K \gtrsim 9$
NGC 6334I–MM1	1.3	2.9	47.6	···	16.3	3.9 ± 0.6	>6	CH_3OH, H_2O	K-band invisible
G323.46–0.08	4.8	···	···	···	···	···	···	CH_3OH	K-band visible
G358.93–MM1	6.75	7.6	19.3	12.7	$\gtrsim 2$	···	$\lesssim$0.5	CH_3OH	$K \gtrsim 15$
M17 MIR	2.0	1.4	9.0	1.4	$\gtrsim 10$	···	$\sim 2 \times 15$	H_2O	$K \gtrsim 22$

Figure 2.5: Comparison of different stellar parameters for recently observed accretion bursts in HMYSOs from Chen et al. (2021). Note that there also was a flaring of OH masers in NGC6334I (MacLeod et al., 2018).

been shown to be variable in mid-infrared emission (Chen et al., 2021). Chibueze et al. (2016) studied 22 GHz water maser proper motion in the M17 cluster. They found outward proper motions indicative of an expanding bubble with a dynamic timescale of ∼12.5 years. The source of the water masers was not visible in many infrared wavebands, except in the 4.5 and 5.8 μm *Spitzer* wavebands. (Chen et al., 2021) investigated this source further, looking into multi-wavelength archival infrared data from 1993 until the date of publication. In IR, they found two flux peaks, in 1993 and 2017. In 22 GHz water masers, they found a similar flux density time series. They modelled SEDs for the source in 2005 and 2017 using the methods of Robitaille (2017). They found changes in stellar parameters comparable to that in NGC6334I. Another source that has been hypothesized to be an accretion bursting source is the periodic methanol maser source G323.460.08 (Proven-Adzri et al., 2019). The reason for the author's hypothesis of an accretion burst was a sudden rise, as well as a decay, of the 6.7 GHz methanol masers. Unfortunately, an accretion burst cannot be confirmed based only on maser time series data without infrared or millimetre observations.

2.7.2 Simulations

A question relevant for this discussion is whether all the processes involved in the formation of high-mass stars are the same as for lower mass stars. As discussed in Section 2.6, it is well established that low-mass stars gain a significant portion of their initial mass during relatively short periods of high-mass gain $\dot{M}$ relative to their quiescent periods. Simulations of primordial star formation, which investigate the possibilities for the formation of the very first stars in the universe suggest that early high-mass stars might also have had significant episodic accretion events (Stacy et al., 2010; Hosokawa et al., 2016). Radiative hydrodynamic simulations of a 100 $M_\odot$ protostellar cluster of a single HMYSO indicated that episodic accretion events in HMYSOs may be possible (Meyer et al., 2017). In there simulations they found that accretion disks of HMYSOs may be prone to gravitational instabilities, forming spiral arms, which in turn form clumps of material which loses their angular momentum through gravitational interactions with the spiral arms, and ultimately fall into the protostar. The simulations can be compared to the observations, to constrain the physical mechanism.

Figure 2.5 shows a table of basic burst parameters of six possible bursting sources from Chen et al. (2021). Of the four confirmed and studied bursting sources, NGC6334I-MM1 had the highest luminosity increase, a factor of 16.4±4.4 (Hunter et al., 2021). G358-MM1 was the least luminous and the shortest burst, while the burst in NGC6334I-MM1 is ongoing. The mechanisms of thermal instability, MRI combined with gravitational instability, and protoplanetary disruption was modelled by Elbakyan et al. (2021) for a $15M_\odot$ protostar using 1D disk modelling. They found that the thermal instability and magneto-rotational instability scenarios produced too long duration bursts as well as

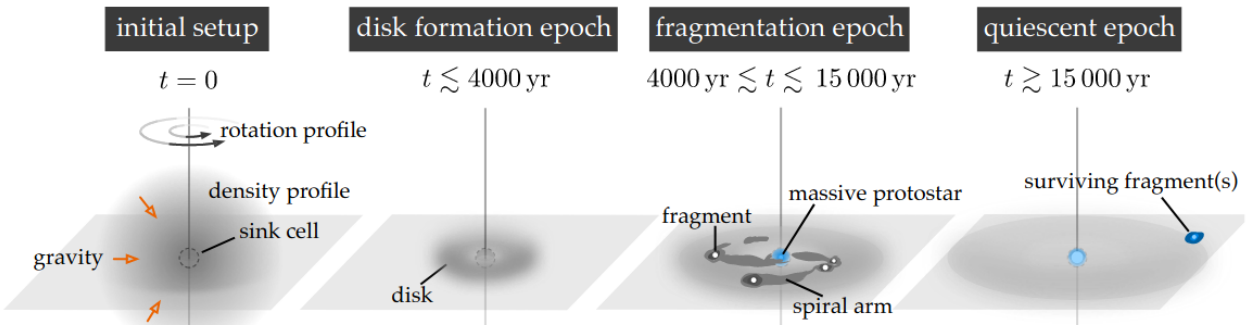

Figure 2.6: A schematic of disk fragmentation through gravitational instability. Each panel shows the density distribution in a simulation of a YSO at different times (shown above). Figure from Oliva and Kuiper (2020).

too low $\dot{M}$. On the other hand, they found that if a protoplanetary fragment of $R_{\rm p} \geq 10$ Jupiter radii is in the accretion disk, then the tidal disruption by the fragment could produce the burst duration and $\dot{M}$ consistent with the observations thus far. The results of Elbakyan et al. (2021) show that either N-body interactions or gravitational instabilities are the main mechanism driving accretion bursts in HMYSOs.

Hydrodynamic modelling of gravitational instabilities suggested that HMYSOs may gain up to $\sim 50\%$ of their initial mass in $\leq 2\%$ of their formation time in episodic accretion events (Meyer et al., 2019b). They grouped episodic accretion events by calculating the accretion luminosity $L_{\rm acc}$ as a function of accretion onto the star $\dot{M}$. They grouped bursts into 1, 2, 3 and 4 magnitude bursts by isolating the times when the total luminosity ($L_* + L_{\rm acc}$) was 2.5, 2.5^2, 2.5^3 and 2.5^4 times the quiescent accretion luminosity. From this grouping they found lower intensity bursts to be significantly more common, and to last longer than shorter, brighter bursts.

In addition, it was also suggested that accretion bursts through gravitational instabilities happen in HMYSOs in a range of physical conditions. A series of radiative hydrodynamic simulations with various initial cloud masses $M_{\rm c}$ and ratio of rotational-to-gravitational energies β found accretion bursts to occur even for very low initial rotation energies (Meyer et al., 2021). An in-depth study on the nature of the fragments and the disk of HMYSOs was done with high resolution radiative-hydrodynamics simulations by Oliva and Kuiper (2020). Their simulation reached some important conclusions regarding the nature of disk fragmentation. Figure 2.6 illustrates their results. They found that disk fragmentation happens sequentially, first spiral arms are formed within the disk (third panel of Figure 2.6, and then the spiral arms fragment. The spiral arms were found to fragment in two ways, either through GI in a single spiral arm, or through GI induced by the collision of two spiral arms. Measuring the Toomre parameter Q as a function of time and space, they found the disk to be *globally* stable, but sometimes *locally* unstable. Observationally, this has the consequence that observations that do not resolve the spiral arms or fragments of a disk might find the disk to not undergo GI, even if fragmentation is taking place at a smaller scale. Lastly, they also found the fragments to be highly dynamic. Fragments could merge, destroy one another through close approaches, dissipate through thermal expansion or even form their own disks, spiral arms and fragments. These results point to the highly dynamical nature of HMSF, with changes over relatively short timescales.

It is important to note some serious simulation caveats. Firstly, none of the simulations mentioned above included MHD effects in their treatment of the protostellar disk (Elbakyan et al., 2021, except).

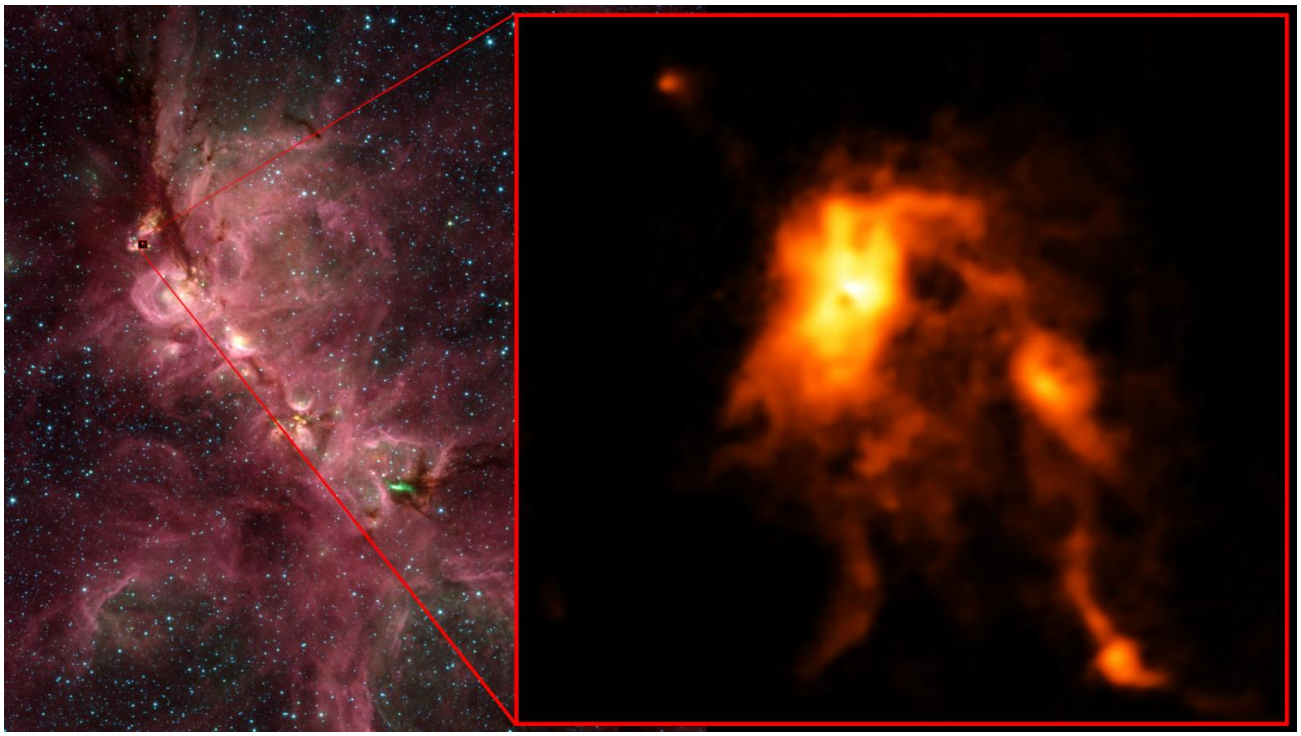

Figure 2.7: Left: An infrared image with the Spitzer Space Telescope of the NGC6334 protostellar cluster. Right: An ALMA image of NGC6334I during the recent accretion burst. Credit: ALMA (ESO/NAOJ/NRAO), T. Hunter; C. Brogan, B. Saxton (NRAO/AUI/NSF); GLIMPSE, NASA/JPL-Caltech

This could have significant effects on the accretion history due to possible effects of magnetic braking and MRI. Secondly, these simulations only take into account one disk in isolation. High-mass stars form in clusters (Zinnecker and Yorke, 2007), so binary and N-body gravitational interactions would definitely affect disk fragmentation of individual HMYSOs, which could change the burst regularity. Other effects neglected include photoionization, photoevaporation of dust, chemical composition (which could affect thermal cooling) as well as feedback and pressure due to stellar radiation.

2.8 Accretion burst in NGC6334I

NGC6334I is found in the high-mass SFR NGC6334 (otherwise known as the Cat's Paw Nebula). Figure 2.7 shows a multicolour infrared image of NGC6334 and a millimetre ALMA image of NGC6334I. NGC6334 contains multiple compact sources, named I, II, ..., V as well as I(N), north of I (McBreen et al., 1979; Rodriguez et al., 1982). The brightest sources are NGC6334I and I(N), with both harbouring water masers and NGC6334I harbouring the UCHII region NGC6334F. NGC6334 contains multiple H II regions, filaments and sub-regions at multiple evolutionary stages (Russeil et al., 2013). The region contains multiple massive clumps, with masses ranging from 3 $M_{\odot} - 6 \times 10^3 M_{\odot}$ at sizes ranging from 0.1 pc to 1.0 pc (Muñoz et al., 2007). Tigé et al. (2017) studied the distribution of MDCs in NGC6334. They derived a lower mass limit for MDCs of 75 $M_{\odot}$ and could confirm no starless MDCs. This finding supports the hypothesis that the protostellar cores do not have their final mass at the initial stages, but grow in mass over time due to mass inflow from the larger cloud. Chandra X-Ray observatory observations indicate that the region harbours between 2×10^4 and 3×10^4 protostars (Feigelson et al., 2009). The region harbours more than 100 OB (high-mass) stars (Russeil et al.,

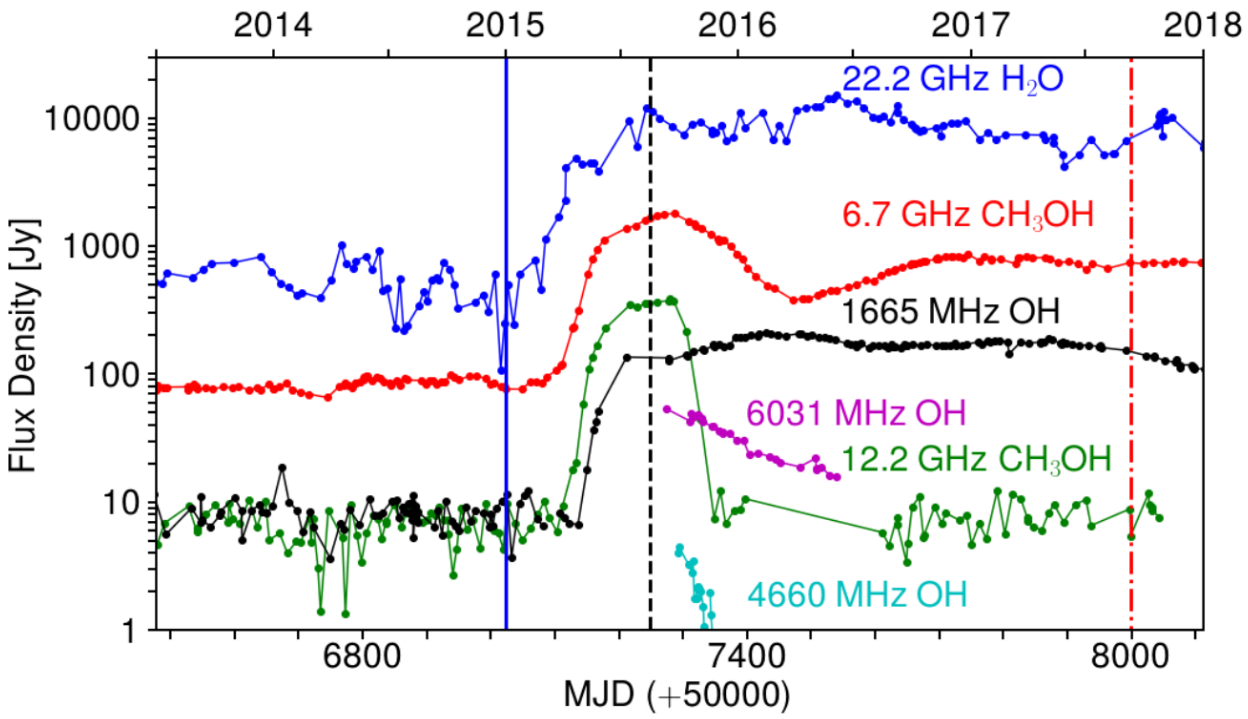

Figure 2.8: Time series for specific velocity components of various maser species in NGC6334I as seen through long-term maser monitoring at HartRAO. The velocity components which were shown of each species is described in the source of this figure, MacLeod et al. (2018).

2020). Atacama Pathfinding Experiment 345 GHz HCO^+ velocity mapping indicated that the region is undergoing global gravitational collapse, with the filaments observed in IR acting as mass reservoirs (Zernickel et al., 2013). $70 - 500$ μm Herschel Space Telescope observations revealed H II regions play an important role in changing the morphology of the region (Russeil et al., 2013), with a central filament with a line mass of $\sim 500-\sim 2000 M_\odot$ pc^{-1} over 10 pc and a width of 0.15 ± 0.05 pc, much denser than the filaments observed in the Gould Belt (André et al., 2016). The region's magnetic field was also mapped and studied by (Arzoumanian et al., 2021).

The first interferometric image of the massive protostellar cluster NGC6334I (Chibueze et al., 2014; Reid et al., 2014, $d = 1.3$ kpc) was done with the Submillimetre Array (SMA) at 1.3 mm by Hunter et al. (2006). They identified four distinct millimetre cores in the field, which were later called MM1, ..., MM4 by other authors. MM1 is the brightest, and MM3 was associated with the UCHII region NGC6334F. Later higher resolution 3 mm and 1.3 mm 2015 ALMA observations combined with 5 cm (C band), 1.5 cm (K band) and 0.7 cm (Q band) 2011 VLA observations by Brogan et al. (2016) revealed up to nine millimetre cores, named MM1, ..., MM9 respectively. They also resolved the UCHII region NGC6334F, some centimetre emission in MM1 and a previously undetected centimetre source CM2. From the K band observations, they detected 22 GHz water masers in MM1, MM3, MM4 and CM2, with the brightest masers in CM2. They also detected Class II 6.7 GHz methanol masers in MM2 and MM3 indicating that these regions harbour high-mass stars or protostars. They did not detect 6.7 GHz methanol masers in MM1.

On January 1st, 2015, multiple maser transitions of water, methanol and hydroxyl were found to be flaring in NGC6334I due to long-term maser monitoring at HartRAO (MacLeod et al., 2018). They

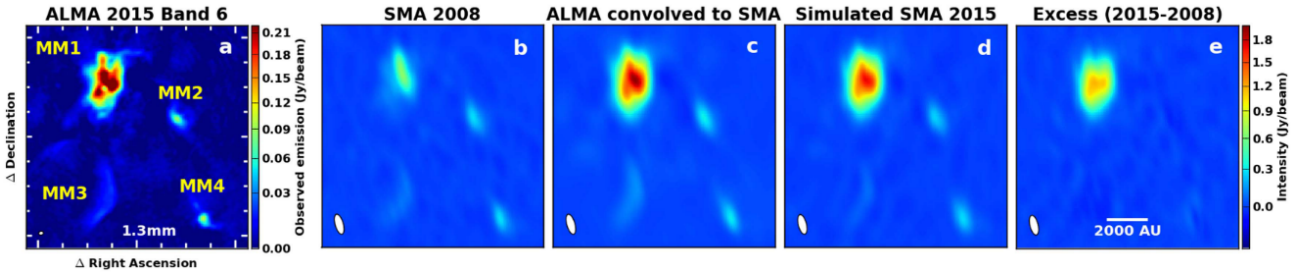

Figure 2.9: The difference in millimetre flux confirming the accretion burst. a) ALMA 1.3 mm continuum from Brogan et al. (2016) of NGC6334I. The regions MM1...MM4 are marked in the figure. The colourbar next to the figure shows the flux densities corresponding to the colourscale. b)SMA 1.3 mm continuum from Hunter et al. (2006). c) Image of a) convolved to the SMA beam. d) CASA simulation of what SMA would have seen had it observed NGC6334I in 2015 based on c) as the sky model. d) Excess in the emission between 2015 and 2008. The colourscale next to e) is the colourscale for b) to e). The figure is taken from Hunter et al. (2017).

found flaring in 22 GHz water masers, 6.7 GHz, 12.2 GHz methanol masers and multiple hydroxyl maser transitions. Certain transitions stayed in the flaring state until the last date of observation in the publication (2018), such as 22 GHz water, 6.7 GHz methanol and 1665 MHz OH, while other maser species monotonically decreased after the flare peak such as 6031 MHz OH, 12.2 GHz methanol and other OH maser species. Figure 2.8 shows a time series of specific velocity components of various maser species as observed by single-dish monitoring. The flaring maser species can be clearly seen, as well as which masers stayed in the flaring state, and which decayed.

Hunter et al. (2017) reported that the dust continuum flux in MM1 was 4 ± 0.3 times more than was observed with the SMA in 2008, as shown in Figure 2.9. To make sure the difference between the flux measured by ALMA in 2015 and the flux measured by SMA in 2008 is a real difference, the authors convolved the ALMA observations with an SMA beam. They then subtracted the continuum maps of 2015 and 2008 from one another, and found a residual in MM1 alone. They interpreted this increase in millimetre flux density as a possible consequence of an accretion burst in the source.

Extensive follow-up maser observations were done by Hunter et al. (2018) with C band VLA observations, Brogan et al. (2018) with K band VLA observations and VLBI water maser observations by Chibueze et al. (2021). Hunter et al. (2018) observed NGC6334I 6.7 GHz water masers, as well as excited OH (6.030 and 6.035 GHz) masers in 2016. Although 6.7 GHz methanol masers had not been found in MM1 during previous 2011 observations (Green et al., 2015), new bright masers were seen in MM1 during the accretion burst. The methanol masers were seen to be distributed mostly outside the 40% level of the 1.3 mm dust continuum, possibly tracing the walls of an ejection cavity seen in the 1.3 mm continuum (Hunter et al., 2018). An ALMA thermal methanol 11(2)-10(3) ($E_{\rm lower} \approx 180$ K) map that they reported showed that quite a large area around MM1 and MM2 has quite a high gas temperature $T_{\rm gas} > 180$ K, which these authors used to explain the emergence of the new methanol masers. Hunter et al. (2018) did not see methanol masers in the hottest regions, MM1A, MM1B and MM1D. They attributed the lack of methanol masers to the high densities of the regions containing HMYSOs.

Multi-epoch water maser observations of NGC6334I were done by Brogan et al. (2018) at epochs 2011, 2017.0 and 2017.8 with the JVLA. They found that the water masers in CM2 flared significantly between 2017.0 and 2017.8 and that the water masers in MM1 dampened due to the burst. They

also detected a North-South outflow in CS (6-5) molecular line emission. Recent VLBI observations of water maser proper motions were done by Chibueze et al. (2021). They observed 22 GHz water masers in NGC6334I during three epochs (2015.89-2016.01) with the VLBI array KaVA[3]. They confirmed the existence of a high-velocity protostellar jet inclined NW-SE of MM1B with an inclination angle relative to the sky-plane of -2.3 ± 0.3. This result implied that NGC6334I-MM1 harbours four different protostellar jets or outflows (also see Figure 1 of Hunter et al. (2021), tracing these outflows in SiO and CS molecular line emission). Neither of these observations were done immediately before and after the accretion burst.

[3]KaVA is a collaboration between the Korean VLBI Network (KVN) and the Japanese VLBI Network VERA. For more information, see the instrument's website. https://radio.kasi.re.kr/kava/

Chapter 3

Method

3.1 Introduction

This chapter describes the methods employed in this study. The theoretical basis for radio astronomy and radio interferometry is introduced, and the procedures involved in interferometric data calibration. Section 3.3 describes central ideas related to single-dish radio telescopes, such as sensitivity, angular resolution, beam patterns and antenna temperature. Section 3.4 introduces the concepts of interferometer response, complex visibilities, the UV-plane, and the foundational theorem of radio interferometry: the van Cittert-Zernicke theorem. Section 3.5 describes the measurement equation, regridding in the UV-plane, and the CLEAN algorithm for imaging. The last section of the chapter, Section 3.6, describes the steps used to calibrate and image the four datasets used.

3.2 The Radio Waveband

The radio waveband can be roughly defined as frequencies 10 MHz $\leq \nu \leq$ 1.5 THz (Wilson et al., 2013). The lower limit is due to the opacity of the ionosphere, which has a plasma frequency between 4.5 MHz and 11 MHz. There are also frequency ranges below 1.5 THz that are difficult to observe with ground telescopes due to absorption by abundant molecules in the atmosphere, such as N_2, O_2, H_2O and CO_2. Absorption by water vapor can be partially mitigated by observing at higher altitude in dry regions. Some frequency ranges can only be observed by getting outside the atmosphere with space telescopes.

Radio telescopes are used to observe a wide variety of astrophysical objects. The nature of the objects determines the kind of radio telescope to be used. One needs to take into account the frequency at which to observe, the required angular resolution, and the sensitivity needed to detect the object. The kind of object under study will also determine whether or not to do wide-band continuum observations, or narrow-band spectral line observations. Lastly, some objects are variable in time, and may require multiple observations over a certain period of time to achieve a specific scientific goal. All of these requirements should be taken into account when planning observations with radio telescopes.

3.3 Single Dish Radio Telescopes

A radio telescope is any device used to intercept incident radiation of a cosmic origin, and translates the detection into voltages over time. A radio telescope can either function as a radiometer, spectrometer or polarimeter (Burke and Graham-Smith, 2014). A radiometer measures the total power over its entire bandwidth for a polarization determined by the type of antenna. A spectrometer measures the

frequency dependent power, with the bandwidth divided into smaller frequency bands. A polarimeter is able to distinguish the relative intensities of radiation with different polarizations.

The most basic steps for radiometer inputs to be converted to voltages are signal amplification, bandpass filtering, square-law detection and integration (Burke and Graham-Smith, 2014). Signal amplification is an important step for radio telescopes, as very faint sources are observed. Common ways to amplify the signals are with low-noise-amplifiers (e.g., Pospieszalski, 2012) or superconductor-insulator-superconductor diodes (e.g., Tucker, 2009). After amplification, signal outside of the intended bandpass is filtered out and sent through a square-law detector which averages the power P after bandpass filtering over an integration time τ. The measured power P is directly proportional to the system temperature $T_{\rm sys}$ (Nyquist, 1928):

$$P = kT_{\rm sys}\Delta\nu \tag{3.1}$$

where k is Boltzmann's constant, and $\Delta\nu$ is the bandwidth of the filtered signal. This relation gives the power that would be measured with a power meter over a resistor of physical temperature $T_{\rm sys}$. Signals with an integration time τ should be sampled $N = 2\tau\Delta\nu$ times according to the Nyquist-Shannon theorem to keep all of the information on the signal (Nyquist, 1928). For any kind of detector, these considerations lead to the following relation, which is called the radiometer equation (Thompson et al., 2017):

$$\sigma_{\rm T} = C\frac{T_{\rm sys}}{\sqrt{\Delta\nu\tau}} \tag{3.2}$$

where $\sigma_{\rm T}$ is defined as the sensitivity of a radiometer for a single observation, and $C \geq 1$ is a factor close to unity, depending on the kind of detector. Equation 3.2 with $C = 1$ gives the minimum possible noise level for radiometer outputs. Therefore, for increased sensitivity, either the system temperature is lowered (e.g., by better cooling of detection and transmission components) or the integration time or bandwidth is increased. $T_{\rm sys}$ is the sum of the instrumental noise, and signal from the astrophysical source. Averaging $n_{\rm obs}$ observations of the same time independent source with the same values of σ_T divides the sensitivity by $\sqrt{n_{\rm obs}}$ (Kraus, 1966).

The radiometer equation gives a lower limit on noise from an instrumental perspective, but it is also important to ask what the lowest detectable flux density F is from space. The sensitivity in terms of flux density can be written as (Kraus, 1966):

$$\sigma_F = \frac{2kC}{A_{\rm e}}\frac{T_{\rm sys}}{\sqrt{\Delta\nu\tau}} \tag{3.3}$$

with $A_{\rm e}$ the effective area of the receiver and the factor of $2k/A_{\rm e}$ arising from the units of flux density (W m^{-2} Hz^{-1}), and the factor of two due to the fact that only one polarization is observed by any single receiver. Equation 3.3 gives a measure of sensitivity for any single-dish radio telescope. The $A_{\rm e}$ is the area of the dish if corrections are made for imperfections in the reflective surface, or blockages from arms holding receivers or mirrors. $A_{\rm e}$ is always smaller than the real area of the reflector.

To quantify the angular resolution of a radio telescope, the concept of an antenna beam pattern should be introduced. All radio antennas have a directional dependent gain, which is represented by the beam pattern $G_n(\theta, \phi)$. The precise shape of $G_n(\theta, \phi)$ is governed by diffraction theory and the geometry of the receiver. For example, a dipole antenna has a different beam pattern than a prime focus parabolic dish. There are many possible antenna geometries for various astrophysical applications. In this thesis, all observations were done with parabolic dishes, therefore only $G_n(\theta, \phi)$ for parabolic dishes are discussed. Single-dish beam patterns consist of a main beam, which is the part of the beam that

is most sensitive to radiation, nulls, which do not measure any radiation, and sidelobes, which are less sensitive to radiation. The importance of the beam pattern and its relation to the angular resolution of a single-dish radio telescope can be shown by the argument below:

The brightness temperature distribution of a source $T_{\mathrm{B}}(\theta, \phi)$ related to the sky intensity distribution $I_\nu(\theta, \phi)$ is defined by:

$$I_\nu(\theta, \phi) = \frac{2kT_{\mathrm{B}}(\theta, \phi)}{\lambda^2} \tag{3.4}$$

where λ is the wavelength of the radiation. T_{B} should be understood as the temperature a source would have been if it was a blackbody radiating an intensity I_ν at that particular wavelength. It is not necessarily representative of the physical temperature of the source. The antenna temperature of a telescope with a gain pattern $G_n(\theta, \phi)$ observing a source with brightness temperature $T_{\mathrm{B}}(\theta, \phi)$ is given by:

$$T_A = \frac{A_{\mathrm{e}}}{\lambda^2} \int \int T_{\mathrm{B}}(\theta, \phi) G_n(\theta, \phi) d\Omega \tag{3.5}$$

Equation 3.5 shows that the observed antenna temperature is a convolution of the beam pattern and brightness temperature distribution. All information from the main lobes and side lobes are condensed in a single data point for a single-dish radio telescope. For example, if the antenna is pointing at the source, but the sidelobes are pointed toward another bright radio source (e.g., the ground, or a source of radio frequency interference), then the voltage from the antenna will be a combination of both signals. If $G_n(\theta, \phi)$ is well known, the real brightness temperature distribution $T_{\mathrm{B}}(\theta, \phi)$ is then well known from the observations. The angular resolution of a single-dish radio telescope is quantified by the full width at half maximum (FWHM) of the main antenna beam. For a parabolic dish with diameter D, the FWHM is given by (Wilson et al., 2013):

$$FWHM = \frac{K\lambda}{D} \tag{3.6}$$

with K a factor of the order unity, which is dependent on whether or not the receiver is uniformly illuminated. K is determined by whether the dish is a perfect parabola with no blockages in front of the dish. This is almost never the case in practice, as the dish might deform due to temperature changes, gravity or engineering errors. Different kinds of feeds in single-dish radio telescopes also block the radiation, and reduce the resolution.

3.4 Basic Radio Interferometer Theory

This section introduces the mathematical background that underlies radio interferometry. An idealized two-element interferometer is introduced. The relationship between the sky brightness and the interferometer's response, which is grounded on the van Cittert Zernicke theorem, is then derived. This section aims to derive many expressions from first principles and follows the discussions found in Wilson et al. (2013), Burke and Graham-Smith (2014) and Thompson et al. (2017). This section gives context for Section 3.5.1, which discusses calibration and imaging for radio interferometers.

3.4.1 Interferometer Response

See Figure 3.1, which represents two antennas observing a sky intensity distribution $I_\nu(\theta, \phi)$. The antennas are pointing at the source centre $\vec{s}_0$, and are separated by a baseline distance $\vec{b}_\lambda = \frac{\vec{b}}{\lambda}$, where $\vec{b}$ is the projected distance between the two antennas from the perspective of the source in the sky. The observation wavelength is λ. It is assumed that the antennas are only sensitive to signal within a

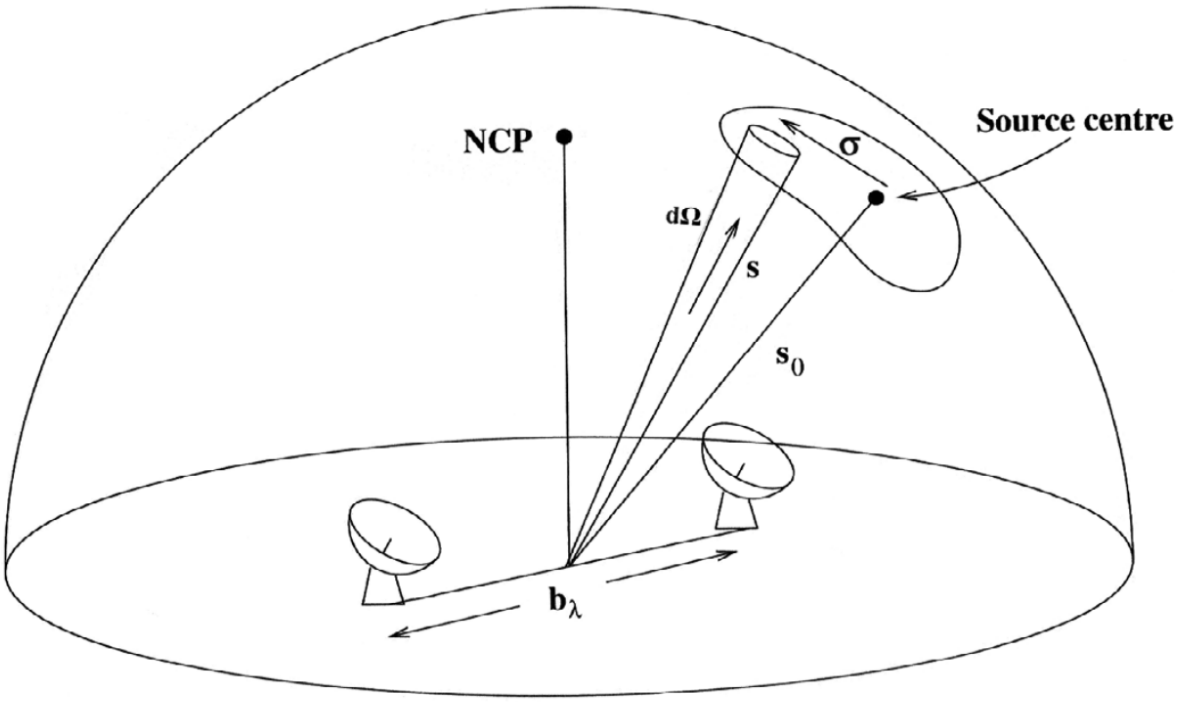

Figure 3.1: The basic setup for a single baseline of two antennas. Two identical antennas are separated by a baseline vector $\vec{b_\lambda}$, pointing at a centre $\vec{s_0}$. $\vec{s}$ is a direction displaced by a vector σ from the centre, and $d\Omega$ is a differential solid angle in the sky. Image from (Burke and Graham-Smith, 2014).

bandwidth $\Delta\nu$ around a centre frequency ν_0. The response of the interferometer to radiation from a small patch of the sky with solid angle $d\Omega$, in a direction $\vec{s}$, displaced $\vec{\sigma}$ from $\vec{s_0}$ in the sky is derived before the response from the entire sky is considered. Consider a plane wave going toward the antenna from the direction of $\vec{s}$. The plane wave will reach the further antenna τ_g seconds after it reaches the closer antenna. $\tau_g = \frac{\vec{b}\cdot\vec{s}}{c}$ is the geometric delay due to the path length difference between the antennas. The phase difference between the signals is given by $\phi = 2\pi\nu\tau_g = 2\pi\vec{b_\lambda}\cdot\vec{s}$.

If the antennas are only sensitive to a single frequency, the voltage measured by the closer antenna can be written as $V_C(t) = V_{C,0}\cos 2\pi\nu(t)$ and for the further antenna $V_F(t) = V_{F,0}\cos(2\pi\nu(t-\tau_g))$. The effect of a finite bandwidth $\Delta\nu$ is discussed in a subsequent paragraph. These signals are cross-correlated with the cross-correlation function:

$$R_{xy}(\tau) = \langle x(t)y(t-\tau)\rangle \tag{3.7}$$

with the brackets indicating time averaging, $R_{xy}(\tau)$ the cross-correlation, $x(t)$ and $y(t)$ are two time series and τ some delay. For two voltages, the cross-correlation will be given as:

$$R_{FC}(\tau_g) = \langle \tfrac{1}{2}V_{F,0}V_{C,0}\cos(2\pi\vec{b_\lambda}\cdot\vec{s})\rangle \tag{3.8}$$

antennas are not isotropic, and have an angle dependent effective area $A(\theta,\phi) = \sqrt{A_F(\theta,\phi), A_C(\theta,\phi)}$, with A_F and A_C the effective area of the further and closer antenna respectively. This leads to the following expression:

$$R_{FC}(\tau_g) = A(\theta,\phi)S_\nu\cos(2\pi\vec{b_\lambda}\cdot\vec{s}) \tag{3.9}$$

where S_ν is the flux density of the radiation from the sky. This shows that the cross-correlation has a cosine dependence on the projected baseline $\vec{b_\lambda} \cdot \vec{s}$. Equation 3.9 describes the response of the interferometer that is like a gain pattern $G_{\rm n}(\theta, \phi)$ for single-dishes. If the behaviour of $R_{\rm FC}$ is considered over the whole sky, $R_{\rm FC}$ has angle dependent fringes with a width determined by the projected baseline in wavelengths $\vec{b_\lambda}$ modulated by the beam pattern produced by effective area. This indicates that an interferometer acts as a spatial filter in the sky plane. Lastly, the Fourier transform of the cross-correlation is called the cross-spectrum power density $S_{\rm xy}(\nu, \theta, \phi) = A(\theta, \phi) S_\nu \exp(2i\pi \vec{b_\lambda} \cdot \vec{s})$, which is the complex equivalent of Equation 3.9 (Burke and Graham-Smith, 2014).

All interferometers have a finite bandwidth $\Delta\nu$. This means that radiation of different wavelengths, and hence projected baselines, are cross-correlated into the interferometer response. Cross-correlation over too wide a range of wavelengths will lead to a low correlation (which might cause the source to be undetectable). Quantitively, for a bandwidth function $F_{\rm B}(\nu)$, the power density $S_{\rm xy}$ is multiplied by $F_{\rm B}$. The response to the sky $R_{\rm FC}$ is multiplied by the Fourier transform of $F_{\rm B}$. For example, if the bandpass is square, the Fourier transform is a sinc function.

In summary, the response of an interferometer is given by the product of the primary beam $A(\theta, \phi)$, fringe pattern $\cos(2\pi \vec{b_\lambda} \cdot \vec{s})$ and delay beam $F_{\rm B}$ convolved with the sky intensity distribution over the whole sky. The primary beam $A(\theta, \phi)$ is comparable to a single-dish beam pattern. It is a complicated combination of the beams of all the antennas in the array. The fringe pattern is $R_{\rm FC}$ as discussed above, and the delay beam is the bandwidth function that is the Fourier transform of $F_{\rm B}$. The complex visibility $\mathcal{V}$ is the result of this convolution. If the total response beam is $A_{\rm N}(\theta, \phi) = A(\theta, \phi) F_{\rm B}(\theta, \phi)$ then $\mathcal{V}$ is defined as:

$$\mathcal{V} = |\mathcal{V}| e^{i\phi_v} = \int_{4\pi} A_{\rm N}(\vec{\sigma}) I(\vec{\sigma}) \exp(-2i\pi \vec{b_\lambda} \cdot \vec{\sigma}) d\Omega \tag{3.10}$$

Note that the effect of the fringe pattern is given in the exponential term. The following paragraphs give a short argument for the van Cittert-Zernicke theorem (Wilson et al., 2013; Burke and Graham-Smith, 2014; Thompson et al., 2017).

See Figure 3.2, the (u, v, w) coordinates and (l, m, n) coordinates are defined in terms of the pointing direction $\vec{s_0}$. The (l, m, n) system consists of a plane tangent to the source in the sky. (l, m, n) are direction cosines, where $l = \cos\alpha$, $m = \cos\beta$, $n = \cos\gamma$. They are the components of a unit vector so $l^2 + m^2 + n^2 = 1 \rightarrow n = \sqrt{1 - l^2 - m^2}$. The (u, v, w) coordinate system has units of wavelengths, defined as the separation between the antennas in a number of wavelengths. u in terms of Right Ascension, v in terms of Declination and w in terms of distance to the source. From these considerations, the following terms can be derived (Thompson et al., 2017):

$$\begin{aligned} \vec{b_\lambda} \cdot \vec{s_0} &= w \\ \vec{b_\lambda} \cdot \vec{s} &= \left(ul + vm + w\sqrt{1 - l^2 - m^2} \right) \\ d\Omega &= \frac{dl dm}{\sqrt{1 - l^2 - m^2}} \end{aligned}$$

If the source is in the far field $w \ll \sqrt{l^2 + m^2}$ and the size of the field is not too large, then $\mathcal{V}$ can be written in terms of (l, m, n) and (u, v, w) coordinates:

$$\mathcal{V}(u, v) = \int_{-\infty}^{\infty} \int_{-\infty}^{\infty} \frac{A_{\rm N}(l, m) I(l, m)}{\sqrt{1 - l^2 - m^2}} e^{-2i\pi(ul + vm)} dl dm \tag{3.11}$$

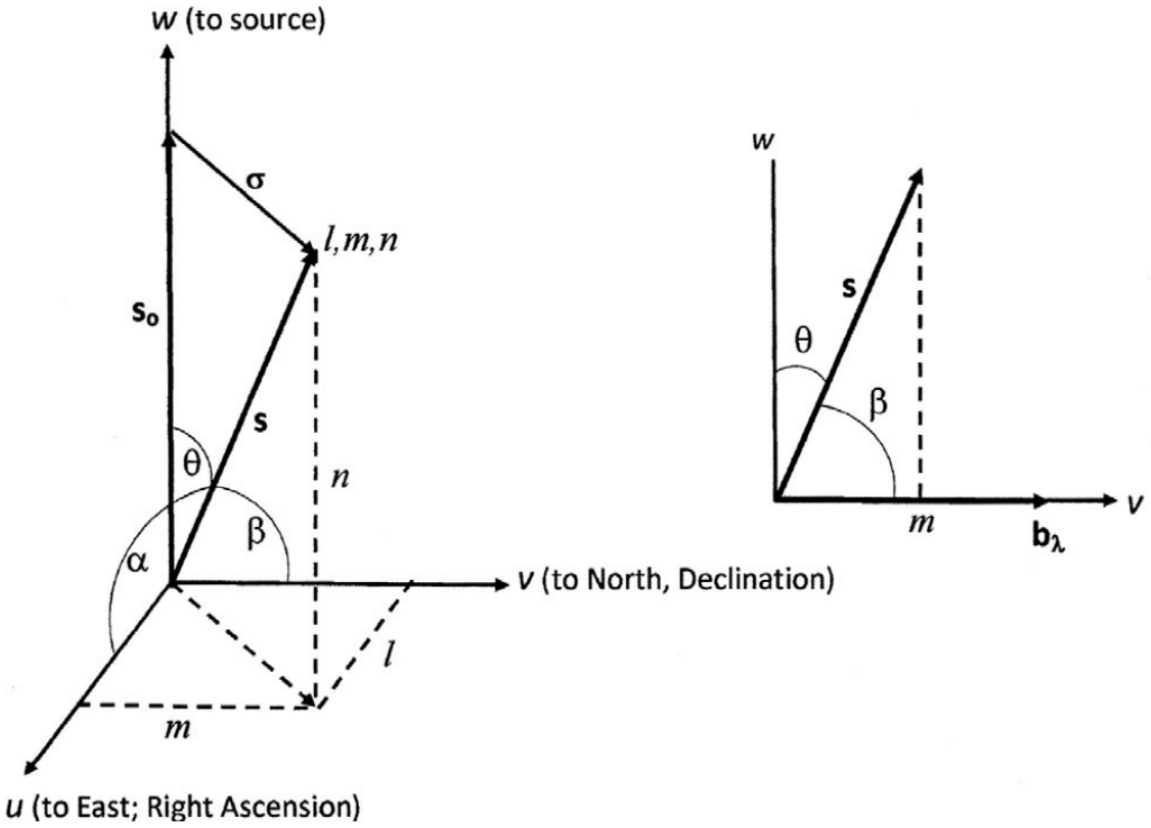

Figure 3.2: Definition of the (u, v, w) and (l, m, n) coordinates. The u and v are the separations between the antennas from the source's perspective in units of wavelength. w is the distance to the source in units of wavelength. (l, m) is the separation from the source in the sky, defined by the angles α, β, θ which is the angle between $\vec{s}$ and the East, North and source direction respectively. Image from Burke and Graham-Smith (2014)

Equation 3.11 shows a Fourier relationship between the the visibilities in the (u, v) plane, the product of the beam pattern, and the intensity in the (l, m) plane. This result is the foundation of radio interferometry and is a form of the van Cittert-Zernicke theorem. The aim of interferometric observations is to accurately measure $\mathcal{V}(u, v)$, to take its Fourier transform, and then to deconvolve the beam A_{N} from the sky intensity I_ν.

3.4.2 UV Coverage

In interferometry, the term "UV coverage" is often used. UV coverage refers to the collection of all baselines in the (u, v) plane for which visibilities have been measured. One projected baseline corresponds to two points in the (u, v) plane, as visibility is complex, but a real value is measured, which implies that its conjugate is also measured. The effective beam pattern in the sky of an interferometer is the Fourier transform of the UV coverage. Therefore UV coverage can be seen as a spatial filter for the sky brightness distribution. If an interferometer only has wide spacings, it has high angular resolution, but is not able to measure extended emission. On the other hand, the angular resolution of an observation goes roughly as λ/b_{max}, where b_{max} is the largest projected baseline. A procedure for significantly improving the UV coverage is aperture synthesis. Aperture synthesis is the technique of observing the source as the Earth rotates. This causes the (u, v) plane to be filled significantly better than with a short observation.

3.4.3 Sensitivity

For an interferometer, the minimum possible sensitivity obtainable is given by:

$$\Delta I_{\mathrm{m}} = \frac{SEFD}{\eta_{\mathrm{c}}\sqrt{n_{\mathrm{pol}}N(N-1)t_{\mathrm{int}}\Delta\nu}} \tag{3.12}$$

with ΔI_{m} the theoretical sensitivity, SEFD is the system equivalent flux density (in Jy), η_c is the correlator efficiency, N the number of antennas, t_{int} the integration time (in s), n_{pol} is the number of polarizations averaged and $\Delta\nu$ the channel width (in Hz).

3.5 Calibration and Imaging

This section offers a short discussion of possible sources of error in measurements of $\mathcal{V}$ and how to correct them. Thereafter, regridding of visibilities and the CLEAN algorithm for deconvolving the interferometer response from the sky brightness distribution is discussed.

3.5.1 Interferometric Data Calibration

Data calibration is the process of accounting for non-source interference in the received signal. Interferometry requires very precise measurements of visibility amplitudes, phases and timestamps. The effects that can affect the received signal are well quantified in the the Measurement Equation[1] (Hamaker et al., 1996; Sault et al., 1996). The measurement equation is given by:

$$\vec{V}_{ij} = M_{ij}B_{ij}G_{ij}D_{ij}E_{ij}P_{ij}T_{ij}\vec{V}_{ij}^{\mathrm{IDEAL}}. \tag{3.13}$$

Each matrix has components for each baseline (with i the first antenna and j the second). This way of setting up the calibration is often called antenna-based calibration where the corrections are done per

[1] This paragraph is also heavily influenced by the NRAO discussion on the measurement equation at https://casa.nrao.edu/casadocs/casa-5.4.1/reference-material/the-measurement-equation-calibration.

antenna. $\vec{V}_{ij}$ is the observed visibilities, and $\vec{V}_{ij}^{\mathrm{IDEAL}}$ is the "real" visibilities which the interferometer would have measured if it was an ideal interferometer. Observing with an ideal interferometer would mean that the visibility is the Fourier transform of the sky brightness sampled with the sampling function $A_{\mathrm{N}}(\theta, \phi)$. To obtain the best estimate for $\vec{V}_{ij}^{\mathrm{IDEAL}}$ is the aim of data calibration.

The calibration steps can be grouped into a-priori, frequency dependent (bandpass), time dependent (gain), polarization, and the absolute flux scale calibration. The frequency, time, polarization and absolute flux calibration require observations of calibrator sources. These sources have well-behaved emission with regard to the quantity that is being calibrated for.

A-priori calibration does not require the measurement of calibrator sources, and is usually done before the other calibration steps. This part of the calibration procedure would require the following terms: T_{ij} are polarization independent terms caused by the troposphere. P_{ij} is parallactic angle changes due to the antenna's orientation in terms of the sky, which affects how polarization components are measured. E_{ij} are antenna efficiency effects. T_{ij} and E_{ij} contain corrections for atmospheric or ionospheric opacity, as well as the altitude dependent gain effects of the antennas. For high frequency observations, these steps can also include corrections for system temperature measurements or water vapour (e.g., in the case of ALMA).

The bandpass calibration term B_{ij} concerns the fact that a spectrometer does not necessarily have an equal gain in all frequencies in the bandwidth. The bandpass calibrator that is observed is typically a point source with a flat spectral index. In calibration, the deviations from a flat spectral index are seen as instrumental effects and are subtracted from the target source. The bandpass calibrator is typically observed after the observation has completed.

The gain calibration term G_{ij} concerns the instrumental or atmospheric time variability of the visibility amplitudes and phases. The gain calibrator is observed regularly between observations of the target. There are three main requirements for a gain calibrator source. Firstly, it must be close to a point source at the resolution of the observation. Point sources have zero phases for all baselines, so deviations from zero for the gain calibrator are seen as extrinsic to the source. Secondly, the gain calibrator should not change its brightness in the course of the observation, as it is also used to correct possible errors in the amplitude over time. Lastly, it should be relatively close to the target source, so that it can be assumed the non-source input is the same between the calibrator and target observations.

The absolute flux correction is a correction on the visibility amplitudes or phases. Rather, it is a scaling factor between the instrumental visibility amplitudes and flux density. At the end of an observation, a source with a known flux model at the observing frequency is observed. A scaling factor for each baseline is calculated so that the final maps can be in terms of flux density. D_{ij} is the polarization response of the feeds. The polarization corrections are outside the scope of this work. Lastly, M_{ij} is non-closing errors, which are consequences of the antenna-based calibration, rather than baseline-based calibration.

This equation describes what should be corrected for any interferometric observation. Not all these matrices need to be considered for each observation. After the visibilities have been corrected with calibration, they are ready to be prepared for imaging.

3.5.2 Preparing the Fourier transform

The most efficient way of calculating the Fourier transform of a calibrated visibility function $\mathcal{V}$ is with the Fast Fourier Transform (FFT, Cooley et al., 1969). The requirement for the FFT is that the visibility function be evenly spaced. Therefore the data required regridding. $\mathcal{V}$ is regridded in the following way (Wilson et al., 2013):

$$\mathcal{V}'(u,v) = \mathrm{III}(u,v)\{G(u,v) \otimes \mathcal{V}\} \tag{3.14}$$

with $\mathcal{V}$ the visibilities measured on the irregular grid u_i, v_i, $G(u,v)$ is a convolving function that must be chosen, $\otimes$ is the convolution operator and $\mathrm{III}(u,v)$ is the Sha function (Equation 9.31 of Wilson et al., 2013). This gives regridded visibilities $\mathcal{V}'$ in terms of the regridded coordinates u_k, v_k. The Fourier transform of $\mathcal{V}'$ can then be written as (Wilson et al., 2013):

$$I_\mathrm{D}(l,m) = \sum_k g(u_k,v_k)\mathcal{V}'(u_k,v_k)e^{-2i\pi(u_k l + v_k m)} \tag{3.15}$$

with $I_\mathrm{D}(l,m)$ the "dirty image" of the sky intensity distribution and $g(u_k,v_k)$ a weighting function. The weighting function can have an important effect on the kind of image obtained. There are three kinds of weighting: uniform, natural and robust. Uniform weighting has $g(u_k,v_k) = 1/N_s(k)$, where $N_s(k)$ is the number of measurements within a grid cell size in the (u,v) plane. Natural weighting uses $g(u_k,v_k) = 1$ and robust weighting is described in Briggs (1995). Uniform weighting leads to a high angular resolution and lower sensitivity than natural weighting, while robust weighting is in between the two according to a robust parameter. For example, in CASA, the parameter ranges between -2 and 2, where -2 and 2 correspond to uniform and natural weighting respectively. The gridding function also affects the point spread function (PSF), which is the Fourier transform of the regridded and weighted. It is given by:

$$P_\mathrm{D} = \sum_k g(u_k,v_k)e^{-2i\pi(u_k l + v_k m)} \tag{3.16}$$

The PSF can be seen as a transfer function that changes the image, it is also known as the "dirty beam". The dirty image $I_\mathrm{D}(l,m)$ is then the first approximation of the real sky distribution $I(l,m)$.

3.5.3 Imaging

The most common algorithm for a final approximation of $I(l,m)$ by deconvolving the dirty image and the dirty beam is the CLEAN algorithm. The algorithm was invented by Högbom (1974). The following discussion follows Wilson et al. (2013) and Thompson et al. (2017). The CLEAN algorithm runs as follows: After the dirty image $I_\mathrm{D}(l,m)$ and the PSF $P_\mathrm{D}(l,m)$ are calculated, the algorithm models $I(l,m)$ as a collection of point sources with positive intensity at positions (l_i, m_i) according to the following equation:

$$I(l,m) = \sum_i A_i(l_i,m_i)P_\mathrm{D}(l-l_i, m-m_i) + I_\epsilon(l,m) \tag{3.17}$$

with $I_\epsilon(l,m)$ the residual image which is a measure of the image noise. This is done by identifying n brightest points in $I_\mathrm{D}(l,m)$ and subtracting each point multiplied with the loop gain $0 < \gamma < 1$ and P_D. These points are subtracted until the algorithm has made n iterations or the amplitude of the point sources reaches the RMS value of the image. The collection of these points is then stored in a "model image" by convolving the points with a Gaussian with a FWHM equal to the FWHM of $P_\mathrm{D}(l,m)$. Often one iteration of this process is not enough, and many "major cycles" following the steps in this paragraph are repeated, until the residual image consists only of random noise. Lastly, the final model and residual images are added together to make the final image. In the next section, the steps taken to calibrate and image the data reported in this thesis are discussed.

Epoch	Observation Date	Decimal Date	Phase Centre		R_V
			R.A. (J2000)	Decl. (J2000)	($\mathrm{km\,s^{-1}}$)
1	19 Sep 2014	2014.72	$17^h13^m09^s.9415$	$-35°47'02''.200$	0.42
2	25 Nov 2014	2014.90	$17^h13^m09^s.9415$	$-35°47'02''.200$	0.42
3	31 Jan 2015	2015.08	$17^h20^m53^s.440$	$-35°47'02''.200$	0.42
4	14 Apr 2015	2015.28	$17^h20^m53^s.440$	$-35°47'02''.200$	0.40
5	17 Nov 2015	2015.88	$17^h20^m53^s.378$	$-35°46'55''.847$	0.42
6	09 Feb 2016	2016.11	$17^h20^m53^s.367$	$-35°46'56''.930$	0.42
7	12 Mar 2016	2016.19	$17^h20^m53^s.367$	$-35°46'56''.930$	0.42

Table 3.1: Summary of VERA observations, containing the dates of each observation, the phase tracking centre and the spectral resolution R_V.

3.6 Data reduction

The data used in this thesis consist of four results: Firstly, 2014 − 2016 multi-epoch K band VLBI observations with VERA, which has been calibrated and imaged by T. Hirota. For completeness, the calibration and imaging procedure is described in Section 3.6.1. Secondly, 2019 C band spectral line observations with JVLA were extracted from the archive and were calibrated and imaged by the author, as described in Section 3.6.2. Two published continuum images were also used in this thesis. 2015.6 1.3 mm ALMA continuum from Hunter et al. (2017) and 2016.9 5 cm JVLA continuum from Brogan et al. (2018). The technical setup and calibration procedure for these images is described briefly in Sections 3.6.3 and 3.6.4.

3.6.1 VERA Multi-Epoch K Band Spectral Line Observations

About VERA

VLBI Exploration for Radio Astrometry (VERA) is a VLBI array that consists of four 20m antennas (Iriki in Kagoshima, Mizusawa, Ishigaki-jima and Ogasawara) in Japan (Kobayashi et al., 2003). One of VERA's science goals has been to accurately measure parallaxes to water maser sources, to get an accurate distance model of the Milky Way (VERA Collaboration et al., 2020).

Observations

Seven epochs observing NGC6334I were done with the VERA telescope to observe masers of the 22.23501 GHz water transition. Information on the date, phase tracking centre and spectral resolution of the observations is shown in Table 3.1. All observations were done with all four 20m VERA antennas. NRAO530 was used as a phase and bandpass calibrator and J1713-3418 was used as an absolute flux calibrator. The data from each of the antennas were correlated at the Korean-Japanese Correlation Centre (Lee et al., 2015). The author of this thesis would like to acknowledge T. Hirota for calibrating and imaging the dataset used in this study. The paragraphs below contain a short description of the calibration procedure of the data, followed by the steps taken to the positional uncertainty for the water masers.

AIPS Data Reduction

Data calibration and imaging were done with the Astronomical Image Processing System (AIPS) (van Moorsel et al., 1996). As discussed in Section 3.6.2 of Chapter 3, calibration is the procedure of correcting the observed visibilities with certain algorithms and calibration observations. Calibration

with AIPS works with the use of different kinds of tables. For example, calibration corrections is stored in calibration (CL) tables, bandpass information is stored in BP tables, source information from observations are stored in SU tables and complex gain solutions that were calculated with calibration sources are stored in SN tables. These different tables are then applied to the source (SU) tables before imaging.

To begin the data calibration, the visibilities were first loaded onto the computing system with the AIPS task `FITLD`. The task `ANTAB` in conjunction with `APCAL` was used to generate a calibration table that corrects the visibility amplitudes based on variations in the antenna temperatures of the different antennas. Thereafter, the task `ACCOR` was used to correct for errors due to the correlator. The antenna temperature and correlator corrections were merged with the task `CLCAL`. The frequency dependent (bandpass) calibration table was generated with the task `BPASS`. Corrections on the phases of the complex visibilities were done with the task `FRING`. The antenna temperature, correlator errors, bandpass and time dependent phase corrections were applied to the NGC6334I dataset with the task `SPLAT`. Thereafter, the absolute flux calibration was done with `SETJY` and the doppler corrections were done with `CVEL`. Self-calibration[2] was also done with `FRING` using the channel containing the strongest emission as a reference. The corrections from the self-calibration were then applied with `SPLAT`.

The deconvolution with the CLEAN algorithm was done with the task `IMAGR`. `IMAGR` requires the pixel size (in square arcsec), the number of pixels, and the number of CLEAN iterations to be specified. `IMAGR` then produces an image cube, with the intensities (in Jy beam^{-1}) as a function of position in space (R.A. and Dec.) and radial velocity (km s^{-1}). To produce the water maser maps, the AIPS task `SAD` (Search and Destroy) was used to fit 2D Gaussians to the image cube to get the positions, intensities and radial velocities of the water maser spots. These positions, intensities and radial velocities were written into text files for use in the steps described in the following sections.

Positional Uncertainties

The relative uncertainty in Right Ascension and Declination was calculated with the following expression:

$$\Delta\theta_{\text{form}} = 2 \cdot \frac{BW}{SNR} \tag{3.18}$$

with $\Delta\theta_{\text{form}}$ the formal uncertainty of a single 2D Gaussian fit in Right Ascension and Declination, BW is the beamwidth at those coordinates and SNR is the signal to noise ratio of the single 2D Gaussian fit. The formal uncertainty was overestimated by a factor of four to increase the reliability of the results. The beamwidth cannot be deduced *a-priori*, and must be calculated for each individual observation. The beamwidth was estimated as follows: Chibueze et al. (2014) report a synthesized beam size of "$\sim$ 1.3 milliarcseconds" for 22 GHz VERA observations toward NGC6334I(N), with the same observational setup as ours. NGC6334I(N) is very close to NGC6334I, so the beam sizes are assumed to be the same between the two observations. The 1.3 mas beam size likely refers to the smaller beam size, in Right Ascension. Due to VERA's position in the northern hemisphere and the $-30°$ Declination of NGC6334I (and NGC6334I(N)), the beam is elongated in the Declination direction. Chibueze et al. (2021) report a beam size of 2.48 mas $\times$ 0.97 mas for the first observation with KaVA. It was assumed that KaVA has the same ratio of the beamwidth between Right Ascension and Declination of 2.556 as the VERA observations. That leads us to an estimated beamwidth of 1.3 $\times$ 3.3 mas for the seven observations with VERA. These values of the beamwidth were used to estimate the positional uncertainty. The ratio between the peak intensity value and its uncertainty

[2]See Section 3.6.2 of Chapter 3 for more information on self-calibration.

was used to estimate SNR. The values for BW and SNR described above were then used with Equation 3.18 to estimate the relative positional accuracy of each 2D Gaussian fit.

3.6.2 JVLA C Band Spectral Line Observations

About the JVLA

The Karl Jansky Very Large Array (JVLA) consists of 27 25m antennas connected to act as an interferometer in the plains of San Agustin in New Mexico[3]. The antennas are positioned in a "Y"-shaped formation, with four configurations A−D. The antennas are on rail tracks, which allow changes in the size of the "Y"-shape, which in turn changes the UV coverage. The A configuration is the most extended, with the furthest baseline extending 36 km (angular resolution ~ 0.04 arcsec), to maximize angular resolution, while the D configuration has a maximum baseline of 1 km (angular resolution ~ 0.2 arcsec), to maximize sensitivity to extended emission. The JVLA is a connected array, which means that the data are correlated on-site, and not recorded for individual antennas and correlated later as in VLBI. The frequency range of a specific JVLA observation is specified by the observing band. Some important bands for star formation research are the L-band ($1.0 - 2.0$ GHz), C-band ($4.0 - 8.0$ GHz), X-band ($8.0 - 12.0$ GHz) and K-band ($18.0 - 26.5$ GHz) depending on the specific science goal.

Data Extraction

Recent C band archival data[4] were extracted from the Karl Jansky Very Large Array pointing at NGC6334I with a phase center (α,δ) = (17h20m53.3s,$-35°47'00''$) on 19 August 2019. The data were extracted to image 6.7 GHz methanol masers. The principal investigator for this observation was T.R. Hunter. Table 3.2 shows the parameters for the observation. The 2019.6 data was calibrated and imaged using the Common Astronomy Software Applications (CASA, THE CASA TEAM et al., 2022).

Calibration

The datasets were calibrated by a script written by the author of this thesis based on JVLA standard calibration procedures. In summary, the calibration procedure proceeded as follows:

1. Data loading and initial a-priori flagging.
2. Generating a-priori calibration tables and setting flux models.
3. Frequency dependent bandpass calibration.
4. Time dependent gain calibration.
5. Absolute flux calibration.
6. Post-calibration manual flagging.
7. Correcting for the bandpass spectral index.
8. Rerunning steps 3−6.
9. Applying the calibration tables to the target source.

[3]The information in this section is from the JVLA's official website: https://public.nrao.edu/telescopes/vla/
[4]The VLA archive can be found at: https://archive.nrao.edu/archive/archiveproject.jsp

Parameter	C Band Spectral	C Band Continuum	mm Continuum
Project code	19A-256	16B-402	2013.1.00600.S
Observation date(s)	19 Aug 2019	19 Nov 2016	29 Aug 2015
Epoch	2019.6	2016.9	2015.6
Configuration	A	A	C32-6
Time on source (min)	269	58	49.3
Number of antennas	27	7	32
FWHM of primary beam ($'$)	7	7	0.4
Frequency Range (GHz)	$4.2 - 12.2$	$4 - 8$	$220 - 238.76$
Polarization products	dual circular	dual circular	–
Gain calibrator	J1717-3342	J1717-3342	J1717-3342
Bandpass calibrator	J1924-2914	J1924-2914	J1733-1304
Flux calibrator	3C286	3C286	Titan
Spectral windows	87	32	7
Channel spacing (narrow, wide kHz)	0.977, 1000	1.953, 1000	–
Total bandwidth (GHz)[a]	8.4	3.9	3.047
Proj. baseline range (kλ)	$4.6 - 980$	$4.6 - 980$	$11 - 1140$
Robust clean parameter	0	-1	-1
Cont. Resolution ($''\times''$ (P.A. $^\circ$))	–	0.63×0.14 (-2.9)	$0.20 \times 0.15(-80)$
Cont. RMS noise (mJy beam^{-1})	–	0.022	1.2
Line resolution ($''\times''$ (P.A. $^\circ$))	1.23×0.64 (1.79)	–	–
Line channel width (km s^{-1})	0.088	–	–

Table 3.2: Description of the observation parameters for the connected array observations used in this thesis. [a]For the ALMA observation of Brogan et al. (2016), it was difficult to find line-free channels, the 3 GHz bandwidth is calculated by the number of line-free channels. More description is given in the text.

These steps are described in more detail in the following paragraphs.

For the C band data, the log file was downloaded from the National Radio Astronomical Observatory's website[5]. The log files contained information on antennas that were not in use. Thereafter, the observation files were generated by the `listobs` task in CASA, which lists specific information about the different sources and spectral windows. From the observation and log files, bad antennas, edge channels, system configuration spectral windows and configuration scans were flagged. The shadowing of antennas[6] and the first 10 seconds of each scan were flagged using the CASA `flagdata` task. The frequency data were smoothed using the `hanningsmooth` task, which calculates a running average in both phase and amplitude. This halves the spectral resolution, but removes Gibbs ringing, an artifact of strong spectral features. `Hanningsmooth` creates a new measurement set which was used for the remainder of the calibration.

The antenna position, gaincurve[7] and atmospheric opacity corrections were calculated with the `gencal` task. The flux model for the flux calibrator 3C286 was set with the `setjy` task. Before solving for frequency dependent effects, the geometric delay correction was calculated with `gaincal` on the bandpass calibrator J1924-2914, remembering to apply the previous calibration tables when calculating the correction. Thereafter, time dependent phase corrections were calculated for the bandpass calibrator with `gaincal` with short averaging times, to correct for short-term phase variations due to the atmosphere and electronic gain variations. These tables were then used in conjunction with the `bandpass` task to calculate frequency dependent solutions for both phase and amplitude. These tables were then applied to the bandpass calibrator to see if the solutions were correct. Additional flagging was done either through the interactive flag tool in `plotms` or done with `flagdata`.

Solving for the time dependent corrections was done by using `gaincal` on the gain calibrator J1717-3342. The gain calibration involved solving for phase solutions, with short averaging times followed by amplitude and phase solutions, averaged over each scan. The absolute flux calibration was done by running `fluxscale` on the amplitude phase calibration table, using the flux calibrator as a reference. This fixed the flux values to be in units of Jy. After the above-mentioned calibration steps, the a-priori, bandpass, gain and flux calibration solutions were applied to all three calibrators. More bad spectral windows, baselines and scans were identified and flagged.

The bandpass calibrator had a significant spectral index over the total bandwidth, and this spectral index had to be corrected. This was done by running `fluxscale` on the gain calibration table transferring the flux scaling from the flux calibrator (with a known flux model), to the bandpass calibrator. This made a flux model of the bandpass calibrator. The bandpass calibrator flux model could then be set to the bandpass calibrator visibilities using `setjy`. The calibration procedure was rerun from the bandpass calibration to the absolute flux calibration, with the new bandpass calibrator flux model taken into account. This ensured that the spectral index of the bandpass calibrator does not introduce an artificial spectral index to the target data. Finally, the calibration tables were applied to the target source. The different narrow band spectral windows and the continuum were split into separate measurement sets using `split` to ease processing in the next steps.

[5] From http://www.vla.nrao.edu/cgi-bin/oplogs.cgi

[6] When the beams of antennas in the array overlap with neighbouring dishes, blocking signal from the sky.

[7] The elevation dependence of the antenna gain. This is especially important for low elevation sources, or long observation times where the atmospheric optical depth is either large or variable respectively.

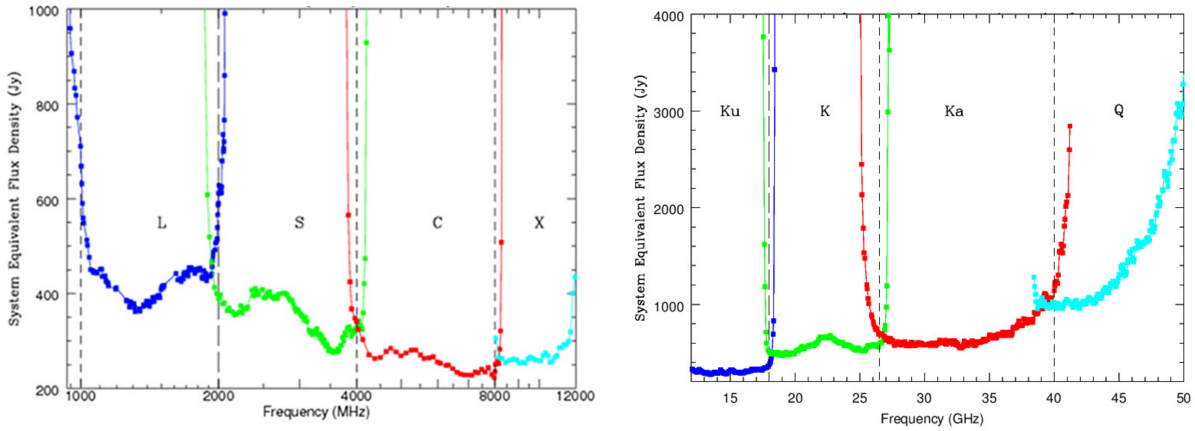

(a) SEFD for the low frequency bands of the JVLA. (b) SEFD for the high frequency bands of the JVLA.

Figure 3.3: SEFD for the low and high frequency bands of the JVLA.

Self-Calibration

Self-calibration is an iterative process of further improving the quality of an image by extracting residual delay and amplitude solutions from a bright point source in the target data. The gain calibration in CASA has to be done with `gaincal`, specifying the type of calibration (amplitude or phase or both), averaging time for the solutions t_{int}, the reference antenna, and the minimum signal to noise for acceptable solutions. A typical procedure for self-calibration involves calculating consecutive phase solutions with shorter integration times, applying the previous solution to calculate the newest solutions. The initial t_{int} is a very important parameter to calculate. Using the radiometer equation, Equation 3.12, the required integration time was calculated. For successful self-calibration ΔI_m should be less or equal to a third of the flux density of the maser used for the self-calibration. The $SEFD$ is given by Figures 3.3a and 3.3b.[8]

For 6.7 GHz, $SEFD \sim 255$ Jy. The following values were used to calculate $t_{\rm int}$ for self-calibration. For 8-bit correlators, $\eta_c = 0.93$, and in this observation two polarizations were observed. The N and $\Delta\nu$ are given by their corresponding entries in Table 3.2. The bright channel at -10.31 kms^{-1} with a peak of 6 Jy was used for self-calibration. Therefore, the integration time $t_{\rm int} \geq 73$s. Self-calibration tables were calculated for integration times from 90s down to 6s. The procedure was to calculate the solution table for a given $t_{\rm int}$ with `gaincal` using the bright channel as a reference. The solution table was applied with `applycal`. The corrected data were imaged with `tclean`, which saved the image visibilities to the model data column. Then the solution table was calculated again with `gaincal`, using a shorter $t_{\rm int}$ and the procedure was repeated. The self calibrated images were stored, with corresponding numbering. The self-calibration step with the highest dynamic range (peak flux/non-signal RMS) was applied for the final image. For 6.7 GHz, only one self-calibration phase solution was optimal.

[8]Figures 3.3a and 3.3b is based on the NRAO discussion on their website: https://science.nrao.edu/facilities/vla/docs/manuals/oss/performance/sensitivity

Imaging and Fitting

The images were then made with `tclean`. The important parameters for imaging were the image size, pixel size, spectral mode, weighting mode, flux threshold and iteration number. The image size is the number of pixels in the image. The size is arbitrary, and should optimally only contain the instrument's field of view. An image size of 480 pixels $\times$ 480 pixels was used. The pixel size is the angular size of individual pixels. The pixel size should be such that there are three to five pixels in one beam. In C band, A configuration, the JVLA has an angular resolution of roughly 0.33 arcsec[9]. The resolution of our observation could deviate from this estimated value, as it depends on the source elevation, specific frequency and the weighting of the image. Therefore a pixel size of 0.066×0.066 arcsec was used. The spectral mode specifies how `tclean` handles the frequency axis. For continuum images, the images are averaged over frequency with the multi-frequency synthesis "mfs" option. For spectral line observations, each frequency channel should be imaged separately. The option "cube" of `tclean` also ensures the Doppler correction of the image is done if the rest frequency of the image is specified. The rest frequency was specified as 6.668564 GHz, which is the rest frequency of the methanol masers (Cragg et al., 2005).

The weighting mode determines how individual visibilities are weighed when regridding the uneven UV-coverage to an even grid for the FFT. For weighting, the robust weighting was used and a robust parameter of 0 was chosen for this observation. The flux threshold specifies the maximum residual flux at which the cleaning algorithm should cease. It can be changed either interactively or in the cleaning process. Importantly, the flux threshold should not be lower than the RMS of the residual images, as the clean algorithm may then store erroneous flux in the final model image. The iteration number is a different stopping criterion than the flux threshold, as it is the measure of how many iterations the algorithm should complete before ceasing. It is best to have a reasonable flux threshold rather than to stop with an iteration number. This flux threshold would correspond to three times the RMS outside of the signal and side lobes in the brightest channel. Misjudging the iteration numbers may cause `tclean` to store noise in the final cube, reducing the image quality. `tclean` was used to image the 6.7 GHz methanol masers. The final result was a model image of the maser emission containing the intensity of emission as a function of position for each channel. The final image parameters of each image are described in Table 3.2. The images produced by CASA were exported using `exportfits` as FITS files, which could then be used on a home computer by importing the FITS image in CASA with `importfits`.

Some Observation Caveats

The continuum for this observation was also calibrated and imaged, but the faint centimetre jet was not detected due to dynamic range restrictions caused by the bright UCHII region MM3. Therefore, the 2019 JVLA continuum is not reported in this thesis. Lastly, there was an error in calculating the flux densities of the methanol masers. How this is known, and how it, the flux densities, might have been incorrectly calculated is discussed in Section 5.4.1. The intensities of the methanol masers are therefore not reported.

[9] As per the NRAO page on resolution of JVLA: https://science.nrao.edu/facilities/vla/docs/manuals/oss/performance/resolution

3.6.3 ALMA 1.3 mm Continuum

About ALMA

The Atacama Large (Sub)Millimetre Array (ALMA) is a 66-antennas interferometer stationed at Chajnantor in the Atacama Desert in Chile. The instrument consists of 54 × 12m antennas, and 12 × 7m antennas, with baselines ranging from 150m to 16 km. In the most compact configuration, the angular resolution ranges from 0.5″ at 950 GHz to 4.8″ at 110 GHz. In the most extended configuration the angular resolution ranges from 20 mas at 230 GHz to 43 mas at 110 GHz. ALMA has ten frequency bands planned, with operational bands within 84 − 950 GHz at time of writing[10].

Calibration and Imaging

The original description of the calibration and imaging for the 2015.6 ALMA 1.3 mm continuum is given in Brogan et al. (2016). The observational setup is described in Table 3.2. The data were calibrated with the CASA calibration pipeline (version 4.3.1). Brogan et al. (2016) did not give information on most of the the specific steps of the calibration with the pipeline. It is therefore assumed that the calibration proceeded with the standard steps found in the reference manual[11]. The following steps were likely followed:

First the task `hifa_flagdata` flagged data manually specified by the user, autocorrelation data (individual antennas correlated with themselves), shadowed antennas, and channels at the edges of spectral windows. Thereafter the task `hifa_fluxcalflag` was run, which flags known spectral lines from the flux calibrators if the flux calibrator is a solar system object. The task `hifa_rawflagchans` flagged bad data points in the raw visibilities automatically. The reference antenna was identified and stored with the task `hif_refant`.

ALMA observes at high frequencies for a radio telescope, which can cause the antennas to have high system temperatures $T_{\rm sys}$ relative to the astronomical signal. Therefore, $T_{\rm sys}$ is continually measured for ALMA data. The task `hifa_tsyscal` derives and applies the calibration table from the $T_{\rm sys}$ measurements. Data points with bad $T_{\rm sys}$ tables are then flagged with `hifa_tsysflag`. Radio emission at ALMA observing bands is also affected by absorption and emission due to water spectral lines. A continual measurement is made with a Water Vapour Radiometer (WVR) to be able to account for this effect. The task `hifa_wvrgcalflag` generates calibration tables based on the WVR data, applies the table to the visibilies, flags visibilities with unreasonably high phases for calibrators, and checks whether the WVR step has improved the visibilities. If yes, it applies the WVR table to the data.

antennas with unusually high or low gains compared to the other antennas are then flagged with `hif_lowgainflag`. The flux density model is then set with `hif_setjy` and the bandpass calibration table is generated and applied with `hifa_bandpass`. A spectral window map from narrow spectral windows to wider spectral windows was generated with `hifa_spwphaseup`. This is valuable if calibration tables cannot be generated from specific spectral windows, then an interpolated calibration solution is applied from other spectral windows to this spectral window. `hifa_gfluxscale` derives the flux densities of the gain calibrators to test whether the flux calibration was correct. In the case of Brogan et al. (2016), the flux density of the bandpass calibrator J1733-1304 was within 2% of the expected value. The time dependent amplitude and phase corrections were calculated with `hifa_timegaincal`

[10] From https://www.eso.org/public/teles-instr/alma/receiver-bands/.

[11] The reference manual can be found at: https://almascience.eso.org/documents-and-tools/alma-science-pipeline-quickstart-guide-for-casa-4.3.1.

and all previous calibration tables were applied with `hif_applycal`. A list of all the images that had to be imaged was made with `hif_makecleanlist` and initial dirty images were made with `hif_cleanlist`.

Creating line-free continuum images at 1.3 mm was not straightforward, as both MM1 and MM2 in NGC6334I contain line emission from complex organic molecules. Brogan et al. (2016) imaged the region for each spectral window with both the continuum and spectral line emission. They wrote a script that identifies a channel as line-free for a specific threshold, and then only imaged these spectral windows with the line-free channels. This caused the "continuum" bandwidth to be only 3.047 GHz. The final images were then made with the multi-frequency synthesis, accounting for a possibly linear spectral index. The images were also cleaned with scales of [0, 5, 15] pixels. The images were then iteratively self-calibrated and the final images were corrected for effects from the primary beam.

3.6.4 JVLA C Band Continuum

The observational setup of the 2016.9 JVLA 5 cm continuum observation is given in Table 3.2. The original description of the calibration and imaging of the dataset described in this section is given in Hunter et al. (2018). The data were calibrated with a copy of the VLA pipeline script. The calibration and imaging steps are similar to those described in Section 3.6.2. The pipeline follows a standard procedure[12]. First the pipeline converts the observation data into a measurement set and applies Hanning smoothing to the data. After that, the initial flagging is done of shadowed antennas, and the edge channels of bands. Hunter et al. (2018) disabled the automatic radio frequency interference flagging step so that strong maser lines are not flagged. Thereafter, the flux density model for the flux calibrator is loaded. A-priori calibration tables were created, and the initial delay and bandpass calibration tables were created. Time dependent gain calibration is then done, followed by correction for a possible spectral index in the bandpass calibrator. The final delay, bandpass and time dependent gain calibration tables are calculated and applied to the target data and `statwt` is used to calculate the weights of the data. A bright 6.7 GHz methanol maser channel in the data was used for self-calibration, which improved the dynamic range of the continuum images. The images were cleaned with scales of [0, 5, 15] pixels to produce the final images.

[12] A description of the procedure and further information can be found at https://science.nrao.edu/facilities/vla/data-processing/pipeline/scripted-pipeline

Chapter 4

Results

4.1 Introduction

This chapter presents the main results of this thesis. Section 4.2 describes the 1.3 mm ALMA and 5 cm JVLA continuum images. Section 4.3 describes the 2014 − 2016 VERA observations of 22 GHz water masers. The water maser observations follow on those reported by Brogan et al. (2018) and Chibueze et al. (2021). The observations reported in this thesis have the benefit of being both before and during the accretion burst, whereas the previous observations were only during the accretion burst. Section 4.4 describes the proper motions derived from the water maser maps. The methodology used in proper motion calculations are introduced, and the pre-burst and post-burst proper motions as derived with the spot and spectral methods are described. The differences and similarities between these two methods are also discussed. Section 4.5 describes the spatial distributions of the 2019 JVLA observation of 6.7 GHz methanol masers. Section 4.6 summarizes the key findings of this chapter.

4.2 Archival Continuum Images

Figure 4.1 shows the 2015.6 ALMA 1.3 mm continuum image (left) of NGC6334I from Brogan et al. (2016) and the 2016.9 JVLA 5 cm continuum image (right) from Brogan et al. (2018). The images have a logarithmic scale in intensity to show faint emission more clearly. In both panels the linear scale is shown in the top left. The beam sizes are shown in the bottom right. The locations of the largest millimetre regions MM1, ..., MM4 are shown in white. The locations of individual cores within these regions are shown in red, with the nomenclature of Brogan et al. (2016). The subsections below describe these images in more detail. The descriptions in Section 4.2.1 and 4.2.2 include a brief review of previous work to give context on the SFR before describing the water and methanol maser results.

4.2.1 ALMA 1.3 mm Continuum

See the left panel of Figure 4.1. Extended and compact emission was detected over $\sim 16''$ (20800 AU), with a peak intensity of 0.58 Jy beam^{-1} and a flux density of 30.3 Jy. This region consists of nine millimetre regions MM1,..., MM9 (Brogan et al., 2016), diffuse emission between the four largest regions MM1,..., MM4. This diffuse emission is also seen in 2015.6 thermal methanol emission as reported by Hunter et al. (2018). The other millimetre sources MM5,..., MM9 mostly consists of isolated cores in the field. Only the three largest emission regions MM1,..., MM3 are considered in this thesis.

MM1 consists of a $3.8'' \times 2.1''$ (4900 AU $\times$ 2700 AU) region with the brightest emission in the field. The region has a maximum intensity of 0.58 Jy beam^{-1} and a flux density of 18.8 Jy. Between MM1 and the other regions, there is a $4'' \times 2''$ (5200 AU $\times$ 2600 AU) region of faint extended emission with

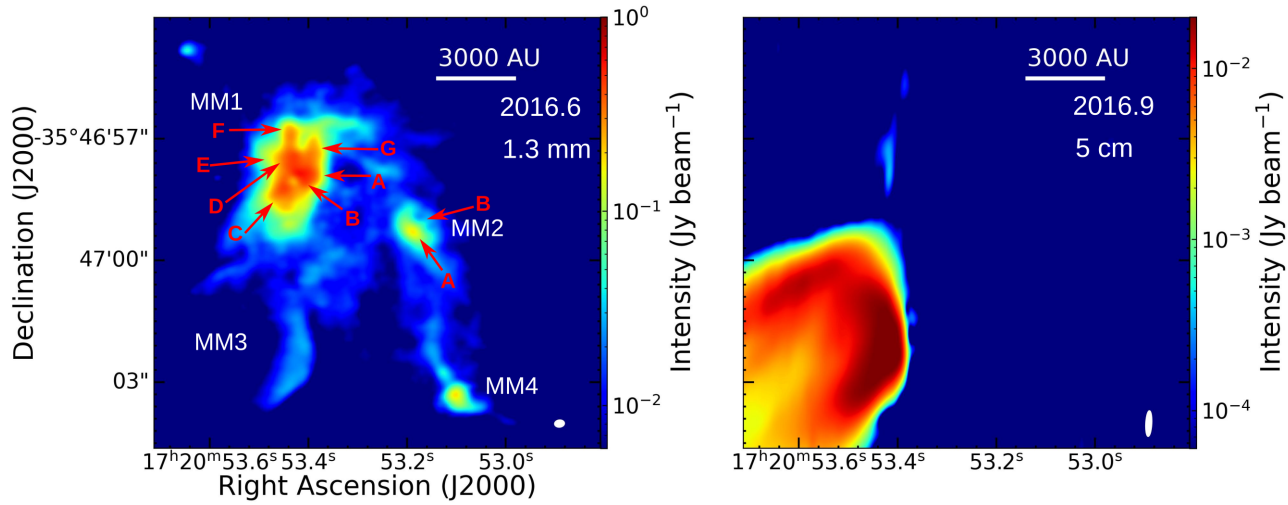

Figure 4.1: Left: 2015.6 ALMA 1.3 mm emission in NGC6334I as reported by Brogan et al. (2016). The main millimetre regions MM1, ...,MM4 are indicated with white text and the decomposition of these regions into separate cores by Brogan et al. (2016) is shown in red. Right: 2016.9 JVLA 5 cm emission in NGC6334I as reported by Brogan et al. (2018). The colour scale of both images is logarithmic to show faint emission clearly, and the corresponding intensity is shown at the right of both panels. The declination scale of the right panel is the same as the right panel. The linear scale for $d = 1.3$ kpc and the beam size of both observations are shown in white at the top right and bottom right of the panels respectively.

a mean intensity of 0.016 Jy beam^{-1}, which is more than ten times the RMS noise of 1.2 mJy beam^{-1}. MM1 consists of seven cores MM1A−G that were decomposed by Brogan et al. (2016). They found the largest core to be MM1E with a linear size of 356±65 AU, and the most compact core to be MM1B with a linear size $<$ 155 AU. From multi-wavelength SED fits for the individual cores, they also calculated the dust temperatures $T_{\rm dust}$, gas masses $M_{\rm gas}$, column densities $N_{\rm H_2}$ and brightness luminosities $L_{\rm brightnesss}$ (Table 5 of Brogan et al., 2016). MM1E was the faintest ($L_{\rm brightness} = 1.1^{+0.4}_{-0.3} \times 10^1 L_\odot$), coldest (38 K $\leq T_{\rm dust} \leq$ 100 K and most massive ($1.0 M_\odot \leq M_{\rm gas} \leq 6.2 M_\odot$). MM1B was the hottest ($T_{\rm dust} = 442^{+419}_{-120}$ K) and least massive ($M_{\rm gas} = 1.0^{+1.3}_{-0.3} M_\odot$). MM1A, MM1C and MM1D were also hot ($T_{\rm dust} > 200$ K) and bright ($L_{\rm brightness} > 10^4 L_\odot$). Brogan et al. (2016) termed this region a "hot multi-core". The region also hosts multiple jets and outflows, indicating it is hosting multiple YSOs. It contains a 6″ (7800 AU) north-south outflow identified in CS(6-5) thermal line emission (Brogan et al., 2018), a 4″ (5200 AU) northwest-southeast jet identified by water maser proper motions (Chibueze et al., 2021), a $\sim$ 0.5 pc northeast-southwest wide angle outflow identified in CO(9-8) thermal line emission (Qiu et al., 2011) and a single blue-shifted lobe of a northwest outflow in CS(6-5) (Brogan et al., 2018). There is a notable dip in 1.3 mm continuum emission in the north of MM1. This has been interpreted as a cavity excavated either by the N-S outflow (Brogan et al., 2018) or the NE-SW outflow (Chibueze et al., 2021).

MM2 consists of a 1.5″ × 1.2″ (1900 AU × 1600 AU) region of emission. The peak intensity is 0.17 Jy beam^{-1} and the flux density is 1.24 Jy. Two cores (MM2A, MM2B) were identified in this region by Brogan et al. (2016). MM2A had a radius of 178 ± 26 AU, a dust temperature of $T_{\rm dust} = 152^{+48}_{-19}$ K, a gas mass of $M_{\rm gas} = 1.7^{+1.3}_{-0.4} M_\odot$ and a brightness luminosity of $L_{\rm brightness} = 1.8^{+0.3}_{-0.3} \times 10^2 L_\odot$. Brogan et al. (2016) did not detect MM2B in enough wavelengths to calculate its SED, and therefore did not report its physical quantities. No clear outflow or jet could be seen in MM2 with CS(6-5) line emission

(Brogan et al., 2018).

MM3 consists of faint extended emission. It traces a "half-moon" shape with a thickness of 1.2″ (1600 AU) and an outer perimeter of 5.1″ (6600 AU). The region has a peak intensity of 0.023 Jy beam^{-1} and flux density of 1.39 Jy. The millimetre continuum in this region traces hot dust at the northern edge of the UCHII region NGC6334F (See Section 4.2.2).

4.2.2 JVLA 5 cm Continuum

The 2016.9 JVLA 5 cm observations detected three sources associated with MM1 and MM3. The right panel of Figure 4.1 shows these detections. The centimetre emission in MM1 is elongated 1.6″ × 0.3″ (2100 AU × 390 AU) in the N-S direction, as well as emission pointing toward the point source CM2. The centimetre emission in MM1 overlaps with the cavity seen in the millimetre emission of MM1. The region has been interpreted to be free-free emission from a radio jet (Brogan et al., 2018). CM2 is a point source with a peak flux of 0.14 mJy beam^{-1} and a flux density of 0.16 mJy. The spectral index of CM2 is consistent with synchrotron emission (Brogan et al., 2018). In centimetre emission, MM3 consists of a 11″ × 6.2″ (14300 AU × 8100 AU) cometary region with the highest intensity emission orientated towards the north-west. The peak intensity for the region is 0.0023 Jy beam^{-1} and flux density is 2.1 Jy. The spectral index of the region is close to 0 (Brogan et al., 2016), indicating optically thin free-free emission as the dominant emission.

4.3 Water Masers in NGC6334I

This section describes the results for the water maser observations before and during the accretion burst in NGC6334I. Water masers were detected in five regions: CM2, MM1-W1, UCHII-W1, UCHII-W2 and UCHII-W3 (see also Vorster et al., 2021). Figure 4.2 shows the positions and radial velocities of the water maser spots for each of the seven epochs. Table 4.1 shows the general characteristics of the detections of water maser spots: The number of detections per epoch in total and per region, the velocity extent of the detected water masers and summed intensity $\sum I_i$ per epoch. According to MacLeod et al. (2018), the onset of the accretion burst was 2015.01 and the methanol maser flare peak was 2015.62. The peak of the CH_3OH flare was between the fourth and the fifth epochs in our VERA dataset. The total number of detected water maser spots increase monotonically with time, until a drop from 462 − 362 between 2015.28 and 2015.88. After that the number of detections rises again with each epoch.

The majority of spots were detected in CM2, showing the same behaviour as the total number of water maser detections. The number of water maser spots in MM1-W1 declined with time. UCHII-W1, UCHII-W2 and UCHII-W3 shows no clear trend and displays significant variability in the number of maser spots. Most notable is UCHII-W2's very low number of maser spots in the epochs directly before and after the burst. The $V_{\rm LSR}$ range also is quite variable. Epochs 1 and 2 have similar ranges, epochs 3 and 4 have similar ranges, and then the $V_{\rm LSR}$ range is at a maximum in the last two epochs. The $V_{\rm LSR}$ range reported in this work is definitely not a representation of the full physical scenario, as more sensitive observations by Brogan et al. (2018) with JVLA show a much wider velocity extent for the water masers.

4.3.1 Intensities over Time

The summed intensity shows a sharp rise in the epoch directly before the methanol peak, whereafter the summed intensity is almost completely constant. Table 4.2 shows $\sum I_i$ for each region over each

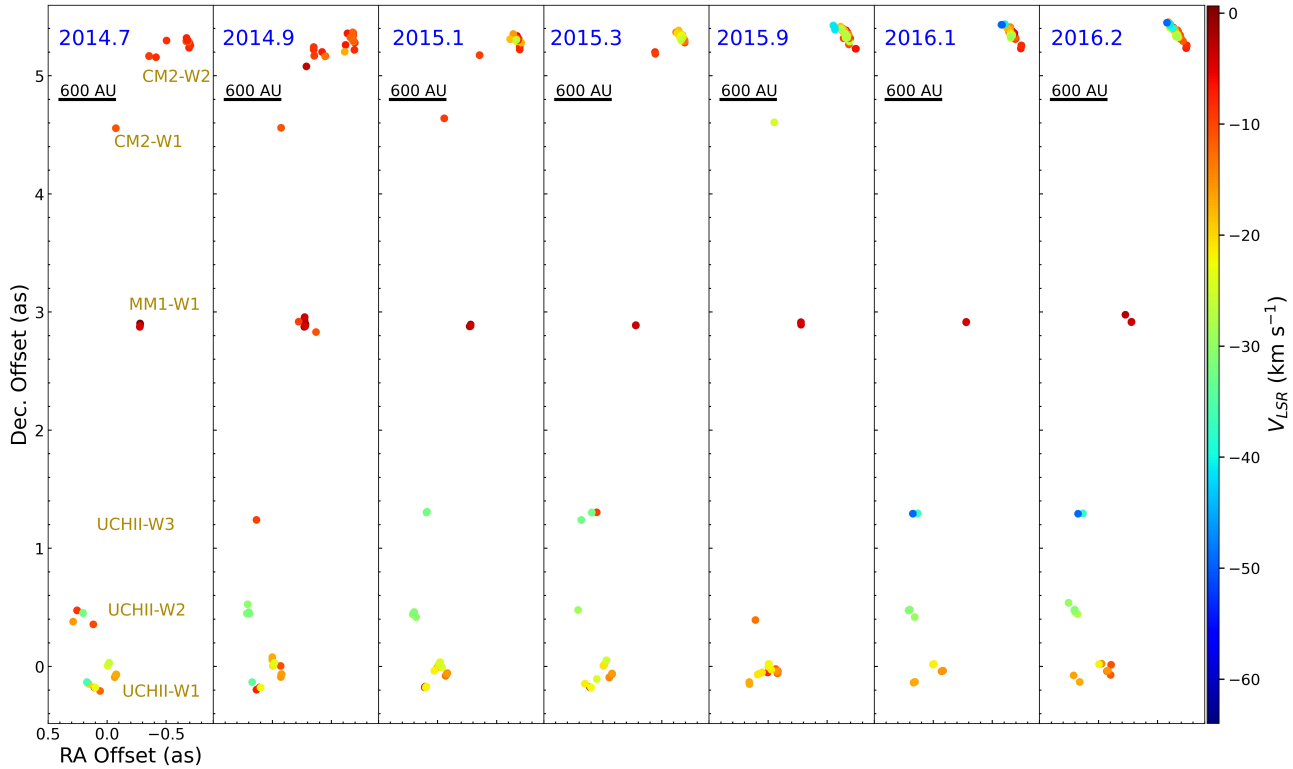

Figure 4.2: Detected water maser spot positions as detected by VERA for each epoch. The position of the spots indicates the position of the maser spots while the colour indicates the radial velocity according to the colour scale shown at the right of the figure. The blue text in the upper left of each panel indicates the date of the observation. The linear distance scale is shown by the black reference line. The brown text in the leftmost panel shows the name of each association discussed in the text.

Epoch	Total	CM2	MM1	MM3-UCHII			$\Delta V_{\rm LSR}$	$\sum I_i$
		W1	W1	W1	W2	W3		
							($\rm kms^{-1}$)	($\rm Jy\,beam^{-1}$)
2014.72	250	60	50	0	19	111	37.1	3628
2014.90	280	112	43	2	30	89	40.9	2022
2015.08	407	156	41	11	26	168	33.7	4935
2015.28	462	321	16	10	3	110	33.7	12085
2015.88	362	259	11	0	2	86	39.6	7994
2016.11	440	333	12	8	30	49	51.0	7845
2016.19	469	362	9	8	28	45	48.9	8000

Table 4.1: Numbers of maser spots per region per epoch, as well as $V_{\rm LSR}$ ranges and summed intensities for each epoch in NGC6334I, as detected by VERA.

Ep	CM2	MM1-W1	UCHII-W1	UCHII-W2	UCHII-W3
2014.72	1046	1203	1135	167	–
2014.90	916	339	567	171	3
2015.08	3110	273	1359	108	32
2015.28	10447	155	1448	4	21
2015.88	6787	191	963	2	–
2016.11	6816	114	195	112	16
2016.19	6864	30	299	81	14

Table 4.2: $\sum I_i$ for each region over time in $\rm Jy\,beam^{-1}$. Note that these values do not represent the true intensities densities as VERA has uneven UV coverage, which may have filtered out emission from the source.

epoch. Comparison with the detection counts from Table 4.1 shows that detection counts do not always correlate with $\sum I_i$. CM2 is the main contributor of flux to the entire region, with a similar behaviour to $\sum I_i$ of the whole region. MM1-W1 is a bright source at the beginning, but decreases monotonically with time. It should be noted that MM1-W1 is the region closest to the protostellar core. UCHII-W1, UCHII-W2 and UCHII-W3 have variable intensities, comparable with the variable number of detected maser spots. It should be pointed out that $\sum I_i$ peaks in 2015.28. The time dependence of $\sum I_i$ shows the same behaviour as the same water masers observed in single-dish monitoring by MacLeod et al. (2018). It begins low compared to the later epochs, and rises steeply, followed by a slight drop where the maser flux is relatively constant. It should be noted that a comparison of flux densities over time is affected by the detection limit of the array. The flux densities of many dimmer maser features could affect the value of $\sum I_i$.

4.3.2 Spatial and $V_{\rm LSR}$ Distributions

Figure 4.2 shows the spatial and $V_{\rm LSR}$ distributions of the water masers as detected by VERA. Figure 4.3 shows a zoom-in for some regions of water maser detections. The horizontal panels show the same region over time. In each region there are changes both before and during the accretion burst. Before the regions are discussed in detail, the concept of spectral feature in maser maps is introduced in the following paragraph.

When obtaining an image of masers, peaks in individual channel maps are termed "maser spots". These do not reflect individual cloudlets of maser gas, as often the maser has a larger linewidth

than the channel width of the observation. Therefore, if the spectral resolution of the observation is narrower than the maser linewidth, the maps in the sky plane will show collections of maser spots with a characteristic linear size of the maser. These collections of maser spots are collectively termed a "maser feature", and have a characteristic size of 1 AU (Gwinn, 1994a). This has been described in many previous studies (e.g., Gwinn, 1994b; Torrelles et al., 2001; Marvel et al., 2008). Figure 4.4 shows an example of this. The top panels of the figure show the positions of the maser spots of the brightest maser feature in CM2-W2. The maser spots show a close association, and have a spectral profile that is well approximated by a Gaussian function. For two epochs, the spectral distribution shows a double peak, and was fitted to two Gaussians. It should be pointed out that this feature shows variability in both its centre velocity, peak intensity and linear scale throughout all epochs. The paragraphs below describe the regions in terms of maser features instead of maser spots, as maser features are more descriptive of the physical masing gas. An in-depth discussion of each individual maser feature's properties is outside the scope of this thesis, but might be a meaningful avenue of inquiry with the higher resolution and sensitivity KaVA data during the accretion burst.

CM2-W1 is an isolated association south of CM2-W2. It consisted of $1-3$ features at ~ 8 km s^{-1}, which were only detected in the pre-burst epochs. CM2-W2 was the brightest and most complicated region. In the early epochs the masers traced a small bow shock with a size of ~ 120 AU, with -5 km s^{-1} $\leq V_{\rm LSR} \leq -12.5$ km s^{-1}. In the epochs after the burst, the masers traced a bow shock structure more clearly. The size of the structure traced by the masers grew to ~ 420 AU. Highly blue-shifted features at the apex of the bow structure, at $V_{\rm LSR} \sim -50$ km s^{-1} were also detected. Brogan et al. (2018) also detected these features, and attributed them to backflow at the apex of the bow shock. The brightest maser features were detected in CM2-W2 in the post-burst epochs, and were also the maser features that flared most significantly (MacLeod et al., 2018). In MM1-W1, the masers formed a linear structure of ~ 15 AU in epochs 2014.7 $-$ 2015.1, with a velocity range of -4 km s^{-1} $\leq V_{\rm LSR} \leq 0$. The masers were displaced in the epochs after 2015.3, with the same velocity range and an extent of 7 AU.

The spatial and velocity distribution of the masers in the southern regions was also variable. UCHII-W1 consisted of multiple associations over 1000 AU. The associations had a combined velocity extent of -37 km s^{-1} $\leq V_{\rm LSR} \leq -5$ km s^{-1}. The associations are discussed in more detail in Section 4.4, but the qualitative changes can be described briefly. Most of the associations consisted only of single maser features, which appeared and disappeared between the epochs. Two persistent associations are UCHII-W1a and UCHII-W1b in Figure 4.3. Both associations consisted of $2-3$ features in epochs 2014.7 $-$ 2014.9, and which shifted slightly in position at the onset of the burst. In 2015.9 after the peak of the burst, these associations were not detected, but other masers were detected north of the original masers with similar velocity ranges. UCHII-W2 consisted of a single -30 km s^{-1} feature before the burst. It was not detected in epochs after 2015.3, but a new association, with a double peaked spectral profile, peaking at -31 km s^{-1} and -26 km s^{-1} were detected in 2016.1 and 2016.2. UCHII-W3 had the first maser detection in 2015.1, a single feature at -31 km s^{-1}. It was not detected in 2015.9, and two new features at -36 km s^{-1} and -49 km s^{-1} were detected in 2016.1 and 2016.2.

4.4 Water Maser Proper Motions

Before the method employed in this work to measure the water maser proper motions in NGC6334I is discussed, a brief survey of the methodology used by other authors to calculate water maser proper motions in other sources follows. The basic procedure of any proper motion measurement is to accurately measure the position of a persistent source over multiple epochs. The observed proper motion is often the result of a linear sum of multiple components. For water maser observations, the persistent

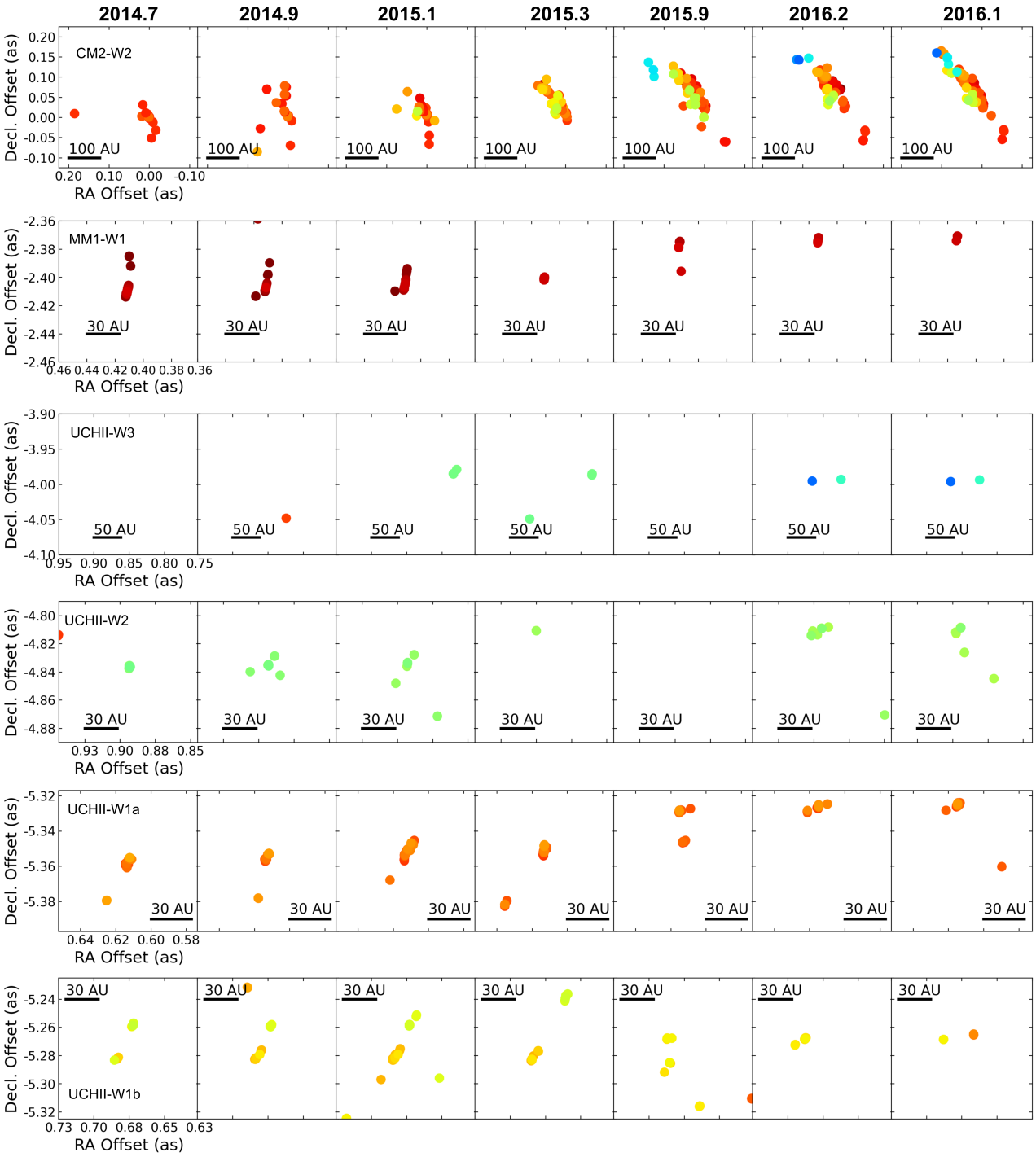

Figure 4.3: Water maser detections by VERA for epochs 2014.7−2016.1. Each horizontal panel shows a different region over time, with the name of the region in the leftmost panel. The offset scale for the plot of each region is constant. The dates of observation are shown above the top panel. A linear scale is also shown in each panel. The colour scale is the same as Figure 4.2.

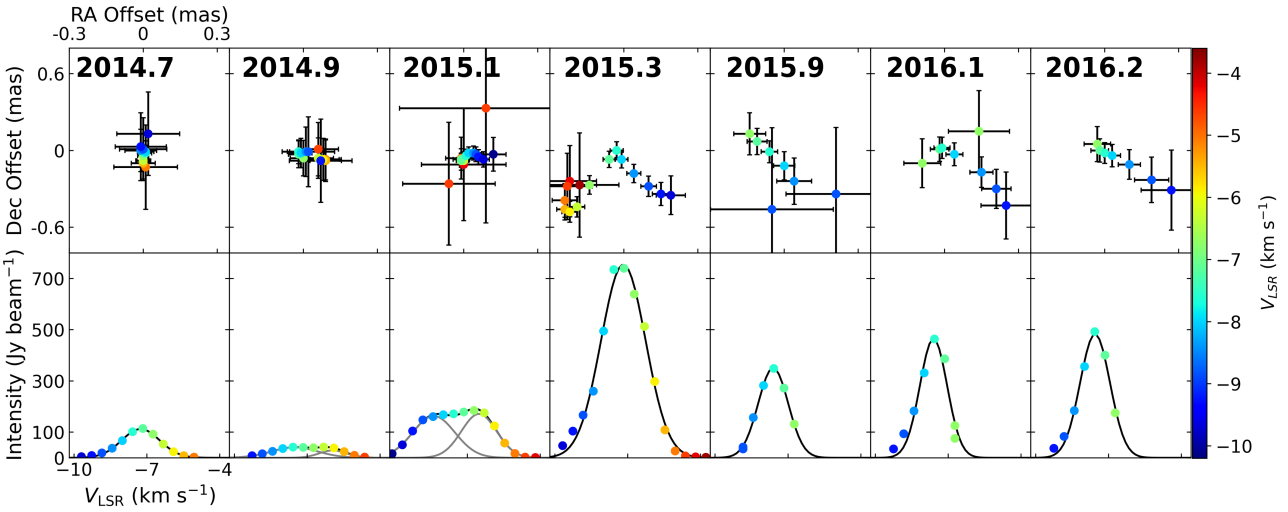

Figure 4.4: Top panels: Offsets and $V_{\rm LSR}$ of maser spots in the brightest feature of CM2-W2 for each epoch. The coloured dots show the positions of the spot detections. The scale of each panel is the same. The $V_{\rm LSR}$ scale is shown at the left. Bottom panels: Spectral profile of the maser spots in the panel above, with Gaussian fits shown in black. Some features show a double Gaussian, and was fit accordingly.

source that is observed over multiple epochs is termed a "maser feature", which is defined differently in different studies. The precise definition of a maser feature is discussed in Section 4.4.1 below. For water maser observations in SFRs, the proper motion consists of the following components:

$$\vec{\mu}(t) = \vec{\mu}_{\rm pec}(t) + \vec{\mu}_{\rm rot}(t) + \vec{\mu}_{\pi}(t) + \vec{\mu}_{\rm int}(t) \tag{4.1}$$

with $\vec{\mu}(t) = (\mu_\alpha, \mu_\delta) = (\frac{d\alpha}{dt}\cos(\delta), \frac{d\delta}{dt})$, t as time, α the Right Ascension, and δ the Declination of the maser feature. $\vec{\mu}_{\rm pec}$ is the peculiar motion[1] of the cloud (assuming a constant linear peculiar motion for the cloud during the extent of the observations), projected onto the sky plane. $\vec{\mu}_{\rm rot}$ is the proper motion due to the relative galactic rotation between the sun and the cloud. $\vec{\mu}_{\pi}$ is proper motion due to the annual parallax. $\vec{\mu}_{\rm int}$ is the absolute proper motions due to the internal motions in the cloud, projected onto the sky plane. Often, $\vec{\mu}_{\rm pec}$, $\vec{\mu}_{\rm int}$ and $\vec{\mu}_{\rm rot}$ are assumed to be linear during the observations, while $\vec{\mu}_{\pi}$ is sinusoidal (Trinidad et al., 2021). To study the kinematics of a specific SFR, $\vec{\mu}_{\rm int}$ is the component of interest as it is governed by the internal gas motions of the cloud, insofar as water maser proper motions trace gas motion.

The principal difficulty in measuring water maser proper motions is the variability in water maser intensity over a time span comparable to the separation between epochs. Water maser features might disappear between epochs, and new features might appear. Water masers could have variability at timescales of weeks (Felli et al., 2007). Variability at timescales comparable to the separations of the epochs can make accurate calculation of water maser proper motions a difficult task. There are a few methods employed in the literature to calculate reliable proper motions, these methods are discussed in Section 4.4.1.

[1]The motion of the whole cloud in the rest frame of the galaxy, i.e., if there was no galactic rotation.

4.4.1 Procedure for calculating proper motions

The procedure of calculating maser proper motions after imaging and 2D Gaussian fitting follows a fairly standard outline (Chibueze et al., 2014; Burns et al., 2015, 2016). The individual detections, termed "maser spots" are grouped into "maser features", which signify the position of a single masing gas cloud. The methods employed to group spots into features may differ between authors. For example: Immer et al. (2013) calculated the proper motions maser spots within the same velocity channel, while Burns et al. (2015) used entire spectral features. Trinidad et al. (2021) grouped maser spots into features if they are within 1 mas from one another and have radial velocities within 2 $\mathrm{km\,s^{-1}}$.

Therefore, there is some ambiguity regarding the grouping of maser features for use in proper motions in the current literature. In this work, the proper motions were calculated with two different methods to see if there is a significant change in the resulting proper motions. Section 4.4.2 describes the "spot" method, which groups maser spots in the same velocity channel into features. Section 4.4.3 describes proper motions calculated with the "spectral" method, which groups maser spots into features if they share a Gaussian spectral feature.

After maser spots were grouped into features (with any method), persistent features over multiple epochs are identified. Typically in water maser proper motion measurements, proper motions are only calculated for maser features detected in three or more consecutive epochs (e.g. Burns et al., 2016). In the case of this work, the requirement was relaxed to two consecutive epochs, as the masers were highly variable during the onset of the accretion burst. Physically unrealistic proper motions and non-consecutive detections were flagged carefully by hand to minimize false detections. Then, a linear fit is made to the positions vs time of the persistent maser features to get the relative proper motions from the gradient of the linear fit. Proper motions are termed "relative" if they are in terms of a reference maser spot or point and "absolute" if phase reference maps have been used for proper motion measurements. The benefits of relative proper motions are that galactic rotation, peculiar motion and parallax motions are cancelled out, as they are the same for all spots on the map and relative proper motions only trace the motions in terms of a reference maser feature.

Only relative proper motions were calculated as this thesis is only concerned with studying water maser proper motions to better understand the accretion burst in NGC6334I. The VERA epochs were grouped into "pre-burst" (epochs $1-4$) and "burst" (epochs $5-7$) epochs, to see the effect of the accretion burst on water maser proper motions. In Section 4.4.2 the spot method is described, which has been used by e.g., Reid et al. (1988); Immer et al. (2013); Chibueze et al. (2021). In Section 4.4.3 the spectral method is described, which has been used by e.g., Gwinn (1994a); Burns et al. (2015).

4.4.2 Spot Method for Proper Motions

The first method used to group maser features, the spot method, was done as follows. A program `region_identification.py` was written to identify clusters of maser spots. The program plots the positions of the maser spots for each epoch, and allows the user to choose rectangles in the form ($\alpha_{min}, \alpha_{max}$,$\delta_{min}, \delta_{max}$) that correspond with a possible maser feature. Two additional functions were written in order to calculate the relative water maser proper motions, the functions `maser_feature` and `calcpm`. `Maser_feature` served to average maser spots into maser features, and to make it easy to calculate proper motions. The function took as an input a rectangle created by `region_identification.py` and the maser positions and V_{LSR} for each epoch. Then the function isolated all the maser spots inside the rectangle. All maser spots of the same epoch and V_{LSR} channel ($\Delta V_{\mathrm{LSR}} = 0.44$ $\mathrm{km\,s^{-1}}$) were averaged into a single position. It should be noted that there was a small V_{LSR} difference of maser due to differing channelization of the bandwidth in different observations, so the V_{LSR} was rounded to

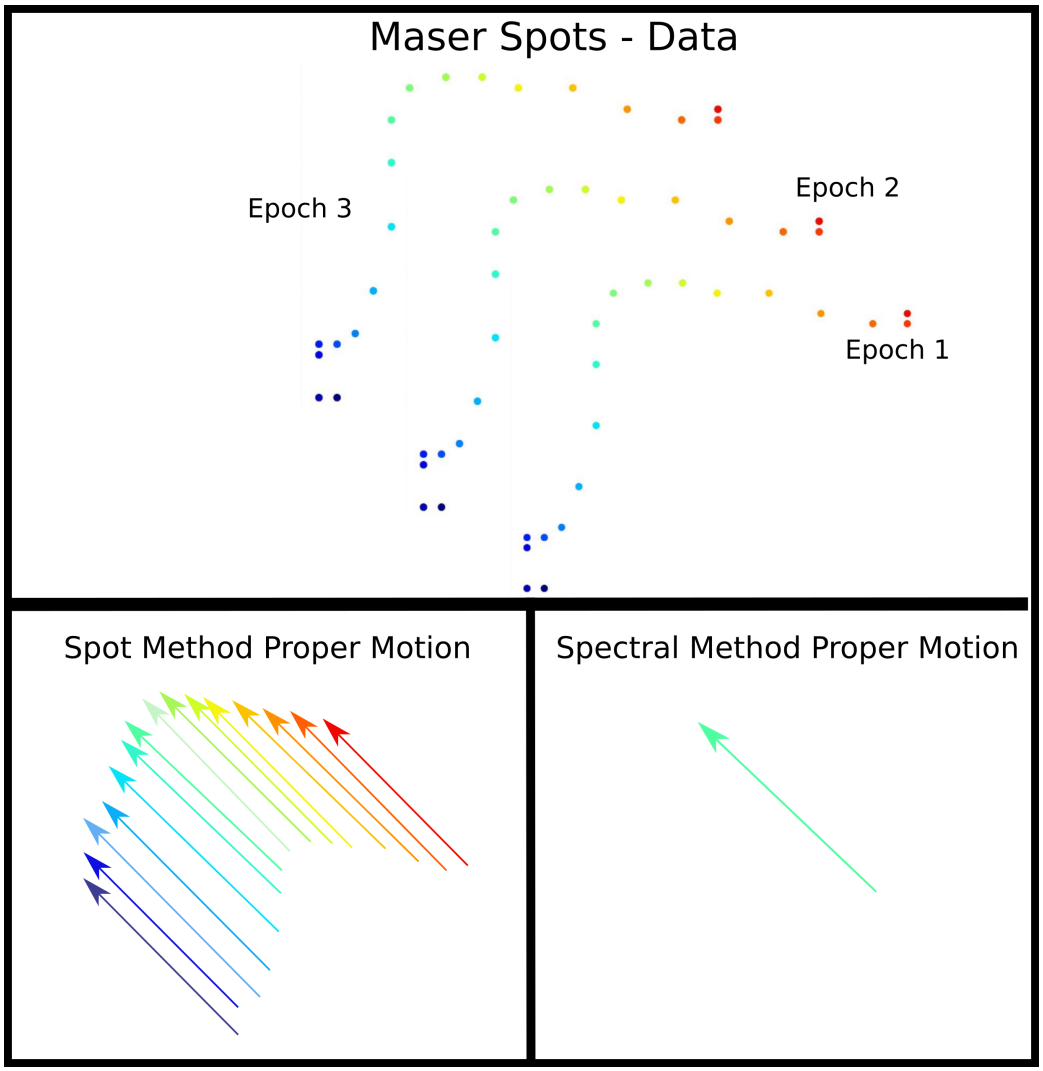

Figure 4.5: Schematic representation of the spot and spectral methods. The top panel shows a schematic representation of the maser spots for a single maser feature for three epochs. The bottom two panels show the resulting proper motions for the spot method (left) and the spectral method (right). The main difference is that the spectral method "averages" many proper motions into one proper motion for each feature.

the first decimal. `Maser_feature` also made a detection string signifying for which epochs there was a detection. The final output was a list containing the $V_{\rm LSR}$ in question, positions, position errors and a detection string. The detection string showed 0 for a non-detection and 1 for a detection. So, for four observations the detection string "0110" indicates detections in the second and third epoch. The output of `maser_feature` was then used as an input for `calcpm`. `Calcpm` calculates the proper motion by fitting a linear regression line with time and the position axes (α, δ). The proper motions (μ_α, μ_δ) are then given by the slopes of the respective fits. The `Python` code written by the author to calculate these proper motions can be found in Section A.7.

4.4.3 Spectral Method for Proper Motions

The second way in which maser features were identified, the spectral method, was by identifying a single maser feature with a single Gaussian peak in flux vs $V_{\rm LSR}$. It has been found that VLBI instruments observe single maser features as multiple maser spots with a continuous $V_{\rm LSR}$ gradient and close to a Gaussian distribution in flux vs $V_{\rm LSR}$ (Gwinn, 1994a; Torrelles et al., 2001). The reason why many spots are visible for a single feature is that the channels in the antennas are narrower in $V_{\rm LSR}$ than the maser emission, which causes detections in multiple channels for a single maser feature. Authors like Gwinn (1994a); Burns et al. (2015) have used these "microstructures" to calculate proper motions with water masers, treating many maser spots with a Gaussian distribution in flux vs $V_{\rm LSR}$ as a single feature.

To test whether this method of proper motion calculation may be more reliable, the pre-burst and burst proper motion calculations were replicated with the second method. Clusters of maser spots were identified, which show a spectral profile in the form:

$$G(V_{\rm LSR}) = A\exp\left(\frac{-(V_{\rm LSR} - V_{\rm centre})^2}{2\sigma^2}\right) \tag{4.2}$$

With $G(V_{\rm LSR})$ the Gaussian function, A the peak intensity in Jy beam^{-1}, $V_{\rm centre}$ the centre velocity in km s^{-1} and σ the standard deviation in km s^{-1}. Instead of working with σ, the Full Width at Half Maximum (FWHM) was used, given by $2\sqrt{2\ln 2}\sigma$. Then the position of the feature was calculated with the intensity weighted centroid:

$$x_{\rm IWC} = \frac{1}{\Sigma I_i}\Sigma I_i x_i \tag{4.3}$$

with x the coordinate (α,δ) in question, I_i the intensity of spot i, x_i the coordinate in question for spot i. The formal uncertainty on the position of the intensity weighted centroid was calculated with a Monte Carlo simulation. The Monte Carlo simulation calculated the intensity weighted centroid of each maser feature for 10^5 different variations of the spot positions which were sampled from a normal distribution with a width equal to the astrometric error of the maser spots. The mean of the various intensity weighted centroids was used for the feature position, and three times the standard deviation for the positional error reported in Table A.4. After the maser features were grouped with the intensity weighted centroid, persistent maser features over consecutive epochs with similar spectral profiles were identified. Small changes ($\Delta V_{\rm LSR} \leq 0.5$ km s^{-1}) in $V_{\rm LSR}$ and FWHM, as well as large changes in peak intensity were allowed. These identified persistent maser features were used to do the linear fits, in the same way as in the section above, to get the relative proper motions. The `Python` code written by the author to calculate these proper motions can be found in Section A.8.

4.4.4 Shifting to Absolute Frames

The water maser maps in this thesis have not been phase referenced, and the offsets of the water masers are in terms of the position of a -7.6 km s^{-1} reference maser in CM2-W2. The maps have not

been phase referenced, as the phase reference source was not bright enough during the observations to give sufficient SNR for absolute positioning. This means that the water maser maps and proper motions are not well-defined in the sky. Further, the proper motions are in the reference frame of the water maser in CM2-W2, and do not reflect the real internal motions in the rest frame of the clouds in NGC6334I. This section describes the procedures followed to shift to both an absolute position and velocity frame.

Absolute Position

To get absolute positions for the water masers and proper motions, the VERA water maps were shifted from the position and velocity frame of the reference maser in CM2-W2 to the reference maser for the KaVA observations in UCHII-W1 at $(\alpha, \delta) = (17^{\rm h}20^{\rm m}52{\rm s}.600, -35°46'50''.508)$ (Chibueze et al., 2021). This allows the VERA proper motions calculated in this work to be accurately compared to the continuum images. The procedure described in this section was identically applied to the proper motions calculated with both the spot and spectral methods described above.

Relative proper motions give freedom to change to any other frame of relative proper motions by adding a constant velocity vector $\vec{\mu}_{\rm T}$ to all the proper motions to transform it into a different frame. To make the results of this work comparable with the previous work, the maps were shifted so that the proper motion of the -7.6 km s^{-1} feature in CM2-W2 detected by VERA is equal to the average proper motions of the same maser detected by KaVA. This can be done as the burst epochs of the VERA observations is co-temporal with the KaVA observations. Note that the velocity frame of the KaVA observations is also not the rest frame of the cloud. Section 4.4.4 describes the shift to the absolute velocity frame.

The -7.6 km s^{-1} reference maser for VERA was detected in all epochs of the KaVA measurements (proper motion IDs: 70-73 of Table 1 in Chibueze et al., 2021). The change in velocity frame was done by changing the maser maps, and not by adding a vector to the proper motions. The maps were shifted with the following equation:

$$\alpha_{\rm shifted} = \alpha_{\rm unshifted} + \mu_{\alpha,T} t_{\rm obs} + P_{\alpha,T}$$
$$\delta_{\rm shifted} = \delta_{\rm unshifted} + \mu_{\delta,T} t_{\rm obs} + P_{\delta,T}$$

with $(\alpha_{\rm (un)shifted}, \delta_{\rm (un)shifted})$ the (un)shifted positions of the maser spots. $\vec{\mu}_T$ is the difference between the proper motion of the -7.6 km s^{-1} reference feature in the unshifted VERA observations and the KaVA observations by Chibueze et al. (2021). $t_{\rm obs}$ is the date of each observation from the first observation in years, and $\vec{P}_T$ is a term that changes the $(0, 0)$ positions of the maps to align with the KaVA observations.

For the pre-burst proper motions $\vec{\mu_T} = (-1.9 \pm 0.3, 17.3 \pm 0.4)$ mas yr^{-1} with the position shift $\vec{P_T} = (-0.68921, 5.28800)$ arcseconds. For the post-burst proper motions $\vec{\mu_T} = (-2.0 \pm 0.3, 16.9 \pm 0.4)$ mas yr^{-1} and the position shift $\vec{P_T} = (-0.68921, 5.28800)$ arcseconds. As the proper motion for the VERA reference feature was calculated in Chibueze et al. (2021), the uncertainty in the calculated proper motions is given by:

$$\Delta\vec{\mu} = \sqrt{(\Delta\mu_V)^2 + (\Delta\mu_K)^2} \tag{4.4}$$

With $\Delta\mu_V$ the uncertainty in proper motion of the VERA reference maser feature in the KaVA results. This gives $\Delta\mu_V = 0.38$ mas yr^{-1} $= 2.36$ kms^{-1}. $\Delta\mu_K$ is the uncertainty in the relative proper motions of the KaVA results, which is quoted to be less than 10% of the average proper motions. In that result, the average proper motion was 85 kms^{-1}. In other words $\Delta\mu_K < 1.38$ mas yr^{-1} $= 8.5$ kms^{-1}. This

	Pre-burst	Burst
Spot	$\mu_\alpha + 1.15$, $\mu_\delta - 14.074$	$\mu_\alpha + 1.0$, $\mu_\delta - 14.373$
Spectral	$\mu_\alpha + 0.7$, $\mu_\delta - 15.292$	$\mu_\alpha + 0.7$, $\mu_\delta - 15.301$

Table 4.3: Shifts of velocity frame applied to the proper motions. The values are in units of mas yr^{-1}.

adds a further systematic uncertainty smaller than 1.43 mas yr^{-1} = 8.8 kms^{-1} due to the velocity frame shift. The position shifts had a negligible uncertainty.

Absolute Velocity Frame

After the maser maps were shifted to the KaVA proper motion frame, the proper motions calculated were still in an arbitrary velocity reference frame, from which no physical conclusions could be made. And estimate of the absolute proper motions of water masers in CM2-W2 were made by Brogan et al. (2018). They concluded that the masers in the bow structure had a proper motion of less than 3.8 mas yr^{-1}. If it is assumed the masers are moving in the direction of $-79.4°$ as calculated by Chibueze et al. (2021), this implies $\mu_\delta/\mu_\alpha = \tan(-79.4) = -5.34$. If $\sqrt{\mu_\alpha^2 + \mu_\delta^2} < 3.8$ mas yr^{-1}, it implies upper limits for μ_α and μ_δ:

$$\begin{aligned} \mu_\alpha &< -0.7 \text{ mas yr}^{-1} \\ \mu_\delta &< 3.735 \text{ mas yr}^{-1} \end{aligned} \tag{4.5}$$

The water maser proper motions were shifted so that the mean proper motions in CM2-W2 were equal to the upper limits shown in Equation 4.5. The consequence of adopting proper motions equal to an upper limit is that the northern proper motions could be smaller, and the southern proper motions could be larger. The values of the shifts were a little bit different for pre-burst and burst proper motions, and also differed between the spot and spectral method. It should be noted that it is standard practice in water maser proper motions to shift to the rest frame of the proper motions by assuming symmetrical outflow velocities (e.g., Burns et al., 2016). This assumption was not obviously valid in the case of NGC6334I, hence this alternative method was applied so that the proper motions could be physically interpreted. The table below states the shifts adopted to produce the final proper motions. Section 4.4.5 and 4.4.6 describe the proper motions after the absolute position and velocity shift for the spot and spectral methods respectively. This implies four sets of proper motion: Pre-burst and burst proper motions for both methods.

4.4.5 Results: Spot Method

Tables A.2 and A.3 show the calculated proper motions for the pre-burst and burst proper motions respectively. A total of 227 proper motions were detected between the pre-burst and burst epochs. Tables 4.4 and 4.5 show summaries of the general trends of the proper motion results such as the number of detections, average transverse speeds (in 3D), and the velocity range of the proper motions per region. The 3D speeds were calculated assuming a linear distance of 1.3 kpc (Reid et al., 2014; Chibueze et al., 2014). The following equation was used to calculate the linear speeds:

$$v_t \text{ (km s}^{-1}\text{)} = \mu \text{ (mas yr}^{-1}\text{)} \cdot d \text{ (kpc)} \cdot 4.74 \text{ (rad yr km mas}^{-1}\text{ kpc}^{-1}\text{ s}^{-1}\text{)} \tag{4.6}$$

with v_t the linear velocity in a direction, μ the proper motion in either α or δ, d the distance to the source and 4.74 a factor arising from unit conversions. Equation 4.6 is a very useful equation to calculate linear velocities quickly if the distance and proper motion are known. The 3D speed is then

Region	#Detections	$\bar{v}^{a}$ (km s^{-1})	$\delta\bar{v}^{b}$ (km s^{-1})	V_{LSR} min, max (km s^{-1})
All	123	47	37	−34.1, 1.3
CM2	47	33	21	−21.1, −3.8
MM1-W1	14	19	17	−4.2, 1.3
UCHII-W1	44	59	31	−34.1, −3.4
W1B-i	10	76	27	−22.8, −3.4
W1B-ii	3	93	1	−34.1, −33.3
W1B-iii	17	31	23	−15.2, −8.8
W1B-iv	14	73	14	−24.0, −16.4
UCHII-W2	10	56	9	−32.0, −27.8
UCHII-W3	4	179	30	−32.4, −31.2

Table 4.4: H_2O maser proper motion summary per region as calculated by the spot method for the pre-burst epochs (epochs of 2014.72 2015.28). a) Average 3D linear velocity. b) Standard deviation on the mean of the 3D linear velocity.

calculated with the Pythagorean equation with the three linear velocity components, as in the small angle approximation $\theta \ll 1$ radian, proper motions add quadratically.

Figures 4.6 and 4.7 show the proper motions for both the pre-burst and burst epochs in the northern (CM2 and MM1-W1) and southern (UCHII-W1, W2 and W3) regions respectively (for the spot method). In both figures, the left and right panels show the pre-burst and burst proper motions respectively. The positions of the arrows show the positions of the maser features in the first epoch in question, the direction and length of the arrows represent the direction and magnitude of the proper motions. The colours of the arrows indicate the V_{LSR} of the proper motions according to the colour bar in the figures. The average transverse velocities remained constant in general, with $\bar{v} \pm \delta\bar{v} = 47 \pm 37$ km s^{-1} in the pre-burst epochs and $\bar{v} \pm \delta\bar{v} = 51 \pm 40$ km s^{-1} in the burst epochs respectively. $\delta\bar{v}$ is the standard deviation of the proper motions. The large standard deviation shows that the proper motions had a large scatter. There was a dramatic change in the velocity ranges between the pre-burst and burst epochs, with $-34.1 \leq V_{LSR} \leq 1.3$ km s^{-1} in the pre-burst epochs and $-49.3 \leq V_{LSR} \leq -1.7$ km s^{-1} in the burst epochs. In the following paragraphs the individual regions are discussed.

Northern Proper Motions

CM2-W2 had 49 and 55 proper motion detections in the pre-burst and burst epochs respectively. CM2-W2 is ~ 2800 AU from the bursting source MM1B. With a 3D speed $< 31 \pm 18$ km s^{-1}, the jet has a dynamic age > 428 yr. The average proper motion remained constant as well, although this is expected as the VERA proper motions were shifted in position and velocity frame as described in Section 4.4.4. An important difference in CM2 is that many new radial velocity features were detected in the burst epochs. The V_{LSR} range changed from $\Delta V_{LSR} = 17.3$ km s^{-1} to $\Delta V_{LSR} = 38.3$ km s^{-1}. From the top panel of Figure 4.6 it can be seen that more red and blue features were excited along the north and south of the bow shape of CM2. It is important to note that these observations had worse sensitivity and UV coverage than other observations that have observed water masers in this region. Therefore far fewer maser spots and features were detected than with previous observations with KaVA (Chibueze et al., 2021) or JVLA (Brogan et al., 2018).

In MM1-W1 14 and 7 proper motions were detected pre-burst and burst epochs respectively. The average speed did not change significantly between epochs with $\bar{v} = 19 \pm 17$ km s^{-1} for the pre-burst

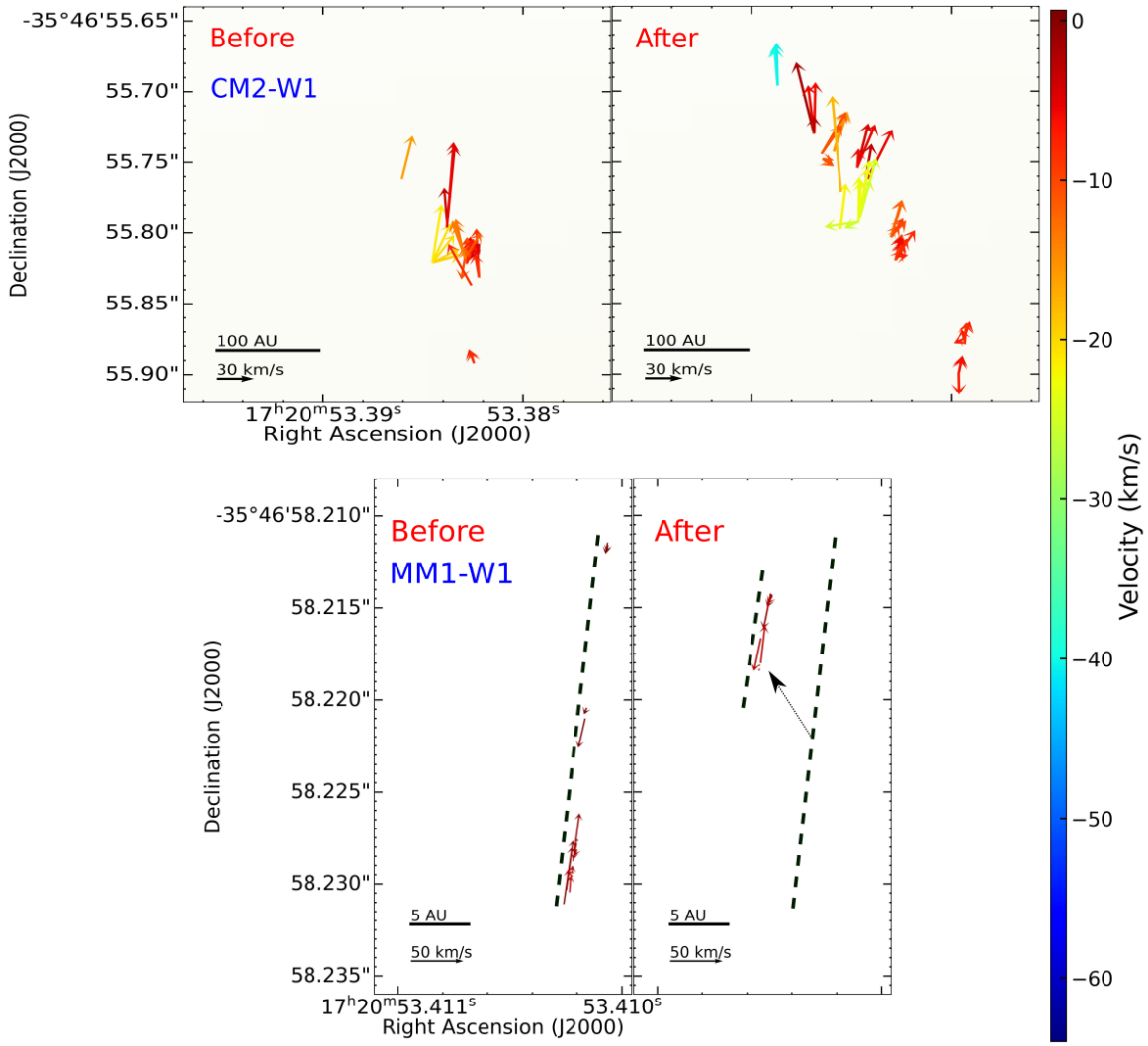

Figure 4.6: Proper motions of 22 GHz water masers in the northern regions of NGC6334I, before and during the accretion burst. The proper motions are calculated by the spot method. The positions, orientations and colours of the arrows show the positions, proper motions and $V_{\rm LSR}$ of the maser features respectively. The colour scale is on the righthand side. The left panels show the pre-burst epochs (epochs of 2014.72 2015.28) and the right panels show the burst epochs (epochs of 2015.88 2016.19). The linear scales in position and space are shown in the bottom left corner of each panel. In the bottom panel, black dashed lines show the position and orientation of the linear features shown in the maser features, and the black arrow shows the displacement of the maser features after the accretion burst.

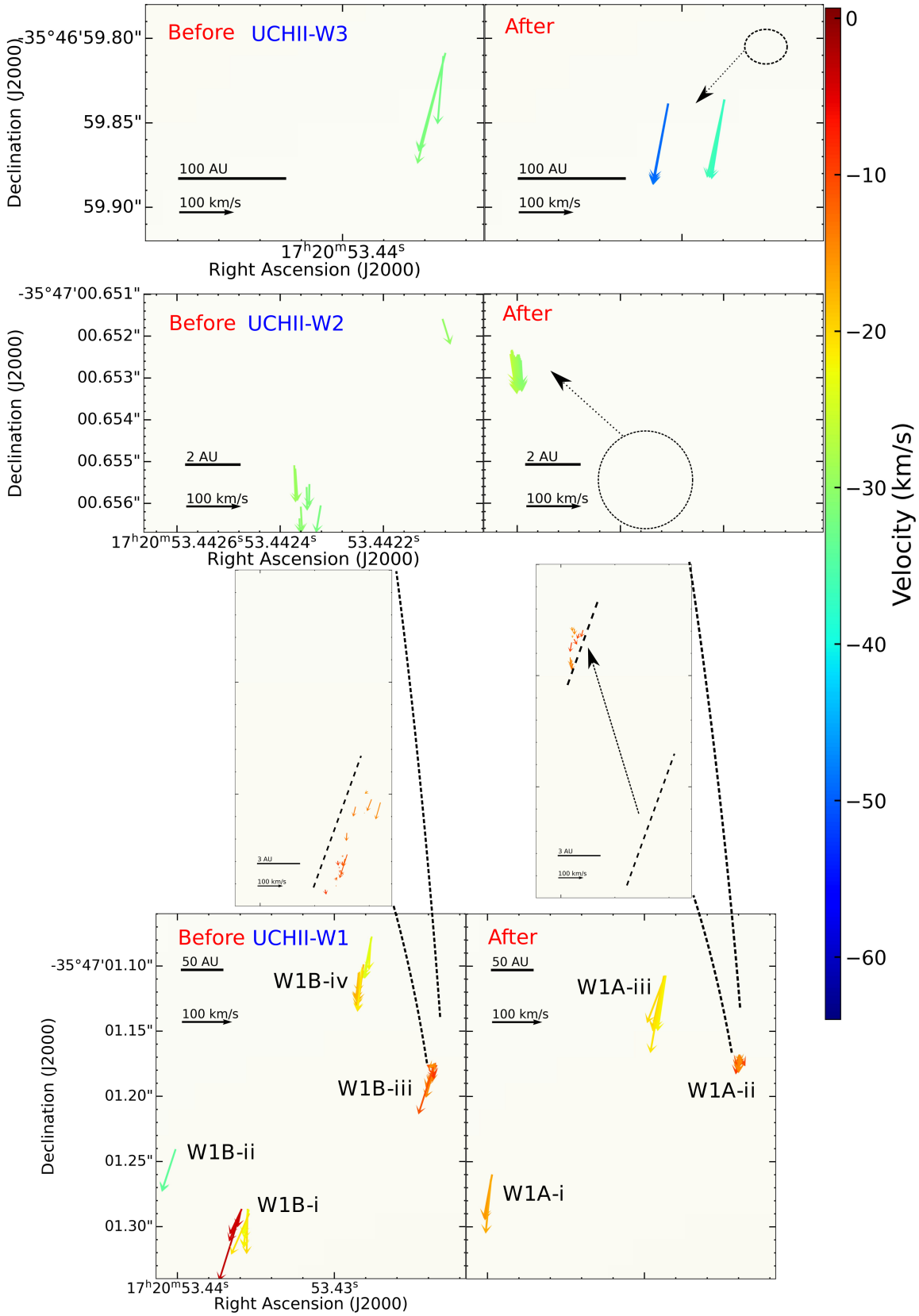

Figure 4.7: Proper motions of 22 GHz water masers in the southern regions of NGC6334I. The proper motions are calculated by the spot method. The figure is like Figure 4.6.

Region	#Detections	$\bar{v}$ ($\mathrm{km\,s^{-1}}$)	$\delta\bar{v}$ ($\mathrm{km\,s^{-1}}$)	V_{LSR} min, max ($\mathrm{km\,s^{-1}}$)
All	102	51	40	−49.3, −1.7
CM2	55	31	18	−40.4, −2.1
MM1-W1	7	19	13	−4.2, −1.7
UCHII-W1	20	68	41	−21.9, −9.3
W1A-i	4	93	10	−16.8, −15.6
W1A-ii	10	29	6	−15.6, −9.3
W1A-iii	6	116	14	−21.9, −19.8
UCHII-W2	13	71	9	−30.7, −25.7
UCHII-W3	7	153	3	−49.3, −36.2
W3A-i	4	155	3	−49.3, −48.0
W3A-ii	3	151	1	−37.1, −36.2

Table 4.5: H_2O maser proper motion summary per region as calculated by the spot method for the burst epochs (epochs of 2015.88 2016.19). a) Average 3D linear velocity. b) Standard deviation on the mean of the 3D linear velocity.

epochs and $\bar{v} = 19 \pm 13$ $\mathrm{km\,s^{-1}}$ in the burst epochs. As seen in the bottom panel of Figure 4.6, the proper motions pointed in various directions. An interesting result between the epochs is that the MM1-W1 water masers showed linear features in all epochs. Before the burst, MM1-W1 showed a linear feature with a linear extent of 21 AU. During the burst, those masers were not detected, with a centroid displacement of $\sim$ 15 AU from the previous detections. The features detected in the burst epochs had a linear extent of 7 AU. This observation is consistent either with the original masers dropping below detection limits during the burst, and new maser features brightening, or with the same maser features having a bulk displacement of 118 $\mathrm{km\,s^{-1}}$ in the 0.6 yr between 2015.3 and 2015.9. Destruction and re-excitation of water masers have been seen before in this region, although between 2017.0 and 2017.8 (Brogan et al., 2018).

Southern Proper Motions

UCHII-W1 consisted of four separate maser clusters before the burst and three after (See Figure 4.7). They were named W1B i, ..., iv before the burst and W1A i, ..., iii after the burst. The region had 44 total proper motions before the burst with $\bar{v} = 59 \pm 31$ $\mathrm{km\,s^{-1}}$. During the burst, 20 proper motions were detected with $\bar{v} = 68 \pm 41$ $\mathrm{km\,s^{-1}}$. The region had a substantial narrowing in V_{LSR} range with $\Delta V_{\mathrm{LSR}} = 30.7$ $\mathrm{km\,s^{-1}}$ before the burst and $\Delta V_{\mathrm{LSR}} = 12.6$ $\mathrm{km\,s^{-1}}$ after the burst. This change in ΔV_{LSR} can be ascribed to the non-detection of various maser clusters. W1B-i had two clusters of proper motions, one with $V_{\mathrm{LSR}} = -22.8$ $\mathrm{km\,s^{-1}}$ and another with $V_{\mathrm{LSR}} = -3.4$ $\mathrm{km\,s^{-1}}$ and had an average linear speed of 76 ± 27 $\mathrm{km\,s^{-1}}$. These proper motions generally pointed northward. W1B-ii only had three proper motion detections, with a well-defined proper motion of 93 ± 1 $\mathrm{km\,s^{-1}}$ to the east. W1B-iii was the most interesting region, with 17 proper motions pointing in various directions with $\bar{v} = 31 \pm 23$ $\mathrm{km\,s^{-1}}$ and a velocity range of 6.4 $\mathrm{km\,s^{-1}}$. This region was the only persistent region in UCHII-W1. Fourteen proper motions were detected in W1B-iv, the region consisted of two clusters. One had $V_{\mathrm{LSR}} = -24.0$ $\mathrm{km\,s^{-1}}$ and the other had $V_{\mathrm{LSR}} = -16.4$ $\mathrm{km\,s^{-1}}$. Both were pointing northward with $\bar{v} = 73 \pm 14$ $\mathrm{km\,s^{-1}}$. Note that W1B-i, ii and iv had no counter part in the burst epochs. After the burst W1A-i was detected, with 4 proper motions, and $\bar{v} = 93 \pm 10$ around $V_{\mathrm{LSR}} = -16$ $\mathrm{km\,s^{-1}}$. The region consisted of completely new maser features that had not been detected before the burst. W1A-ii had some interesting behaviour similar to MM1-W1. Before the burst the region consisted of northward pointing proper motions with a linear extent of 17 AU. These maser features were not

detected during the burst, but another region 12 AU to the north-east with a linear extent of 20 AU was detected, with northward pointing proper motions. Six proper motions were detected in W1A-iii, with a narrow $V_{\rm LSR}$ range around -21 km s^{-1} and $\bar{v} = 116 \pm 14$ km s^{-1}. The region was detected south of W1B-iv, with most of the proper motions pointing downward.

UCHII-W2 consists of a small group of maser spots with southward proper motions in all epochs and is shown in the second panel of Figure 4.7. Before the burst, the masers consisted of 10 extended proper motions over 2 AU with $\bar{v} = 56 \pm 9$ km s^{-1}, and a $V_{\rm LSR}$ of about -30 km s^{-1}. After the burst, the previous region was not detected, and a new maser group with a linear extent < 1 AU was detected 6 AU from the before burst cluster. These masers were faster, with $\bar{v} = 71 \pm 9$ km s^{-1}.

The water maser features in the UCHII-W3 region are the most transient of the features in this observation. Four proper motions were detected before the burst and 7 during the burst. See the top panel of Figure 4.7 and UCHII-W3 in Figure 4.2. Before the accretion burst, a region with $V_{\rm LSR}$ around -32 km s^{-1} was detected with high speeds of $\bar{v} = 179 \pm 30$ km s^{-1}. Note that these proper motions were only detected in the two epochs preceding the burst peak. During the burst, the previous features were undetected. Two regions with $V_{\rm LSR} = -48.5$ km s^{-1} (W3A-i) and -36.5 km s^{-1} (W3A-ii) were detected. Both regions had high average speeds, with $\bar{v} = 153 \pm 3$ km s^{-1} for UCHII-W3. W3A-i and W3A-ii was detected 61 AU and 110 AU respectively from the before burst maser features.

4.4.6 Results: Spectral Method

The proper motions derived with the spectral method were in many ways similar to those derived with the spot method, pointing to the reliability of both methods. For brevity, the similarities between the results for the two methods of proper motion calculations are not repeated, but the differences are pointed out. A total of 42 proper motions were detected between the pre-burst and burst epochs. The smaller number of proper motion detections is due to the fact that in the spectral method, more maser spots are used for a single proper motion than in the spot method. Table A.3 shows the positions and Gaussian fit parameters of each feature identified in each epoch. Tables A.5 and A.6 show the positions, radial velocities and proper motions of each individual proper motion calculated with the spectral method, while Tables 4.6 and 4.7 show the summaries of these proper motion by region. Figures A.1 and A.2 show the positions, proper motions and radial velocities for the northern and southern regions respectively. Table 4.8 shortly lists the regions with similar and different proper motions between the box and spectral methods, as well as the reason for difference, if any. Proper motions were deemed similar between the two methods if their 3D velocities were within a half of a standard deviation on each other's means, or if there was not a significant (> 1 km s^{-1}) change in the $V_{\rm LSR}$ range. The possible reasons for the differences between the methods will be discussed in more detail in Section 4.4.7.

4.4.7 Differences between methods of proper motion calculation.

In Section 4.4.1 the two main methods of maser feature identification for maser proper motions were introduced. The spot method identified features by calculating the centroid of all maser spots in the same velocity channel for each epoch. The proper motion is then determined by the change in position of the centroid for each velocity channel over time. Note that this method corresponds with the assumption that maser features do not accelerate over time. The second method introduced is the spectral method. In this method a maser feature is defined by maser spots that are relatively close to one another (in comparison to the field) and which show a Gaussian spectral distribution. The proper motions are then defined by the movement of the intensity weighted centroid of the Gaussian

Region	#Detections	$\bar{v}^{a}$ ($\mathrm{km\,s^{-1}}$)	$\delta\bar{v}^{b}$ ($\mathrm{km\,s^{-1}}$)	V_{LSR} min, max ($\mathrm{km\,s^{-1}}$)
All	20	50	40	−34.04, −2.77
CM2	8	33	25	−25.45, −7.34
MM1-W1	2	11	4	−3.01, −2.77
UCHII-W1	6	68	36	−34.04, −10.3
W1B-i	1	85	N/A	−21.63, −21.63
W1B-ii	1	99	N/A	−34.04, −34.04
W1B-iii	2	17	3	−15.21, −10.3
W1B-iv	2	94	7	−23.59, −17.47
UCHII-W2	2	70	10	−30.64, −30.51
UCHII-W3	1	147	N/A	−31.79, −31.79

Table 4.6: H_2O maser proper motion summary per region as calculated by the spectral method for the pre-burst epochs (epochs of 2014.72 2015.28). a) Average 3D linear velocity. b) Standard deviation on the mean of the 3D linear velocity.

Region	#Detections	$\bar{v}$ ($\mathrm{km\,s^{-1}}$)	$\delta\bar{v}$ ($\mathrm{km\,s^{-1}}$)	V_{LSR} min, max ($\mathrm{km\,s^{-1}}$)
All	22	54	42	−48.53, −0.96
CM2	14	33	15	−39.98, −0.96
MM1-W1	2	28	17	−3.24, −2.61
UCHII-W1	3	92	21	−21.07, −13.87
W1A-i	1	97	N/A	−16.15, −16.15
W1A-ii	1	64	N/A	−13.87, −13.87
W1A-iii	1	115	N/A	−21.07, −21.07
UCHII-W2	1	76	N/A	−28.33, −28.33
UCHII-W3	2	158	2	−48.53, −36.75
W3A-i	1	160	N/A	−48.53, −48.53
W3A-ii	1	156	N/A	−36.75, −36.75

Table 4.7: H_2O maser proper motion summary per region as calculated by the spectral method for the burst epochs (epochs of 2015.88 2016.19). a) Average 3D linear velocity. b) Standard deviation on the mean of the 3D linear velocity.

Similarities	Differences	Reason for Difference
CM2	UCHII-W1 (preburst)	v_{spectral} more precise than v_{spot}
MM1-W1	UCHII-W2 (preburst)	$v_{\mathrm{spectral}} > v_{\mathrm{spot}}$
W1A-iii	W1A-ii	$v_{\mathrm{spectral}} \gg v_{\mathrm{spot}}$
UCHII-W2 (post)		
UCHII-W3		

Table 4.8: Similarities and differences between 3D speeds calculated with the box and spectral methods. $\bar{v}_{\mathrm{spectral}}$ refers to the 3D speed calculated with the spectral method and $\bar{v}_{\mathrm{spot}}$ the 3D speed calculated with the spot method. The items in the table list the regions for which the proper motions were similar or different.

distribution over time. Note that this method assumes that small changes in the $V_{\rm LSR}$ can happen, in other words: acceleration is not zero for maser features.

The proper motions using these two methods of maser feature identification were calculated in Sections 4.4.2 and 4.4.3. It was found that the mean pre-burst and burst 3D speeds in NGC6334I are largely the same between the two methods. There were differences in the 3D speeds between the two methods in UCHII-W1 (preburst), UCII-W2 (preburst) and UCHII-W1Aii. In this section possible reasons for the differences are discussed. The scientific reliability of these two methods are considered after that.

In UCHII-W1 (preburst), the difference between the proper motions calculated by the two methods is that the spectral method produced proper motions with a much smaller standard deviation. This is due to the fact that the spectral method filters out maser spots due to sidelobes, which limits the number of false detections due to calibration errors. Detections due to sidelobes do not make a Gaussian spectral distribution. On the other hand, the spot method sees these detections as real, and may therefore calculate proper motions with spurious spots for complicated regions like UCHII-W1.

In UCHII-W2 (preburst), and W1A-ii, the proper motions have a similar orientation and positions between the two methods. So the difference can therefore be attributed to the different averaging methods between the two methods. The spectral method calculates an intensity weighted centroid over multiple channels while the spot method only looked at the proper motions of spots at fixed $V_{\rm LSR}$ values, this can reasonably explain the small velocity differences in these regions.

The main difference between these two methods is whether or not maser features could accelerate. Water masers form in highly turbulent shock environments (Hollenbach et al., 2013). Sanna et al. (2010a) mentioned possible velocity drifts in the water masers in G16.59-0.05, but did not look into it in any detail. Chibueze et al. (2012) showed that many of their water masers in Cepheus A underwent velocity drifts. Further, long-term single-dish monitoring by Valdettaro et al. (2002) found velocity drifts in the water masers in 2 of the 14 sources that they monitored. Recently, MacLeod et al. (2021) found systematic velocity drifts in the 6.7 GHz methanol masers in G9.62+0.20E. The evidence from the literature indicates that multiple SFRs contain maser sources that undergo systematic velocity drifts, although it is not in all cases. The consequence of this is that the spot method may not be a reliable method of maser feature identification in many SFRs. In some cases it might give incorrect proper motions under the assumption of zero velocity drift.

4.5 Methanol Masers in NGC6334I

The positions and radial velocities of 6.7 GHz CH_3OH masers in NGC6334I on 19 August 2019 were obtained. In this section, the results are described in detail. To simplify the analysis of the maser features, 2D Gaussians were fit to emission peaks in the spectral cubes. For an instrument with a beam size that is much larger than the intrinsic angular size of a maser, a 2D Gaussian fit is a good approximation (Richards et al., 2020). This was done for each channel with the CASA task `imfit`. An initial guess was given of the peak position and peak intensity for each emission peak in each channel. Some channels had multiple emission peaks. For this chapter, a "maser spot" refers to a single emission peak in a single channel.

There were 189 methanol maser spots detected in MM1, MM2 and MM3-UCHII. Methanol maser emission was not detected in CM2 and MM4. Masers were detected in a velocity range of -12.07

Association	Centroid Position (J2000)		Velocity
	R.A.	Dec.	(kms^{-1})
UHCII-Met1	17:20:53.4501	−35:47:03.104	−9.34, −6.1
UHCII-Met2	17:20:53.4330	−35:47:02.289	−9.08, −7.85
UHCII-Met3	17:20:53.4550	−35:47:01.160	−8.73, −7.85
UHCII-Met4	17:20:53.3912	−35:47:01.172	−11.8, −8.73
UHCII-Met5	17:20:53.4731	−35:47:00.192	−9.96, −9.78
MM1-Met1	17:20:53.3453	−35:46:57.585	−9.52, −4.34
MM1-Met2	17:20:53.4388	−35:46:56.625	−8.2, −4.16
MM2-Met1	17:20:53.1958	−35:46:58.821	−12.07, −9.78
MM2-Met2	17:20:53.1711	−35:46:58.643	−9.61, −7.94

Table 4.9: Summary of the positions and velocity extents for the CH_3OH maser associations in the 2019.6 observations.

$\mathrm{km\,s^{-1}} \leq V_{\mathrm{LSR}} \leq -4.16\ \mathrm{km\,s^{-1}}$. Figure 4.8 shows the spatial distribution of the methanol masers, overlaid on the 2015.6 1.3 mm continuum and the 2016.9 5 cm continuum described above. Hunter et al. (2018) imaged the 6.7 GHz methanol masers and excited hydroxyl masers at 2016.9. Comparison of panel a) of Figure 4.8 to Figure 1 of Hunter et al. (2018) shows good agreement in the positions and radial velocities of the maser spots in MM1, MM2 and MM3. Table A.1 shows the positions, radial velocities of each maser spot. Maser spots were categorized into different associations within each region, numbered from south to north. Table 4.9 shows a summary of each association, containing their centroid position and velocity information. The following paragraphs describe the methanol maser results for each region.

In MM1 67 maser spots were detected in two maser associations, MM1-Met1 on the western edges of MM1 and MM1-Met2, north of the millimetre continuum peak, close to the cavity and MM1F. MM1-Met1 is around 1200 AU from the closest 1.3 mm continuum peak, MM1A. The masers in this region coincide with the western edge of the 2015.6 thermal methanol 11(2)−10(3) lines, shown in Hunter et al. (2018). The association formed an arrow-shaped collection of blue-shifted masers with a length of 1400 AU and a velocity range of $-9.52\ \mathrm{km\,s^{-1}} \leq V_{\mathrm{LSR}} \leq -7.94\ \mathrm{km\,s^{-1}}$. MM1-Met2 shows a "V" shape, first seen in Hunter et al. (2018). Closer inspection shows that the association is two separate groups of masers. The left part of the "V"-shape consists of a 600 AU group maser spots with $V_{\mathrm{LSR}} > -6$ $\mathrm{km\,s^{-1}}$. The right part of the "V"-shape is a 360 AU ring with $-8.5\mathrm{km\ s^{-1}} \leq V_{\mathrm{LSR}} \leq -5.8\mathrm{km\ s^{-1}}$ which overlaps the cavity shown in 1.3 mm continuum and the radio jet shown in 5 cm.

In MM2, 46 maser spots were detected in two associations, MM2-Met1 and MM2-Met2. These two associations look like axially symmetric "wings". The axis of symmetry is in the same orientation as the millimetre core, but offset by around 500 AU. MM2-Met1 has a linear scale of 200 AU and a radial velocity around $-11\ \mathrm{km\,s^{-1}}$, which is slightly blue-shifted compared to MM2-Met2, which is a 280 AU $V_{\mathrm{LSR}} \sim -9\ \mathrm{km\,s^{-1}}$. The two associations look like they are tracing the cross-section of a torus with an inner radius of 160 AU, and an outer radius of 270 AU.

In MM3-UCHII, 76 methanol maser spots in five associations were detected, UCHII-Met1 to UCHII-Met5. UCHII-Met1 consists of two linear features, a 100 AU blue-shifted feature with $V_{\mathrm{LSR}} \sim -9.26$ $\mathrm{km\,s^{-1}}$ and a 460 AU redder linear feature with $-7.41\ \mathrm{km\,s^{-1}} \leq V_{\mathrm{LSR}} \leq -6.10\ \mathrm{km\,s^{-1}}$. UCHII-Met2 consists of a compact feature inside the dust continuum contour with a radial velocity close to −8 $\mathrm{km\,s^{-1}}$. UCHII-Met3 is also a compact association with a narrow velocity range around $-8.5\ \mathrm{km\,s^{-1}}$,

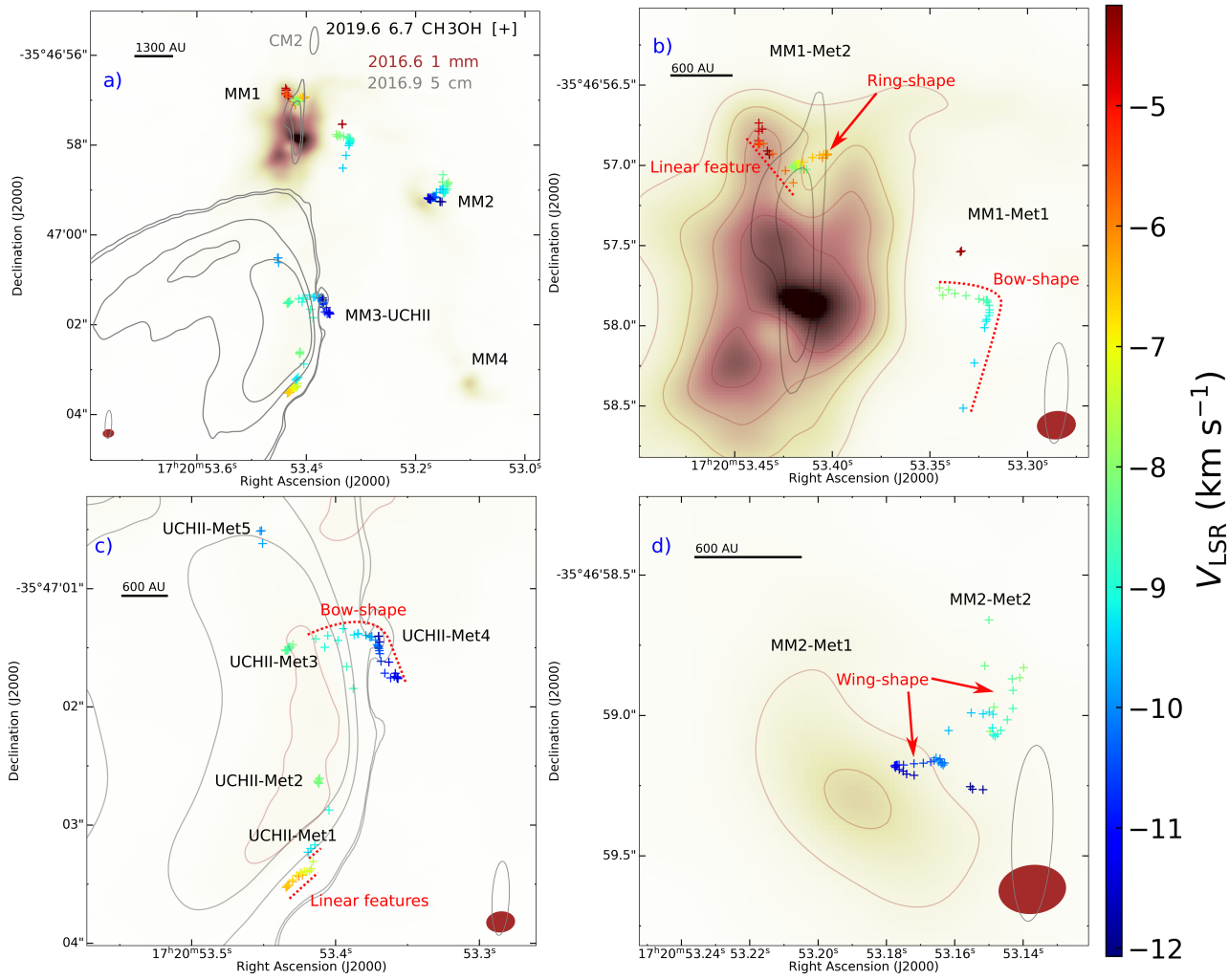

Figure 4.8: Maps of detected 6.7 GHz methanol masers at different zoom levels. Methanol masers [+] superimposed on epoch 2015.6 ALMA 1.3 mm dust continuum from Brogan et al. (2016) (brown) and epoch 2016.9 JVLA 5 cm continuum emission from Brogan et al. (2018). The positions of the crosses and colour scale indicate the positions of the maser peaks and their radial velocities respectively. For all the panels, the linear distance scale at 1.3 kpc is shown in the top left. The ALMA and JVLA continuum beams are shown in the bottom left for panel a) and in the bottom right for panels b) - d). Panel a) The entire field. b) Methanol masers in MM1, shown in coloured crosses. The names of the detected maser associations are shown in black text, note that these names are not the same as in Hunter et al. (2018). c) Methanol masers MM3-UCHII. d) Methanol masers in MM2. Red annotations indicate the morphology of selected maser associations.

close to the edge of the dust continuum contours. The masers in UCHII-Met4 show a "bow" shape centred on the cavity in the 5 cm continuum contours (see panel c) of Figure 4.8. According to Hunter et al. (2018), UCHII-Met4 contains the brightest masers in the field, and three principle features centred at -11.1 km s^{-1}, -10.3 km s^{-1} and -9.7 km s^{-1} in velocity space. Lastly, UCHII-Met5 is a compact -9.9 km s^{-1} association north of the other masers.

4.6 Summary of Key Findings

Overall, the water maser observations with VERA have shown that the accretion burst has affected the intensities, spatial and velocity distributions of water masers in NGC6334I. These changes were in effect very soon after the onset of the burst, with changes already observed between 2015.08 and 2015.28. The methanol masers that were detected were in the same regions and with the same radial velocities as reported in previous works. The following list is a more detailed enumeration of the results presented in this chapter.

4.6.1 Continuum Images

- 1.3 mm 2015.6 ALMA continuum of NGC6334I from Brogan et al. (2016) was reviewed. The region consists of nine millimetre cores MM1, ..., MM9, extended over about 10 000 AU. MM1, MM2 and MM3 are the brightest and largest cores in the region.
- MM1 consists of multiple hot cores, MM1A, MM1B, MM1C, and MM1D, likely harbouring multiple YSOs. The region is also the origin of multiple outflows, and a cavity ploughed through the cloud by these outflows.
- MM2 consists of a hot core, and a millimetre peak in some wavelengths.
- MM3 traces a half moon shape which is likely hot gas and dust at the edge of the UCHII region NGC6334F.
- 5 cm 2016.9 JVLA continuum of NGC6334I from Hunter et al. (2018) was also reviewed. Three continuum peaks were detected: The bright cometary shaped UCHII region NGC6334F, a faint elongated emission in the N-S direction, and the point source CM2.

4.6.2 22 GHz Water Masers

- 22 GHz water masers were detected before and during the recent accretion burst in NGC6334I. Water masers were detected in CM2-W1, CM2-W2, MM1-W1, UCHII-W1, UCHII-W2 and UCHII-W3.
- Each region, except CM2 during the burst epochs, showed significant variability in peak intensity throughout all epochs.
- The spatial distributions of the water masers changed over time, and proper motions were calculated.
  - In CM2-W2, new blue-shifted features were detected at the apex of the bow shock, similar to what was seen by Brogan et al. (2018). The bow shape was also more clearly traced as the epochs progressed.
  - In MM1-W1, a linear feature had a bulk displacement of 7 AU between the pre-burst and burst epochs. The region showed complicated proper motions.

  - In UCHII-W1, four clusters of water masers were detected before the burst and three clusters after the burst. Only a single cluster was persistent (W1B-iii, corresponding to W1A-ii). Most of the proper motions were high-velocity $v > 50$ km s^{-1} southward proper motions.
  - UCHII-W2 consisted of a single high-velocity cluster which displaced by 6 AU between the pre-burst and burst epochs.
  - UCHII-W3 consisted of a single high-velocity feature with $V_{\rm LSR} = -28$ km s^{-1} before the burst, which disappeared after the burst. Two new high-velocity features at $V_{\rm LSR} = -49$ km s^{-1} and $V_{\rm LSR} = -37$ km s^{-1} were excited after the burst 61 AU and 110 AU respectively from the original maser feature.

- Water maser proper motions were calculated with two methods of maser feature identification. The spot method and the spectral feature method.

  - The spot method defines a maser feature as spots that are within the same channel between epochs. This is equivalent to the assumption that proper motions cannot be traced between features that have radial acceleration between epochs.
  - The spectral method defines a maser feature as a collection of maser spots that have a Gaussian spectral distribution, whereas a persistent maser feature has a similar centre velocity between epochs. This method assumes proper motions can be traced with maser features undergoing radial acceleration and that the Gaussian spectral profile for a group of localized spots is the observational definition of a maser feature in VLBI images.
  - The proper motions that were traced were largely the same between the two methods, although there were differences in the proper motions traced in UCHII-W1 (preburst), UCHII-W2 (preburst) and W1A-ii.

4.6.3 6.7 GHz Methanol Masers

- 6.7 GHz methanol masers were detected with 2019.6 JVLA observations of NGC6334I. Methanol masers were detected in MM1, MM2 and MM3-UCHII.

- Two associations were detected in MM1: MM1-Met1 and MM1-Met2. MM1-Met1 was a 1400 AU bow shape at $V_{\rm LSR} \sim -8.5$ km s^{-1}, which is co-spatial with thermal methanol emission reported by Hunter et al. (2018). MM1-Met2 looked like a "V"-shape, and was also detected by Hunter et al. (2018), but the "V"-shape actually consisted of two associations. The left part was a linear feature with $V_{\rm LSR} > -6$ km s^{-1}. The right part is a ring shape co-spatial with the cavity traced in millimetre continuum in MM1.

- Two associations were detected in MM2: MM2-Met1 and MM2-Met2, which has a symmetrical "wing" morphology.

- Five associations were detected in MM3-UCHII. Each association was associated with the millimetre continuum at the edge of MM3-UCHII. UCHII-Met4 also showed a bow shape and some of it's masers were co-spatial with a bulge in the UCHII region.

Chapter 5

Discussion

5.1 Introduction

This chapter discusses the results of this thesis in light of other observations and theory. First, the variability of the water masers in NGC6334I is discussed. Then the water maser proper motions are discussed by comparing them to similar previous observations. The validity of water maser proper motions as a tracer of gas motion is discussed briefly, followed by an estimation of outflow parameters such as the dynamic timescale, outflow force, driving source luminosity and driving source mass for both NGC6334I and S255IR-NIRS3, another accretion bursting source. The last section is a critical analysis of the 2019.6 JVLA methanol maser observations, and a comparison of the methanol maser maps to previous work.

Figure 5.1 gives a large scale view of the main results from chapter 4, and will be used to frame some of the discussions in this chapter. The figure consists of 1.3 mm 2015.6 ALMA continuum in brown background, 5cm 2016.9 JVLA continuum in grey contours, 2019.6 methanol masers indicated by crosses [+] and the VERA 22 GHz burst proper motions with the spectral method. Note that the methanol masers and proper motions use a different colour scale. Annotations were added to the figure. The green and blue dotted lines show jets identified in previous work, the N-S and NW-SE bipolar outflows and the NW jet with only a blue-shifted lobe (Brogan et al., 2018; Chibueze et al., 2021). The ~ 0.5 pc large-scale wide-angle outflow from Qiu et al. (2011) is shown in the red and blue bow shapes.

5.2 Variability of Water Masers

Observations have found many water masers to be highly variable in flux density (Gwinn, 1994a; Ladeyschikov et al., 2022). If water masers are formed behind shocks, as suggested by Hollenbach et al. (2013), it would be expected that all water masers show a kind of "hydrodynamic variability" that has variability on the timescale of density perturbations in the masing gas. Velocity coherent material moving in and out of the line of sight would significantly affect the flux density of unsaturated masers, where the flux has an exponential dependence on column density. On the other hand, for accretion bursting sources, the hydrodynamic variability intrinsic to all water masers behind shock fronts should be differentiated from "pump variability" which is caused by changes in the pump efficiency in the masing gas due to changes in other variables than column density, such as $T_{\rm kin}$, $T_{\rm dust}$ and $n_{\rm H_2}$. Pump variability will be of the same timescale as the physical changes in the source that cause the changes in pump efficiency. Pump variability in NGC6334I has likely been observed both in other observations and in the observations reported in this thesis.

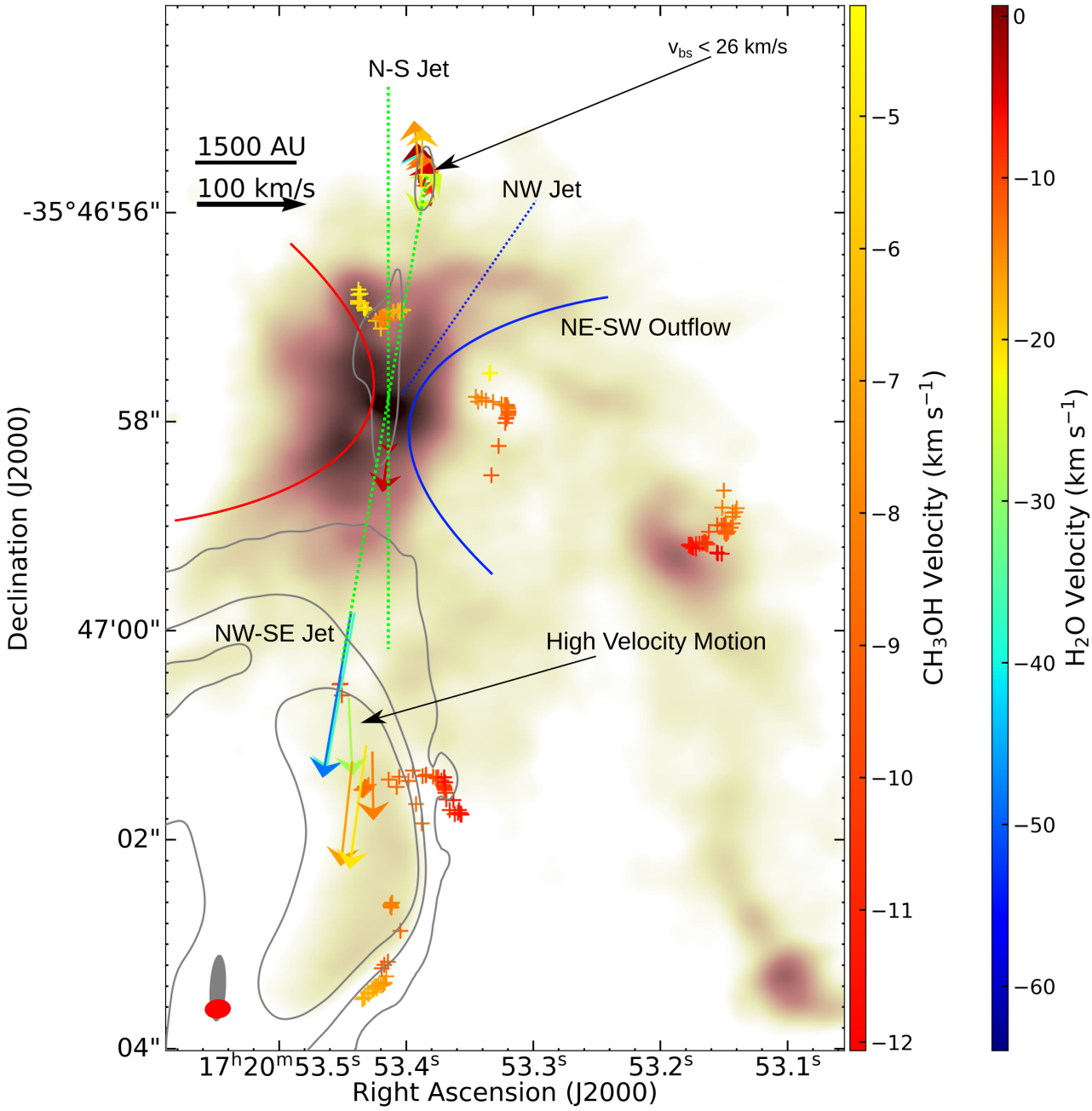

Figure 5.1: Summary of the main discussion items of this thesis. Coloured arrows: Burst proper motions calculated with the spectral method from 22 GHz water masers. Brown background: 2015.6 ALMA 1.3 mm continuum. Grey Contours: 2016.9 JVLA 5 cm continuum. The coloured dashed lines show the orientation of known outflows. The red and blue bow shapes show the red and blue lobes of the large scale NE-SW outflow. The linear and velocity scale is shown in the top left, and the beam shapes of the continuum images are shown in the bottom right. The names of the water and methanol maser associations are excluded from the figure for clarity and can be found in Figures 4.2 and 4.8 respectively.

MacLeod et al. (2018) reported water maser flares in various velocity components with factors ranging from $15 - 300$. The masers stayed in a flaring state until the last observation they reported. Another indication that the water maser flare is likely due to intrinsic changes is that the water maser flare was co-temporal with flares in other maser species (MacLeod et al., 2018) and an increase in millimetre continuum (Hunter et al., 2018).

In chapter 4, variability was clearly seen in maser summed intensities, positions and radial velocities for all regions in which water masers were detected. This is most clearly seen in CM2. The summed intensities of CM2 followed a similar pattern of a dip, peak and smaller dip as the time series observed in HartRAO shown in Figure 2.8 (from MacLeod et al., 2018). The masers in CM2 trace a bow structure more clearly with time up to the last epoch in the VERA observations. This process of more clearly tracing the bow shock actually continues up to 2017.8, which can be seen by comparing the 2017.0 and 2017.8 JVLA water maser observations by Brogan et al. (2018). The velocity width of CM2 also increased systematically, with new blue-shifted features at the apex of the shock. This points to the conclusion that the water maser variability in CM2 is likely dominated by pump variability, as a consequence of the accretion burst.

The water masers in MM1-W1 showed a trend of decreasing intensity, and physically grew smaller with a linear extent of 15 AU before the burst and 7 AU after the burst. Brogan et al. (2018) saw a similar change in the region, where masers near MM1B dampened significantly between 2011 and 2017. They attributed the water maser variability to an increase in infrared radiation that could have blocked the sink transition, which decreased the pump effiency of water masers in the region. The masers in UCHII-W2 and UCHII-W3 consisted of one or two maser features that disappeared during the initial epochs of the accretion burst, and had new maser features appear in later epochs. It is not immediately apparent if the changes in the maser features in UCHII-W2 and UCHII-W3 are due to the burst or hydrodynamic variability that was coincident with the burst epochs. The same can be said of UCHII-W1, which is a more complicated region. The flux variability in UCHII-W1 did not show a particular trend, nor did the appearance or disappearance of the water maser features. The masers in UCHII-W1 shown by Brogan et al. (2018) also do not show clear flux variability with the accretion burst. Therefore it is not clear whether the variability in UCHII-W1 can reasonably be attributed to the accretion burst.

Mention should be made of the study of the pre-burst and burst water masers in S255IR-NIRS3 by Hirota et al. (2021). They did not find a discernible pattern in the water maser flux variability, which suggests hydrodynamic variability rather than pump variability due to the accretion burst. This comparison shows that significant water maser flaring is not found in all accretion bursting sources.

5.3 Water Maser Proper Motions

5.3.1 Comparison with Chibueze et al. (2021)

Chibueze et al. (2021) (hereafter JOC21) reported water maser proper motions for NGC6334I with epochs covering 2015.89−2016.01 with the KaVA VLBI array (hereafter KaVA observations). These observations fall between epochs five and six of the VERA observations discussed in this work (hereafter VERA observations). The main technical differences between the KaVA observations and the VERA observations are that the KaVA observations had a higher spectral resolution (0.21 $\mathrm{km\,s^{-1}}$ vs 0.42 $\mathrm{km\,s^{-1}}$), more sensitive observations due to a larger total collecting area and a better angular resolution (KaVA beam: 0.97 mas $\times$ 2.48 mas, VERA beam: 1.3 mas $\times$ 3.3 mas). The procedure JOC21 used to calculate proper motions was the spot method discussed in Section 4.4.2. The results from JOC21

will be compared to the results from the spot method in this work. The largest systematic differences is that the VERA observations had a reference maser in CM2, and JOC21 had a reference maser in UCHII-W1. The second difference is that the proper motions in this thesis were shifted to an absolute velocity frame, while the proper motions in JOC21 were relative.

As the KaVA and the post-burst VERA results cover the same time period, one would expect to trace the same proper motions if technical and systematic differences are accounted for. Both results also show a similar bipolar outflow pattern for the proper motions. The KaVA observations did detect more proper motions and a marginally wider velocity range. The region MM1-W3 that is reported in JOC21 was not detected in the VERA observations, likely due to the masers in that region falling below the VERA detection limits. The authors of JOC21 did state that there is a possibility of the motions in MM1-W1 being influenced by multiple outflows. One should note that certain water maser regions are so complicated that unambiguous identification of maser features is difficult with the methods employed in this chapter and in JOC21. Both observations found the same linear morphology for the water masers, and that only the proper motion vectors differ significantly. The differences in the proper motion vectors can then be attributed to a combination of instrumental differences between the arrays, and the possibility of misidentification of maser features due to the method employed in this study and in JOC21.

One of the scientific conclusions of JOC21 can be addressed. They found northward proper motion in UCHII-W1 with a mean speed of 64 $\mathrm{km\,s^{-1}}$. If these proper motions would have been shifted to the same absolute reference frame as used in this work, they would not have shown northward motion. This is the case because the mean proper motion that they reported for CM2 was 112 $\mathrm{km\,s^{-1}}$. That is a $\sim$ 80 $\mathrm{km\,s^{-1}}$ difference from the upper limit set by the observations by Brogan et al. (2018). Chibueze et al. (2021) reported a mean (mostly upward) speed of 64 $\mathrm{km\,s^{-1}}$ for the water maser in UCHII-W1. Therefore, if the $\sim$ 80 $\mathrm{km\,s^{-1}}$ proper motion shift was done, the southern proper motions would point south. Therefore, the discussion in Section 4.3 of JOC21 on the possibility that UCHII-W1 being affected by the UCHII region NGC6334F and not the N-S jet in MM1 is likely a consequence of interpreting relative proper motions without correcting for the absolute reference frame.

5.3.2 Conditions for Water Masers to Trace Gas Motion

The assumption of all water maser proper motion studies of protostellar jets is that the maser features that are identified are in fact a physical cloud of gas moving in space and not merely a propagation of pumping conditions, which may be different from the gas motion. For water maser observations gas motion refers to the motion of the $T \sim 400$ K gas some distance behind the shock front, where the masers are found (Hollenbach et al., 2013). Goddi et al. (2006) specifically defended this assumption. They did three epochs of water maser observations with the Very Long Baseline Array and found persistent emission with systematic motions in their source. Their discussion concluded that if water maser proper motions traced a propagation of pumping conditions rather than gas motion, the motions would not be ordered, and there would be significant changes in the water maser morphology in their observations. Note that logically, they have only proved that *some* water maser proper motions trace gas motion, but not necessarily *all*. Moscadelli et al. (2020) report a larger scale survey of the water maser proper motions of 38 high-mass SFRs. They found a large fraction (84%) of water maser proper motions to be closer than 1000 AU to young stellar objects and that 55% of the proper motions are within 30° of the jet axis originating in the YSO. The association of water masers with protostellar jets led Moscadelli et al. (2020) to conclude that most water maser proper motions are associated with gas motion.

The results in this thesis support the above-mentioned hypothesis if a few considerations kept in mind when calculating proper motions. Firstly, the multi-epoch water maser observations in NGC6334I show that maser spots can have major changes in their spatial and velocity distributions in a short time if there are changes in the SFR on the same timescale as the observations. This is analogous, but not the same as the fast destruction and excitation of methanol masers observed by Burns et al. (2020). Secondly, the method (spot or spectral) of grouping maser features does affect the result in some cases. For a simple maser distribution, or observations with coarse ($\geq$ 1 km s^{-1}) spectral resolution, it is not possible to use the spectral method, as the line profile of the maser feature will be narrower than the channel width. For complex regions where the spectral resolution is fine ($\leq$ 1 km s^{-1}), both methods are applicable, and can have slightly different results. The spectral method is more robust than the spot method against falsely identifying side lobes, which are due to calibration errors, as maser features.

5.3.3 Outflow Parameters

Dynamic Timescales

Figure 5.1 summarizes the multiple outflows originating in MM1. Four jets/outflows can be identified. Proper motions were associated with two of these outflows. The N-S jet, first seen by Brogan et al. (2018) is traced by the high-velocity proper motions in UCHII-W1 and UCHII-W2. As the choice of velocity frame gives us a lower limit on the proper motions, the burst proper motions with the spectral method of UCHII-W1 imply a jet speed $v_{\text{N-S}} > 92^{+47}_{-21}$ km s^{-1}. From Figure 8 of Brogan et al. (2018), it can be seen that the N-S outflow is 4450 AU from MM1B. This implies a dynamic timescale $t_{\text{N-S}} = d_{\text{N-S}}/v_{\text{N-S}}$ of 230^{+50}_{-120} yr. This value is consistent, but less precise, with the dynamic timescale estimates of the same outflow of 170 ± 18 yr from water maser bulk motion and 102 yr from thermal line tracers by Brogan et al. (2018).

For the NW-SE jet identified by Chibueze et al. (2021), CM2-W2 traces the one end of the jet and UCHII-W3 the other end. UCHII-W3 shows much higher proper motion than CM2-W2. This is likely due to the edges of the jet propagating through different densities of the ISM. The NW-SE jet has a size of 3250 AU by Figure 8 of Brogan et al. (2018). With a velocity of $v_{\text{NW-SE}}$ km s^{-1} of 155 ± 14 km s^{-1}, the dynamic time of the jet can be estimated $t_{\text{NW-SE}} = 99 \pm 9$ yr. The N-S jet and the NW-SE jet have a similar dynamic timescale. These outflows might either be associated with the same driving source and have changed their angle due to disk precession (e.g., Bate et al., 2000), or the outflows might have different driving sources but seem to be associated due to projection effects. This region has multiple YSOs (Brogan et al., 2016), which adds to the complexity of the region.

Two other outflows were identified by previous authors. The NE-SW outflow has a size of $\sim$ 0.5 pc, and a dynamic time of 2600 yr (Qiu et al., 2011). The NW blue-shifted lobe has an estimated dynamic time of $\sim 1280 \tan\theta_{\text{inc}}$ yr, with θ_{inc} the unknown inclination angle of the outflow (Brogan et al., 2018).

Empirical Estimates of Outflow Force, Driving Source Luminosity and Mass

To compare the evolutionary stages of NGC6334I-MM1 and S255IR-NIRS3, the outflow force $\dot{P}$ from water maser observations were estimated. P is the gas momentum. The method of Li et al. (2012) was adopted, where the outflow force for a water maser jet can be estimated by the following expression:

$$\dot{P} = 1.5 \times 10^{-3} V_{10}^2 R_{100}^2 \frac{\Omega}{4\pi} M_\odot \text{yr}^{-1} \text{km s}^{-1} \tag{5.1}$$

In the expression above V_{10} is the average 3D maser speed in units of 10 km s^{-1}, R_{100} is the distance from the source to the jet in units of 100 AU, and Ω is the solid angle subtended by the jet from the

source's perspective. The constant value of 1.5×10^3 comes from assuming the pre-shock density to be 10^8 cm^{-3}, and that the outflow consists exclusively of hydrogen. Li et al. (2012) observed their source with multi-epoch maser and continuum observations, so they could estimate Ω by combining both results. If it is assumed that the jet is axisymmetric, the solid angle of the jet is given as $\Omega = 2\pi(1-\cos\theta)$, with θ the jet semi-opening angle in radians. The jet opening angle θ can be inferred either by the bow structure in water masers, or the jet width in continuum. In the case of NGC6334I and S255IR-NIRS3, multi-epoch continuum observations are not available, so an estimate for Ω for the jets in S255IR-NIRS3 and NGC6334I-MM1 by using the width of the water maser bow shocks.

The main determining factor for the outflow force is the luminosity of the driving source, with a power law relationship (Bontemps et al., 1996; Maud et al., 2015b; Rosen and Krumholz, 2020). The empirical power law relationship in Maud et al. (2015b) is given by:

$$\log_{10}\dot{P} = -4.8 + 0.61 \times \log_{10}L(L_\odot) \tag{5.2}$$

with $\dot{P}$ in units of $M_\odot$ yr^{-1} km s^{-1}. Further, protostellar luminosity has also been found to have an empirical power law relationship with mass, under certain assumptions (Maud et al., 2015a). This relationship is given by (Maud et al., 2015a):

$$L = KM^{1.08\pm0.50} \tag{5.3}$$

with K = 47.7. The derived mass and luminosity can then in turn be compared to the accretion burst models of Meyer et al. (2017, 2021).

Outflow Parameters in S255IR-NIRS3

For S255IR-NIRS3, V_{10} was estimated by using the bulk motion of the maser features. The outflow force for S255IR-NIRS3 was not estimated by either Burns et al. (2016) or Hirota et al. (2021), so it was estimated using the procedure described here. First the spot maps for the first eleven epochs of Burns et al. (2016) were obtained (Burns, R, private communication). The data used were taken at 2008−2010, but the water masers in S255 did not change dramatically due to the accretion burst, (Hirota et al., 2021), so comparing pre-burst water masers in S255 to the burst water masers in NGC6334I should be reliable. A parabola was fit to the spot maps for each epoch to measure the propagation of the bulk motion. For S255 this was spots in the region of α offset $\in [-7.78, 19]$ mas and δ offset $\in [-22.95, 5]$ mas, with the offset defined in Burns et al. (2016). Figure 5.2 shows the positions of the maser detections in colour, as well as the parabolic fits to those spots. The intersections of the parabolic fits and the dashed lines is shown in black squares. The positions over time of these black squares were used for the proper motion calculation. Note that hundreds of these lines perpendicular to the parabola of the first epoch could be calculated. The red dashed line shows the proper motion adopted for the bulk motion calculation.

Epoch two complicated the analysis, as the fitted parabola for this epoch did not follow the bulk motion shown by the other epochs. The assumption of bulk motion is that the displacement from the source changes monotonically with time, epoch two had less displacement than epoch four. Epochs five, seven, eleven and twelve were very close in time to the epochs prior to them, and were excluded in the bulk motion calculation. After fitting the parabolas, normal lines on the first epoch between α offset $\in [0, 7]$ mas were calculated, the intersection of the normal line and the parabolas of the consecutive epochs were used as data points for the linear fits of α and δ vs time to calculate proper motions. It was expected that the proper motions would not be uniform along the bow structure. In S255, it was found that the proper motion μ had a minimum magnitude along the normal line

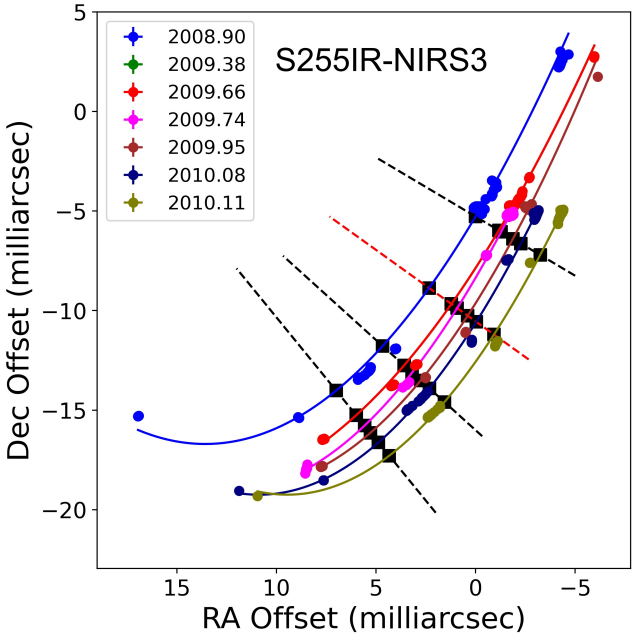

Figure 5.2: Left: The water masers in the bow-shock of S255IR-NIRS3 over time from Burns et al. (2015). The coloured dots show the positions of the water maser detections. The lines of the same colours are parabola fits to the water maser positions. The dashed lines show some of the normal lines used to calculate the proper motion perpendicular to the bow structure in the first epoch. The red dashed line shows the direction in which the proper motion was the highest, and was used for the calculation of the outflow momentum.

$\delta(\alpha)$ (mas) $= 0.72\alpha - 10.54$ (mas). This direction aligns with the propagation direction of the bow shock. Therefore it was calculated that $\mu_\alpha = -2.80 \pm 0.25$ mas yr^{-1} and $\mu_\delta = -1.93 \pm 0.09$ mas yr^{-1} as the bulk motion in S255. The uncertainties on the position of the bow structure for each epoch were calculated by using the sums in quadrature of the uncertainties on the parabolic fits, and the uncertainties in the maser positions. The $V_{\rm LSR}$ was estimated by calculating an $\overline{V}_{\rm LSR} \pm \delta V_{\rm LSR}$. The standard deviation on the mean for each epoch was averaged to calculate $\delta V_{\rm LSR}$. It was calculated that $V_{\rm LSR} = 3.09 \pm 1.47$ km s^{-1}. Adopting the distance of $1.78^{+0.12}_{-0.11}$ kpc, $V_{\rm 3D} = 28.85 \pm 2.25$ km s^{-1} for S255. Although this procedure calculated relative proper, the systemic proper motion (0.563 ± 0.036 mas yr^{-1}) of the reference maser calculated by Burns et al. (2016) could be neglected in the calculation.

From the described procedure, it was calculated that $V_{10} = 2.885 \pm 0.225$. It was simpler to calculate R_{100} and Ω. R_{100} was the distance from the driving source to the bow shock, in the first epoch of Burns et al. (2016). Taking the uncertainty of the position of the driving source into account (from Hirota et al., 2021), it was calculated that $R_{100} = 2.98 \pm 0.78$ and a semi-opening angle $\theta = 13.0^{+4.9}_{-3.2}$ degrees, which implies $\Omega = 0.16^{+0.14}_{-0.07}$ steradian. Finally, the outflow force for S255 is then given by $\dot{P} = 1.4^{+1.3}_{-0.3} \times 10^{-3} M_\odot$ yr^{-1} km s^{-1}.

For S255IR-NIRS3, the value of $\dot{P}$ implies a driving source luminosity of $1.5^{+3.0}_{-0.5} \times 10^3 L_\odot$. The driving source of S255IR-NIRS3 has a luminosity smaller than $2.4 \times 10^4 L_\odot$ (the HMYSOs bolometric luminosity) (Caratti o Garatti et al., 2017). The core mass calculated with Equation 5.3 with the driving source luminosity is $29^{+58}_{-16} M_\odot$. The large uncertainty in mass is due to the large uncertainty in the power law fit of Maud et al. (2015a). The stellar luminosity calculated from the outflow force of S255IR-NIRS3 is consistent with a mass of 20 $M_\odot$, which gives support to the method used here. From Figure 3 of Meyer et al. (2021) S255IR-NIRS3 corresponds with a protostar undergoing one of its first accretion bursts.

Outflow Parameters in NGC6334I

For NGC6334I, it was difficult to find a unique fit of parabolas for the water masers in CM2. Therefore, the upper limit on $\dot{P}$ was estimated with the upper limit of the bow shock speed by Brogan et al. (2018). They reported $V < 26$ km s^{-1}. This implies $V_{10} < 2.6$. R_{100} and Ω of the outflow are most reliably calculated with the high sensitivity JVLA water maser observations by Brogan et al. (2018), as these observations trace the bow-shock much better than the VLBI observations by detecting much weaker masers. The position of the driving source is the position of MM1B, from Brogan et al. (2016). From this $R_{100} = 24.4 \pm 2.1$ and $\theta = 0.15 \pm 0.01$ radians, corresponding to $\Omega = 0.07 \pm 0.01$ steradian. Finally, an outflow force is obtained as $\dot{P} < 33.6 \times 10^{-3} M_\odot$ yr^{-1} km s^{-1}.

The outflow force for NGC6334I and S255IR-NIRS3 can be compared to other values of $\dot{P}$ in literature, like $200 \times 10^{-3} M_\odot$ yr^{-1} km s^{-1} for G28.87+0.07 (Li et al., 2012), $8 \times 10^{-3} M_\odot$ yr^{-1} km s^{-1} in G16.59–0.05 (Sanna et al., 2010a) and $\dot{P} \geq 100 \times 10^{-3} M_\odot$ yr^{-1} km s^{-1} for G23.01-0.41 (Sanna et al., 2010b).

From the calculations for NGC6334I-MM1, $\dot{P} < 33.6 \times 10^{-3} M_\odot$yr^{-1} km s^{-1}. This implies a driving source luminosity of $L_{\rm ds} < 10^{5.45} L_\odot$ from Equation 5.2. This luminosity implies a driving source mass $M_{\rm ds} < 10^{6.5} M_\odot$, by Equation 5.3. The mass upper limit is very large and not very meaningful, and was due to the ∼50% uncertainty on the power law of Equation 5.3. The fact that the analysis employed in this section for S255IR-NIRS3 is consistent with mass and luminosity estimates using other methods, show that the method in this section is reliable. Better constraints on the bulk motion of CM2 would allow $L_{\rm ds}$ and $M_{\rm ds}$ to be measured with greater precision. The estimates of L and $M_{\rm ds}$ are with power laws, so small uncertainties can magnify the uncertainty in the parameters significantly.

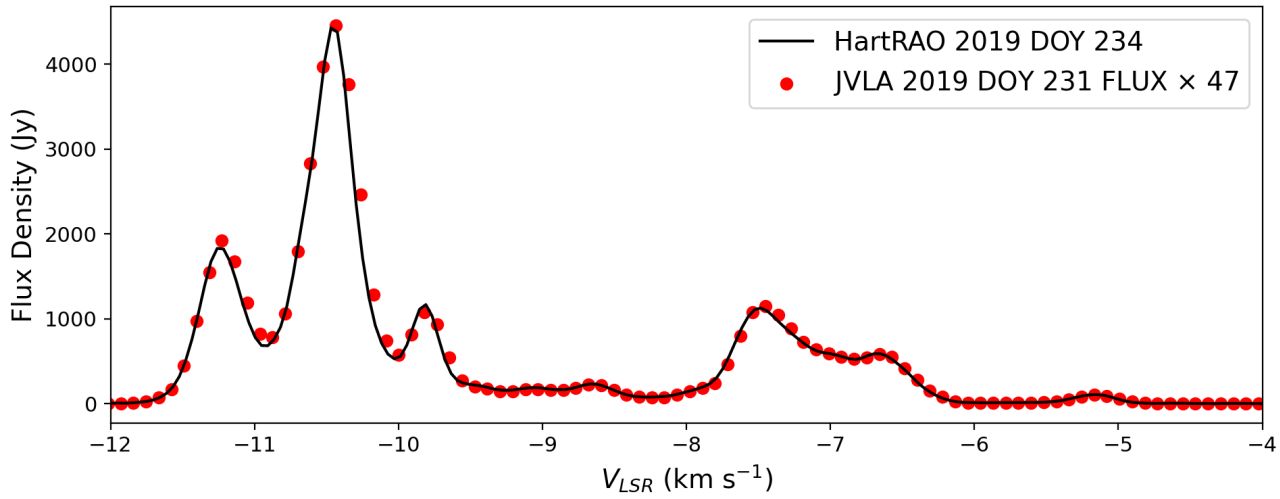

Figure 5.3: Comparison of HartRAO and JVLA spectra of 6.7 GHz methanol masers in NGC6334I. The black line represents the spectra taken with the HartRAO telescope, while the red dots indicate the integrated spectrum of the 2019.6 JVLA methanol masers multiplied by a factor of 47.

5.4 Methanol Masers

5.4.1 Critical Analysis of Results

In Section 4.5, 6.7 GHz methanol masers observed by the JVLA on 2019.6 were reported. The flux densities from the final images were compared to those reported by Hunter et al. (2018) (hereafter TRH18). It was found that the maser integrated flux densities from the JVLA 2019.6 observations reported in this thesis were significantly less than those observed in 2016.9. This difference could either be real or due to a mistake in the calibration of the 2019.6 dataset. See Figure 5.3, it shows the single-dish maser spectra as observed with HartRAO (MacLeod, G, private communication) on a date very close to the JVLA 2019.6 observations. The HartRAO spectra were calibrated with standard single-dish procedures (e.g., MacLeod et al., 2018). Note that the left-circular polarization, and right-circular polarization spectra were added to produce the total power spectrum, in conformity with the usage in maser monitoring. The comparison between the 2019.6 JVLA result reported in this thesis and that of a single-dish spectra show that there is a flux density difference of a factor of 47. The relative values of the flux densities for different velocity channels is the same.

The positions and radial velocities of the 2019.6 JVLA methanol masers can be compared to those of the 2016.9 JVLA observations by TRH18. Compare Figure 4.8 and Figures 1 and 2 of TRH18. All of the methanol maser associations reported in Chapter 4 have counterparts in TRH18. This indicates that the phase calibration of the results reported in this thesis was good enough to not significantly change the positions of the masers. Two drawbacks with the methanol maser results presented in Chapter 4 can be identified. Firstly it is clear that the flux density values were wrongly calibrated by some constant factor. Secondly, many faint masers that can be seen in TRH18 are not detected in the 2019.6 results. This could either be due to the dampening of these masers in reality, or due to the error in flux calibration. There are a few points in the data calibration where an error could have been made. The parts in the calibration procedure where flux densities are scaled are either the two uses of the task `fluxscale` before and during corrections for the spectral index of the bandpass calibrator or the amplitude self-calibration before final imaging.

Final comments should be made regarding the results produced in Section 4.5. The comparison with single-dish data showing that the integrated spectra of the 2019.6 JVLA results are directly proportional to the single-dish spectra shows that there are not mistakes in the radial velocity of the emission. Further, alignment in the position and radial velocities between the detected methanol maser regions described in Section 4.5 and those reported by TRH18 implies that the detections in the 2019.6 are real, even if the flux density is not known. It is due to the flux density error that the flux densities and brightness temperature of the 2019.6 methanol masers were not reported. Therefore, a comparison between the 2019.6 methanol masers and those of TRH18 is limited to the brightest masers in the field.

5.4.2 Comparison with Hunter et al. (2018)

Methanol Masers in MM1

See Figure 4.8 or 5.1, MM1-Met1 shows a bow-shaped structure, with a continuous velocity gradient, pointing away from MM1. A structure at the same position with a similar $V_{\rm LSR}$ was detected by TRH18. In their observations the bow shape is more diffuse than the results in this thesis, where the bow shape is well-defined. Another association, MM1-Met2, shows a clear "V" shape, that was also described by TRH18. On further inspection, this region shows two independent components that make out the two "arms" of the "V" shape. The first is a linear feature with $-5.7\ \mathrm{km\,s^{-1}} \leq V_{\rm LSR} \leq -4.5\ \mathrm{km\,s^{-1}}$ and the second is an ellipse-shaped feature with $-8.2\ \mathrm{km\,s^{-1}} \leq V_{\rm LSR} \leq -6\ \mathrm{km\,s^{-1}}$. The linear feature is co-spatial with MM1F as identified by Brogan et al. (2016). This feature might either be associated with the YSO at MM1F or trace the interface between the dust envelope of MM1 and the cavity excavated by the wide-angle outflow reported by Qiu et al. (2011). The second feature is ellipse-shaped and co-spatial with the cavity traced by the millimetre dust continuum from Brogan et al. (2016). These masers in MM1-Met2 may be tracing material in the dust envelope entrained to co-rotate with the NW-SE or N-S protostellar jet. This is possibly the case, as Chibueze et al. (2021) detected northward water maser proper motions co-spatial with the ellipse in MM1-Met2. This hypothesis can be further tested with thermal line observations of the jet, which is outside the scope of this work.

Methanol Masers in MM2

MM2 is a small protostellar core in NGC6334I that is not associated with the accretion burst in MM1. The methanol maser associations in MM2 seem to show two "wings" with MM2-Met2 redshifted compared to MM2-Met1 (Figure 4.8 or 5.1). TRH18 detected MM1-Met1 but only a few masers in MM1-Met2. It is not clear whether MM2-Met1 and MM2-Met2 are associated with one another or not. MM2-Met1 is centred on a millimetre point source MM2B detected by Brogan et al. (2016), while MM2-Met2 is not associated with any dust continuum sources.

Methanol Masers in MM3-UCHII

The methanol masers in MM3-UCHII consist of five clusters (UCHII-Met1, ... , UCHII-Met5). These methanol masers all lie on the western edge of the UCHII region NGC6334F. The millimetre dust continuum (Figure 4.1, and thermal methanol line emission (from TRH18) show that the methanol masers are placed within a thin sheet of hot gas at the edge of the UCHII region. These methanol masers did not change during the accretion burst, as they are not associated with MM1 (TRH18). The 2019 results are consistent with the 2016 observations of TRH18, except that some of the fainter masers were not detected. In TRH18, all the maser associations except UCHII-Met3 and UCHII-Met4 are part of a 5000 AU filament along the edge of the centimetre continuum tracing the edge of the UCHII region. These long filaments have also been seen in W3(OH) (Harvey-Smith and Cohen, 2006).

These long filaments are likely not due to protostellar disks (their position-velocity diagrams fail the two-quadrant test of Norris et al., 1998), but rather seem to be methanol maser gas compressed and heated by the ionization front of the UCHII to such an extent to favour 6.7 GHz methanol maser pumping (TRH18). UCHII-Met4 shows a $-11.8\ \mathrm{km\,s^{-1}} \leq V_{\mathrm{LSR}} \leq -8.73\ \mathrm{km\,s^{-1}}$ bow shape that is about 1200 AU long. The central masers are concentrated within a bulge shown in the centimetre continuum (see panel c of Figure 4.8).

Chapter 6

Conclusion

This study embarked on a multi-scale study of the high-mass star-forming region NGC6334I. It was done with a combination of archival continuum images and new maser observations. This chapter concludes this thesis, then the main research questions are individually answered, highlighting the specific contribution of this thesis, followed by a concluding summary. Possible future avenues of inquiry are lastly outlined with the limitations of this work.

6.1 Replies to Scientific Aims

The primary aim of this thesis was to compare the pre-burst and burst 22 GHz water masers in NGC6334I. Water masers were detected in CM2-W1, CM2-W2, MM1-W1, UCHII-W1, UCHII-W2 and UCHII-W3. The masers in all the regions were variable throughout all epochs in peak intensity, position and radial velocity. The systematic variability in CM2-W2 and MM1-W1 show that the variability of water masers in these regions was dominated by effects due to the accretion burst rather than intrinsic hydrodynamic variability. On the other hand, the variability in UCHII-W1, UCHII-W2 and UCHII-W3 does not show a particular trend that indicates effects due to the accretion burst.

Proper motions were calculated in the pre-burst (2014.72 − 2015.28) and burst (2015.88 − 2016.19) epochs. Two methods of maser feature identification was used for the proper motion calculation, the spot method and the spectral method. The spot method identifies maser features as single non-accelerating maser spots while the spectral method uses groups of maser spots that have a Gaussian spectral profile. It was found that there was not a significant difference between these two methods for the observation reported in this thesis. The proper motion calculations in this thesis were compared to prior observations by Chibueze et al. (2021). It was found that the major differences can be attributed to a combination of instrumental differences and proper motion calculation methodology.

The proper motions showed a bipolar outflow morphology associated with outflows that have been identified in molecular line emission. The proper motions in CM2-W2 and UCHII-W3 were associated with the NW-SE jet originating in MM1. The proper motions in CM2 were fixed to the upper limit set by Brogan et al. (2018) to be around 26 $\mathrm{km\,s^{-1}}$. The mean speed calculated was 33 ± 15 $\mathrm{km\,s^{-1}}$. The proper motions in UCHII-W3 changed slightly from 147 $\mathrm{km\,s^{-1}}$ before the burst to 158 $\mathrm{km\,s^{-1}}$ after the burst. The burst proper motions implied a dynamic timescale of 99 ± 9 yr for the NW-SE jet. This was due to the non-detection of the pre-burst maser feature and the detection of a new maser feature in the last two epochs. The proper motions in UCHII-W1 and UCHII-W2 were associated with the N-S jet originating in MM1. The proper motions in UCHII-W2 were unchanged before and after the burst with mean speeds of 70 ± 10 $\mathrm{km\,s^{-1}}$ and 76 $\mathrm{km\,s^{-1}}$ respectively. The masers in UCHII-W1

showed significant variability. Four associations were detected in UCHII-W1 before the burst, with a mean speed of 68 ± 36 km s^{-1}. After the burst, three associations were detected with a mean speed of 92 ± 21 km s^{-1}. The burst proper motions implied a dynamic timescale of 230^{+50}_{-120} yr for the N-S jet, consistent with 170 ± 18 yr calculated with water maser bulk motion observations from previous authors (Brogan et al., 2018). The multiple outflows could be consistent either with jet precession or multiple outflows originating in MM1.

Outflow parameters such as outflow force $\dot{P}$, driving source luminosity $L_{\rm ds}$ and driving source mass $M_{\rm ds}$ were estimated for S255IR-NIRS3 and NGC6334I. For S255IR-NIRS3, $\dot{P} = 1.4^{+1.3}_{-0.3} \times 10^{-3} M_{\odot}$ yr^{-1} km s^{-1}, implying $L_{\rm ds} = 1.5^{+3.0}_{-0.5} \times 10^{3} L_{\odot}$ and $M_{\rm ds} = 29^{+58}_{-16} M_{\odot}$ from empirical scaling relationships. The mass estimate was consistent with the mass estimation by other methods. For NGC6334I it was estimated that $\dot{P} < 33.6 \times 10^{-3} M_{\odot}$yr^{-1} km s^{-1} implying $L_{\rm ds} < 10^{5.45} L_{\odot}$ and $M_{\rm ds} < 10^{6.5} M_{\odot}$. The driving source luminosity and mass estimates for NGC6334I were too high, and the high values were attributed to uncertainties in the scaling relationships.

The secondary aim of this thesis was to compare 2019.6 JVLA methanol maser observations with previous post-burst observations from Hunter et al. (2018). There were detections of 6.7 GHz methanol masers in MM1, MM2 and MM3-UCHII. It was found that there was likely an error in the flux density calibration of the methanol masers, causing a factor of 47 discrepancy with single-dish observations. The error was possibly introduced during either the flux scaling when correcting for the spectral index in the bandpass, or an error in the amplitude self-calibration. The relative flux densities of the 2019.6 JVLA observations were found to align well with single-dish observations, and the spatial distributions of the masers were similar to that found in previous observations of the same source with the same instrument.

Two associations were detected in MM1, MM1-Met1 and MM1-Met2. MM1-Met1 displayed a 1400 AU bow shape structure offset from the millimetre dust emission, but within thermal methanol emission reported by Hunter et al. (2018). MM1-Met2 consisted of a "V"-shape with two separate associations. The right side of the "V"-shape consisted of an ellipse-shaped group of maser spots which are co-spatial with the dust cavity traced in millimetre continuum. It may be hot entrained gas at the interface of the N-S (or NW-SE) jet and the MM1 clump as water maser proper motions reported by Chibueze et al. (2021) are also found there. MM2 consisted of two associations with a symmetric "wing" morphology, and five associations were detected in MM3-UCHII at the edge of the UCHII region NGC6334F.

In conclusion, the water maser observations indicate systematic variability due to the accretion burst in water masers at CM2-W2 and MM1-W1. The water masers in UCHII-W1, UCHII-W2 and UCHII-W3 are associated with young ($t_{\rm dyn} < 200$ yr) high-velocity ($v \sim 150$ km s^{-1}) outflows that originate in MM1. Methanol masers in the MM1-Met1 and MM1-Met2 are associated with outflow cavities, while methanol masers in MM3-UCHII were at the edges of an UCHII region. The masers in NGC6334I are as dynamic and complex as the star formation in the region.

6.2 Limitations and Future Work

The main limitations of this thesis is the incorrect flux calibration of the 2019.6 JVLA methanol masers. Although the results that were obtained gave reliable information on the existence, position and radial velocity of many maser spots, many faint masers were not detected and quantities like brightness temperature could not be calculated. The second limitation of this work is that the author of this

thesis lacked AIPS calibration and imaging skills. Some spurious detections (sidelobes) were identified in the VERA water maser maps. They are known by symmetric detections around a bright maser feature, and often lack a Gaussian spectral profile. The VERA water maser data could have been re-calibrated and imaged to remove these features, but that was not possible within the time frame of this thesis. The spectral method of proper motion calculation at least ensured that the proper motions were not calculated with these spurious detections.

This thesis did not study the region at scales larger than 10000 AU, so processes at larger scales were not taken into account. Studying the relationship between the larger scales in NGC6334 and the specific high-mass SFR NGC6334I would contribute to testing the model by Tigé et al. (2017). On a smaller scale, at the scale of this study, thermal line emission would have shed valuable light on some questions raised by this thesis, like the nature of the outflows. Observations with ALMA of this region exist, but were outside the scope of this thesis. Further maser observations can also be done, as the masers in the region are time variable on human timescales. Lastly, mathematical modelling of some the time dependence of water and methanol masers could be tested against the observations in this region, and may be a valuable avenue of inquiry for maser theory.

Appendix A

Tables, Figures and Code

A.1 JVLA Observations

Table A.1: Associations, positions and radial velocities of 6.7 GHz CH_3OH maser detections as detected by the 2019.6 JVLA observations of NGC6334I.

Number	Association	Velocity (kms^{-1})	Fitted Position (J2000) R.A.	Dec.
1	MM1-Met2	−4.16	17:20:53.4538	−35:46:56.578
2	MM1-Met2	−4.25	17:20:53.4540	−35:46:56.573
3	MM1-Met2	−4.34	17:20:53.4549	−35:46:56.555
4	MM1-Met1	−4.34	17:20:53.3561	−35:46:57.184
5	MM1-Met1	−4.43	17:20:53.3555	−35:46:57.178
6	MM1-Met2	−4.52	17:20:53.4575	−35:46:56.420
7	MM1-Met2	−4.60	17:20:53.4593	−35:46:56.380
8	MM1-Met2	−4.69	17:20:53.4593	−35:46:56.432
9	MM1-Met2	−4.78	17:20:53.4595	−35:46:56.491
10	MM1-Met2	−4.87	17:20:53.4594	−35:46:56.507
11	MM1-Met2	−4.95	17:20:53.4595	−35:46:56.514
12	MM1-Met2	−5.04	17:20:53.4595	−35:46:56.515
13	MM1-Met2	−5.13	17:20:53.4595	−35:46:56.516
14	MM1-Met2	−5.22	17:20:53.4595	−35:46:56.515
15	MM1-Met2	−5.31	17:20:53.4594	−35:46:56.513
16	MM1-Met2	−5.39	17:20:53.4592	−35:46:56.509
17	MM1-Met2	−5.48	17:20:53.4587	−35:46:56.508
18	MM1-Met2	−5.57	17:20:53.4568	−35:46:56.510
19	MM1-Met2	−5.66	17:20:53.4521	−35:46:56.572
20	MM1-Met2	−5.74	17:20:53.4456	−35:46:56.678
21	MM1-Met2	−5.83	17:20:53.4417	−35:46:56.754
22	MM1-Met2	−5.92	17:20:53.4361	−35:46:56.669
23	MM1-Met2	−6.01	17:20:53.4267	−35:46:56.599
24	MM1-Met2	−6.10	17:20:53.4242	−35:46:56.580
25	UHCII-Met1	−6.10	17:20:53.4471	−35:47:03.078
26	MM1-Met2	−6.18	17:20:53.4239	−35:46:56.575
27	UHCII-Met1	−6.18	17:20:53.4446	−35:47:03.068
28	MM1-Met2	−6.27	17:20:53.4247	−35:46:56.573

29	UHCII-Met1	−6.27	17:20:53.4515	−35:47:03.124
30	MM1-Met2	−6.36	17:20:53.4260	−35:46:56.575
31	UHCII-Met1	−6.36	17:20:53.4541	−35:47:03.153
32	MM1-Met2	−6.45	17:20:53.4282	−35:46:56.582
33	UHCII-Met1	−6.45	17:20:53.4554	−35:47:03.167
34	MM1-Met2	−6.53	17:20:53.4317	−35:46:56.596
35	UHCII-Met1	−6.53	17:20:53.4561	−35:47:03.172
36	MM1-Met2	−6.62	17:20:53.4366	−35:46:56.625
37	UHCII-Met1	−6.62	17:20:53.4549	−35:47:03.153
38	MM1-Met2	−6.71	17:20:53.4402	−35:46:56.645
39	UHCII-Met1	−6.71	17:20:53.4516	−35:47:03.108
40	MM1-Met2	−6.80	17:20:53.4407	−35:46:56.649
41	UHCII-Met1	−6.80	17:20:53.4484	−35:47:03.069
42	MM1-Met2	−6.89	17:20:53.4397	−35:46:56.646
43	UHCII-Met1	−6.89	17:20:53.4464	−35:47:03.048
44	MM1-Met2	−6.97	17:20:53.4386	−35:46:56.639
45	UHCII-Met1	−6.97	17:20:53.4451	−35:47:03.046
46	MM1-Met2	−7.06	17:20:53.4385	−35:46:56.637
47	UHCII-Met1	−7.06	17:20:53.4433	−35:47:03.037
48	MM1-Met2	−7.15	17:20:53.4392	−35:46:56.638
49	UHCII-Met1	−7.15	17:20:53.4414	−35:47:03.040
50	MM1-Met2	−7.24	17:20:53.4397	−35:46:56.638
51	UHCII-Met1	−7.24	17:20:53.4396	−35:47:03.032
52	MM1-Met2	−7.33	17:20:53.44	−35:46:56.638
53	UHCII-Met1	−7.33	17:20:53.4385	−35:47:03.014
54	MM1-Met2	−7.41	17:20:53.4402	−35:46:56.638
55	UHCII-Met1	−7.41	17:20:53.4372	−35:47:02.952
56	MM1-Met2	−7.50	17:20:53.4404	−35:46:56.640
57	MM1-Met2	−7.59	17:20:53.4406	−35:46:56.642
58	MM1-Met2	−7.68	17:20:53.4412	−35:46:56.647
59	MM1-Met2	−7.76	17:20:53.4422	−35:46:56.656
60	MM1-Met2	−7.85	17:20:53.4425	−35:46:56.658
61	UHCII-Met3	−7.85	17:20:53.4568	−35:47:01.164
62	UHCII-Met2	−7.85	17:20:53.4334	−35:47:02.257
63	MM1-Met2	−7.94	17:20:53.4420	−35:46:56.657
64	MM1-Met1	−7.94	17:20:53.3668	−35:46:57.408
65	MM2-Met2	−7.94	17:20:53.1615	−35:46:58.474
66	UHCII-Met3	−7.94	17:20:53.4560	−35:47:01.165
67	UHCII-Met2	−7.94	17:20:53.4341	−35:47:02.274
68	MM1-Met2	−8.03	17:20:53.4405	−35:46:56.668
69	MM1-Met1	−8.03	17:20:53.3650	−35:46:57.454
70	MM2-Met2	−8.03	17:20:53.1626	−35:46:58.510
71	UHCII-Met3	−8.03	17:20:53.4545	−35:47:01.154
72	UHCII-Met2	−8.03	17:20:53.4339	−35:47:02.272
73	MM1-Met2	−8.12	17:20:53.4382	−35:46:56.669
74	MM1-Met1	−8.12	17:20:53.3621	−35:46:57.419
75	MM2-Met2	−8.12	17:20:53.1713	−35:46:58.701
76	UHCII-Met3	−8.12	17:20:53.4527	−35:47:01.140
77	UHCII-Met2	−8.12	17:20:53.4337	−35:47:02.285

78	MM1-Met2	−8.20	17:20:53.4348	−35:46:56.670
79	MM1-Met1	−8.20	17:20:53.3588	−35:46:57.443
80	MM2-Met2	−8.20	17:20:53.1702	−35:46:58.615
81	UHCII-Met3	−8.20	17:20:53.4512	−35:47:01.119
82	UHCII-Met2	−8.20	17:20:53.4332	−35:47:02.294
83	MM1-Met1	−8.29	17:20:53.3532	−35:46:57.457
84	MM2-Met2	−8.29	17:20:53.1729	−35:46:58.468
85	UHCII-Met3	−8.29	17:20:53.4537	−35:47:01.140
86	UHCII-Met2	−8.29	17:20:53.4326	−35:47:02.249
87	MM1-Met1	−8.38	17:20:53.3466	−35:46:57.478
88	MM2-Met2	−8.38	17:20:53.1716	−35:46:58.304
89	UHCII-Met3	−8.38	17:20:53.4562	−35:47:01.170
90	MM1-Met1	−8.47	17:20:53.3440	−35:46:57.486
91	MM2-Met2	−8.47	17:20:53.1648	−35:46:58.515
92	UHCII-Met3	−8.47	17:20:53.4556	−35:47:01.170
93	MM1-Met1	−8.55	17:20:53.3428	−35:46:57.485
94	MM2-Met2	−8.55	17:20:53.1646	−35:46:58.555
95	UHCII-Met3	−8.55	17:20:53.4555	−35:47:01.170
96	MM1-Met1	−8.64	17:20:53.3422	−35:46:57.485
97	MM2-Met2	−8.64	17:20:53.1646	−35:46:58.620
98	UHCII-Met3	−8.64	17:20:53.4547	−35:47:01.163
99	UHCII-Met3	−8.73	17:20:53.4542	−35:47:01.138
100	UHCII-Met4	−8.73	17:20:53.4139	−35:47:01.305
101	MM1-Met1	−8.73	17:20:53.3420	−35:46:57.498
102	MM2-Met2	−8.73	17:20:53.1662	−35:46:58.660
103	MM1-Met1	−8.82	17:20:53.3413	−35:46:57.517
104	MM2-Met2	−8.82	17:20:53.1681	−35:46:58.698
105	UHCII-Met4	−8.82	17:20:53.4354	−35:47:01.070
106	UHCII-Met4	−8.82	17:20:53.4093	−35:47:01.490
107	MM1-Met1	−8.91	17:20:53.3411	−35:46:57.545
108	MM2-Met2	−8.91	17:20:53.1692	−35:46:58.711
109	UHCII-Met4	−8.91	17:20:53.4198	−35:47:01.083
110	MM1-Met1	−8.99	17:20:53.3411	−35:46:57.562
111	MM2-Met2	−8.99	17:20:53.1698	−35:46:58.719
112	UHCII-Met4	−8.99	17:20:53.4291	−35:47:01.141
113	MM1-Met1	−9.08	17:20:53.3414	−35:46:57.581
114	MM2-Met2	−9.08	17:20:53.1704	−35:46:58.714
115	UHCII-Met4	−9.08	17:20:53.4270	−35:47:01.042
116	UHCII-Met2	−9.08	17:20:53.4262	−35:47:02.518
117	MM1-Met1	−9.17	17:20:53.3425	−35:46:57.605
118	MM2-Met2	−9.17	17:20:53.1706	−35:46:58.689
119	UHCII-Met4	−9.17	17:20:53.4163	−35:47:00.984
120	UHCII-Met1	−9.17	17:20:53.4361	−35:47:02.812
121	MM1-Met1	−9.26	17:20:53.3429	−35:46:57.617
122	MM2-Met2	−9.26	17:20:53.1704	−35:46:58.640
123	UHCII-Met4	−9.26	17:20:53.4088	−35:47:01.037
124	UHCII-Met1	−9.26	17:20:53.4389	−35:47:02.843
125	MM1-Met1	−9.34	17:20:53.3437	−35:46:57.657
126	MM2-Met2	−9.34	17:20:53.1715	−35:46:58.633

127	UHCII-Met4	−9.34	17:20:53.4058	−35:47:01.023
128	UHCII-Met1	−9.34	17:20:53.4408	−35:47:02.875
129	MM1-Met1	−9.43	17:20:53.3489	−35:46:57.877
130	MM2-Met2	−9.43	17:20:53.1734	−35:46:58.639
131	UHCII-Met4	−9.43	17:20:53.4061	−35:47:01.029
132	MM1-Met1	−9.52	17:20:53.3546	−35:46:58.158
133	MM2-Met2	−9.52	17:20:53.1768	−35:46:58.635
134	UHCII-Met4	−9.52	17:20:53.4005	−35:47:01.040
135	MM2-Met2	−9.61	17:20:53.1834	−35:46:58.698
136	UHCII-Met4	−9.61	17:20:53.3980	−35:47:01.053
137	MM2-Met1	−9.78	17:20:53.1871	−35:46:58.795
138	UHCII-Met5	−9.78	17:20:53.4723	−35:47:00.263
139	UHCII-Met4	−9.78	17:20:53.3971	−35:47:01.057
140	MM2-Met1	−9.87	17:20:53.1864	−35:46:58.810
141	UHCII-Met4	−9.87	17:20:53.3964	−35:47:01.048
142	UHCII-Met5	−9.87	17:20:53.4731	−35:47:00.154
143	UHCII-Met5	−9.96	17:20:53.4740	−35:47:00.158
144	MM2-Met1	−9.96	17:20:53.1856	−35:46:58.816
145	UHCII-Met4	−9.96	17:20:53.3938	−35:47:01.079
146	UHCII-Met4	−10.05	17:20:53.3928	−35:47:01.120
147	MM2-Met1	−10.05	17:20:53.1851	−35:46:58.821
148	MM2-Met1	−10.13	17:20:53.1846	−35:46:58.814
149	UHCII-Met4	−10.13	17:20:53.3921	−35:47:01.129
150	MM2-Met1	−10.22	17:20:53.1853	−35:46:58.813
151	UHCII-Met4	−10.22	17:20:53.3919	−35:47:01.131
152	UHCII-Met4	−10.31	17:20:53.3918	−35:47:01.139
153	MM2-Met1	−10.31	17:20:53.1859	−35:46:58.8
154	MM2-Met1	−10.40	17:20:53.1877	−35:46:58.804
155	UHCII-Met4	−10.40	17:20:53.3915	−35:47:01.152
156	MM2-Met1	−10.49	17:20:53.1887	−35:46:58.810
157	UHCII-Met4	−10.49	17:20:53.3911	−35:47:01.170
158	MM2-Met1	−10.57	17:20:53.1908	−35:46:58.814
159	UHCII-Met4	−10.57	17:20:53.3908	−35:47:01.195
160	MM2-Met1	−10.66	17:20:53.1936	−35:46:58.816
161	UHCII-Met4	−10.66	17:20:53.39	−35:47:01.260
162	MM2-Met1	−10.75	17:20:53.1966	−35:46:58.821
163	UHCII-Met4	−10.75	17:20:53.3874	−35:47:01.360
164	MM2-Met1	−10.84	17:20:53.1979	−35:46:58.821
165	UHCII-Met4	−10.84	17:20:53.3834	−35:47:01.4
166	MM2-Met1	−10.92	17:20:53.1985	−35:46:58.821
167	UHCII-Met4	−10.92	17:20:53.3807	−35:47:01.388
168	MM2-Met1	−11.01	17:20:53.1987	−35:46:58.822
169	UHCII-Met4	−11.01	17:20:53.3790	−35:47:01.390
170	MM2-Met1	−11.10	17:20:53.1989	−35:46:58.822
171	UHCII-Met4	−11.10	17:20:53.3783	−35:47:01.4
172	MM2-Met1	−11.19	17:20:53.1992	−35:46:58.824
173	UHCII-Met4	−11.19	17:20:53.3782	−35:47:01.406
174	MM2-Met1	−11.28	17:20:53.1992	−35:46:58.824
175	UHCII-Met4	−11.28	17:20:53.3784	−35:47:01.406

176	MM2-Met1	−11.36	17:20:53.1990	−35:46:58.830
177	UHCII-Met4	−11.36	17:20:53.3788	−35:47:01.4
178	MM2-Met1	−11.45	17:20:53.1979	−35:46:58.837
179	UHCII-Met4	−11.45	17:20:53.38	−35:47:01.362
180	MM2-Met1	−11.54	17:20:53.1967	−35:46:58.843
181	UHCII-Met4	−11.54	17:20:53.3845	−35:47:01.266
182	MM2-Met1	−11.63	17:20:53.1957	−35:46:58.853
183	UHCII-Met4	−11.63	17:20:53.3910	−35:47:01.096
184	MM2-Met1	−11.72	17:20:53.1935	−35:46:58.858
185	UHCII-Met4	−11.72	17:20:53.3918	−35:47:01.048
186	UHCII-Met4	−11.80	17:20:53.3916	−35:47:01.047
187	MM2-Met1	−11.89	17:20:53.1764	−35:46:58.907
188	MM2-Met1	−11.98	17:20:53.1734	−35:46:58.909
189	MM2-Met1	−12.07	17:20:53.1771	−35:46:58.898

A.2 VERA Proper Motions

A.2.1 Pre-Burst Proper Motions

Table A.2: Associations, positions, proper motions and radial velocities of the pre-burst proper motions (epochs of 2014.72 − 2015.28) as calculated by the spot method. The detection string in the last column show for which epochs maser spots were detected.

ID	Region	Offset		Proper Motion				Radial Motion	Detections
		α	δ	μ_x	$\sigma\mu_x$	μ_y	$\sigma\mu_y$	$V_{\rm LSR}$	
		($''$)		(mas yr^{-1})				(kms^{-1})	
1	CM2-W2	−0.6404	5.3458	−1.39	0.47	6.48	1.05	−16.0	0011
2	CM2-W2	−0.6745	5.3126	0.41	0.32	5.75	0.40	−3.8	0011
3	CM2-W2	−0.6741	5.3114	−1.02	0.50	12.17	2.27	−4.6	0011
4	CM2-W2	−0.6741	5.3112	−0.86	0.45	12.80	2.03	−5.5	0011
5	CM2-W2	−0.6897	5.2900	0.08	0.62	2.35	0.98	−8.4	0011
6	CM2-W2	−0.6875	5.2893	0.44	1.21	−3.06	6.41	−10.9	0011
7	CM2-W2	−0.6876	5.2892	−2.01	0.32	3.84	0.40	−11.4	1111
8	CM2-W2	−0.6877	5.2892	0.14	0.31	1.81	0.39	−12.2	1111
9	CM2-W2	−0.6876	5.2892	−0.04	0.31	1.38	0.39	−11.8	1111
10	CM2-W2	−0.6881	5.2891	1.70	0.87	5.73	1.49	−13.9	0111
11	CM2-W2	−0.6881	5.2891	1.72	0.86	5.48	1.43	−13.5	0111
12	CM2-W2	−0.6878	5.2891	1.19	0.31	5.12	0.39	−12.6	1111
13	CM2-W2	−0.6879	5.2881	1.24	0.93	6.17	2.80	−13.1	0111
14	CM2-W2	−0.6892	5.2880	−0.98	0.31	2.87	0.39	−6.7	1111
15	CM2-W2	−0.6892	5.2880	−0.59	0.31	2.67	0.39	−9.3	1111
16	CM2-W2	−0.6892	5.2880	−1.40	0.31	2.49	0.39	−4.6	0111
17	CM2-W2	−0.6892	5.2880	−0.62	0.31	2.54	0.39	−8.8	0111
18	CM2-W2	−0.6892	5.2880	−0.86	0.31	3.15	0.39	−7.2	1111
19	CM2-W2	−0.6892	5.2880	−0.83	0.31	3.27	0.39	−7.6	1111
20	CM2-W2	−0.6891	5.2880	−0.02	0.32	3.50	0.40	−10.1	0011
21	CM2-W2	−0.6892	5.2880	−0.80	0.31	3.15	0.39	−8.0	1111
22	CM2-W2	−0.6892	5.2880	−0.71	0.31	2.95	0.39	−8.4	1111

23	CM2-W2	−0.6892	5.2879	−1.06	0.31	2.66	0.39	−6.3	1111
24	CM2-W2	−0.6892	5.2879	−1.11	0.31	2.60	0.39	−5.9	1111
25	CM2-W2	−0.6892	5.2879	−1.72	0.32	1.60	0.40	−5.0	0011
26	CM2-W2	−0.6892	5.2879	−1.68	0.32	2.60	0.40	−4.2	0011
27	CM2-W2	−0.6892	5.2879	−0.44	0.32	3.58	0.40	−5.1	1100
28	CM2-W2	−0.6892	5.2879	−1.15	0.31	2.67	0.39	−5.5	1111
29	CM2-W2	−0.6634	5.2866	−3.63	0.32	1.15	0.40	−18.9	0011
30	CM2-W2	−0.6633	5.2866	−3.51	0.32	2.05	0.40	−19.8	0011
31	CM2-W2	−0.6634	5.2866	−3.59	0.32	1.25	0.40	−19.4	0011
32	CM2-W2	−0.6633	5.2866	−2.82	0.32	4.10	0.40	−20.2	0011
33	CM2-W2	−0.6632	5.2865	−1.19	0.32	8.75	0.40	−21.1	0011
34	CM2-W2	−0.6633	5.2865	−2.33	0.78	5.80	1.95	−20.6	0011
35	CM2-W2	−0.6890	5.2859	−1.01	0.31	3.01	0.39	−7.2	0111
36	CM2-W2	−0.6888	5.2858	−0.72	0.34	3.66	0.85	−6.7	0110
37	CM2-W2	−0.6981	5.2764	0.51	0.76	3.44	2.25	−8.0	1100
38	CM2-W2	−0.6982	5.2761	0.36	0.32	7.28	0.40	−8.4	1100
39	CM2-W2	−0.6925	5.2706	2.96	0.43	6.15	0.94	−8.0	0011
40	CM2-W2	−0.6944	5.2156	0.45	0.59	1.78	0.53	−8.0	0110
41	CM2-W2	−0.6945	5.2155	0.69	0.61	2.08	0.54	−7.6	0110
42	CM2-W1	−0.3558	5.1675	2.57	0.31	3.66	0.39	−9.3	1110
43	CM2-W1	−0.3549	5.1674	2.39	0.32	1.45	0.40	−8.8	0110
44	CM2-W1	−0.3557	5.1672	2.70	0.31	2.90	0.39	−8.4	1110
45	CM2-W1	−0.3557	5.1671	3.01	0.32	4.61	0.40	−8.0	1100
46	CM2-W1	−0.3545	5.1655	0.01	0.32	16.65	0.40	−8.8	0110
47	CM2-W1	−0.3553	5.1654	0.90	0.31	16.87	0.40	−8.4	1110
48	CM2-W1	−0.0742	4.5558	3.06	0.32	3.96	0.40	−10.1	1100
49	CM2-W1	−0.0742	4.5558	3.14	0.32	3.79	0.40	−10.5	1100
50	CM2-W1	−0.0743	4.5558	3.23	0.32	3.58	0.40	−11.0	1100
51	CM2-W1	−0.0742	4.5556	3.41	0.32	3.09	0.40	−9.7	1100
52	MM1-W1	−0.2802	2.8961	0.32	0.32	−1.71	0.40	0.4	1100
53	MM1-W1	−0.2803	2.8960	0.27	0.32	−1.00	0.40	0.8	1100
54	MM1-W1	−0.2789	2.8872	0.40	0.32	−1.00	0.40	1.3	0110
55	MM1-W1	−0.2787	2.8866	1.04	0.89	−4.57	3.98	0.4	0110
56	MM1-W1	−0.2782	2.8799	0.18	0.43	0.55	1.63	−1.7	1111
57	MM1-W1	−0.2782	2.8798	0.56	0.31	−2.56	0.39	−2.1	1111
58	MM1-W1	−0.2782	2.8795	0.35	0.37	−1.04	1.62	−2.5	1111
59	MM1-W1	−0.2779	2.8788	−1.00	0.31	7.46	0.39	−1.3	1111
60	MM1-W1	−0.2779	2.8782	−0.04	0.36	1.24	1.48	−3.4	1111
61	MM1-W1	−0.2779	2.8780	0.80	0.32	0.96	0.40	−4.2	1100
62	MM1-W1	−0.2776	2.8780	−0.08	0.38	1.04	1.78	−2.9	0111
63	MM1-W1	−0.2775	2.8773	−1.07	0.31	7.69	0.39	−0.8	1111
64	MM1-W1	−0.2777	2.8771	−0.16	0.37	2.55	1.57	−3.8	1111
65	MM1-W1	−0.2773	2.8765	−1.29	0.31	8.85	0.39	−0.4	1111
66	UCHII-W3	0.0938	1.2989	8.27	5.22	−32.83	8.35	−31.2	0011
67	UCHII-W3	0.0938	1.2989	7.92	5.26	−29.25	8.83	−32.0	0011
68	UCHII-W3	0.0938	1.2989	7.84	5.27	−28.82	8.90	−31.6	0011
69	UCHII-W3	0.0954	1.2971	1.69	0.39	−20.25	3.07	−32.4	0011
70	UCHII-W2	0.2001	0.4560	−2.34	0.32	−7.70	0.40	−29.9	0110
71	UCHII-W2	0.2044	0.4525	−0.40	0.39	−11.10	0.79	−29.1	1110

72	UCHII-W2	0.2044	0.4524	−0.68	0.31	−9.71	0.61	−29.5	1110
73	UCHII-W2	0.2039	0.4521	0.11	0.31	−6.55	0.99	−31.6	1110
74	UCHII-W2	0.2040	0.4520	−0.16	0.43	−7.10	0.53	−31.2	1110
75	UCHII-W2	0.2036	0.4516	1.38	0.73	−8.22	1.69	−32.0	1100
76	UCHII-W2	0.2042	0.4515	−0.41	0.45	−7.52	0.57	−30.3	1110
77	UCHII-W2	0.2042	0.4512	−0.18	0.91	−4.27	2.21	−30.8	1100
78	UCHII-W2	0.2045	0.4498	−1.05	0.32	−7.26	0.40	−27.8	0110
79	UCHII-W2	0.2046	0.4496	−1.67	0.34	−6.31	1.50	−28.2	0110
80	UCHII-W1	−0.0171	0.0302	2.42	0.43	−13.40	1.55	−24.0	1110
81	UCHII-W1	−0.0169	0.0293	2.71	0.33	−13.10	0.66	−23.6	1110
82	UCHII-W1	−0.0168	0.0292	2.19	0.33	−13.10	0.64	−23.2	1110
83	UCHII-W1	−0.0167	0.0291	2.35	1.78	−12.00	2.50	−22.8	1100
84	UCHII-W1	−0.0162	0.0287	0.65	0.31	−10.04	0.39	−22.3	1110
85	UCHII-W1	−0.0094	0.0088	2.46	0.69	−13.50	2.17	−18.1	0110
86	UCHII-W1	−0.0092	0.0086	1.55	0.81	−11.70	2.75	−17.7	0110
87	UCHII-W1	−0.0080	0.0056	1.55	0.32	−13.86	0.40	−20.6	0110
88	UCHII-W1	−0.0080	0.0055	1.64	0.32	−13.47	0.40	−21.1	0110
89	UCHII-W1	−0.0055	0.0031	0.58	0.32	−10.59	0.40	−19.8	0110
90	UCHII-W1	−0.0048	0.0024	0.12	1.91	−6.44	4.23	−18.1	0110
91	UCHII-W1	−0.0047	0.0024	0.97	2.03	−9.06	4.41	−17.7	0110
92	UCHII-W1	−0.0046	0.0023	0.73	2.02	−8.73	4.35	−17.3	0110
93	UCHII-W1	−0.0045	0.0023	0.45	2.06	−8.56	4.33	−16.4	0110
94	UCHII-W1	−0.0771	−0.0673	1.87	0.31	−1.40	0.39	−15.2	1111
95	UCHII-W1	−0.0773	−0.0676	2.89	0.32	−7.53	0.81	−13.9	1111
96	UCHII-W1	−0.0778	−0.0678	3.08	0.31	−10.76	0.39	−14.3	1111
97	UCHII-W1	−0.0765	−0.0680	1.53	0.31	−6.28	0.67	−13.5	1111
98	UCHII-W1	−0.0770	−0.0682	0.51	0.88	−0.29	0.71	−14.7	0110
99	UCHII-W1	−0.0760	−0.0691	0.33	0.36	−5.18	1.47	−13.1	1111
100	UCHII-W1	−0.0760	−0.0701	4.84	1.86	−15.08	4.05	−10.9	0011
101	UCHII-W1	−0.0757	−0.0702	−0.69	0.89	1.09	1.95	−12.2	1111
102	UCHII-W1	−0.0759	−0.0703	1.01	0.48	−4.95	1.38	−12.6	1111
103	UCHII-W1	−0.0757	−0.0704	−0.33	0.33	−2.77	0.42	−9.7	1111
104	UCHII-W1	−0.0755	−0.0704	−0.36	0.40	−3.04	0.88	−9.3	1111
105	UCHII-W1	−0.0755	−0.0706	−0.59	0.53	−0.76	0.92	−10.1	1111
106	UCHII-W1	−0.0755	−0.0709	−1.52	0.84	0.98	0.95	−10.5	1111
107	UCHII-W1	−0.0758	−0.0710	2.16	1.76	1.11	1.29	−11.0	1100
108	UCHII-W1	−0.0753	−0.0712	−1.05	0.76	1.98	1.31	−11.4	1111
109	UCHII-W1	−0.0754	−0.0715	−0.27	0.61	−0.04	1.28	−11.8	1111
110	UCHII-W1	−0.0748	−0.0717	−0.64	0.54	−3.14	2.22	−8.8	0111
111	UCHII-W1	0.1705	−0.1330	4.34	0.32	−13.20	0.40	−33.7	1100
112	UCHII-W1	0.1705	−0.1330	4.47	0.32	−13.42	0.40	−33.3	1100
113	UCHII-W1	0.1704	−0.1331	4.47	0.32	−13.64	0.40	−34.1	1100
114	UCHII-W1	0.1016	−0.1787	0.32	0.31	−14.51	0.39	−20.2	1110
115	UCHII-W1	0.1072	−0.1788	4.09	0.32	−10.43	0.40	−4.2	1111
116	UCHII-W1	0.1072	−0.1789	3.90	0.32	−8.11	0.40	−3.8	1111
117	UCHII-W1	0.1013	−0.1790	1.31	0.73	−12.43	0.84	−21.9	1111
118	UCHII-W1	0.1014	−0.1791	0.94	0.36	−9.67	0.74	−22.3	1111
119	UCHII-W1	0.1010	−0.1791	1.51	0.75	−11.97	0.96	−21.5	1111
120	UCHII-W1	0.1004	−0.1794	1.95	0.32	−8.03	0.40	−22.8	1100

121	UCHII-W1	0.1084	−0.1811	1.01	1.99	−4.91	4.48	−4.6	0110
122	UCHII-W1	0.1000	−0.1822	5.87	0.31	−13.20	0.39	−20.6	0111
123	UCHII-W1	0.1087	−0.1822	6.84	1.82	−21.56	4.49	−3.4	0011

A.2.2 Post-Burst Proper Motions

Table A.3: Associations, positions, proper motions and radial velocities of the burst proper motions (epochs of 2015.88 − 2016.19) as calculated by the spot method. The detection string in the last column show for which epochs maser spots were detected.

ID	Region	Offset		Proper Motion				Radial Motion	Detections
		α	δ	μ_x	$\sigma\mu_x$	μ_y	$\sigma\mu_y$	$V_{\rm LSR}$	
		($''$)		(mas yr^{-1})				(kms^{-1})	
1	CM2-W2	−0.6008	5.4116	0.23	0.34	5.69	0.43	−40.0	011
2	CM2-W2	−0.6008	5.4116	0.13	0.34	6.40	0.43	−40.4	011
3	CM2-W2	−0.6008	5.4116	0.42	0.34	5.81	0.43	−39.6	011
4	CM2-W2	−0.6278	5.3786	−0.04	0.73	2.42	0.95	−2.5	011
5	CM2-W2	−0.6282	5.3777	0.81	0.34	7.23	1.06	−5.5	110
6	CM2-W2	−0.6282	5.3776	−0.14	0.56	7.68	1.83	−5.9	110
7	CM2-W2	−0.6281	5.3773	2.32	0.31	10.74	0.39	−2.1	111
8	CM2-W2	−0.6428	5.3649	−1.53	0.31	5.98	0.40	−15.6	111
9	CM2-W2	−0.6428	5.3648	−1.80	0.31	6.01	0.40	−15.2	110
10	CM2-W2	−0.6337	5.3632	−2.64	1.45	4.34	1.36	−10.9	011
11	CM2-W2	−0.6337	5.3631	−3.16	0.96	6.28	4.27	−10.5	011
12	CM2-W2	−0.6344	5.3597	−1.43	0.94	−0.22	2.37	−10.9	011
13	CM2-W2	−0.6344	5.3596	−1.44	1.04	−1.02	1.43	−10.1	011
14	CM2-W2	−0.6344	5.3596	−1.42	0.75	−1.10	2.89	−10.5	011
15	CM2-W2	−0.6606	5.3537	−0.16	0.33	2.81	0.46	−5.9	011
16	CM2-W2	−0.6606	5.3535	−1.44	1.05	6.63	1.18	−4.2	011
17	CM2-W2	−0.6604	5.3533	−2.33	0.94	6.51	0.67	−5.5	011
18	CM2-W2	−0.6671	5.3469	−0.73	0.32	4.98	0.41	−3.4	011
19	CM2-W2	−0.6680	5.3455	−3.21	0.31	7.41	0.40	−5.5	110
20	CM2-W2	−0.6482	5.3364	1.13	0.96	14.34	1.44	−17.7	011
21	CM2-W2	−0.6625	5.3192	−1.25	0.55	8.34	2.08	−23.6	011
22	CM2-W2	−0.6626	5.3190	−2.07	0.91	8.72	3.42	−24.8	011
23	CM2-W2	−0.6626	5.3190	−1.30	0.42	5.42	1.76	−24.4	011
24	CM2-W2	−0.6619	5.3177	−1.11	0.32	7.51	0.42	−21.9	011
25	CM2-W2	−0.6620	5.3177	−0.20	0.75	5.63	0.57	−22.3	011
26	CM2-W2	−0.6616	5.3153	−0.06	0.57	6.69	1.36	−23.2	011
27	CM2-W2	−0.6619	5.3152	4.51	2.63	−0.82	2.49	−24.8	011
28	CM2-W2	−0.6616	5.3151	1.85	2.05	−1.02	4.34	−25.3	011
29	CM2-W2	−0.6477	5.3096	−0.73	0.33	6.93	0.40	−21.9	011
30	CM2-W2	−0.6860	5.3050	−1.90	2.44	2.28	10.87	−10.1	011
31	CM2-W2	−0.6858	5.3044	−0.48	0.31	0.83	0.40	−11.4	111
32	CM2-W2	−0.6859	5.3044	−1.43	0.45	5.50	1.52	−10.5	111
34	CM2-W2	−0.6859	5.3040	−1.55	0.32	2.86	0.40	−9.3	110
35	CM2-W2	−0.6857	5.3040	−1.40	0.34	5.69	0.43	−11.8	011
36	CM2-W2	−0.6904	5.2965	−0.48	0.31	1.65	0.40	−5.5	111

37	CM2-W2	−0.6903	5.2965	−0.82	0.34	1.45	0.43	−5.9	011
38	CM2-W2	−0.6898	5.2901	−1.49	0.34	0.27	0.43	−7.6	011
39	CM2-W2	−0.6898	5.2901	−2.40	0.78	3.98	1.92	−8.0	011
40	CM2-W2	−0.6894	5.2883	−0.84	0.32	1.50	0.40	−6.7	110
42	CM2-W2	−0.6893	5.2881	−0.85	0.31	2.51	0.40	−7.6	111
43	CM2-W2	−0.6891	5.2880	−1.49	0.34	3.22	0.43	−8.4	011
44	CM2-W2	−0.6893	5.2880	−0.92	0.31	2.80	0.40	−8.0	111
45	CM2-W2	−0.6891	5.2878	−1.06	0.31	2.83	0.40	−8.8	111
46	CM2-W2	−0.6890	5.2877	−0.82	0.34	3.92	0.43	−9.3	011
47	CM2-W2	−0.7405	5.2323	0.27	1.42	1.39	0.75	−7.1	011
48	CM2-W2	−0.7404	5.2323	1.28	1.45	−0.67	1.24	−6.7	011
49	CM2-W2	−0.7404	5.2322	−0.78	1.42	2.63	1.31	−7.6	011
50	CM2-W2	−0.7412	5.2288	0.70	1.39	0.33	1.11	−7.6	011
51	CM2-W2	−0.7411	5.2286	−0.20	1.77	3.22	0.64	−8.0	011
52	CM2-W2	−0.7366	5.2085	−0.06	1.19	−3.32	0.62	−7.1	011
53	CM2-W2	−0.7366	5.2084	0.04	0.34	0.04	0.43	−6.7	011
54	CM2-W2	−0.7367	5.2084	−0.38	0.31	2.26	0.40	−6.3	111
55	CM2-W2	−0.7367	5.2082	−0.49	0.32	2.60	0.40	−5.9	111
56	MM1-W1	−0.2739	2.8933	0.75	0.32	−1.92	1.04	−2.1	111
57	MM1-W1	−0.2738	2.8933	1.11	0.76	−5.43	2.78	−1.7	110
58	MM1-W1	−0.2739	2.8932	0.67	0.31	−1.27	0.40	−2.5	111
59	MM1-W1	−0.2731	2.8909	1.09	3.18	−5.08	17.92	−2.9	011
60	MM1-W1	−0.2731	2.8896	−0.67	0.59	5.89	2.78	−3.4	111
61	MM1-W1	−0.2731	2.8895	0.39	0.31	−0.10	0.40	−3.8	111
62	MM1-W1	−0.2730	2.8893	0.02	0.47	−0.41	0.48	−4.2	110
63	UCHII-W3	0.1380	1.2714	3.76	0.34	−23.63	0.43	−37.1	011
64	UCHII-W3	0.1377	1.2713	5.19	0.34	−23.16	0.43	−36.2	011
65	UCHII-W3	0.1379	1.2713	4.43	0.34	−23.27	0.43	−36.6	011
66	UCHII-W3	0.1788	1.2690	4.62	0.34	−23.98	0.43	−48.4	011
67	UCHII-W3	0.1788	1.2690	4.52	0.34	−23.39	0.43	−48.9	011
68	UCHII-W3	0.1788	1.2690	4.24	0.34	−22.57	0.43	−49.3	011
69	UCHII-W3	0.1788	1.2689	4.43	0.34	−24.10	0.43	−48.0	011
70	UCHII-W2	0.2079	0.4553	−1.30	0.34	−13.03	0.43	−26.9	011
71	UCHII-W2	0.2079	0.4552	−1.30	0.34	−12.80	0.43	−27.4	011
72	UCHII-W2	0.2080	0.4552	−1.21	0.34	−12.32	0.43	−26.5	011
73	UCHII-W2	0.2077	0.4552	−0.92	0.34	−11.26	0.43	−29.5	011
74	UCHII-W2	0.2078	0.4552	−0.54	0.34	−10.91	0.43	−29.1	011
75	UCHII-W2	0.2080	0.4552	−1.11	0.34	−11.15	0.43	−26.1	011
76	UCHII-W2	0.2080	0.4552	−1.21	0.34	−8.56	0.43	−25.7	011
77	UCHII-W2	0.2077	0.4551	−1.11	0.34	−10.32	0.43	−29.9	011
78	UCHII-W2	0.2078	0.4551	−0.06	0.34	−9.50	0.43	−28.6	011
79	UCHII-W2	0.2078	0.4551	−0.25	0.34	−9.50	0.43	−28.2	011
80	UCHII-W2	0.2079	0.4551	−0.82	0.34	−11.03	0.43	−27.8	011
81	UCHII-W2	0.2077	0.4551	−0.92	0.34	−9.15	0.43	−30.3	011
82	UCHII-W2	0.2077	0.4550	−0.44	0.34	−7.50	0.43	−30.7	011
83	UCHII-W1	−0.0016	0.0004	4.23	1.81	−17.87	0.47	−20.6	111
84	UCHII-W1	−0.0016	0.0003	2.62	0.34	−17.77	0.41	−21.9	111
85	UCHII-W1	−0.0016	0.0003	3.19	0.34	−17.07	0.40	−21.5	111
86	UCHII-W1	−0.0010	0.0002	5.85	3.53	−15.15	2.12	−20.2	110

87	UCHII-W1	−0.0000	0.0001	3.77	0.32	−16.88	0.40	−19.8	110
88	UCHII-W1	0.0010	−0.0037	4.09	0.45	−23.10	4.30	−21.0	011
89	UCHII-W1	−0.0718	−0.0602	−0.50	0.32	−2.57	1.62	−15.2	110
90	UCHII-W1	−0.0720	−0.0603	−0.07	0.38	−3.87	0.70	−14.7	111
91	UCHII-W1	−0.0724	−0.0604	1.28	0.32	−4.60	0.40	−10.5	111
92	UCHII-W1	−0.0722	−0.0605	1.29	0.91	−3.25	1.20	−10.1	111
93	UCHII-W1	−0.0718	−0.0606	−0.08	0.31	−1.62	0.40	−15.6	111
94	UCHII-W1	−0.0719	−0.0608	−1.98	0.34	−3.53	0.43	−9.7	111
95	UCHII-W1	−0.0718	−0.0609	1.12	0.31	−6.10	0.40	−9.3	111
96	UCHII-W1	−0.0717	−0.0616	−0.16	1.13	−4.97	0.51	−14.3	011
97	UCHII-W1	−0.0718	−0.0617	0.18	0.37	−5.38	4.52	−13.9	011
98	UCHII-W1	−0.0719	−0.0619	0.75	0.41	−4.26	6.34	−13.5	011
99	UCHII-W1	0.1643	−0.1522	2.70	0.31	−14.08	0.40	−16.4	111
100	UCHII-W1	0.1644	−0.1523	2.68	0.31	−14.07	0.40	−16.0	111
101	UCHII-W1	0.1654	−0.1557	1.75	0.34	−17.51	0.43	−16.8	011
102	UCHII-W1	0.1655	−0.1562	1.95	0.34	−13.03	0.43	−15.6	011

A.3 VERA Microstructure Details

Table A.4: Parameters of maser features as identified by the spectral method, for each epoch. This table contains the maser feature offset positions as calculated by the intensity weighted centroid, as well as the Gaussian fit parameters for the feature: peak intensity, centre velocity and FWHM. Uncertainties are shown in parentheses.

ID	Offset		Gaussian Parameters		
	α	δ	Peak	V_{LSR}	FWHM
	($''$)		(Jy beam^{-1})	(km s^{-1})	(km s^{-1})
		Epoch 1			
1	0.41127 (0.00003)	−2.40973 (0.00008)	111.1 (1.02)	−2.82 (0.003)	1.3 (0.01)
2	0.61498 (0.00006)	−0.73223 (0.00014)	22.3 (0.34)	−10.39 (0.007)	1.0 (0.02)
3	0.33347 (0.00005)	−0.12076 (0.00012)	54.3 (0.61)	−8.50 (0.010)	1.3 (0.02)
4	−0.00899 (0.00029)	−0.01210 (0.00075)	10.7 (0.86)	−8.04 (0.044)	1.0 (0.14)
5	0.00157 (0.00009)	0.00120 (0.00024)	4.5 (0.11)	−11.80 (0.020)	1.3 (0.05)
6	0.00000 (0.00002)	−0.00003 (0.00005)	110.8 (0.54)	−7.30 (0.004)	1.9 (0.01)
7	0.01860 (0.00015)	0.00321 (0.00040)	6.0 (0.27)	−10.30 (0.016)	1.0 (0.04)
8	0.00882 (0.00024)	0.01142 (0.00063)	10.6 (0.88)	−7.09 (0.062)	1.4 (0.31)
9	−0.00899 (0.00029)	−0.01210 (0.00074)	10.7 (0.86)	−8.04 (0.044)	1.0 (0.14)
10	0.89347 (0.00003)	−4.83565 (0.00007)	30.8 (0.24)	−30.55 (0.004)	1.4 (0.01)
11	0.89304 (0.00008)	−4.83641 (0.00020)	8.5 (0.15)	−31.44 (0.019)	1.8 (0.05)
12	0.67231 (0.00002)	−5.25873 (0.00006)	85.5 (0.54)	−23.81 (0.003)	1.5 (0.01)
13	0.61214 (0.00003)	−5.35531 (0.00007)	19.0 (0.15)	−15.32 (0.005)	1.8 (0.01)
14	0.61430 (0.00003)	−5.35868 (0.00007)	26.3 (0.19)	−10.08 (0.008)	2.5 (0.02)
15	0.61302 (0.00010)	−5.35872 (0.00025)	10.5 (0.32)	−10.32 (0.015)	1.2 (0.04)
16	0.85962 (0.00003)	−5.42107 (0.00008)	12.6 (0.11)	−34.41 (0.007)	1.9 (0.01)
17	0.79087 (0.00004)	−5.46673 (0.00010)	22.4 (0.23)	−21.21 (0.005)	1.4 (0.01)
18	0.79514 (0.00005)	−5.46715 (0.00013)	14.6 (0.20)	−6.63 (0.015)	2.0 (0.04)
19	0.68367 (0.00003)	−5.28234 (0.00007)	23.1 (0.17)	−17.66 (0.005)	1.7 (0.01)

		Epoch 2			
1	0.41044 (0.00011)	−2.40115 (0.00028)	3.8 (0.13)	0.92 (0.012)	0.9 (0.04)
2	0.41154 (0.00006)	−2.40950 (0.00015)	54.5 (0.91)	−2.80 (0.006)	1.3 (0.01)
3	0.41231 (0.00007)	−2.41239 (0.00019)	16.8 (0.33)	−0.88 (0.010)	1.1 (0.02)
4	0.41902 (0.00010)	−2.41650 (0.00027)	1.5 (0.05)	6.01 (0.037)	1.9 (0.16)
5	0.89381 (0.00011)	−4.83824 (0.00028)	19.6 (0.70)	−30.48 (0.016)	1.3 (0.05)
6	0.89340 (0.00015)	−4.83799 (0.00038)	10.1 (0.43)	−30.54 (0.015)	1.7 (0.03)
7	0.67330 (0.00013)	−5.26209 (0.00033)	1.8 (0.07)	−23.45 (0.045)	2.0 (0.19)
8	0.68454 (0.00007)	−5.28567 (0.00016)	49.1 (0.94)	−17.55 (0.010)	1.7 (0.02)
9	0.68117 (0.00017)	−5.28240 (0.00042)	2.6 (0.13)	−21.13 (0.029)	1.1 (0.10)
10	0.68007 (0.00025)	−5.27937 (0.00062)	14.7 (1.08)	−17.57 (0.070)	1.7 (0.16)
11	0.61247 (0.00008)	−5.35608 (0.00020)	6.3 (0.14)	−15.09 (0.029)	2.2 (0.08)
12	0.61441 (0.00007)	−5.35905 (0.00017)	13.4 (0.26)	−10.46 (0.024)	3.1 (0.05)
13	0.61399 (0.00017)	−5.35992 (0.00044)	5.5 (0.28)	−10.57 (0.059)	3.2 (0.15)
14	0.61588 (0.00009)	−0.73215 (0.00024)	10.7 (0.29)	−10.38 (0.011)	1.0 (0.03)
15	0.33433 (0.00007)	−0.12060 (0.00017)	30.1 (0.63)	−8.60 (0.012)	1.3 (0.03)
16	0.00117 (0.00006)	0.00116 (0.00016)	8.8 (0.14)	−12.59 (0.010)	1.6 (0.02)
17	0.00384 (0.00014)	0.00331 (0.00036)	4.7 (0.17)	−11.60 (0.020)	1.1 (0.06)
18	0.00002 (0.00003)	−0.00004 (0.00008)	46.2 (0.37)	−7.14 (0.009)	2.6 (0.01)
19	0.00527 (0.00013)	0.07229 (0.00034)	18.2 (0.80)	−6.22 (0.037)	1.7 (0.14)
20	0.05327 (0.00040)	0.06735 (0.00101)	5.4 (0.68)	−6.35 (0.147)	1.7 (0.43)
21	0.05338 (0.00032)	0.06646 (0.00080)	6.5 (0.83)	−5.96 (0.086)	1.3 (0.37)
22	0.79047 (0.00012)	−5.46999 (0.00031)	2.9 (0.11)	−21.97 (0.036)	1.9 (0.13)
23	0.86086 (0.00013)	−5.42409 (0.00033)	1.8 (0.08)	−33.67 (0.032)	1.4 (0.16)
		Epoch 3			
1	0.41068 (0.00002)	−2.40182 (0.00006)	19.9 (0.14)	0.46 (0.002)	1.1 (0.00)
2	0.41190 (0.00004)	−2.41094 (0.00011)	20.1 (0.24)	−2.99 (0.004)	1.1 (0.01)
3	0.41136 (0.00005)	−2.40814 (0.00014)	10.2 (0.15)	−2.46 (0.027)	2.1 (0.03)
4	0.41246 (0.00004)	−2.41344 (0.00012)	13.9 (0.17)	−2.75 (0.005)	1.4 (0.01)
6	0.78454 (0.00006)	−3.99137 (0.00015)	5.1 (0.08)	−31.64 (0.015)	1.5 (0.05)
7	0.77984 (0.00013)	−3.98505 (0.00033)	2.2 (0.10)	−31.59 (0.024)	1.2 (0.10)
8	0.89361 (0.00003)	−4.84018 (0.00008)	11.5 (0.11)	−29.96 (0.006)	2.0 (0.01)
9	0.78646 (0.00015)	−5.46584 (0.00038)	1.7 (0.08)	−21.69 (0.043)	1.7 (0.17)
10	0.79901 (0.00007)	−5.47143 (0.00018)	4.8 (0.10)	−2.60 (0.013)	2.2 (0.04)
11	0.79844 (0.00012)	−5.47220 (0.00030)	3.1 (0.08)	−3.53 (0.033)	2.0 (0.09)
12	0.79733 (0.00014)	−5.46842 (0.00036)	2.4 (0.10)	−2.72 (0.085)	3.7 (0.29)
13	0.60954 (0.00009)	−5.35357 (0.00024)	16.1 (0.40)	−10.82 (0.028)	2.7 (0.05)
14	0.61441 (0.00004)	−5.35976 (0.00010)	44.8 (0.49)	−10.39 (0.012)	2.5 (0.02)
15	0.61430 (0.00005)	−5.36080 (0.00012)	31.5 (0.42)	−10.82 (0.010)	2.6 (0.02)
16	0.68552 (0.00003)	−5.28892 (0.00009)	32.5 (0.33)	−17.21 (0.004)	1.7 (0.01)
17	0.68385 (0.00008)	−5.28591 (0.00020)	28.1 (0.68)	−17.09 (0.011)	1.3 (0.02)
18	0.67382 (0.00007)	−5.26432 (0.00017)	6.4 (0.12)	−23.53 (0.012)	1.7 (0.03)
19	0.67368 (0.00005)	−5.26492 (0.00012)	10.0 (0.13)	−23.56 (0.008)	1.5 (0.02)
20	0.01672 (0.00029)	0.00910 (0.00073)	11.8 (1.00)	−6.37 (0.063)	1.6 (0.17)
21	0.02384 (0.00005)	0.00894 (0.00012)	1.4 (0.02)	−25.49 (0.018)	2.0 (0.09)
22	0.02592 (0.00003)	−0.00145 (0.00007)	6.2 (0.05)	−20.42 (0.006)	1.8 (0.01)
23	0.02041 (0.00007)	0.01997 (0.00017)	4.5 (0.08)	−12.32 (0.024)	1.5 (0.06)
24	0.01481 (0.00003)	0.02460 (0.00007)	52.3 (0.31)	−5.39 (0.006)	1.3 (0.01)

25	−0.00322 (0.00012)	−0.01722 (0.00030)	52.3 (1.29)	−7.57 (0.007)	0.6 (0.01)
26	0.00002 (0.00001)	−0.00005 (0.00003)	210.6 (0.65)	−7.63 (0.003)	2.7 (0.00)
27	0.00286 (0.00006)	0.00214 (0.00015)	5.4 (0.07)	−13.12 (0.011)	1.6 (0.02)
28	0.00187 (0.00003)	0.00081 (0.00008)	28.0 (0.26)	−11.10 (0.008)	1.6 (0.02)
29	0.00139 (0.00004)	0.00127 (0.00010)	7.2 (0.08)	−13.34 (0.007)	1.3 (0.02)
30	−0.01839 (0.00037)	−0.01436 (0.00096)	1.6 (0.22)	−17.17 (0.114)	1.4 (0.50)
31	0.01672 (0.00029)	0.00909 (0.00072)	11.8 (1.00)	−6.37 (0.063)	1.6 (0.17)
32	0.04890 (0.00004)	0.05781 (0.00011)	2.6 (0.03)	−14.92 (0.011)	1.9 (0.03)
33	−0.00532 (0.00025)	−0.05105 (0.00064)	18.3 (1.34)	−7.13 (0.042)	1.1 (0.15)
34	0.63440 (0.00031)	−0.65516 (0.00078)	13.4 (1.63)	−7.73 (0.205)	3.5 (0.86)
		Epoch 4			
1	0.41213 (0.00008)	−2.41040 (0.00021)	8.0 (0.18)	−0.60 (0.015)	1.3 (0.03)
2	0.41182 (0.00010)	−2.40960 (0.00026)	8.6 (0.24)	−2.68 (0.021)	1.7 (0.04)
3	0.41211 (0.00003)	−2.41155 (0.00008)	35.8 (0.37)	−3.03 (0.004)	1.1 (0.01)
4	0.78526 (0.00006)	−3.99643 (0.00014)	4.8 (0.08)	−31.94 (0.009)	1.2 (0.02)
5	0.87356 (0.00016)	−4.05857 (0.00041)	1.7 (0.08)	−32.45 (0.028)	1.1 (0.11)
6	0.90117 (0.00012)	−4.82046 (0.00029)	1.6 (0.06)	−28.48 (0.047)	1.5 (0.20)
7	0.79990 (0.00025)	−5.47446 (0.00065)	1.6 (0.10)	−3.62 (0.126)	1.5 (0.35)
9	0.79227 (0.00015)	−5.47641 (0.00037)	2.1 (0.09)	−21.38 (0.046)	1.9 (0.15)
10	0.79138 (0.00020)	−5.47512 (0.00049)	1.7 (0.10)	−21.70 (0.043)	1.5 (0.15)
11	0.84267 (0.00011)	−5.44467 (0.00028)	2.6 (0.08)	−21.04 (0.015)	1.0 (0.05)
12	0.61303 (0.00013)	−5.35936 (0.00033)	36.1 (1.24)	−10.29 (0.027)	2.4 (0.05)
13	0.61460 (0.00003)	−5.36172 (0.00008)	127.4 (1.09)	−10.41 (0.006)	2.4 (0.01)
14	0.61449 (0.00019)	−5.36095 (0.00049)	23.2 (1.16)	−10.84 (0.074)	3.2 (0.09)
15	0.68584 (0.00003)	−5.29294 (0.00009)	16.8 (0.17)	−18.85 (0.006)	2.1 (0.01)
16	0.66227 (0.00014)	−5.25074 (0.00035)	4.5 (0.15)	−24.03 (0.012)	0.7 (0.02)
17	0.66194 (0.00004)	−5.24890 (0.00010)	8.8 (0.10)	−24.11 (0.007)	1.5 (0.02)
18	0.66030 (0.00019)	−5.24611 (0.00048)	1.9 (0.12)	−24.07 (0.057)	1.7 (0.21)
19	0.24921 (0.00018)	−0.09765 (0.00046)	258.0 (12.32)	−7.66 (0.016)	0.7 (0.04)
20	−0.00193 (0.00006)	−0.00834 (0.00015)	53.6 (0.88)	−11.35 (0.011)	1.1 (0.02)
21	−0.00008 (0.00002)	−0.00020 (0.00004)	729.9 (3.55)	−7.27 (0.003)	2.1 (0.00)
22	0.00200 (0.00005)	0.00005 (0.00013)	66.0 (0.92)	−11.18 (0.008)	1.2 (0.02)
23	0.00163 (0.00008)	−0.00022 (0.00020)	21.3 (0.38)	−13.67 (0.009)	1.1 (0.02)
24	0.00279 (0.00005)	0.00221 (0.00014)	20.4 (0.29)	−13.16 (0.011)	1.5 (0.04)
25	0.00960 (0.00038)	0.00841 (0.00096)	10.3 (1.29)	−11.29 (0.065)	1.1 (0.23)
26	0.02523 (0.00007)	−0.00161 (0.00018)	6.0 (0.10)	−19.73 (0.010)	1.2 (0.03)
27	0.02362 (0.00003)	0.01012 (0.00008)	5.2 (0.05)	−23.34 (0.019)	2.4 (0.06)
28	0.02341 (0.00005)	0.01147 (0.00012)	3.1 (0.04)	−25.41 (0.017)	1.8 (0.05)
29	0.02053 (0.00003)	0.04449 (0.00007)	15.5 (0.11)	−22.05 (0.003)	1.2 (0.01)
31	0.04659 (0.00022)	0.05356 (0.00054)	13.4 (0.73)	−9.63 (0.093)	1.6 (0.39)
32	0.04854 (0.00002)	0.05847 (0.00005)	46.2 (0.24)	−14.57 (0.004)	1.7 (0.01)
33	0.07000 (0.00009)	0.06941 (0.00022)	12.0 (0.22)	−12.45 (0.018)	1.3 (0.05)
34	0.05800 (0.00012)	0.05914 (0.00030)	1.9 (0.07)	−19.34 (0.037)	2.1 (0.14)
35	0.05574 (0.00003)	0.06455 (0.00008)	12.2 (0.09)	−16.38 (0.008)	1.6 (0.02)
36	0.05786 (0.00002)	0.06999 (0.00004)	33.8 (0.15)	−1.10 (0.003)	2.0 (0.01)
37	0.03688 (0.00006)	0.02399 (0.00015)	5.1 (0.08)	−21.12 (0.014)	1.3 (0.04)
		Epoch 5			
1	0.41590 (0.00009)	−2.39751 (0.00022)	66.2 (1.66)	−3.14 (0.005)	1.2 (0.01)
2	0.68604 (0.00022)	−5.28774 (0.00055)	19.3 (1.64)	−21.05 (0.024)	1.4 (0.08)

3	0.68931 (0.00007)	−5.28778 (0.00019)	47.0 (1.06)	−21.02 (0.008)	1.4 (0.02)
4	0.68754 (0.00018)	−5.30510 (0.00046)	22.2 (1.36)	−21.04 (0.016)	1.3 (0.04)
5	0.66628 (0.00029)	−5.33590 (0.00074)	13.9 (1.68)	−21.01 (0.039)	1.0 (0.16)
6	0.61525 (0.00013)	−5.36625 (0.00033)	15.6 (0.65)	−10.83 (0.037)	2.7 (0.11)
7	0.00393 (0.00013)	−0.01938 (0.00033)	28.0 (1.18)	−24.82 (0.014)	2.0 (0.03)
8	−0.00004 (0.00004)	−0.00004 (0.00009)	352.1 (3.37)	−7.61 (0.006)	1.4 (0.01)
9	0.03674 (0.00032)	0.01244 (0.00082)	17.8 (1.87)	−24.69 (0.067)	1.5 (0.25)
10	0.02517 (0.00008)	0.01181 (0.00021)	38.9 (0.90)	−24.87 (0.008)	2.0 (0.01)
11	0.00334 (0.00011)	0.01585 (0.00029)	101.9 (2.98)	−9.25 (0.020)	1.3 (0.06)
12	0.02686 (0.00003)	0.02870 (0.00009)	86.2 (0.77)	−24.88 (0.003)	2.0 (0.01)
13	0.03904 (0.00006)	0.04740 (0.00017)	53.5 (0.94)	−24.89 (0.006)	2.0 (0.01)
14	0.02295 (0.00009)	0.04804 (0.00022)	105.5 (2.81)	−8.30 (0.019)	1.1 (0.06)
15	0.02148 (0.00007)	0.05701 (0.00017)	28.9 (0.49)	−4.92 (0.019)	1.7 (0.04)
17	0.03386 (0.00014)	0.07554 (0.00036)	14.2 (0.62)	−4.64 (0.030)	1.3 (0.13)
18	0.06718 (0.00004)	0.08883 (0.00010)	122.0 (1.25)	−18.24 (0.003)	1.5 (0.01)
19	0.07939 (0.00011)	0.10748 (0.00027)	74.7 (2.01)	−18.21 (0.028)	1.4 (0.04)
20	0.12890 (0.00009)	0.09824 (0.00023)	3.2 (0.09)	−40.68 (0.016)	1.4 (0.05)
		Epoch 6			
1	0.41586 (0.00005)	−2.39591 (0.00012)	18.8 (0.23)	−2.61 (0.007)	1.2 (0.01)
2	0.41645 (0.00005)	−2.39872 (0.00013)	16.4 (0.23)	−3.14 (0.007)	1.5 (0.01)
3	0.82716 (0.00005)	−4.01679 (0.00014)	2.3 (0.04)	−36.66 (0.012)	1.4 (0.06)
4	0.86808 (0.00004)	−4.01918 (0.00011)	3.4 (0.05)	−48.46 (0.006)	1.4 (0.02)
5	0.89707 (0.00002)	−4.83301 (0.00006)	10.1 (0.08)	−28.83 (0.008)	3.6 (0.02)
6	0.69034 (0.00005)	−5.29225 (0.00013)	5.4 (0.09)	−21.00 (0.008)	1.7 (0.02)
7	0.69740 (0.00027)	−5.29625 (0.00070)	1.3 (0.13)	−21.01 (0.098)	1.7 (0.61)
8	0.61816 (0.00009)	−5.35072 (0.00023)	17.4 (0.43)	−9.69 (0.021)	1.3 (0.05)
9	0.61753 (0.00012)	−5.34942 (0.00031)	2.4 (0.08)	−14.60 (0.060)	2.8 (0.29)
10	0.85472 (0.00006)	−5.44416 (0.00017)	4.3 (0.09)	−16.19 (0.015)	1.5 (0.05)
11	−0.04733 (0.00013)	−0.07972 (0.00034)	93.0 (2.49)	−6.65 (0.021)	1.1 (0.03)
12	−0.05119 (0.00011)	−0.05585 (0.00029)	163.5 (4.64)	−7.07 (0.010)	0.9 (0.02)
13	0.00002 (0.00003)	−0.00004 (0.00008)	416.9 (3.55)	−7.63 (0.005)	1.6 (0.01)
14	−0.00297 (0.00013)	0.00362 (0.00033)	78.3 (2.64)	−8.31 (0.036)	1.3 (0.06)
15	0.00353 (0.00004)	0.01583 (0.00011)	71.2 (0.76)	−10.57 (0.013)	2.3 (0.04)
16	0.03630 (0.00008)	0.01716 (0.00019)	1.8 (0.04)	−28.74 (0.021)	1.3 (0.08)
17	0.04153 (0.00010)	0.02141 (0.00026)	2.4 (0.06)	−22.29 (0.018)	1.3 (0.07)
18	0.02721 (0.00002)	0.02902 (0.00004)	19.4 (0.09)	−24.13 (0.003)	2.5 (0.01)
20	0.02223 (0.00016)	0.03802 (0.00040)	13.3 (0.66)	−10.50 (0.041)	1.4 (0.20)
21	0.01121 (0.00007)	0.04409 (0.00017)	12.4 (0.24)	−4.07 (0.011)	1.2 (0.02)
22	0.04435 (0.00025)	0.04441 (0.00066)	1.4 (0.14)	−18.88 (0.092)	1.6 (0.55)
23	0.04113 (0.00002)	0.04824 (0.00006)	13.1 (0.09)	−18.86 (0.003)	1.4 (0.01)
24	0.05111 (0.00025)	0.05583 (0.00063)	62.6 (5.16)	−7.59 (0.047)	1.2 (0.21)
25	0.02217 (0.00004)	0.05867 (0.00009)	23.7 (0.23)	−3.87 (0.005)	1.1 (0.01)
26	0.02852 (0.00017)	0.06713 (0.00043)	3.1 (0.15)	−0.43 (0.018)	0.8 (0.04)
27	0.02895 (0.00004)	0.06530 (0.00010)	6.2 (0.08)	−0.86 (0.005)	1.5 (0.02)
28	0.02871 (0.00006)	0.06524 (0.00016)	16.6 (0.25)	−4.97 (0.011)	1.3 (0.03)
29	0.04626 (0.00003)	0.07748 (0.00008)	19.5 (0.16)	−15.40 (0.007)	1.4 (0.01)
30	0.04897 (0.00002)	0.07551 (0.00005)	195.6 (1.09)	−12.41 (0.003)	1.5 (0.00)
31	0.05215 (0.00004)	0.08017 (0.00010)	20.1 (0.22)	−14.57 (0.006)	1.2 (0.02)
32	0.06235 (0.00003)	0.09141 (0.00008)	9.5 (0.09)	−0.74 (0.003)	1.1 (0.01)

34	0.06670 (0.00007)	0.08891 (0.00018)	2.9 (0.05)	−16.91 (0.022)	1.5 (0.09)
35	0.08847 (0.00006)	0.12343 (0.00015)	1.5 (0.03)	−40.04 (0.015)	1.4 (0.07)
		Epoch 7			
1	0.41599 (0.00007)	−2.39618 (0.00018)	3.8 (0.08)	−2.62 (0.020)	1.8 (0.09)
2	0.41670 (0.00006)	−2.39947 (0.00015)	6.4 (0.12)	−3.34 (0.009)	1.1 (0.03)
3	0.82775 (0.00006)	−4.01898 (0.00015)	2.8 (0.05)	−36.85 (0.007)	1.1 (0.02)
4	0.86866 (0.00007)	−4.02139 (0.00018)	2.1 (0.05)	−48.60 (0.014)	1.5 (0.05)
5	0.89714 (0.00003)	−4.83412 (0.00008)	6.9 (0.06)	−27.84 (0.011)	3.8 (0.03)
6	0.69078 (0.00007)	−5.29400 (0.00018)	2.1 (0.05)	−21.19 (0.019)	1.7 (0.07)
7	0.61765 (0.00012)	−5.35042 (0.00030)	5.5 (0.18)	−13.13 (0.088)	2.7 (0.18)
8	0.85503 (0.00006)	−5.44561 (0.00016)	6.1 (0.12)	−16.10 (0.010)	1.2 (0.03)
9	−0.04723 (0.00014)	−0.07993 (0.00037)	106.3 (2.86)	−6.63 (0.012)	0.9 (0.02)
11	−0.02008 (0.00028)	−0.02036 (0.00070)	15.0 (1.16)	−10.58 (0.050)	1.2 (0.13)
12	0.00002 (0.00003)	−0.00003 (0.00007)	452.8 (3.81)	−7.57 (0.005)	1.6 (0.01)
13	0.00090 (0.00027)	−0.00118 (0.00071)	13.8 (1.08)	−10.41 (0.108)	1.6 (0.25)
14	0.02456 (0.00011)	0.01212 (0.00028)	5.8 (0.20)	−24.58 (0.026)	1.7 (0.07)
15	0.00356 (0.00005)	0.01569 (0.00014)	64.8 (1.10)	−10.56 (0.012)	1.5 (0.04)
16	0.02766 (0.00007)	0.02711 (0.00018)	13.1 (0.31)	−24.63 (0.031)	1.4 (0.10)
17	0.02811 (0.00020)	0.02644 (0.00053)	3.7 (0.22)	−24.58 (0.043)	1.6 (0.10)
18	0.02720 (0.00002)	0.02916 (0.00006)	17.0 (0.12)	−24.33 (0.003)	2.0 (0.01)
19	0.02543 (0.00016)	0.03986 (0.00042)	12.4 (0.67)	−12.66 (0.036)	1.7 (0.11)
20	0.02220 (0.00008)	0.05884 (0.00021)	17.0 (0.25)	−4.11 (0.010)	1.1 (0.01)
21	0.04124 (0.00003)	0.04885 (0.00008)	14.7 (0.13)	−18.74 (0.005)	1.5 (0.01)
22	0.04648 (0.00009)	0.05874 (0.00024)	16.7 (0.49)	−12.49 (0.027)	2.1 (0.09)
23	0.05492 (0.00021)	0.07143 (0.00053)	21.3 (1.39)	−10.52 (0.036)	1.2 (0.15)
24	0.04906 (0.00003)	0.07577 (0.00007)	63.4 (0.47)	−12.58 (0.005)	1.7 (0.01)
25	0.04650 (0.00005)	0.07814 (0.00013)	15.3 (0.21)	−15.97 (0.006)	1.0 (0.02)
26	0.05221 (0.00004)	0.08047 (0.00010)	26.4 (0.32)	−14.76 (0.005)	1.1 (0.02)
27	0.08968 (0.00005)	0.09169 (0.00012)	2.9 (0.05)	−20.60 (0.010)	1.3 (0.04)
28	0.06252 (0.00003)	0.09178 (0.00007)	15.2 (0.13)	−1.17 (0.003)	1.2 (0.01)
29	0.08860 (0.00004)	0.12372 (0.00011)	6.3 (0.08)	−39.92 (0.005)	1.3 (0.01)
30	0.11543 (0.00006)	0.13490 (0.00015)	2.6 (0.05)	−48.86 (0.009)	1.1 (0.04)
31	0.10331 (0.00017)	0.13630 (0.00044)	7.3 (0.36)	−14.86 (0.035)	1.1 (0.10)

A.4 VERA Preburst Gaussian Features Proper Motions

Table A.5: Associations, positions, proper motions and radial velocities of the pre-burst proper motions (epochs of 2014.72 2015.28) as calculated by the "spectral" method. The detection string in the last column show for which epochs maser spots were detected. The numbers in square brackets, show the IDs of the maser features used in proper motion calculation from Table A.4. The id's are written EP-XX, e.g., [1-12 2-22] which states maser feature 12 of epoch 1 and maser feature 22 of epoch 2 was used for the proper motion calculation. The uncertainties on the values are shown in parentheses.

ID	Region	Offset		Proper Motion		$V_{\rm LSR}$	Detections
		α	δ	μ_x	μ_y		
		($''$)		(mas yr^{-1})		(km s^{-1})	
1	CM2-W2	−0.35653	5.17924	2.6 (0.4)	2.9 (1.1)	−8.55	1100 [1-3 2-15]

2	CM2-W1	−0.07502	4.56777	2.7 (0.5)	2.5 (1.5)	−10.38	1100 [1-2 2-14]
3	MM1-W1	−0.27873	2.89027	−0.4 (0.1)	2.4 (0.5)	−2.77	1101 [1-1 2-2 4-2]
4	MM1-W1	−0.27810	2.88906	−0.4 (0.2)	−1.1 (0.7)	−3.01	0011 [3-2 4-3]
5	CM2-W2	−0.69000	5.29997	−1.3 (0.0)	1.7 (0.1)	−7.34	1111 [1-6 2-18 3-25 4-20]
6	CM2-W2	−0.68813	5.30081	−0.7 (0.2)	−1.8 (0.8)	−11.14	0011 [3-27 4-21]
7	CM2-W2	−0.66408	5.29855	−4.0 (0.3)	1.2 (0.9)	−20.08	0011 [3-21 4-25]
8	CM2-W2	−0.66616	5.30894	−3.0 (0.3)	14.7 (0.9)	−25.45	0011 [3-20 4-27]
9	CM2-W2	−0.64110	5.35781	−2.7 (0.2)	5.3 (0.6)	−14.75	0011 [3-31 4-30]
10	CM2-W2	−0.68843	5.30120	−0.9 (0.1)	0.1 (0.5)	−12.85	1111 [1-5 2-16 3-28 4-22]
11	CM2-W2	−0.68714	5.30214	−1.5 (0.3)	2.4 (1.0)	−13.14	0011 [3-26 4-23]
12	UCHII-W3	0.09454	1.30863	1.7 (0.3)	−23.3 (1.0)	−31.79	0011 [3-5 4-4]
13	UCHII-W1	−0.07786	−0.05531	0.2 (0.4)	−2.2 (1.2)	−15.21	1100 [1-13 2-11]
14	UCHII-W1	−0.07698	−0.05872	−1.2 (0.2)	0.9 (0.7)	−10.30	1001 [1-15 4-11]
15	UCHII-W1	−0.01769	0.04127	2.2 (0.1)	−13.4 (0.5)	−23.59	1110 [1-12 2-7 3-17]
16	UCHII-W1	−0.00633	0.01766	2.9 (0.1)	−15.9 (0.3)	−17.47	1110 [1-19 2-8 3-15]
17	UCHII-W1	0.10087	−0.16673	−1.0 (0.3)	−13.4 (0.8)	−21.63	1101 [1-17 2-22 4-9]
18	UCHII-W1	0.16962	−0.12107	4.2 (0.6)	−14.5 (1.9)	−34.04	1100 [1-16 2-23]
19	UCHII-W2	0.20347	0.46435	0.3 (0.5)	−12.1 (1.6)	−30.51	1100 [1-10 2-5]
20	UCHII-W2	0.20304	0.46359	0.0 (0.2)	−8.4 (0.6)	−30.64	1110 [1-11 2-6 3-7]

A.5 VERA Postburst Gaussian Features Proper Motions

Table A.6: Associations, positions, proper motions and radial velocities of the burst proper motions (epochs of 2015.88 − 2016.19) as calculated by the "spectral" method. The detection string in the last column show for which epochs maser spots were detected. The numbers in square brackets, show the IDs of the maser features used in proper motion calculation from Table A.4. The id's are written EP-XX, e.g., [1-12 2-22] which states maser feature 12 of epoch 1 and maser feature 22 of epoch 2 was used for the proper motion calculation. The uncertainties on the values are shown in parentheses.

ID	Region	Offset		Proper Motion		$V_{\rm LSR}$	Detections
		α	δ	μ_x	μ_y		
		($''$)		(mas yr^{-1})		(km s^{-1})	
1	MM1-W1	−0.27355	2.90128	1.0 (0.7)	−7.2 (2.4)	−3.24	011 [6-2 7-2]
2	MM1-W1	−0.27414	2.90409	−0.0 (0.8)	−1.6 (2.6)	−2.61	011 [6-1 7-1]
3	UCHII-W3	0.13716	1.28321	4.4 (0.8)	−24.2 (2.4)	−36.75	011 [6-3 7-3]
4	UCHII-W3	0.17808	1.28082	4.2 (0.8)	−24.3 (2.5)	−48.53	011 [6-4 7-4]
5	UCHII-W2	0.20707	0.46699	−0.6 (0.4)	−11.5 (1.2)	−28.33	011 [6-5 7-5]
6	UCHII-W1	0.16472	−0.14416	1.7 (0.9)	−15.5 (2.8)	−16.15	011 [6-10 7-8]
7	UCHII-W1	−0.00069	0.01222	2.5 (0.3)	−18.3 (0.8)	−21.07	111 [3 6-6 7-6]
8	CM2-W2	−0.73733	5.22028	−0.4 (1.9)	−0.9 (5.9)	−6.64	011 [6-11 7-9]
9	CM2-W2	−0.60153	5.42343	−0.0 (0.7)	5.0 (2.2)	−39.98	011 [6-33 7-28]
10	CM2-W2	−0.69004	5.29996	−1.1 (0.1)	1.6 (0.4)	−7.60	111 [5-8 6-13 7-11]
11	CM2-W2	−0.62282	5.38883	−3.0 (0.3)	2.0 (0.9)	−17.57	110 [5-17 6-32]
12	CM2-W2	−0.66279	5.32902	−1.3 (0.3)	3.3 (0.8)	−24.23	011 [6-18 7-17]
13	CM2-W2	−0.63785	5.38017	−0.7 (0.5)	5.1 (1.7)	−14.66	011 [6-30 7-25]
14	CM2-W2	−0.62765	5.39141	0.4 (0.4)	5.9 (1.3)	−0.96	011 [6-31 7-27]
15	CM2-W2	−0.64374	5.37748	1.0 (0.6)	9.4 (1.8)	−15.68	011 [6-28 7-24]
16	CM2-W2	−0.64103	5.37551	−0.5 (0.3)	4.6 (1.0)	−12.50	011 [6-29 7-23]
17	CM2-W2	−0.68647	5.31583	−1.1 (0.7)	−0.1 (2.1)	−10.57	011 [6-15 7-14]

18	CM2-W2	−0.66783	5.35867	−1.1 (0.9)	3.5 (2.8)	−3.99	011 [6-24 7-19]
19	CM2-W2	−0.64887	5.34824	−0.2 (0.4)	8.8 (1.2)	−18.80	011 [6-22 7-20]
20	CM2-W2	−0.66483	5.31181	−2.9 (0.4)	2.6 (1.1)	−24.72	101 [5-10 7-13]
21	CM2-W2	−0.66314	5.32870	0.8 (0.2)	−3.5 (0.6)	−24.75	101 [5-12 7-15]
22	UCHII-W1	−0.07247	−0.04942	−0.2 (1.6)	−10.2 (5.1)	−13.87	011 [6-9 7-7]

A.6 Gaussian Fit Proper Motions Figures

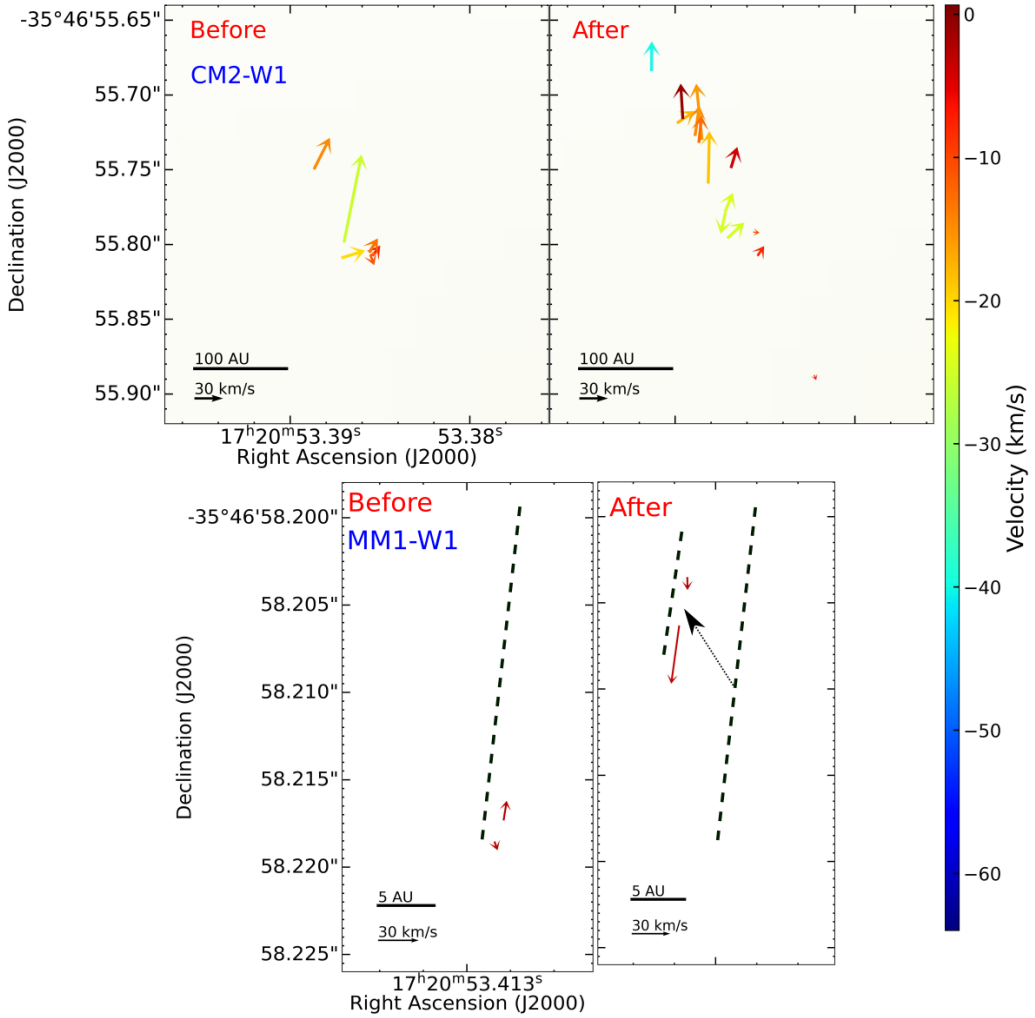

Figure A.1: Proper motions of 22 GHz water masers in the northern regions of NGC6334I, before and during the accretion burst. The proper motions are calculated by the spectral method. The positions, orientations and colours of the arrows show the positions, proper motions and $V_{\rm LSR}$ of the maser features respectively. The colour scale is on the righthand side. The left panels show the pre-burst epochs (epochs of 2014.72 2015.28) and the right panels show the burst epochs (epochs of 2015.88 2016.19). The linear scales in position and space are shown in the bottom left corner of each panel. In the bottom panel, black dashed lines show the position and orientation of the linear features shown in the maser features, and the black arrow shows the displacement of the maser features after the accretion burst.

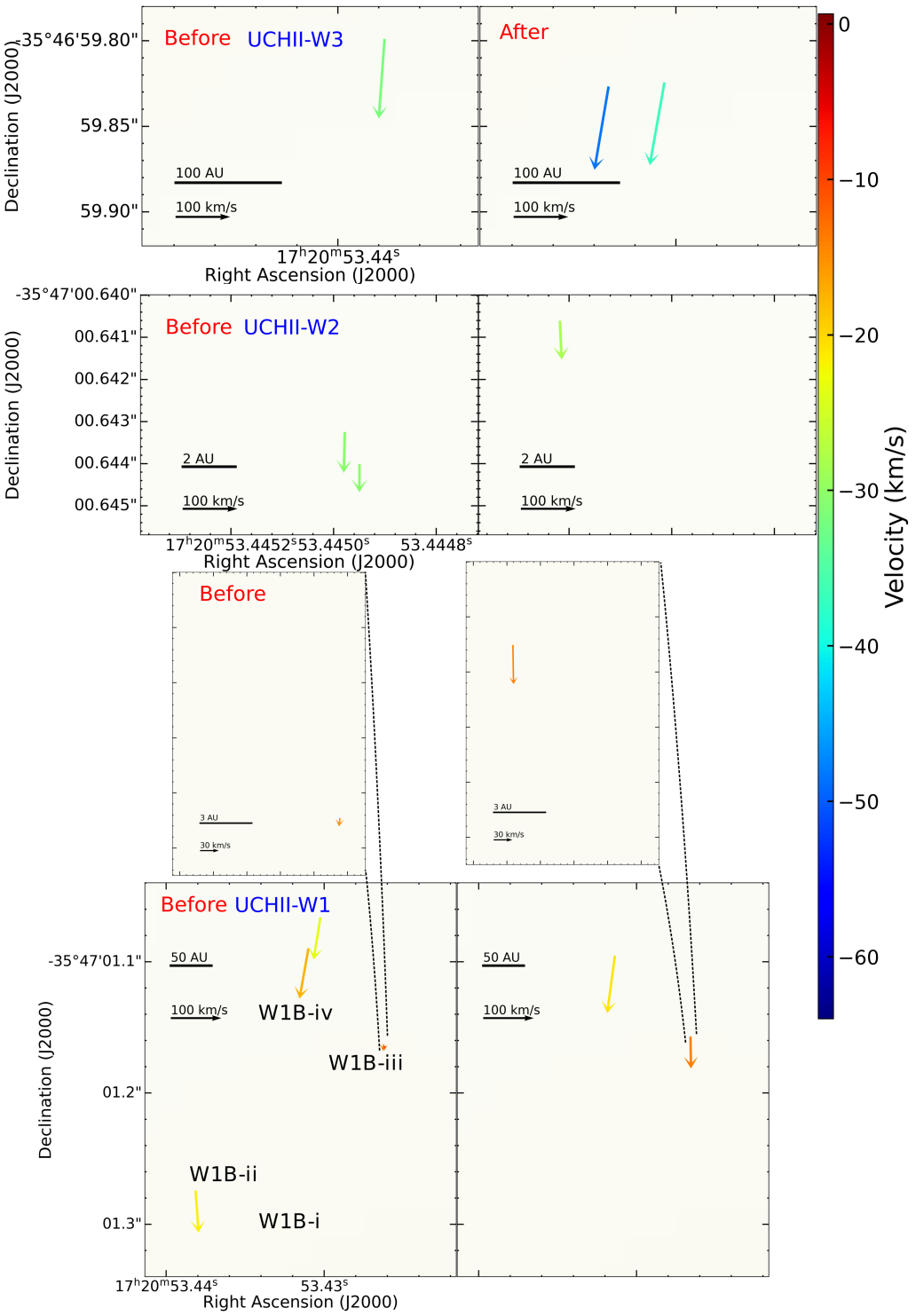

Figure A.2: Like Figure A.1, but for the southern regions.

A.7 Spot Method Proper Motion Code

Below is the code used to calculate proper motions with the spot method. The code was written in `Python 3.6` and the dependencies can be seen from the import statements at the top of the scripts. If this code has been used in a publication of any kind (even in a modified form), please cite this thesis. If you have any questions regarding its implementation, please contact the author of this thesis at *JOBVORSTER8@GMAIL.COM*. These scripts were used as-is to calculate the relative proper motions from tables containing the columns "RA, DEC, DRA, DDEC, VLSR, FLUX" where (RA,DEC) are right ascension and declination offsets in arcseconds and (DRA,DDEC) are the uncertainties in milliarcseconds. VLSR and FLUX are the radial velocities and peak flux densities of the maser spots.

A.7.1 region_identification.py

```
#(*****************************************************
#PROGRAM NAME - region-identification

#PROGRAMMER - Job Vorster - 2021/02/03

#USAGE - Compile using normal python terminal input python(3) region-identification.py FOLDERNAME
#With FOLDERNAME the data folder with the corresponding metadata.
#The program assumes you have a folder data containing the maser spot information in the format
#with the columns RA DEC VLSR FLUX DFLUX and separated by commas. The utils code should also be in the
#same directory.


#DATE - Started 2021/02/03
       #Version 0.5.0 2021/02/03
       #Current Version 0.6.0 2021/09/05

#DESCRIPTION - Program to easily identify regions with maser proper motion. Opens an interactive plot, which you can
#zoom in, and save data points into a text file, this text file is then used by the relative_pm.py python code
#to calculate the proper motions for the maser spots in the regions specified. The program has the following features:
#- Makes interactive plots of all epochs measured using normal python interactive plot.
#- Pressing "m" puts you into "box mode", which saves a box every time you click. With the box's corners being your two
#click positions. All the maser spots within will be processed as a single maser feature in relative_pm.py. So make sure to keep the boxes the right size
#If you make the boxes two big, you will have huge unphysical proper motions, that might be flagged. If the boxes are two small, you might miss multi epochs of the
#same maser, which will let you not detect its proper motions.
#- When using "box mode", try to box around masers with the same Vlsr.

#*****************************************************)



#*************************************************************

#        Import all libraries
```

```
36
37 #*****************************************************************
38 import matplotlib.pyplot as plt
39 import numpy as np
40 import pandas as pd
41 #Note the utils file should be in your directory.
42 from utils import extract_from_df,isolate,read_data
43 from glob import glob
44 from itertools import chain
45 from matplotlib import patches as pat
46 import os
47 import sys
48
49 #*****************************************************************
50
51 #        Define all local functions.
52
53 #*****************************************************************
54
55
56 def onclick(event):
57     '''Event handler for mouse clicks - Used for zooming in and out, and to choose
    regions for proper motion calculation. Currently, it is only used for
58     box mode'''
59     global click_no, saved_coords, RA,DEC,VLSR,FLUX,DFLUX, prev_click_x, prev_click_y
    ,fig, mode1, o_no,zoom_coords,plot_boxes,plotboxnum,data_boxes,databoxnum
60
61     #If special zoom mode is turned on. NOTE Removed.
62     #if dot_no == 1:
63         #zoom_coords = [[],[]]
64         #zoom_coords[0].append(event.xdata)
65         #zoom_coords[1].append(event.ydata)
66
67     #Zooming must be turned off to mark regions to save.
68
69     #prev_click arrays store two click values, that later gets saved.
70     if mode1 == 'box' and o_no == 0 and dot_no == 0:
71         if click_no == 0:
72             click_no = 1
73             prev_click_x.append(event.xdata)
74             prev_click_y.append(event.ydata)
75         else:
76             click_no = 0
77             prev_click_x.append(event.xdata)
78             prev_click_y.append(event.ydata)
79             prev_click_x.sort()
80             prev_click_y.sort()
81             saved_coords.append([prev_click_x,prev_click_y])
82             INDS = []
83             for i in range(0,len(RA)):
84                 inds = isolate(RA[i],DEC[i],prev_click_x,prev_click_y)
85                 INDS.append(inds)
86                 del inds
87             if len(INDS)!=0:
88                 print("Saved  box [[x0,x1],[y0,y1]:\n[[%.4f,%.4f],[%.4f,%.4f]]"%(
    prev_click_x[0],prev_click_x[1],prev_click_y[0],prev_click_y[1]))
89                 plot_boxes.append([prev_click_x[0],prev_click_x[1],prev_click_y[0],
    prev_click_y[1]])
90                 data_boxes.append([prev_click_x[0],prev_click_x[1],prev_click_y[0],
    prev_click_y[1]])
```

```
                plotboxnum += 1
                databoxnum += 1
            prev_click_x = []
            prev_click_y = []


def onkey_press(event):
    '''Event handler - For key presses. The options (other than the normal interactive python plot options - https://matplotlib.org/3.1.1/users/navigation_toolbar.html)
    available:
    - o key - This is the normal zoom option for the plots.
    - , key - NOT IMPLEMENTED, DOES NOT WORK. This is a special zoom mode, that restricts the clim for the colourbar to the masers on the screen, useful for identifying masers that might be associated over
    different epochs. After pressing the key, a message in the terminal indicates that "Zoom mode is now on", then you can zoom in using a mouse drag. Note that the clim updates sometimes stop working.
    - m key - This puts the plots into box mode, this mode one specifies a box from which proper motions will be calculated. Please note that the box should only
    contain masers that are suspected to be from the same maser feature. If you make too big boxes, the proper motions might be flagged further down the code. After pressing the key, a terminal message "Box mode is now on" signifies that you can save regions by clicking at two corners a box containing the masers in question. When you turn it off, it saves the regions into a textfile "DATADIR/pm_pars.txt" that will be piped into relative_pm.py. With "DATADIR" the directory where your data is.
    - r key - Resets the plot, keeping all maser position boxes saved and on the screen.'''
    global mode1,o_no,dot_no,data_boxes,databoxnum
    if event.key == 'o':
        if o_no == 0:
            o_no = 1
        else:
            o_no = 0
    #if event.key == ',': #Not working.
        #if dot_no ==0:
            #print("Zoom mode is now on")
            #dot_no = 1
        #else:
            #print("Zoom mode is now off")
            #dot_no = 0
    if event.key == 'r':
        plt.clf()
        all_scatter(RA,DEC,VLSR)
        plt.draw()
    if event.key == 'm':
        if mode1 != 'box':
            print('Box mode is now on')
            mode1 = 'box'
        else:
            print("Box mode is now off")
            plt.clf()
            all_scatter(RA,DEC,VLSR)
            plt.draw()
            print("Saving to data file")
#TODO add option to start a new parameter file or use an old one.
            if len(data_boxes)!= 0:
                f = open(data_dir + "/pm_pars.txt", "a")
```

```
136                 #Saving data boxes gave unequal data format, with some lines having
    two square brackets instead of one. The if below fixes that problem.
137                 if databoxnum == 1:
138                     f.write(str(data_boxes)[2:-2] + '\n')
139                 else:
140                     for i in range(0,databoxnum):
141 
142                         f.write(str(data_boxes[i])[1:-1]+'\n')
143                 f.close()
144                 data_boxes =[]
145                 databoxnum = 0
146             mode1 = 'none'
147 
148 #Not in use.
149 #def onrelease(event):
150     #'''Event handler for mouse key releases. Only use at this moment is with the
    special zoom mode. NOTE This is not used at the moment. '''
151     #global RA,DEC,VLSR,zoom_coords,dot_no
152     #if dot_no == 1:
153         #zoom_coords[0].append(event.xdata)
154         #zoom_coords[1].append(event.ydata)
155         #zoom_coords[0].sort()
156         #zoom_coords[1].sort()
157         #plt.clf()
158         #all_scatter(RA,DEC,VLSR,zoom_coords)
159         #plt.draw()
160 
161 
162 def all_scatter(RA,DEC,VLSR,lims = []):
163     '''Function for making scatter plots that you interact with. You can change the
    aspect_ratio manually if you want to. It is the ratio of the vertical axis to the
    horizontal axis.'''
164     global plot_boxes,plotboxnum
165     #Initializes the plot, plotsize is the x-size of the plot.
166     plotsize =7
167     aspect_ratio = 4
168     x_size = plotsize
169     figsize = (x_size,x_size*aspect_ratio)
170     newparams = {'figure.figsize': figsize, 'axes.grid': False,
171                 'lines.linewidth': 1.5, 'lines.markersize': 10,
172                 'font.size': 14}
173     plt.rcParams.update(newparams)
174     #Calculates the colorbar limits for the plots, to make sure each epoch has the
    same colorbar.
175     clims = [min([i for l in VLSR for i in l]),max([i for l in VLSR for i in l])]
176     INDS = []
177     FV =[]
178     CLIMS = []
179     for i in range(0,len(RA)):
180         #This code only runs when the image is zoomed in by the special zoom mode.
    NOTE Not in use.
181         if len(lims) != 0:
182             inds = isolate(RA[i],DEC[i],lims[0],lims[1])
183             INDS.append(inds)
184             FV.append(VLSR[i])
185             if len(inds) != 0:
186                 FV[i] = np.array(FV[i])[inds]
187     if len(lims) != 0:
188         #This line collapses an array containing all the vlsr values in the zoomed
    plot. To use the min and max for the clim.
```

```
189         clims = [min(list(chain.from_iterable(FV))),max(list(chain.from_iterable(FV))
    )]
190     for i in range(0,len(RA)):
191         if len(lims) !=0:
192             #Plots all the epochs, this case is for when special zoomed mode is used,
     so only the data points in the zoomed box is plotted NOTE probably not in use.
193             plt.scatter(np.array(RA[i])[INDS[i]],np.array(DEC[i])[INDS[i]],c = np.
    array(VLSR[i])[INDS[i]],marker = "$%d$"%(i+1),cmap = 'jet',label = epdates[i])
194             #Remember to specify the clim after every plot, and to keep it the same.
195             plt.clim(clims)
196         else:
197             plt.scatter(RA[i],DEC[i],c = VLSR[i],marker = "$%d$"%(i+1),cmap = 'jet',
    label = epdates[i])
198             plt.clim(clims)
199     if len(plot_boxes) != 0:
200         ax = plt.gca()
201         for i in range(0,plotboxnum):
202             #Plots a rectangle at boxes which the user has specified proper motion to
     be calculated
203             p =pat.Rectangle((plot_boxes[i][0],plot_boxes[i][2]),plot_boxes[i][1] -
    plot_boxes[i][0],
204                              plot_boxes[i][3]-plot_boxes[i][2],fill = False,linestyle
    = 'dashed',color = 'green')
205             ax.add_patch(p)
206     #To not let the plot invert every time this function is called.
207     if not plt.gca().xaxis_inverted():
208         plt.gca().invert_xaxis()
209     plt.colorbar(label = r"$V_{LSR}$ (km s$^{-1}$)")
210     plt.legend()
211     if len(lims) != 0:
212         plt.xlim(lims[0])
213         plt.ylim(lims[1])
214     plt.xlabel('RA Offset (arcseconds)')
215     plt.ylabel("Dec Offset (arcseconds)")
216     plt.gca().autoscale(False)
217
218 def extract_metadata(data_dir):
219     filename = data_dir + '/metadata.txt'
220     f = open(filename,'r')
221     pars = []
222     for line in f:
223         line = line[:-1]
224         pars.append(line.split('='))
225     return pars
226 #*****************************************************************
227
228 #         Code main body
229
230 #*****************************************************************
231 global epdates,data_dir
232 #Note the capitalized versions of list names, these lists are 2D, containing all data
      of their type. For example, RA contains [ra1,ra2,....]
233 RA = []
234 DEC = []
235 VLSR = []
236 FLUX = []
237 DFLUX = []
238 #The columns containing the data files in the input.
239 cols = ['RA','DEC','VLSR','FLUX','DFLUX']
240 plot_boxes = []
```

```
data_boxes = []
plotboxnum = 0
databoxnum = 0

#Controls of whether different keys have been pressed.
o_no = 0 #whether o has been pressed
click_no = 0 #whether the mouse click has been used.
dot_no = 0 #whether comma has been used NOTE Deprecated, not in use.
prev_click_x = []
prev_click_y = []
saved_coords = []
zoom_coords  = [[],[]]
mode1 = 'none' #The current mode for the plots. The mode is indicated in the terminal
    in the "onkey_press" function.

#Reads data from text files into multidimensional arrays.
#Only need to specify the relative path to the data files folder. DONE (Make the data
    file location an input).

data_dir = sys.argv[1]
pars = extract_metadata(data_dir)
epdates = []
for par in pars:
    if par[0] == 'epdates':
        for date in par[1].split(', '):
            epdates.append(date[1:-1])
if len(epdates)==0:
    print('ERROR : Please make sure the metadata.txt file is in the folder specified
    and the epdates field is included.')
    print('Exiting now...')
    exit()
#Reads the data using a function from utils.py.
RA,DEC,VLSR,FLUX,DFLUX = read_data(data_dir,cols)
print(len(epdates))
#Plots the data.
all_scatter(RA,DEC,VLSR)
fig = plt.gcf()
#Links the event handlers to the functions above.
cid = fig.canvas.mpl_connect('button_press_event', onclick)
#cid2 = fig.canvas.mpl_connect('button_release_event',onrelease)
cid3 = fig.canvas.mpl_connect('key_press_event',onkey_press)
plt.show()
```

A.7.2 relative_pm.py

```
#(*****************************************************
#PROGRAM NAME - relative_pm

#PROGRAMMER - Job Vorster - 2021/02/07

#USAGE - Compile using normal python terminal input python(3) relative_pm.py
    FOLDERNAME
#With FOLDERNAME the data folder with the corresponding metadata.


#DATE - Started 2021/02/03
       #Version 0.5.0 2021/02/03
       #Current Version 0.6.0 2021/09/05

#BUGS - None known.

```

```
#DESCRIPTION - Calculates maser features and their relative proper motions for maser data with averaging boxes supplied by the "pm_pars.txt" file supplied by the
#"region_identification.py" script.

#*****************************************************)

#*****************************************************************

#         Import all libraries

#*****************************************************************


import matplotlib.pyplot as plt
import numpy as np
import pandas as pd
#Note the utils.py file should be in your directory.
from utils import isolate,get_ind,zero_list,err_min,parallax_corr
from glob import glob
from itertools import chain
from matplotlib import patches as pat
import os
from scipy import stats,optimize
import math
import sys
#*****************************************************************

#         Define all local functions.

#*****************************************************************

def extract_from_df(df,cols):
    '''Utility function to get specified columns from a dataframe as a list object.
    Parameters :
    ------------
    df : Pandas DataFrame.
    Pandas dataframe to extract data.

    Returns :
    # TODO Fix this so that you can have or have not the error.
    ---------
    allcols : 2D list containing all the specified dataframe columns.'''
    allcols = []
    for col in cols:
        allcols.append(df[col].values)
    ra = df['RA'].values
    dra = df['RAERR'].values
    dec = df['DEC'].values
    ddec = df['DECERR'].values
    vlsr = df['VLSR'].values
    flux = df['FLUX'].values
    dflux = df['DFLUX'].values

    return ra,dra,dec,ddec,vlsr,flux,dflux

def read_data(data_dir,cols):
    '''Reads maser position data from textfiles in a specified directory. Note that a folder Fileorder.txt should be in the directory,
    containing the order in which the files should be read. Be sure to specify the entire file name in Fileorder.txt.
```

```
    Parameters :
    ------------
    data_dir : string
    Name of directory containing the maser position data and Fileorder.txt file.
    cols : list of strings
    Currently, cols should be set to ['RA','DEC','VLSR','FLUX','DFLUX']. As this function has not been generalized yet.'''
    RA = []
    RAerr =[]
    DEC = []
    DECerr = []
    VLSR = []
    FLUX = []
    DFLUX = []
    data_files = []
    with open(data_dir+'/Fileorder.txt') as f:
        for line in f:
            data_files.append(data_dir + '/'+line[:-1])

    for name in data_files:
        df = pd.read_csv(name,sep = ',')
        ra,dra,dec,ddec,vlsr,flux,dflux = extract_from_df(df,cols)
        RA.append(ra)
        RAerr.append(dra)
        DEC.append(dec)
        DECerr.append(ddec)
        VLSR.append(vlsr)
        FLUX.append(flux)
        DFLUX.append(dflux)
    return RA,RAerr,DEC,DECerr,VLSR,FLUX,DFLUX

def maser_feature(RA,RAerr,DEC,Decerr,VLSR,xlim,ylim):
    '''Function that averages multiple maser spots (single data points) into maser features. The function takes in 2D lists of uneven shapes
    where the first dimension is the multiple epochs. The second dimension is the individual data points of each epoch. Further the function takes in a box in
    the form of xlim and ylim that isolates the averaging region. Maser spots of the same vlsr are averaged and grouped together for the multiple epochs.
    This makes it quite easy to compute proper motions using the maser features.

    Parameters :
    ------------
    RA,RAerr,DEC,Decerr,VLSR : 2D array-like
    Data for all the maser spots generated by maser gaussian fitting.
    xlim,ylim : arraylike of the form [min,max]
    Limits in RA,DEC for which the maser features should be averaged. These limits are generated automatically by the region-identification.py script.
    Make sure that the regions are small enough that different proper motions do not overlap. This might cause large errors in position or unphysical proper motions.

    Returns :
    --------
    output : list
    Maser feature data for this box and vlsr, containing information on the average position of the maser feature for all epochs. The list is of the form
    [vlsr,detections,RA,RAerr,DEC,DECerr] - with vlsr being the vlsr of the maser feature (it is assumed to be constant), detections - a string signifying detections and
    RA,...,DECerr which are lists containing the average maser feature information and [99900] if the feature is not detected in that epoch.
```

```
    INDS : 2D list
    List of indices of the dataset that have been used to calculate the maser features. These indices should then be used to delete these data points from the input arrays.
    To make sure there is no double counts.
    '''
    VLSR_detections = []
    FEATURE_RA = []
    FEATURE_Dec = []
    FEATURE_RAerr = []
    FEATURE_Decerr = []
    INDS = []
    for i in range(0,len(RA)):
        inds = isolate(RA[i],DEC[i],xlim,ylim) #indices of maser spots of specific epoch in specified box.
        INDS.append(inds)
        isoRA = np.array(RA[i])[inds]
        isoRAerr = np.array(RAerr[i])[inds]
        isoDec = np.array(DEC[i])[inds]
        isoDecerr = np.array(Decerr[i])[inds]
        isoVlsr = np.array(VLSR[i])[inds]

        del inds
        #With all maser spots in the box isolated - Sort maser spots according to their vlsr so that they
        #can be averaged.
        VLSR_detections.append(list(dict.fromkeys(isoVlsr)))
        for vlsr in list(dict.fromkeys(isoVlsr)):
            ind = get_ind(isoVlsr,vlsr) #Gets the indices of maser spots of a specific vlsr
            feature_RA = round(np.mean(isoRA[ind]),6) #Averages the RA of the maser spots
            feature_Dec = round(np.mean(isoDec[ind]),6)

            if len(ind) ==1:
                feature_RAerr = isoRAerr#10e-6 #G24 4.330729166666667e-07 #10 microarcseconds error on VERA positioning.
                feature_Decerr = isoDecerr#10e-6 #G24 1.17171875e-05
            else:
                feature_RAerr = sum(isoRAerr**2)/np.sqrt(len(isoRAerr))#round(np.std(isoRA[ind])/np.sqrt(len(ind)),6) #Uses error on the mean.
                feature_Decerr = sum(isoDecerr**2)/np.sqrt(len(isoDecerr))#round(np.std(isoDec[ind])/np.sqrt(len(ind)),6)


            #Adds the calculated feature's values to a big storage list that stores all the values.
            #The index in the collapsed version of VLSR_detections corresponds to the index of the value
            #in the FEATURE_xx arrays. This will later be used to gather all detections of a specific vlsr over all epochs.
            FEATURE_RA.append(feature_RA)
            FEATURE_Dec.append(feature_Dec)
            FEATURE_RAerr.append(feature_RAerr)
            FEATURE_Decerr.append(feature_Decerr)

    epoch_Flags = [0] #List containing the first index of a new epoch for the FEATURE_xx arrays.
    total_len = 0
    epoch_indices = []
```

```
170
171     #NOTE I DO NOT THINK THESE COMMENTS NEED BE TAKEN INTO ACCOUNT NOW.
172     #Note that we should correct for the VLSR drift in the instrumental measurements.
        This is the same for all maser spots. The following array
173     #is the change in measurement vlsr in terms of the first epoch:
174     #
        [0.0,0.00601999999999947,0.016969999999999708,0.016649999999999388,0.00495000000000001,0.02259

175     #It should be used to correct the VLSR_detections array.
176     #Remember to take this into account with vlsr averaging and writeup.
177     #vlsr_correction =
        [0.0,0.00601999999999947,0.016969999999999708,0.016649999999999388,0.00495000000000001,0.02259

178     for i in range(0,len(VLSR_detections)):
179         if len(VLSR_detections[i])!=0:
180             for j in range(0,len(VLSR_detections[i])):
181                 VLSR_detections[i][j] = round(VLSR_detections[i][j],1) #NOTE that the
        shift in vlsr is smaller than 0.1 in all epochs. So rounding to the nearest
182                                                                         #tenth is a
        good enough way to judge detections.
183             total_len += len(VLSR_detections[i])
184             epoch_Flags.append(total_len)
185             epoch_indices.append(i)
186     #Now the indices [0...Nepochs-1] corresponds to the N+1th epoch.
187
188
189
190     #Now we have created maser features from maser spots for all epochs and sorted
        them according to vlsr.
191     #We have to sort all detections so that the maser features of specific vlsr
        values can be saved together
192     #This will be our output that is later used to calculate the proper motions.
193
194     epoch_RA = zero_list([0]*len(VLSR_detections),99900) # The integer 99900
        corresponds to "no detection".
195     epoch_Dec = zero_list([0]*len(VLSR_detections),99900)
196     epoch_RAerr = zero_list([0]*len(VLSR_detections),99900)
197     epoch_Decerr = zero_list([0]*len(VLSR_detections),99900)
198
199     output = []
200     detections = list('0'*len(VLSR_detections))
201     for vlsr in list(dict.fromkeys(sum(VLSR_detections,[]))): #Loop over all detected
        vlsr values.
202         ind = get_ind(sum(VLSR_detections,[]),vlsr) #Get all indices corresponding to
        specific vlsr.
203         if len(ind) > 1:
204             for k in ind: #Going through each index to get the epoch.
205                 for i in range(0,len(epoch_Flags)):
206                     if k >= epoch_Flags[i] and k < epoch_Flags[i+1]: #The value of i
        +1 gives the epoch.
207                         #This assigns the value of the maser feature to the specified
        epoch.
208                         epoch_RA[epoch_indices[i]] = FEATURE_RA[k]
209                         epoch_Dec[epoch_indices[i]] = FEATURE_Dec[k]
210                         epoch_RAerr[epoch_indices[i]] = FEATURE_RAerr[k]
211                         epoch_Decerr[epoch_indices[i]] = FEATURE_Decerr[k]
212                         detections[epoch_indices[i]] = '1'
213         #Finally stores the output that will go into the textfile to calculate the
        proper motions.
214         if ''.join(detections)!= '0'*len(VLSR_detections):
```

```
215             output.append([vlsr,''.join(detections),epoch_RA,epoch_RAerr,epoch_Dec,
    epoch_Decerr])
216         #Resets the storing arrays.
217         detections = list('0'*len(VLSR_detections))
218         epoch_RA = zero_list([0]*len(VLSR_detections),99900)
219         epoch_Dec = zero_list([0]*len(VLSR_detections),99900)
220         epoch_RAerr = zero_list([0]*len(VLSR_detections),99900)
221         epoch_Decerr = zero_list([0]*len(VLSR_detections),99900)
222     return output,INDS
223
224 def read_maser_feature(filename,epCount):
225     '''Reads maser_feature output textfile into arrays that can be manipulated in
    code.
226     Parameters :
227     ------------
228     filename : string
229     Name of the file which the function maser_feature saved its output.
230     epCount : int
231     Number of epochs in dataset.
232
233     Returns :
234     --------
235     vlsr,detections,ra,raerr,dec,decerr : array-like
236     Arrays read from the maser_feature text file.'''
237     vlsr = []
238     detections = []
239     ra = np.array([])
240     raerr = np.array([])
241     dec = np.array([])
242     decerr =np.array([])
243     with open(filename,'r') as f:
244         for line in f:
245             line_str = line.split(', ')
246             vlsr.append(float(line_str[0]))
247             detections.append(line_str[1][1:-1])
248             del line_str[0:2]
249             for i in range(0,len(line_str)):
250                 element = line_str[i]
251                 new_element = ''
252                 for char in element:
253                     if not (char == ']' or char == '['):
254                         new_element += char
255                 del element
256                 line_str[i] = new_element
257             ra = np.append(ra,np.array(line_str[0:epCount],dtype = float))
258             del line_str[0:epCount]
259             raerr = np.append(raerr,np.array(line_str[0:epCount],dtype = float))
260             del line_str[0:epCount]
261             dec = np.append(dec,np.array(line_str[0:epCount],dtype = float))
262             del line_str[0:epCount]
263             decerr = np.append(decerr,np.array(line_str[0:epCount],dtype = float))
264             del line_str[0:epCount]
265     newshape = (len(vlsr),epCount)
266     ra = np.reshape(ra.T,newshape)
267     raerr = np.reshape(raerr.T,newshape)
268     dec = np.reshape(dec.T,newshape)
269     decerr = np.reshape(decerr.T,newshape)
270     return vlsr,detections,ra,raerr,dec,decerr
271
272 def lin_f(x,a,b):
```

```
    '''Simple linear function evalueation. With x the dependant variable, a the slope and b the y-intercept. Returns the y value of a specific x value(s)'''
    return a*x+b



def calcpm(mf_RA,mf_RAerr,mf_DEC,mf_DECerr,mf_times,mf_VLSR,mf_DETECTIONS,source_Dec):
    '''Calculates proper motions from the positions and times of different epochs. The user gives as input the positions of the maser spots
    for different epochs, and their measurement time (in units of years) together with the source declination to calculate proper motions. Note
    that this function works only with the output of maser_feature.
    Parameters :
    ------------
    mf_RA,mf_RAerr,mf_DEC,mf_DECerr,mf_times,mf_VLSR,mf_DETECTIONS : array-like
    Positions, errors, detection times and VLSR and detection arrays of maser features from maser_feature and read_maser_feature.
    source_Dec : float
    Declination of the source in degrees.

    Returns:
    -------
    vlsr,ra,raerr,dec,decerr,mux,muxerr,muy,muyerr,detections : array-like
    Information on all detected proper motions.

    P.S. Note that VLSR and detections wont be used in this function, but it is helpful to return it to get all data in one line.'''

    datapoint_no = len(mf_RA)
    vlsr = []
    detections = []
    ra = []
    raerr = []
    dec = []
    decerr = []
    mux = []
    muxerr =[]
    muy = []
    muyerr = []

    for datapoint in range(0,datapoint_no):
        fit_RA = []
        fit_RAerr =[]
        fit_DEC = []
        fit_DECerr = []
        fit_VLSR = []
        fit_times =[]
        #Iterates through all the datapoints.
        for i in range(0,len(mf_RA[datapoint])):
            if mf_RA[datapoint][i] != 99900: #Only uses the data points of detections.
                fit_RA.append(mf_RA[datapoint][i])
                fit_RAerr.append(mf_RAerr[datapoint][i])
                fit_DEC.append(mf_DEC[datapoint][i])
                fit_DECerr.append(mf_DECerr[datapoint][i])
                fit_times.append(mf_times[i])
                fit_VLSR.append(mf_VLSR[datapoint]) # NOTE the mf_VLSR array is only 1D
        dx = fit_RA[-1] - fit_RA[0]  #Get the magnitude of the proper motion from the
```

```
     displacement between the earliest and latest datapoint.
325         dt = fit_times[-1] - fit_times[0]
326         dy = fit_DEC[-1] - fit_DEC[0]
327         popt_RA,pcov_RA = optimize.curve_fit(lin_f,fit_times,fit_RA,sigma = fit_RAerr
    ,absolute_sigma = True)  #Get the slope and error for the proper motion from
    linear fit.
328         perr_RA = np.sqrt(np.diag(pcov_RA)) #Magnitudes of the errors on the
    parameters.
329         popt_DEC,pcov_DEC = optimize.curve_fit(lin_f,fit_times,fit_DEC,sigma =
    fit_DECerr,absolute_sigma = True)
330         perr_DEC = np.sqrt(np.diag(pcov_DEC))
331         mux.append(popt_RA[0]*np.cos(np.deg2rad(source_Dec)))
332         muxerr.append(perr_RA[0]*np.cos(np.deg2rad(source_Dec)))
333         muy.append(popt_DEC[0])
334         muyerr.append(perr_DEC[0])
335         ra.append(fit_RA[0])
336         dec.append(fit_DEC[0])
337         vlsr.append(fit_VLSR[0])
338         detections.append(mf_DETECTIONS[datapoint])
339     return vlsr,ra,raerr,dec,decerr,mux,muxerr,muy,muyerr,detections
340
341 def extract_metadata(data_dir):
342     filename = data_dir + '/metadata.txt'
343     f = open(filename,'r')
344     pars = []
345     for line in f:
346         line = line[:-1]
347         pars.append(line.split('='))
348     return pars
349
350
351 #*****************************************************************
352
353 #         Code main body
354
355 #*****************************************************************
356
357
358 global data_dir
359 #Note the capitalized versions of list names, these lists are 2D, containing all data
      of their type. For example, RA contains [ra1,ra2,....]
360 RA = []
361 DEC = []
362 VLSR = []
363 FLUX = []
364 DFLUX = []
365 #The columns containing the data files in the input.
366 cols = ['RA','RAERR','DEC','DECERR','VLSR','FLUX','DFLUX']
367 plot_boxes = []
368 data_boxes = []
369 plotboxnum = 0
370 databoxnum = 0
371
372
373 #Reads data from text files into multidimensional arrays.
374 data_dir = sys.argv[1]
375 pars = extract_metadata(data_dir)
376
377 RA,RAerr,DEC,Decerr,VLSR,FLUX,DFLUX = read_data(data_dir,cols)
378
```

```
# for i in range(len(RA)):
#     app = []
#     for j in range(len(RA[i])):
#         app.append(1e-6)
#     RAerr.append(app)
#     Decerr.append(app)
parameterfile = data_dir + '/pm_pars.txt' #Filename for the boxes that serve as an input for maser_feature.
if os.path.exists(data_dir + '/maser_features.txt'):
    os.remove(data_dir + '/maser_features.txt')  #Removes the file before it writes on it again.


#TODO Consider adding a heading to the text file.
with open(parameterfile,'r') as f:
    for line in f:
        new_RA = []
        new_DEC = []
        new_VLSR = [] #We need to delete the array elements that are used in maser feature to make sure there is no double counting of maser spots.
        new_FLUX = []
        new_DFLUX = []
        linestring = np.fromstring(line,dtype = float,sep = ' ,')
        xlim = linestring[0:2]
        ylim = linestring[2:]
        output,INDS = maser_feature(RA,RAerr,DEC,Decerr,VLSR,xlim,ylim)
        for i in range(0,len(INDS)):
            for j in range(0,len(RA[i])):
                if j not in INDS[i]:
                    new_RA.append(RA[i][j])
                    new_DEC.append(DEC[i][j])
                    new_VLSR.append(VLSR[i][j]) #This counts all the elements that have not been counted by maser_feature.
                    new_FLUX.append(FLUX[i][j])
                    new_DFLUX.append(DFLUX[i][j])
            RA[i] = new_RA
            DEC[i] = new_DEC
            VLSR[i] = new_VLSR #This selects all the values that are NOT in INDS (INDS being the indices of isolated data points). This is to make sure there are no double counting.
            FLUX[i] = new_FLUX
            DFLUX[i] = new_DFLUX
            new_RA = []
            new_DEC = []
            new_VLSR = []
            new_FLUX = []
            new_DFLUX = []
        f2 = open(data_dir + '/maser_features.txt','a')
        for single_feature in output:
            f2.write(str(single_feature)[1:-1] + '\n')
        f2.close()

mf_VLSR,mf_DETECTIONS,mf_RA,mf_RAerr,mf_DEC,mf_DECerr = read_maser_feature(data_dir + '/maser_features.txt',epCount = len(RA)) #Read maser feature data from textfile. Note the mf_ prefix.


#Reads in the dates from the "metadata.txt" file for the calculation of the proper motions.
epdate_float = []
```

```
for par in pars:
    if par[0] == 'epdate_float':
        for date in par[1].split(', '):
            epdate_float.append(date)
epdate_float=np.array(epdate_float,dtype=float)
if len(epdate_float)==0:
    print('ERROR : Please make sure the metadata.txt file is in the folder specified and the epdate_float field is included.')
    print('Exiting now...')
    exit()

#Reads in the source declination from the "metadata.txt" file for the calculation of the proper motions.

source_Dec = 0
for par in pars:
    if par[0] == 'source_Dec':
        source_Dec = float(par[1])
if source_Dec==0:
    print('ERROR : Please make sure the metadata.txt file is in the folder specified and the source_Dec field is included.')
    print('Exiting now...')
    exit()



#Calculates the proper motions.
vlsr,ra,raerr,dec,decerr,mux,muxerr,muy,muyerr,detections = calcpm(mf_RA,mf_RAerr,mf_DEC,mf_DECerr,epdate_float,mf_VLSR,mf_DETECTIONS,source_Dec)
if os.path.exists(data_dir +'/pm_results.txt'):
    os.remove(data_dir +'/pm_results.txt')  #Removes the file before it writes on it again.

#Saves the proper motions.
with open(data_dir +"/pm_results.txt",'a') as f:
    f.write("Index \t Vlsr \t RA \t DEC \t mux (mas) \t muxerr (mas) \t muy (mas) \t muyerr (mas) \t detections \n")
    for i in range(0,len(vlsr)):
        f.write("%d \t %0.5f \t %0.5f \t %0.5f \t %0.5f \t %0.5f \t %0.5f \t %0.5f \t %s\n"%(i,vlsr[i],ra[i],dec[i],mux[i]*1e3,muxerr[i]*1e3,muy[i]*1e3,muyerr[i]*1e3,detections[i]))
f.close()
#Plots the proper motions.
plt.figure(figsize = (7,7))
plotsize =7
aspect_ratio = 4
x_size = plotsize
figsize = (x_size,x_size*aspect_ratio)
newparams = {'figure.figsize': figsize, 'axes.grid': False,
             'lines.linewidth': 1.5, 'lines.markersize': 10,
             'font.size': 14}
plt.rcParams.update(newparams)
plt.gca().invert_xaxis()
#print("Index \t Vlsr \t\t RA \t\t DEC \t\t mux (mas) \t muxerr (mas) \t muy (mas) \t muyerr (mas) \t detections \n")
#for i in range(0,len(vlsr)):
#    print("%d \t %0.5f \t %0.5f \t %0.5f \t %0.5f \t %0.5f \t %0.5f \t %0.5f \t %s "%(i,vlsr[i],ra[i],dec[i],mux[i]*1e3,muxerr[i]*1e3,muy[i]*1e3,muyerr[i]*1e3,detections[i]))
```

```
plt.quiver(np.array(ra),np.array(dec),-np.array(mux),np.array(muy),vlsr,cmap = 'jet')
plt.xlabel("RA offset (arcsec)")
plt.ylabel("Dec offset (arcsec)")
plt.colorbar(label = r'$V_{LSR}$ (km/s)')
plt.show()
```

A.7.3 flagging_pm.py

```
#(******************************************************
#PROGRAM NAME - flagging_pm

#PROGRAMMER - Job Vorster

#USAGE - Compile using normal python terminal input python(3) relative_pm.py
    FOLDERNAME
#With FOLDERNAME the data folder with the corresponding metadata.


#DATE - Started 2021/02/03
       #Version 0.5.0 2021/02/03
       #Current Version 0.6.0 2021/09/05

#BUGS - None known.

#DESCRIPTION -

#******************************************************)

#*********************************************************************

#        Import all libraries

#*********************************************************************

import fnmatch, argparse
import pandas as pd
import numpy as np
from utils import isolate
import matplotlib.pyplot as plt


global data_dir,fig_int
fig_int = 0
#*********************************************************************

#        Define all local functions.

#*********************************************************************

def read_pm_results(filename):
    df = pd.read_csv(filename,sep='\t',dtype=str)
    delinds = []
    #Drops proper motions with undefined errors.
    for i,v in enumerate(df[' muxerr (mas) '][0:-1].values):
        if v ==' nan ':
            delinds.append(i)
    for i,v in enumerate(df[' muyerr (mas) '][0:-1].values):
        if v ==' nan ':
```

```
            delinds.append(i)
    df = df.drop(delinds)
    ra = np.array(df[' RA '].values,dtype=float)
    dec = np.array(df[' DEC '].values,dtype=float)
    mux = np.array(df[' mux (mas) '].values,dtype=float)
    dmux = np.array(df[' muxerr (mas) '].values,dtype=float)
    vlsr = np.array(df[' Vlsr '].values,dtype=float)
    muy = np.array(np.array(df[' muy (mas) '].values,dtype=float))
    dmuy = np.array(np.array(df[' muyerr (mas) '].values,dtype=float))
    detections = np.array(df[' detections '],dtype=str)
    return ra,dec,mux,muy,dmux,dmuy,vlsr,detections

def extract_metadata(data_dir):
    filename = data_dir + '/metadata.txt'
    f = open(filename,'r')
    pars = []
    for line in f:
        line = line[:-1]
        pars.append(line.split('='))
    return pars


def flag_error(mux,muy,dmux,dmuy,flagerror_rat):
    #Flag all data with an error larger than some ratio.
    pm_sigma = []
    for i in range(len(mux)):
        pm_sigma.append(np.sqrt((dmux[i]/mux[i])**2 + (dmuy[i]/muy[i])**2))
    pm_sigma = np.array(pm_sigma)
    error_flags = np.where(pm_sigma > flagerror_rat)[0]
    return error_flags

#def flag_speed(): TODO - Turn this functionality into a function.
    #Flag all data with a speed above a certain value.
    #return speed_flags

def flag_detections(detections):
    #Flag all data with non-detections in more than N epochs between maser feature
    detections.
    detection_flags = []
    detection_length = len(detections[0])
    detection_strs = []
    if detection_length > 2:
        for i in range(3,detection_length+1):
            detection_strs.append('1' + (i-2)*'0'+'1')
    for i in range(len(detections)):
        for detection_str in detection_strs:
            if detection_str in detections[i]:
                detection_flags.append(i)
            break
    return detection_flags

def flag_manual():
    #Flag data manually.
    return manual_flags

def print_pm_info_angular(ra,dec,mux,muy,dmux,dmuy,vlsr,detections):
    print(40*'*' + 3*' ' +'Proper motion parameters' + 3*' ' + 40*'*')
    print("Index \t Vlsr \t\t RA \t\t DEC \t\t mux (mas) \t dmux (mas) \t muy (mas) \
    t dmuy (mas) \t detections")
    for i in range(len(ra)):
```

```
        print("%d \t %0.5f \t %0.5f \t %0.5f \t %0.5f \t %0.5f \t %0.5f \t %0.5f \t %
    s"%(i,vlsr[i],ra[i],dec[i],mux[i],dmux[i],muy[i],dmuy[i],detections[i]))

def plot_pm_w_error(ra,dec,mux,muy,dmux,dmuy,vlsr):
    plt.quiver(ra,dec,-mux,muy,vlsr,cmap='jet')
    plt.clim(min(vlsr),max(vlsr))
    plt.quiver(ra,dec,-mux-dmux,muy+dmuy,vlsr,cmap='Greys')#,headwidth=0)
    plt.clim(min(vlsr),max(vlsr))
    plt.quiver(ra,dec,-mux+dmux,muy-dmuy,vlsr,cmap='Greys')#,headwidth=0)
    plt.clim(min(vlsr),max(vlsr))
    plt.show()

def plot_pm(ra,dec,mux,muy,vlsr):
    global fig_int
    plt.figure(fig_int)
    fig_int += 1
    plt.quiver(ra,dec,-mux,muy,vlsr,cmap='jet')
    plt.clim(min(vlsr),max(vlsr))
    plt.gca().invert_xaxis()
    plt.xlabel('RA offset (as)')
    plt.ylabel('Dec offset (as)')
    plt.show()


#*****************************************************************

#         Code main body

#*****************************************************************


#TODO There are four possible ways to flag:
    #1. Error.
    #2. Speed.
    #3. Detections.
    #4. Manual flagging.



parser = argparse.ArgumentParser()
parser.add_argument("-d", "--datadir", type=str, default='')
parser.add_argument("-fe", "--flagerror",  type=str, default="N")
parser.add_argument("-fd", "--flagdetections",  type=str, default="0")
parser.add_argument("-fs", "--flagspeed",  type=str, default="N")
parser.add_argument("-fm", "--flagmanual",  type=str, default="N")

args     = parser.parse_args()
data_dir = args.datadir
do_flagerror  = args.flagerror
do_flagdetections = args.flagdetections
do_flagspeed = args.flagspeed
do_flagmanual = args.flagmanual

pars = extract_metadata(data_dir)

proper_motions_file = data_dir + '/pm_results.txt'

ra,dec,mux,muy,dmux,dmuy,vlsr,detections = read_pm_results(proper_motions_file)

```

```
inds_mask = np.ones(mux.size, dtype=bool)
if do_flagerror != 'N':
    print(15*'*' + 3*' ' +'Error flagging' + 3*' ' + 15*'*')
    print_pm_info_angular(ra,dec,mux,muy,dmux,dmuy,vlsr,detections)
    #Plot die proper motions, met hul errors.
    plot_pm(ra,dec,mux,muy,vlsr) #TODO Figure out how to show the errors as well..
    #Vra as input vir 'n ratio wat  geflag moet word.
    flagerror_rat = float(input('What ratio of error to proper motion do you want to flag? (e.g. 0.1 for 10%)\nRatio: '))
    inds_error_flags = flag_error(mux,muy,dmux,dmuy,flagerror_rat)
    inds_mask[inds_error_flags] = False
    print('%d of %d proper motions identified for flagging due to error ratio.'%(len(mux) - sum(inds_mask),len(mux)))
    #Wys nuwe moontlikheid.
    plt.subplot(121)
    plt.quiver(ra,dec,-mux,muy,vlsr,cmap='jet')
    plt.clim(min(vlsr),max(vlsr))
    plt.gca().invert_xaxis()
    plt.xlabel('RA offset (as)')
    plt.ylabel('Dec offset (as)')
    plt.title('Without flags')
    plt.subplot(122)
    plt.quiver(ra[inds_mask],dec[inds_mask],-mux[inds_mask],muy[inds_mask],vlsr[inds_mask],cmap='jet')
    plt.clim(min(vlsr),max(vlsr))
    plt.gca().invert_xaxis()
    plt.xlabel('RA offset (as)')
    plt.ylabel('Dec offset (as)')
    plt.title('With current flags')
    plt.show()
    print("New proper motion list if these flags are applied")
    print_pm_info_angular(ra[inds_mask],dec[inds_mask],mux[inds_mask],muy[inds_mask],dmux[inds_mask],dmuy[inds_mask],vlsr[inds_mask],detections[inds_mask])
    print('Flags due to error ratio added to flag list')
    print('If you are unsatisfied with this ratio, please restart flagging_pm.py and specify a new ratio. In a new version, there will be a query if you want to restart. \nWe apologise for any inconvenience.')
if do_flagdetections != 'N':
    #Flag non-consequetive detections.
    print(15*'*' + 3*' ' +'Detection flagging' + 3*' ' + 15*'*')
    inds_detections_flags = flag_detections(detections)

    print('%d flags applied due to non-consequetive detections'%(len(inds_detections_flags)))
    inds_mask[inds_detections_flags] = False
    print('Flags due to non-consequetive detections added to main flag list')
    print('%d of %d proper motions identified for flagging in total.'%(len(mux) - sum(inds_mask),len(mux)))
if do_flagspeed != 'N':
    print(15*'*' + 3*' ' +'Speed flagging' + 3*' ' + 15*'*')
    #Vra of hul wil flag met 'n maximum angular proper motion, of met linear velocity.
    speed_type = input('Do you want to flag with maximum angular (in mas) or linear (in km/s) speed? (a/l) \n"a" or "l":')
    if speed_type != 'a' and speed_type !='l' :
        print('Please choose "a" for angular and "l" for linear')
        speed_type = input('Do you want to flag with maximum angular (in mas) or linear (in km/s) speed? (a/l)\n"a" or "l":')
    #As linear velocity, vra vir afstand na die source.
    if speed_type == 'l':
```

```
        source_dist = float(input('What is the distance to the source (in kpc)? \
    nDistance: '))
        #Histogram of linear speed.
        linear_magnitudes = np.sqrt(np.array(mux*4.74*source_dist)**2+ np.array(muy
    *4.74*source_dist)**2 + np.array(vlsr)**2)
        plt.hist(linear_magnitudes)
        plt.xlabel(r'3D $\vec{v}|$ (km/s)')
        plt.ylabel('Number of proper motions')
        plt.show()
        linear_max = float(input('Do you want to flag above any maximum proper motion
    ? (in km/s, 0 for none)\nMax proper motion:'))
        if linear_max != 0:
            inds_speed_flags = np.where(linear_magnitudes > linear_max)[0]
        else:
            inds_speed_flags = []
    if speed_type == 'a':
        #Histogram of angular speed.
        angular_magnitudes = np.sqrt(np.array(mux)**2 + np.array(muy)**2)
        plt.hist(angular_magnitudes)
        plt.xlabel(r'$|\vec{\mu}|$ (mas/yr)')
        plt.ylabel('Number of proper motions')
        plt.show()
        angular_max = float(input('Do you want to flag above any maximum proper
    motion? (in mas/yr, 0 for none)\nMax proper motion:'))
        if angular_max!=0:
            inds_speed_flags = np.where(angular_magnitudes > angular_max)[0]
        else:
            inds_speed_flags = []
    print('%d flags applied due to maximum speed.'%(len(inds_speed_flags)))
    inds_mask[inds_speed_flags] = False
    print('%d of %d proper motions identified for flagging in total.'%(len(mux) - sum
    (inds_mask),len(mux)))
    print_pm_info_angular(ra[inds_mask],dec[inds_mask],mux[inds_mask],muy[inds_mask],
    dmux[inds_mask],dmuy[inds_mask],vlsr[inds_mask],detections[inds_mask])
    #Wys nuwe proper motion plot en print die proper motions.
    plt.subplot(121)
    plt.quiver(ra,dec,-mux,muy,vlsr,cmap='jet')
    plt.clim(min(vlsr),max(vlsr))
    plt.gca().invert_xaxis()
    plt.xlabel('RA offset (as)')
    plt.ylabel('Dec offset (as)')
    plt.title('Without flags')
    plt.subplot(122)
    plt.quiver(ra[inds_mask],dec[inds_mask],-mux[inds_mask],muy[inds_mask],vlsr[
    inds_mask],cmap='jet')
    plt.clim(min(vlsr),max(vlsr))
    plt.gca().invert_xaxis()
    plt.xlabel('RA offset (as)')
    plt.ylabel('Dec offset (as)')
    plt.title('With current flags')
    plt.show()
    #Apply die flag.
if do_flagmanual!= 'N':
    print(15*'*' + 3*' ' +'Manual flagging' + 3*' ' + 15*'*')
        #Print proper motions.
    print_pm_info_angular(ra[inds_mask],dec[inds_mask],mux[inds_mask],muy[inds_mask],
    dmux[inds_mask],dmuy[inds_mask],vlsr[inds_mask],detections[inds_mask])
    #Plot die proper motions, met hul errors.
    plot_pm(ra[inds_mask],dec[inds_mask],mux[inds_mask],muy[inds_mask],vlsr[inds_mask
    ]) #TODO Figure out how to show the errors as well..
```

```
    #Vra vir ID's wat hul wil flag in 'n array.
    inds_manual_flags = input('Which proper motions do you want to flag manually?
    Give a list separated by commas, e.g. "0,1,5,15". "None" for none.\nManual flags:
    ')
    if inds_manual_flags == 'None':
        inds_manual_flags = []
    else:
        inds_manual_flags = list(np.array((inds_manual_flags.split(sep = ',')),dtype=
    int))
    print(inds_manual_flags)
    print('%d flags applied manually.'%(len(inds_manual_flags)))
    inds_mask[inds_manual_flags] = False
    print('%d of %d proper motions identified for flagging in total.'%(len(mux) - sum
    (inds_mask),len(mux)))

#Print dat die volgende flags apply was en dat die nuwe data file "NAAM HIER"
    gegenerate was.
print(15*'*' + 3*' ' + 'Summary' + 3*' ' + 15*'*')
print('%d flags applied due to error ratio.'%(len(inds_error_flags)))
print('%d flags applied due to non-consequetive detections'%(len(
    inds_detections_flags)))
print('%d flags applied due to maximum speed.'%(len(inds_speed_flags)))
print('%d flags applied manually.'%(len(inds_manual_flags)))
allflags = []
for i,ind in enumerate(inds_mask):
    if ind == False:
        allflags.append(i)
print('If you want to save the flags, copy the next line to a text file:\n'+str(
    allflags))

#Saves the proper motions.
vlsr = vlsr[inds_mask]
ra = ra[inds_mask]
dec= dec[inds_mask]
mux = mux[inds_mask]
dmux = dmux[inds_mask]
muy = muy[inds_mask]
dmuy = dmuy[inds_mask]
detections = detections[inds_mask]
with open(data_dir +"/pm_results_flagged.txt",'w+') as f:
    f.write("Index \t Vlsr \t RA \t DEC \t mux (mas) \t muxerr (mas) \t muy (mas) \t
    muyerr (mas) \t detections \n")
    for i in range(0,len(vlsr)):
        f.write("%d \t %0.5f \t %0.5f \t %0.5f \t %0.5f \t %0.5f \t %0.5f \t %0.5f \t
     %s\n"%(i,vlsr[i],ra[i],dec[i],mux[i],dmux[i],muy[i],dmuy[i],detections[i]))
f.close()
```

A.7.4 utils.py

This script is used by the other scripts shown above. It should be in the same directory as the codes above.

```
import numpy as np
import pandas as pd
def extract_from_df(df,cols):
    '''Utility function to get specified columns from a dataframe as a list object.
    Parameters :
    ------------
    df : Pandas DataFrame.
    Pandas dataframe to extract data.

```

```
    Returns :
    ---------
    allcols : 2D list containing all the specified dataframe columns.'''
    allcols = []
    for col in cols:
        allcols.append(df[col].values)
    ra = df['RA'].values
    dec = df['DEC'].values
    vlsr = df['VLSR'].values
    flux = df['FLUX'].values
    dflux = df['DFLUX'].values
    return ra,dec,vlsr,flux,dflux

def isolate(x,y,xlim,ylim):
    '''Gives indices for elements in x,y range.
    Parameters :
    ------------
    x : array-like
    x coordinates of element set.
    y : array-like
    y coordinates of element set.
    xlim : array-like of form :[xlimmin,xlimmax]
    specify maximum and minimum x values for elements to isolate.
    ylim : array-like of form :[ylimmin,ylimmax]
    specify maximum and minimum y values for elements to isolate.

    Returns :
    --------
    ind : array-like
    Array containing indices of isolated elements. Can then be easily called, e.g. x-
    coords : x[ind]'''
    if len(xlim) == 0 or len(ylim) ==0:
        return []
    else:
        ind = np.where(np.logical_and(np.logical_and(y>= ylim[0],y<=ylim[1]),np.
    logical_and(x <= xlim[1],x>=xlim[0])))
        return ind[0]

def get_ind(arr,val):
    '''Gives index for any specified value from a list. Does not only give the first
    index with that value.
    Parameters :
    ------------
    arr : array-like.
    1D list
    val : double
    value to search for.

    Returns :
    --------
    ind : array-like
    Array containing indices of specific value in array.'''
    ind = []
    for j in range(len(arr)):
        if arr[j]==val:
            ind.append(j)
    return ind

def zero_list(arr,val = 0):
```

```
66      '''Generates a list of the same shape as the input array, this is for use when
        the array in question does not have
67      a consistent shape so that it can be generated using numpy.
68      Parameters :
69      ------------
70      arr : array-like
71      2D list, where the lists in the second dimension are not of the same length.
72      val : double (optional)
73      value with which to initialize the array.'''
74      nrows = len(arr)
75      ncols = []
76      zero_arr = []
77      for i in range(0,nrows):
78          if isinstance(arr[i], int):
79              ncols.append(1)
80          else:
81              ncols.append(len(arr[i]))
82      for lencol in ncols:
83          zero_arr.append(lencol*[val])
84      return zero_arr
85
86  def err_min(dx,dy):
87      '''Calculates the resultant of two errors for plus or minus of any two errors dx,
        dy.'''
88      df = np.sqrt(dx**2 + dy**2)
89      return df
90
91  def read_data(data_dir,cols):
92      '''Reads maser position data from textfiles in a specified directory. Note that a
        folder Fileorder.txt should be in the directory,
93      containing the order in which the files should be read. Be sure to specify the
        entire file name in Fileorder.txt.
94      Parameters :
95      ------------
96      data_dir : string
97      Name of directory containing the maser position data and Fileorder.txt file.
98      cols : list of strings
99      Currently, cols should be set to ['RA','DEC','VLSR','FLUX','DFLUX']. As this
        function has not been generalized yet.'''
100     RA = []
101     DEC = []
102     VLSR = []
103     FLUX = []
104     DFLUX = []
105     data_files = []
106     with open(data_dir+'/Fileorder.txt') as f:
107         for line in f:
108             data_files.append(data_dir + '/'+line[:-1])
109
110     for name in data_files:
111         df = pd.read_csv(name,sep = ',')
112         ra,dec,vlsr,flux,dflux = extract_from_df(df,cols)
113         RA.append(ra)
114         DEC.append(dec)
115         VLSR.append(vlsr)
116         FLUX.append(flux)
117         DFLUX.append(dflux)
118     return RA,DEC,VLSR,FLUX,DFLUX
119 def parallax_corr(t,parr,parrerr,phi):
```

```
    '''Calculates parallax corrections. According to a cosine formula of correction =
     amp*cos(2*pi*t + phi)
    With
    Parameters :
    ------------
    t : float or array
    Time of observation
    parr : float
    Parallax amplitude
    parrerr : float
    Parallax amplitude error
    phi : float
    Phase offset to align the parallax peak.
    '''
    dx = parr*np.cos(2*np.pi*t+phi)
    dxerr = parrerr*np.cos(2*np.pi*t + phi)
    return dx,dxerr
```

A.8 Spectral Method Proper Motion Code

The code below was used to calculate the proper motions for the spectral method. The code below was used as-is to calculate the proper motions. Note that this code was still in development to generalize its applicability. Contact the author of this thesis at *JOBVORSTER8@GMAIL.COM* to inquire if there might be a more recent and user-friendly public release of the code.

A.8.1 IMProV_identify.py

```
from dash import Dash, dcc, html, callback_context, dash_table
import numpy as np
import pandas as pd
from dash.dependencies import Input, Output, State
import plotly.express as px
import scipy.optimize as optim
import plotly.graph_objs as go
from dash.exceptions import PreventUpdate
from matplotlib import cm
from matplotlib import pyplot as plt

import base64
import datetime
import io

external_stylesheets = ['https://codepen.io/chriddyp/pen/bWLwgP.css']
plotted = False
app = Dash(__name__, external_stylesheets=external_stylesheets)
dfcolumns = ['RA min','RA max','Dec min','Dec max','Peak','Peak err','Center','Center
     err','FWHM','FWHM err']
# make a sample data frame with 6 columns
df = []#pd.read_csv("Ep1_VERA_Shifted.txt", sep=',')
app.layout = html.Div([
    html.Div([html.H1(children='IMProV', style={'textAlign': 'center'}),
                dcc.Upload(
        id='upload-data',
        children=html.Div([
            'Drag and Drop or ',
            html.A('Select Files')
        ]),
```

```
30          style={
31              'width': '100%',
32              'height': '60px',
33              'lineHeight': '60px',
34              'borderWidth': '1px',
35              'borderStyle': 'dashed',
36              'borderRadius': '5px',
37              'textAlign': 'center',
38              'margin': '10px'
39          },
40          # Allow multiple files to be uploaded
41          multiple=True
42      ),
43          html.Div(id='output-data-upload'),
44          dcc.Store(id = 'main-data-store')]),
45      html.Div([
46
47          html.Div(
48              dcc.Graph(id='g1', config={'displayModeBar': True, 'scrollZoom': True},
    style={'height': '80vh'}),
49              className='four columns', style={"border": "2px black solid"}),
50              dcc.Store(id='g1-relayout-data'),
51          html.Div
52              ([
53              html.Div(
54                  dcc.Graph(id='g2', config={'displayModeBar': False}),
55                  className='row', style={"border": "2px black solid"}),
56              html.Div(
57                  [
58                      dcc.Checklist(
59                          id='Gauss_Fit_checkbox',
60                          options=[{'label': "Do Gaussian Fit", 'value': 'bool_Gaussian
    '}],
61                          value=[]
62                      ),
63                      dcc.Store(id='Gauss_Fit_checkbox_data'),
64                      html.Div
65                          ([
66                          html.Div
67                              ([
68                              html.Div(['RA min'], className='two columns'),
69                              html.Div(['RA max'], className='two columns'),
70                              html.Div(['Dec min'], className='two columns'),
71                              html.Div(['Dec max'], className='two columns'), html.Div
    (['Peak'], className='two columns')
72                          ], className='row'),
73                          html.Div
74                              ([
75                              html.Div([' '], id='cont_RA min', className='two columns'
    ),
76                              html.Div([' '], id='cont_RA max', className='two columns'
    ),
77                              html.Div([' '], id='cont_Dec min', className='two columns
    '),
78                              html.Div([' '], id='cont_Dec max', className='two columns
    '),
79                              html.Div([' '], id='cont_Peak', className='two columns')
80                          ], className='row'),
81                          html.Div
82                              ([
```

```
83                              html.Div(['Peak err'], className='two columns'),
84                              html.Div(['Center'], className='two columns'),
85                              html.Div(['Center err'], className='two columns'),
86                              html.Div(['FWHM'], className='two columns'), html.Div(['
    FWHM err'], className='two columns')
87                          ], className='row'),
88                          html.Div
89                              ([
90                              html.Div([' '], id='cont_Peak err', className='two
    columns'),
91                              html.Div([' '], id='cont_Center', className='two columns'
    ),
92                              html.Div([' '], id='cont_Center err', className='two
    columns'),
93                              html.Div([' '], id='cont_FWHM', className='two columns'),
94                              html.Div([' '], id='cont_FWHM err', className='two
    columns')
95                          ], className='row'),
96                      ], className='row', style={'height': '13vh'}),
97                      dcc.Store(id='Gauss_Fit_results_data'),
98                      html.Button("SAVE CURRENT GAUSS FIT", id='btn_curvefit', n_clicks
    =0),
99                  ], className='row', style={"border": "2px black solid", 'height': '
    31.2vh'})
100         ], className='four columns', style={"border": "2px black solid"}),
101         html.Div([
102             dash_table.DataTable(id="table_Gauss_pars",columns = [{"name": i,'id':i}
    for i in dfcolumns],export_format="csv"),
103             html.Div(id = 'test_div'),
104             dcc.Store(id='store_Gauss_Fit_all_results'),
105             dcc.Store(id = 'store_Table')
106         ], className='four columns', style={"border": "2px black solid", 'overflowY':
     'auto'})
107     ], className='row', style={"border": "2px black solid"})
108 ])
109
110 def parse_contents(contents, filename):
111     content_type, content_string = contents.split(',')
112     decoded = base64.b64decode(content_string)
113     df1 = 'Error'
114     try:
115         if 'csv' in filename:
116             # Assume that the user uploaded a CSV file
117             df1 = pd.read_csv(
118                 io.StringIO(decoded.decode('utf-8')))
119         elif 'xls' in filename:
120             # Assume that the user uploaded an excel file
121             df1 = pd.read_excel(io.BytesIO(decoded))
122     except Exception as e:
123         print(e)
124         return html.Div([
125             'There was an error processing this file.'
126         ])
127     return df1
128
129
130 def isolate(x, y, xlim, ylim):
131     '''Gives indices for elements in x,y range.
132     Parameters :
133     ------------
```

```
    x : array-like
    x coordinates of element set.
    y : array-like
    y coordinates of element set.
    xlim : array-like of form :[xlimmin,xlimmax]
    specify maximum and minimum x values for elements to isolate.
    ylim : array-like of form :[ylimmin,ylimmax]
    specify maximum and minimum y values for elements to isolate.

    Returns :
    --------
    ind : array-like
    Array containing indices of isolated elements. Can then be easily called, e.g. x-coords : x[ind]'''
    if len(xlim) == 0 or len(ylim) == 0:
        return []
    else:
        ind = np.where(
            np.logical_and(np.logical_and(y >= ylim[0], y <= ylim[1]), np.logical_and(x <= xlim[1], x >= xlim[0])))
        return ind[0]


def gauss(x, A, mu, sigma):
    return A * np.exp(-1 * (x - mu) ** 2 / (2 * sigma ** 2))


def get_figure(df, x_col, y_col, selectedpoints, selectedpoints_local,fitted_lims, relayout_data):
    # global plotted
    # if not plotted:
    if dict(df):
        fig = px.scatter(df, x=df[x_col], y=df[y_col],error_x = df['RAERR'].values, error_y=df['DECERR'].values, color_continuous_scale='Jet')
        if fitted_lims:
            for xlim,ylim in fitted_lims:
                fig.add_shape(type='rect',x0=xlim[0],x1=xlim[1],y0=ylim[0],y1=ylim[1],fillcolor='green',opacity=0.1)

        fig.update_coloraxes(autocolorscale=True, colorscale='Jet', showscale=True)
        fig.update_traces(selectedpoints=selectedpoints,
                          customdata=df.index,
                          mode='markers', marker={'color': df['VLSR'], 'size': 12},
                          unselected={'marker': {'opacity': 1}}, hovertemplate='x: %{x:.6f} - y: %{y:.6f}')
        # fig.update_yaxes(scaleanchor='x',scaleratio=1) #This options makes an equal aspect ratio.
        fig.update_layout(margin={'l': 20, 'r': 0, 'b': 15, 't': 5}, dragmode='select', colorscale_diverging='Jet')
        if relayout_data:
            if 'xaxis.range[0]' in relayout_data.keys():
                fig.update_xaxes(range=[relayout_data['xaxis.range[0]'], relayout_data['xaxis.range[1]']])
                fig.update_yaxes(range=[relayout_data['yaxis.range[0]'], relayout_data['yaxis.range[1]']])
        fig.update_shapes(dict(xref='x', yref='y'))
        # if all_inds:
        #     fig.add_trace(go.Scatter(x=df[x_col][all_inds],y=df[y_col][all_inds], mode='markers'))
        plotted = True
```

```
        return fig
    else:
        raise PreventUpdate


def get_figure2(df, x_col, y_col, selectedpoints, selectedpoints_local, do_Gaussian, all_inds, Gauss_pars=[]):
    if dict(df):
        fig = px.scatter(df, x=df['VLSR'][selectedpoints], y=df['FLUX'][selectedpoints],error_y = df['DFLUX'][selectedpoints])
        vlsr_ranges = [min(df['VLSR'].values[selectedpoints]), max(df['VLSR'].values[selectedpoints])]
        flux_ranges = [min(df['FLUX'][selectedpoints]), max(df['FLUX'][selectedpoints])]
        fig.update_traces(selectedpoints=selectedpoints,
                          customdata=df.index,
                          mode='markers', marker={'color': df['VLSR'], 'size': 12}, marker_colorscale='Jet',
                          marker_cmax=vlsr_ranges[1], marker_cmin=vlsr_ranges[0],
                          unselected={'marker': {'opacity': 1}, 'textfont': {'color': 'rgba(0, 0, 0, 0)'}})
        if do_Gaussian:
            popt = Gauss_pars[0]
            pcov = Gauss_pars[1]
            x = np.linspace(vlsr_ranges[0], vlsr_ranges[1], 10000)
            fig.add_trace(go.Scatter(x=x, y=gauss(x, *popt)))
        fig.update_xaxes(
            range=[vlsr_ranges[0] - 0.1 * np.diff(vlsr_ranges)[0], vlsr_ranges[1] + 0.1 * np.diff(vlsr_ranges)[0]])
        fig.update_yaxes(range=[0 - 0.07 * flux_ranges[1], flux_ranges[1] + 0.1 * flux_ranges[1]])

        fig.update_layout(margin={'l': 20, 'r': 0, 'b': 15, 't': 5}, dragmode=False,
                          hovermode=False,showlegend=False)
        return fig
    else:
        raise PreventUpdate


# this callback defines 3 figures
# as a function of the intersection of their 2 selections
@app.callback(
    [Output('g1', 'figure'),
     Output('g2', 'figure'),
     Output('Gauss_Fit_results_data', 'data')],
    Input('g1', 'selectedData'),
    Input('g2', 'selectedData'),
    Input('main-data-store','data'),
    Input("Gauss_Fit_checkbox", 'value'),
    State('g1-relayout-data','data'),
    State('store_Gauss_Fit_all_results','data')
)
def callback(selection1, selection2, df, bool_Gaussian, relayout_data ,already_fitted):
    if dict(df):
        df = pd.DataFrame.from_dict(df)
    if 'bool_Gaussian' in bool_Gaussian:
        do_Gaussian = True
        Gauss_pars = []
    else:
```

```
        do_Gaussian = False
        Gauss_pars = []
        points_range = []
    if dict(df):
        selectedpoints = df.index
    else:
        selectedpoints = []
    for selected_data in [selection1, selection2]:
        if selected_data and selected_data['points']:
            selectedpoints = np.intersect1d(selectedpoints,
                                            [p['customdata'] for p in selected_data['
    points']])
    fitted_lims = []
    all_inds = []

    if already_fitted:
        for i in range(len(already_fitted)):
            xlim = [already_fitted[i]['RA min'],already_fitted[i]['RA max']]
            ylim = [already_fitted[i]['Dec min'],already_fitted[i]['Dec max']]
            fitted_lims.append([xlim,ylim])

        for lim in fitted_lims:
            inds = isolate(df['RA'].values,df['DEC'].values,lim[0],lim[1])
            all_inds.extend(inds)
    points_range = []
    if do_Gaussian :
        fluxes = np.array(df['FLUX'][selectedpoints])
        vlsrs = np.array(df['VLSR'][selectedpoints])
        dfluxes = np.array(df['DFLUX'][selectedpoints])
        p0 = [max(fluxes), vlsrs[np.argmax(fluxes)], 1]
        Gauss_pars = optim.curve_fit(gauss, xdata=vlsrs, ydata=fluxes,absolute_sigma=
    True,sigma=dfluxes,
                                     p0=p0)  # I still have to add the calculation
    with the errors.
        points_range = selection1['range']

    return [get_figure(df, "RA", "DEC", selectedpoints, selection1,fitted_lims,
    relayout_data),
            get_figure2(df, "VLSR", "FLUX", selectedpoints, selection2, do_Gaussian,
    all_inds, Gauss_pars),
            [points_range, Gauss_pars]
            ]


@app.callback(
    [Output('cont_RA min', 'children'),
     Output('cont_RA max', 'children'),
     Output('cont_Dec min', 'children'),
     Output('cont_Dec max', 'children'),
     Output('cont_Peak', 'children'),
     Output('cont_Peak err', 'children'),
     Output('cont_Center', 'children'),
     Output('cont_Center err', 'children'),
     Output('cont_FWHM', 'children'),
     Output('cont_FWHM err', 'children')],
    [Input("Gauss_Fit_checkbox", 'value'),
     Input('Gauss_Fit_results_data', 'data')]
)
def show_Gaussian_results(value, data):
    if "bool_Gaussian" in value:
```

```
289         if len(data) == 0:
290             return ['a\t'] * 10
291         else:
292             lims = data[0]
293             xlims = list(np.around(np.array(lims['x'], dtype=float), decimals=6))
294             ylims = list(np.around(np.array(lims['y'], dtype=float), decimals=6))
295             gauss_pars = data[1]
296             popt = list(np.around(gauss_pars[0], decimals=6))
297             pcov = list(np.around(np.sqrt(np.diag(gauss_pars[1])), decimals=6))
298             Peaks = [popt[0], pcov[0]]
299             Centers = [popt[1], pcov[1]]
300             FWHMs = list(np.around(np.array([popt[2] * 2 * np.sqrt(2 * np.log(2)),
    pcov[2] * 2 * np.sqrt(2 * np.log(2))]),decimals=6))
301             return_list = []
302             for lists in [xlims, ylims, Peaks, Centers, FWHMs]:
303                 return_list.extend(lists)
304             return return_list
305     else:
306         return ['0.000000 \n'] * 10
307
308
309 #Callback to store the gauss fit parameters into a store dataframe.
310 @app.callback(
311     Output('store_Gauss_Fit_all_results','data'),
312     Output("Gauss_Fit_checkbox", 'value'),
313     Input('btn_curvefit','n_clicks'),
314     State('store_Gauss_Fit_all_results','data'),
315     State('Gauss_Fit_results_data', 'data'),
316     State("Gauss_Fit_checkbox", 'value')
317              )
318 def store_all_gauss_fits(n_clicks,data_all,data_now,value):
319     changed_id = [p['prop_id'] for p in callback_context.triggered][0]
320     if changed_id=='btn_curvefit.n_clicks':
321         if "bool_Gaussian" in value:
322             if not data_all:
323                 data_all = pd.DataFrame(columns = ['RA min','RA max','Dec min','Dec
    max','Peak','Peak err','Center','Center err','FWHM','FWHM err'])
324             else:
325                 data_all = pd.DataFrame.from_dict(data_all)
326             app_dict = pd.DataFrame(columns=data_all.columns)
327             lims = data_now[0]
328             xlims = list(np.around(np.array(lims['x'], dtype=float), decimals=6))
329             ylims = list(np.around(np.array(lims['y'], dtype=float), decimals=6))
330             gauss_pars = data_now[1]
331             popt = list(np.around(gauss_pars[0], decimals=6))
332             pcov = list(np.around(np.sqrt(np.diag(gauss_pars[1])), decimals=6))
333             Peaks = [popt[0], pcov[0]]
334             Centers = [popt[1], pcov[1]]
335             FWHMs = list(
336                 np.around(np.array([popt[2] * 2 * np.sqrt(2 * np.log(2)), pcov[2] * 2
    * np.sqrt(2 * np.log(2))]),
337                           decimals=6))
338             return_list = []
339             for lists in [xlims, ylims, Peaks, Centers, FWHMs]:
340                 return_list.extend(lists)
341             for i,column in enumerate(data_all.columns):
342                 app_dict[column] = [return_list[i]]
343
344             data_all1 = pd.concat([data_all,app_dict])
345             return [data_all1.to_dict('records'),[]]
```

```
        else:
            raise PreventUpdate
    else:
        raise PreventUpdate

# @app.callback(
#     [Output('table_Gauss_pars','data'),
#      Output('table_Gauss_pars','columns')],
#     Input('store_Table','data')
# )
# def show_pars_data(data):
#     return [data,['1']]
# @app.callback(
#         [Output('store_Gauss_Fit_all_results','data')],
#         [Input('store_Table','data')]
#             )
# def move_data(data):
#     changed_id = [p['prop_id'] for p in callback_context.triggered][0]
#     if "store_Table.data" in changed_id:
#         return [data]
#     else:
#     else:
#         raise PreventUpdate


@app.callback(
        Output('table_Gauss_pars','data'),
        Input('store_Gauss_Fit_all_results','data')
            )
def update_table(data):
        return data

@app.callback(Output('output-data-upload', 'children'),
              Output('main-data-store','data'),
              Input('upload-data', 'contents'),
              State('upload-data', 'filename'))
def update_output(list_of_contents, list_of_names):
    global df
    if list_of_contents is not None:
        df = parse_contents(list_of_contents[0],list_of_names[0])
        return ['Successfully uploaded the file: '+str(list_of_names[0]),dict(df)]
    else:
        return ['Please upload a file.',[]]

@app.callback(
        Output('g1-relayout-data','data'),
        Input('g1','relayoutData')
            )
def update_relayoutdata(relayoutdata):
    if relayoutdata:
        if "xaxis.range[0]" in relayoutdata.keys():
            return relayoutdata
        else:
            raise PreventUpdate
    else:
        raise PreventUpdate


if __name__ == '__main__':
    app.run_server(debug=True)
```

A.8.2 IMProV_proper_motions.py

```
from dash import Dash, dcc, html, callback_context, dash_table
import numpy as np
import pandas as pd
from dash.dependencies import Input, Output, State
import plotly.express as px
import scipy.optimize as optim
import plotly.figure_factory as ff
import plotly.graph_objs as go
from dash.exceptions import PreventUpdate
from matplotlib import cm
from matplotlib import pyplot as plt
import matplotlib
import base64
import datetime
import io

external_stylesheets = ['https://codepen.io/chriddyp/pen/bWLwgP.css']
plotted = False
app = Dash(__name__, external_stylesheets=external_stylesheets)
df = []
cols = ['ID','L value','Epochs','RA','RAerr','Dec','Decerr','mu_alpha','dmu_alpha','
    mu_delta','dmu_delta','VLSR','EpID']
all_dates = []
#Epdate_float: G9.62 [2011+330/365.25,2012+256/365.25,2013+263/365.25] Source_dec:
    -20-31/60.-35/3600
#Epdate_float: NGC6334I  [2014.717808219178, 2014.9013698630138, 2015.0849315068492,
    2015.2849315068493, 2015.8821917808218, 2016.109589041096, 2016.194520547945]
epdate_float = [2008 + 327./365., 2009 + 32./365., 2009 + 138./365, 2009 + 138./365.,
     2009 + 240./365.,
                2009 + 258./365., 2009 + 270./365., 2009 + 297./365., 2009 +
    347./365., 2010 + 41./365., 2010 + 94./365., 2010 + 233./365. ]
#NGC6334I source_Dec= -35.78375
source_Dec = 17 + 59/60 + 22.95890/3600
def straight_line(x,a,b):
    return a*x+b
def calc_mu(x,dx,t):
    m = (x[1]-x[0])/(t[1]-t[0])
    p0 = np.array([m,x[0]+m*t[0]],dtype='float64')
    sigma = np.array(dx,dtype='float64')/np.array(x,dtype='float64')
    popt,pcov = optim.curve_fit(straight_line,xdata=t,ydata=x,sigma=sigma,p0=p0)
    return popt[0],np.sqrt(np.diag(pcov))[0]


def parse_contents(contents, filename):
    content_type, content_string = contents.split(',')
    decoded = base64.b64decode(content_string)
    df1 = 'Error'
    try:
        if 'csv' in filename:
            # Assume that the user uploaded a CSV file
            df1 = pd.read_csv(
                io.StringIO(decoded.decode('utf-8')))
        elif 'xls' in filename:
            # Assume that the user uploaded an excel file
            df1 = pd.read_excel(io.BytesIO(decoded))
    except Exception as e:
        print(e)
        return html.Div([
```

```
            'There was an error processing this file.'
        ])
    return df1

def calculate_likeness(df,inds,a=1,b=3,c=2):
    peaks = df['Peak'].values[inds]
    epochs = df['Epoch'].values[inds]
    fwhms = df['FWHM'].values[inds]
    vlsrs = df['VLSR'].values[inds]
    L = 0
    if epochs.any() and len(epochs) > 1:
        for i in range(len(epochs)):
            for j in range(i+1,len(epochs)):
                L += a*abs(np.log10(peaks[i])-np.log10(peaks[j])) + b*abs(vlsrs[i]-vlsrs[j]) + c*abs(fwhms[i]-fwhms[j])
                # L+= a*abs(np.log10(peaks[i])/np.log10(peaks[j])) + b*abs(2*(vlsrs[i]-vlsrs[j])/(vlsrs[i]+vlsrs[j]))+c*abs(fwhms[i]/fwhms[j])
        L = L/((a+b+c)*sum(np.arange(1,len(epochs))))
        return L
    else:
        return 'N/A'


app.layout = html.Div([
html.Div([html.H1(children='IMProV', style={'textAlign': 'center'}),
              dcc.Upload(
        id='upload-data',
        children=html.Div([
            'Drag and Drop or ',
            html.A('Select Files')
        ]),
        style={
            'width': '100%',
            'height': '60px',
            'lineHeight': '60px',
            'borderWidth': '1px',
            'borderStyle': 'dashed',
            'borderRadius': '5px',
            'textAlign': 'center',
            'margin': '10px'
        },
        # Allow multiple files to be uploaded
        multiple=True
    ),
        html.Div(id='output-data-upload'),
        dcc.Store(id = 'main-data-store')
          ]),
        html.Div([
        html.Div(
            dcc.Graph(id='g1', config={'displayModeBar': True, 'scrollZoom': True}, style={'height': '80vh'}),
            className='five columns', style={"border": "2px black solid"}),
            dcc.Store(id='g1-selection-data'),
        html.Div(
            dash_table.DataTable(id="table_Gauss_pars",columns = [{"name": i,'id':i} for i in cols],
                                 style_table={'overflowX': 'scroll'},export_format="csv"),
                 className= 'four columns', style={"border": "2px black solid"}),
            dcc.Store(id='all_feature_info'),
```

```
            dcc.Store(id='proper_motions'),
        html.Div([
                html.Div([
                        html.Button("SAVE FEATURES", id='btn_features', n_clicks=0),
                ],className='rows'),
                html.Div([
                    html.Button("CALCULATE PROPER MOTIONS", id='btn_proper_motions',
    n_clicks=0)
                ],className='rows'),

                html.Div([dcc.Markdown(r"The likeness parameter $L$ is calculated by:
    " + "\n"
                    r'$L_{ij} = a|log_{10}A_i-log_{10}A_j| + b|\mu_i-\mu_j| + '+
                    r'c |FWHM_i-FWHM_j|$' + '\n \n' +
                    r'with $L = \frac{1}{(a+b+c)\Sigma_n^N (n-1)}\Sigma_i^N\Sigma_{j>
    i}^N L_{ij}$,' + '\n' +
                    r'$a = 1, b = 1, c = 1$',mathjax=True,
                                        style={"white-space": "pre","overflow-x": "
    scroll"})],className='rows'),
                html.Div([
                    dcc.Markdown('L = ',style={"white-space": "pre","overflow-x": "
    scroll"}, mathjax=True),
                    html.Div(children='',id = 'Likeness Parameter')
                ],className='rows'),
                html.Div(id = 'Feature_output',children='')
        ],className='three columns', style={"border": "2px black solid"})


])
])
@app.callback(
    Output('g1-selection-data','data'),
    Output('Likeness Parameter','children'),
    Input('g1','selectedData')
)
def save_selection(selection):
    inds = []
    if selection:
        for i in range(len(selection['points'])):
            inds.append(selection['points'][i]['pointIndex'])
        if inds:
            if type(calculate_likeness(df,inds))== float:
                l_string = str(round(calculate_likeness(df,inds),7))
            else:
                l_string = calculate_likeness(df,inds)
            return [inds,l_string]
    else:
        raise PreventUpdate


@app.callback(
    Output('g1','figure'),
    Input('main-data-store','data'),
    Input('proper_motions','data'),
    State('all_feature_info','data')
              )
def show_figure(data,proper_motions,feature_data):

    if data:
```

```
164         print(feature_data)
165         dfdata = pd.DataFrame.from_dict(data)
166         fig = px.scatter(dfdata, x="RA", y='DEC', color='Epoch', hover_data={
167             'Epoch': True,
168             'RA': False,
169             'DEC': False,
170             'DRA': False,
171             'DDEC': False,
172             'VLSR': True,
173             'Peak': True,
174             'Peak err': False,
175             'Center': False,
176             'Center err': False,
177             'FWHM': True,
178             'FWHM err': False
179         })
180         dot_opacity = np.ones(len(dfdata['RA']))
181         if feature_data:
182             for i in range(len(feature_data)):
183                 inds = feature_data[i][0]
184                 dot_opacity[inds] = 0
185         fig.update_traces(marker=dict(opacity=dot_opacity))
186         fig.update_layout(clickmode='event+select')
187         if proper_motions:
188             ra = np.array(proper_motions['RA'],dtype='float')
189             dec = np.array(proper_motions['Dec'],dtype='float')
190             mu_ra = np.array(proper_motions['mu_alpha'],dtype='float')
191             mu_dec= np.array(proper_motions['mu_delta'],dtype='float')
192             fig2 = ff.create_quiver(x = ra,y = dec,u = mu_ra,v= mu_dec,scale = 100)
193             fig.add_traces(data=fig2.data)
194 
195         return fig
196     else:
197         raise PreventUpdate
198 @app.callback(Output('output-data-upload', 'children'),
199               Output('main-data-store','data'),
200               Input('upload-data', 'contents'),
201               State('upload-data', 'filename'))
202 def update_output(list_of_contents, list_of_names):
203     global df
204     global all_dates
205     dfcolumns = ['Epoch','RA', 'DEC', 'DRA', 'DDEC', 'VLSR', 'Peak', 'Peak err', '
    Center', 'Center err', 'FWHM', 'FWHM err']
206     df = pd.DataFrame(columns= dfcolumns)
207     all_dates = []
208     if list_of_contents is not None:
209         tuples = zip(*sorted(zip(list_of_names,list_of_contents)))
210         list_of_names,list_of_contents = [list(tuple1) for tuple1 in tuples]
211         for i,(content,name) in enumerate(zip(list_of_contents,list_of_names)):
212             df1 = parse_contents(content , name)
213             ind1 = name.find('EP')
214             all_dates.append(epdate_float[int(name[ind1+2])-1])
215             df1['Epoch'] = np.array(np.zeros(len(df1['RA']))+i+1,dtype='int')
216             df = pd.concat([df,df1])
217         return ['Successfully uploaded the files: '+str(list_of_names),dict(df)]
218     else:
219         return ['Please upload a file.',[]]
220 
221 @app.callback(
222         Output("Feature_output","children"),
```

```
        Output('all_feature_info','data'),
        Input('btn_features','n_clicks'),
        State('g1-selection-data','data'),
        State('Likeness Parameter','children'),
        State('all_feature_info','data')
             )
def save_feature(n_clicks,data,likenes_par,feature_data):
    changed_id = [p['prop_id'] for p in callback_context.triggered][0]
    if changed_id == 'btn_features.n_clicks':
        all_epochs = df['Epoch'].values[data]
        all_epochs_set = set(all_epochs)
        if len(all_epochs_set) != len(all_epochs):
            return ['Please choose only one datapoint per epoch. Data not saved.',
    feature_data]
        else:
            if feature_data:
                fets = feature_data
                fets.append([data,likenes_par])
            else:
                fets =[[data, likenes_par]]
            return ['Data points saved. ',fets]
    else:
        raise PreventUpdate


# @app.callback(
#     Output('')
# )


@app.callback(
    Output('table_Gauss_pars','data'),
    Output('proper_motions','data'),
    Input('all_feature_info','data')
)
def update_table(data):
    if data:
        l_pars = []
        epochs = []
        ids = list(range(1, len(data) + 1))
        ra = []
        raerr = []
        dec = []
        decerr = []
        vlsr = []
        mu_alpha = []
        dmu_alpha = []
        mu_delta = []
        dmu_delta = []
        ep_id = []
        for i in range(len(data)):
            l_pars.append(round(data[i][1],5))
            inds = data[i][0]
            t = np.array(all_dates)[list(df['Epoch'].values[inds]-1)]
            ep_id.append(str(list(df.index.values[inds])))
            ra.append(str(round(df['RA'].values[inds][np.argmin(df['Epoch'].values[
    inds])],5)))
            raerr.append(str(round(df['DRA'].values[inds][np.argmin(df['Epoch'].
    values[inds])], 5)))
            dec.append(str(round(df['DEC'].values[inds][np.argmin(df['Epoch'].values[
```

```
    inds])], 5)))
280             decerr.append(str(round(df['DDEC'].values[inds][np.argmin(df['Epoch'].
    values[inds])], 5)))
281             epochs.append(str(df['Epoch'].values[inds]))
282             vlsr.append(str(round(np.mean(df['VLSR'].values[inds]),5)))
283             mu,dmu = calc_mu(df['RA'].values[inds],df['DRA'].values[inds],t)
284             mu_alpha.append(str(round(mu*np.cos(np.deg2rad(source_Dec)),5)))
285             dmu_alpha.append(str(round(dmu*np.cos(np.deg2rad(source_Dec)),5)))
286             mu,dmu = calc_mu(df['DEC'].values[inds],df['DDEC'].values[inds],t)
287             mu_delta.append(str(round(mu,5)))
288             dmu_delta.append(str(round(dmu,5)))
289
290         df_dict = pd.DataFrame.from_dict(
291             {'ID': ids,"L value":l_pars, 'Epochs': epochs,"RA":ra,"RAerr":raerr,'Dec'
    :dec,'Decerr':decerr,
292              'mu_alpha':mu_alpha,'dmu_alpha':dmu_alpha,'mu_delta':mu_delta,'dmu_delta
    ':dmu_delta,'VLSR':vlsr,'EpID':ep_id})
293         return [df_dict.to_dict('records'),dict(df_dict)]
294     else:
295         raise PreventUpdate
296 if __name__ == '__main__':
297     app.run_server(debug=True)
```

Bibliography

André, P., Revéret, V., Könyves, V., Arzoumanian, D., Tigé, J., Gallais, P., Roussel, H., Le Pennec, J., Rodriguez, L., Doumayrou, E., Dubreuil, D., Lortholary, M., Martignac, J., Talvard, M., Delisle, C., Visticot, F., Dumaye, L., De Breuck, C., Shimajiri, Y., Motte, F., Bontemps, S., Hennemann, M., Zavagno, A., Russeil, D., Schneider, N., Palmeirim, P., Peretto, N., Hill, T., Minier, V., Roy, A., and Rygl, K. L. J. (2016). Characterizing filaments in regions of high-mass star formation: High-resolution submilimeter imaging of the massive star-forming complex NGC 6334 with ArTéMiS. *Astronomy and Astrophysics*, 592:A54. 25

Arce, H. G. and Sargent, A. I. (2006). The evolution of outflow-envelope interactions in low-mass protostars. *Astrophysical Journal*, 646(2):1070–1085. 16

Arzoumanian, D., Furuya, R. S., Hasegawa, T., Tahani, M., Sadavoy, S., Hull, C. L. H., Johnstone, D., Koch, P. M., Inutsuka, S., Doi, Y., Hoang, T., Onaka, T., Iwasaki, K., Shimajiri, Y., Inoue, T., Peretto, N., André, P., Bastien, P., Berry, D., Chen, H. R. V., Di Francesco, J., Eswaraiah, C., Fanciullo, L., Fissel, L. M., Hwang, J., Kang, J. h., Kim, G., Kim, K. T., Kirchschlager, F., Kwon, W., Lee, C. W., Liu, H. L., Lyo, A. R., Pattle, K., Soam, A., Tang, X., Whitworth, A., Ching, T. C., Coudé, S., Wang, J. W., Ward-Thompson, D., Lai, S. P., Qiu, K., Bourke, T. L., Byun, D. Y., Chen, M., Chen, Z., Chen, W. P., Cho, J., Choi, Y., Choi, M., Chrysostomou, A., Chung, E. J., Dai, S., Diep, P. N., Duan, H. Y., Duan, Y., Eden, D., Fiege, J., Franzmann, E., Friberg, P., Fuller, G., Gledhill, T., Graves, S., Greaves, J., Griffin, M., Gu, Q., Han, I., Hatchell, J., Hayashi, S., Houde, M., Jeong, I. G., Kang, M., Kang, S. j., Kataoka, A., Kawabata, K., Kemper, F., Kim, M. R., Kim, K. H., Kim, J., Kim, S., Kirk, J., Kobayashi, M. I. N., Könyves, V., Kusune, T., Kwon, J., Lacaille, K., Law, C. Y., Lee, C. F., Lee, Y. H., Lee, S. S., Lee, H., Lee, J. E., Li, H. b., Li, D., Li, D. L., Liu, J., Liu, T., Liu, S. Y., Lu, X., Mairs, S., Matsumura, M., Matthews, B., Moriarty-Schieven, G., Nagata, T., Nakamura, F., Nakanishi, H., Ngoc, N. B., Ohashi, N., Park, G., Parsons, H., Pyo, T. S., Qian, L., Rao, R., Rawlings, J., Rawlings, M., Retter, B., Richer, J., Rigby, A., Saito, H., Savini, G., Scaife, A., Seta, M., Shinnaga, H., Tamura, M., Tang, Y. W., Tomisaka, K., Tram, L. N., Tsukamoto, Y., Viti, S., Wang, H., Xie, J., Yen, H. W., Yoo, H., Yuan, J., Yun, H. S., Zenko, T., Zhang, G., Zhang, C. P., Zhang, Y., Zhou, J., Zhu, L., de Looze, I., Dowell, C. D., Eyres, S., Falle, S., Friesen, R., Robitaille, J. F., and van Loo, S. (2021). Dust polarized emission observations of NGC 6334. BISTRO reveals the details of the complex but organized magnetic field structure of the high-mass star-forming hub-filament network. *Astronomy and Astrophysics*, 647:A78. 25

Audard, M., Ábrahám, P., Dunham, M. M., Green, J. D., Grosso, N., Hamaguchi, K., Kastner, J. H., Kóspál, Á., Lodato, G., Romanova, M. M., Skinner, S. L., Vorobyov, E. I., and Zhu, Z. (2014). Episodic accretion in young stars. In Beuther, H., Klessen, R. S., Dullemond, C. P., and Henning, T., editors, *Protostars and Planets VI*, page 387. 2, 16, 17, 18, 20

Bate, M. R., Bonnell, I. A., Clarke, C. J., Lubow, S. H., Ogilvie, G. I., Pringle, J. E., and Tout, C. A. (2000). Observational implications of precessing protostellar discs and jets. , 317(4):773–781. 74

Batrla, W., Matthews, H. E., Menten, K. M., and Walmsley, C. M. (1987). Detection of strong methanol masers towards galactic H II regions. *Nature*, 326(6108):49–51. 8

Benson, P. J. and Myers, P. C. (1989). A survey for dense cores in dark clouds. *Astrophysical Journals*, 71:89. 13

Blitz, L. (1993). Giant molecular clouds. In Levy, E. H. and Lunine, J. I., editors, *Protostars and Planets III*, page 125. 13

Bloemhof, E. E. (1993). Diagonalization of the velocity variance/covariance matrix as a diagnostic of maser proper motions. *Astrophysical Journal, Letters*, 406:L75. 4

Bonnell, I. and Bastien, P. (1992). A binary origin for FU Orionis stars. *Astrophysical Journal, Letters*, 401:L31. 18

Bonnell, I. A. and Bate, M. R. (2006). Star formation through gravitational collapse and competitive accretion. *Monthly Notices of the Royal Astronomical Society*, 370(1):488–494. 13

Bonnell, I. A., Bate, M. R., Clarke, C. J., and Pringle, J. E. (2001). Competitive accretion in embedded stellar clusters. *Monthly Notices of the Royal Astronomical Society*, 323(4):785–794. 13

Bonnor, W. B. (1956). Boyle's Law and gravitational instability. *Monthly Notices of the Royal Astronomical Society*, 116:351. 13

Bontemps, S., Andre, P., Terebey, S., and Cabrit, S. (1996). Evolution of outflow activity around low-mass embedded young stellar objects. *Astronomy and Astrophysics*, 311:858–872. 75

Breen, S. L., Ellingsen, S. P., Contreras, Y., Green, J. A., Caswell, J. L., Stevens, J. B., Dawson, J. R., and Voronkov, M. A. (2013). Confirmation of the exclusive association between 6.7-GHz methanol masers and high-mass star formation regions. *Monthly Notices of the Royal Astronomical Society*, 435(1):524–530. 9

Breen, S. L., Sobolev, A. M., Kaczmarek, J. F., Ellingsen, S. P., McCarthy, T. P., and Voronkov, M. A. (2019). Discovery of six new Class II methanol maser transitions, including the unambiguous detection of three torsionally excited lines toward G358.931-0.030. *Astrophysical Journal, Letters*, 876(2):L25. 21

Briggs, D. S. (1995). High fidelity interferometric imaging: Robust weighting and NNLS deconvolution. In *American Astronomical Society Meeting Abstracts*, volume 187 of *American Astronomical Society Meeting Abstracts*, page 112.02. 36

Brogan, C. L., Hunter, T. R., Cyganowski, C. J., Chandler, C. J., Friesen, R., and Indebetouw, R. (2016). The massive protostellar cluster NGC 6334I at 220 au resolution: Discovery of further multiplicity, diversity, and a hot multi-core. *Astrophysical Journal*, 832(2):187. 2, 3, 25, 26, 40, 44, 45, 46, 47, 48, 67, 68, 74, 77, 79

Brogan, C. L., Hunter, T. R., Cyganowski, C. J., Chibueze, J. O., Friesen, R. K., Hirota, T., MacLeod, G. C., McGuire, B. A., and Sobolev, A. M. (2018). The extraordinary outburst in the massive protostellar system NGC 6334I-MM1: Flaring of the water masers in a north-south bipolar outflow driven by MM1B. *Astrophysical Journal*, 866(2):87. 2, 26, 37, 46, 47, 48, 51, 58, 59, 62, 67, 68, 70, 72, 73, 74, 77, 81, 82

Brogan, C. L., Hunter, T. R., Towner, A. P. M., McGuire, B. A., MacLeod, G. C., Gurwell, M. A., Cyganowski, C. J., Brand, J., Burns, R. A., Caratti o Garatti, A., Chen, X., Chibueze, J. O., Hirano, N., Hirota, T., Kim, K. T., Kramer, B. H., Linz, H., Menten, K. M., Remijan, A., Sanna, A., Sobolev, A. M., Sridharan, T. K., Stecklum, B., Sugiyama, K., Surcis, G., Van der Walt, J., Volvach, A. E., and Volvach, L. N. (2019). Sub-arcsecond (sub)millimeter imaging of the massive protocluster G358.93-0.03: Discovery of 14 new methanol maser lines associated with a hot core. *Astrophysical Journal, Letters*, 881(2):L39. 21

Bromm, V., Coppi, P. S., and Larson, R. B. (2002). The formation of the first stars. I. The primordial star-forming cloud. *Astrophysical Journal*, 564(1):23–51. 1

Brunthaler, A., Menten, K. M., Dzib, S. A., Cotton, W. D., Wyrowski, F., Dokara, R., Gong, Y., Medina, S. N. X., Müller, P., Nguyen, H., Ortiz-León, G. N., Reich, W., Rugel, M. R., Urquhart, J. S., Winkel, B., Yang, A. Y., Beuther, H., Billington, S., Carrasco-Gonzalez, C., Csengeri, T., Murugeshan, C., Pandian, J. D., and Roy, N. (2021). A global view on star formation: The GLOSTAR Galactic plane survey. I. Overview and first results for the Galactic longitude range 28° ¡ l ¡ 36°. *Astronomy and Astrophysics*, 651:A85. 1

Burke, B. F. and Graham-Smith, F. (2014). *An introduction to radio astronomy*. 28, 29, 30, 31, 32, 33

Burns, R. A., Handa, T., Nagayama, T., Sunada, K., and Omodaka, T. (2016). H_2O masers in a jet-driven bow shock: episodic ejection from a massive young stellar object. *Monthly Notices of the Royal Astronomical Society*, 460(1):283–290. 8, 19, 20, 54, 58, 75, 77

Burns, R. A., Imai, H., Handa, T., Omodaka, T., Nakagawa, A., Nagayama, T., and Ueno, Y. (2015). A 'water spout' maser jet in S235AB-MIR. *Monthly Notices of the Royal Astronomical Society*, 453(3):3163–3173. 4, 54, 56, 76

Burns, R. A., Kobak, A., Garatti, A. C. o., Tolmachev, A., Volvach, A., Alakoz, A., Wootten, A., Bisyarina, A., Dzodzomenyo, A., Sobolev, A., Bartkiewicz, A., Aberfelds, A., Stecklum, B., Kramer, B., Macdonald, C., Cyganowski, C., Paco, C., Garcia Miro, C., Brogan, C. L., Li, D., Smits, D., Engels, D., Ladeyschikov, D., Johnstone, D., Popova, E., Proven-Adzri, E., van den Heever, F., Orosz, G., Surcis, G., Wu, G., MacLeod, G., Linz, H., Imai, H., Van Langevelde, H., Valtts, I., Shmeld, I., Chibueze, J. O., Brand, J., Kumar, J., Green, J., Vorster, J., Eislöffel, J., Kim, J., Sugiyama, K., Menten, K. M., Immer, K., Sunada, K., Kim, K. T., Volvach, L., Moscadelli, L., Jordan, L., Uscanga, L., Gray, M. D., Szymczak, M., Olech, M., Hoare, M., Durjasz, M., Uchiyama, M., Shakhvorostova, N., Bayandina, O., Wolak, P., Gulyaev, S., Khaibrakhmanov, S., Breen, S., Goedhart, S., Casu, S., Ellingsen, S. P., Kurtz, S., Weston, S., Yoshihiro, T., Natusch, T., Hunter, T., Hirota, T., Baan, W., Vlemmings, W. H. T., Chen, X., Gong, Y., Yonekura, Y., Szabó, Z. M., Abraham, Z., and Monitoring Organization (M2O), M. (2022). Recent updates on the Maser Monitoring Organisation. In *European VLBI Network mini-symposium and users' meeting 2021*, page 19. 2, 9, 19

Burns, R. A., Sugiyama, K., Hirota, T., Kim, K.-T., Sobolev, A. M., Stecklum, B., MacLeod, G. C., Yonekura, Y., Olech, M., Orosz, G., Ellingsen, S. P., Hyland, L., Caratti o Garatti, A., Brogan, C., Hunter, T. R., Phillips, C., van den Heever, S. P., Eislöffel, J., Linz, H., Surcis, G., Chibueze, J. O., Baan, W., and Kramer, B. (2020). A heatwave of accretion energy traced by masers in the G358-MM1 high-mass protostar. *Nature Astronomy*, 4:506–510. 2, 21, 74

Caratti o Garatti, A., Stecklum, B., Garcia Lopez, R., Eislöffel, J., Ray, T. P., Sanna, A., Cesaroni, R., Walmsley, C. M., Oudmaijer, R. D., de Wit, W. J., Moscadelli, L., Greiner, J., Krabbe, A., Fischer,

C., Klein, R., and Ibañez, J. M. (2017). Disk-mediated accretion burst in a high-mass young stellar object. *Nature Physics*, 13(3):276–279. 2, 16, 19, 20, 77

Caswell, J. L., Fuller, G. A., Green, J. A., Avison, A., Breen, S. L., Brooks, K. J., Burton, M. G., Chrysostomou, A., Cox, J., Diamond, P. J., Ellingsen, S. P., Gray, M. D., Hoare, M. G., Masheder, M. R. W., McClure-Griffiths, N. M., Pestalozzi, M. R., Phillips, C. J., Quinn, L., Thompson, M. A., Voronkov, M. A., Walsh, A. J., Ward-Thompson, D., Wong-McSweeney, D., Yates, J. A., and Cohen, R. J. (2010). The 6-GHz methanol multibeam maser catalogue - I. Galactic Centre region, longitudes 345° to 6°. *Monthly Notices of the Royal Astronomical Society*, 404(2):1029–1060. 21

Chandrasekhar, S. (1960). *Radiative transfer*. 5

Chen, X., Sobolev, A. M., Breen, S. L., Shen, Z.-Q., Ellingsen, S. P., MacLeod, G. C., Li, B., Voronkov, M. A., Kaczmarek, J. F., Zhang, J., Ren, Z.-Y., Wang, J., Linz, H., Hunter, T. R., Brogan, C., Sugiyama, K., Burns, R. A., Menten, K., Sanna, A., Stecklum, B., Hirota, T., Kim, K.-T., Chibueze, J., and Heever, S. v. d. (2020a). $^{13}CH_3OH$ masers associated with a transient phenomenon in a high-mass young stellar object. *Astrophysical Journal, Letters*, 890(2):L22. 21

Chen, X., Sobolev, A. M., Ren, Z.-Y., Parfenov, S., Breen, S. L., Ellingsen, S. P., Shen, Z.-Q., Li, B., MacLeod, G. C., Baan, W., Brogan, C., Hirota, T., Hunter, T. R., Linz, H., Menten, K., Sugiyama, K., Stecklum, B., Gong, Y., and Zheng, X. (2020b). New maser species tracing spiral-arm accretion flows in a high-mass young stellar object. *Nature Astronomy*, 4:1170–1176. 21

Chen, Z., Sun, W., Chini, R., Haas, M., Jiang, Z., and Chen, X. (2021). M17 MIR: A massive protostar with multiple accretion outbursts. *Astrophysical Journal*, 922(1):90. 22

Cheung, A. C., Rank, D. M., Townes, C. H., Thornton, D. D., and Welch, W. J. (1969). Detection of water in interstellar regions by its microwave radiation. *Nature*, 221(5181):626–628. 8

Chibueze, J. O., Imai, H., Tafoya, D., Omodaka, T., Kameya, O., Hirota, T., Chong, S.-N., and Torrelles, J. M. (2012). A highly collimated water maser bipolar outflow in the Cepheus A HW3d massive young stellar object. *Astrophysical Journal*, 748(2):146. 2, 65

Chibueze, J. O., Kamezaki, T., Omodaka, T., Handa, T., Nagayama, T., Baba, T., Sunada, K., Shizugami, M., Burns, R. A., Honma, M., Ubachukwu, A. A., Chukwude, A. E., and Alhassan, J. A. (2016). Astrometry and expanding bubble of a deeply embedded young stellar object in M17. *Monthly Notices of the Royal Astronomical Society*, 460(2):1839–1845. 22

Chibueze, J. O., MacLeod, G. C., Vorster, J. M., Hirota, T., Brogan, C. L., Hunter, T. R., and van Rooyen, R. (2021). The extraordinary outburst in the massive protostellar system NGC 6334 I-MM1: Spatiokinematics of water masers during a contemporaneous flare event. *Astrophysical Journal*, 908(2):175. , 2, 26, 27, 38, 46, 47, 54, 57, 58, 59, 70, 72, 73, 74, 79, 81, 82

Chibueze, J. O., Omodaka, T., Handa, T., Imai, H., Kurayama, T., Nagayama, T., Sunada, K., Nakano, M., Hirota, T., and Honma, M. (2014). Astrometry and spatio-kinematics of H_2O masers in the massive star-forming region NGC 6334I(North) with VERA. *Astrophysical Journal*, 784(2):114. 4, 25, 38, 54, 58

Churchwell, E. (2002). Ultra-compact HII regions and massive star formation. *Annual Review of Astronomy and Astrophysics*, 40:27–62. 5

Clarke, C. J. and Syer, D. (1996). Low-mass companions to T Tauri stars: a mechanism for rapid-rise FU Orionis outbursts. *Monthly Notices of the Royal Astronomical Society*, 278(1):L23–L27. 18

Compiègne, M., Verstraete, L., Jones, A., Bernard, J. P., Boulanger, F., Flagey, N., Le Bourlot, J., Paradis, D., and Ysard, N. (2011). The global dust SED: tracing the nature and evolution of dust with DustEM. *Astronomy and Astrophysics*, 525:A103. 10

Conselice, C. J. (2014). The evolution of galaxy structure over cosmic time. *Annual Review of Astronomy and Astrophysics*, 52:291–337. 1

Cooley, J. W., Lewis, P. A. W., and Welch, P. D. (1969). The fast Fourier transform and its applications. *IEEE Transactions on Education*, 12(1):27–34. 36

Cragg, D. M., Johns, K. P., Godfrey, P. D., and Brown, R. D. (1992). Pumping the interstellar methanol masers. *Monthly Notices of the Royal Astronomical Society*, 259(1):203–208. 7, 8

Cragg, D. M., Sobolev, A. M., and Godfrey, P. D. (2002). Modelling methanol and hydroxyl masers in star-forming regions. *Monthly Notices of the Royal Astronomical Society*, 331(2):521–536. 8, 9

Cragg, D. M., Sobolev, A. M., and Godfrey, P. D. (2005). Models of class II methanol masers based on improved molecular data. *Monthly Notices of the Royal Astronomical Society*, 360(2):533–545. 9, 43

De Buizer, J. M. (2003). Testing the circumstellar disc hypothesis: a search for H_2 outflow signatures from massive young stellar objects with linearly distributed methanol masers. *Monthly Notices of the Royal Astronomical Society*, 341(1):277–298. 9

de Jong, T. (1973). Water masers in a protostellar gas cloud. *Astronomy and Astrophysics*, 26:297. 8

Digel, S. W., Lyder, D. A., Philbrick, A. J., Puche, D., and Thaddeus, P. (1996). A large-scale CO survey toward W3, W4, and W5. *Astrophysical Journal*, 458:561. 13

Draine, B. T. (2003). Interstellar Dust Grains. *Annual review of astronomy and astrophysics*, 41:241–289. 10, 11

Ebert, R. (1955). Temperatur des interstellaren Gases bei groβen Dichten. Mit 1 Textabbildung. *Zeitschrift fuer Astrophysik*, 36:222. 13

Elbakyan, V. G., Nayakshin, S., Vorobyov, E. I., Caratti o Garatti, A., and Eislöffel, J. (2021). Accretion bursts in high-mass protostars: A new test bed for models of episodic accretion. *Astronomy and Astrophysics*, 651:L3. 22, 23

Elitzur, M. (1979). A dynamical explanation for the high water abundance detected in Orion. *Astrophysical Journal*, 229:560–566. 8

Elitzur, M. (1992). Astronomical masers. *Annual Review of Astronomy and Astrophysics*, 30:75–112. 7

Elitzur, M., Hollenbach, D. J., and McKee, C. F. (1989). H 2O Masers in star-forming regions. *Astrophysical Journal*, 346:983. 7, 8

Ellis, G. F. R., Maartens, R., and MacCallum, M. A. H. (2012). *Relativistic Cosmology*. 1

Feigelson, E. D., Martin, A. L., McNeill, C. J., Broos, P. S., and Garmire, G. P. (2009). Stellar clusters in the NGC 6334 star-forming complex. *Astronomical Journal*, 138(1):227–239. 24

Felli, M., Brand, J., Cesaroni, R., Codella, C., Comoretto, G., Di Franco, S., Massi, F., Moscadelli, L., Nesti, R., Olmi, L., Palagi, F., Panella, D., and Valdettaro, R. (2007). Water maser variability over 20 years in a large sample of star-forming regions: the complete database. *Astronomy and Astrophysics*, 476(1):373–664. 2, 53

Frank, A., Ray, T. P., Cabrit, S., Hartigan, P., Arce, H. G., Bacciotti, F., Bally, J., Benisty, M., Eislöffel, J., Güdel, M., Lebedev, S., Nisini, B., and Raga, A. (2014). Jets and outflows from star to cloud: Observations confront theory. In Beuther, H., Klessen, R. S., Dullemond, C. P., and Henning, T., editors, *Protostars and Planets VI*, page 451. 14, 15, 16

Fujisawa, K., Yonekura, Y., Sugiyama, K., Horiuchi, H., Hayashi, T., Hachisuka, K., Matsumoto, N., and Niinuma, K. (2015). A flare of methanol maser in S255. *The Astronomer's Telegram*, 8286:1. 19

Goddi, C., Moscadelli, L., Torrelles, J. M., Uscanga, L., and Cesaroni, R. (2006). Evidence supporting the kinematic interpretation of water maser proper motions. *Astronomy and Astrophysics*, 447(2):L9–L12. 73

Goldreich, P. and Keeley, D. A. (1972). Astrophysical masers. I. Source size and saturation. *Astrophysical Journal*, 174:517. 6, 7

Gordon, M. A. (1987). The continuum spectra of dust complexes associated with W3 Main, M42, W49A, and W51A. *Astrophysical Journal*, 316:258. 11

Gray, M. (2012). *Maser sources in astrophysics*. 7, 8

Gray, M. D., Baudry, A., Richards, A. M. S., Humphreys, E. M. L., Sobolev, A. M., and Yates, J. A. (2016). The physics of water masers observable with ALMA and SOFIA: model predictions for evolved stars. *Monthly Notices of the Royal Astronomical Society*, 456(1):374–404. 8

Gray, M. D., Etoka, S., Travis, A., and Pimpanuwat, B. (2020). Maser flares driven by variations in pumping and background radiation. *Monthly Notices of the Royal Astronomical Society*, 493(2):2472–2489. 7

Green, J. A., Caswell, J. L., and McClure-Griffiths, N. M. (2015). Excited-state hydroxyl maser polarimetry: who ate all the πs? *Monthly Notices of the Royal Astronomical Society*, 451(1):74–92. 5, 26

Griffiths, D. J. (2017). *Introduction to electrodynamics*. 9

Gwinn, C. R. (1994a). Hypersonic acceleration and turbulence of H 2O Masers in W49N. *Astrophysical Journal*, 429:241. 51, 54, 56, 70

Gwinn, C. R. (1994b). Physical structure of H 2O Masers in W49N. *Astrophysical Journal*, 429:253. 51

Hamaker, J. P., Bregman, J. D., and Sault, R. J. (1996). Understanding radio polarimetry. I. Mathematical foundations. *Astronomy and Astrophysicss*, 117:137–147. 34

Hansen, C. E., Klein, R. I., McKee, C. F., and Fisher, R. T. (2012). Feedback effects on low-mass star formation. *Astrophysical Journal*, 747(1):22. 16

Hartmann, L. and Kenyon, S. J. (1985). On the nature of FU Orionis objects. *Astrophysical Journal*, 299:462–478. 16

Harvey-Smith, L. and Cohen, R. J. (2006). Discovery of large-scale methanol and hydroxyl maser filaments in W3(OH). *Monthly Notices of the Royal Astronomical Society*, 371(4):1550–1558. 79

Hawley, J. F., Gammie, C. F., and Balbus, S. A. (1995). Local three-dimensional magnetohydrodynamic simulations of accretion disks. *Astrophysical Journal*, 440:742. 18

Herbig, G. H. (1977). Eruptive phenomena in early stellar evolution. *Astrophysical Journal*, 217:693–715. 16

Heyer, M. H. and Terebey, S. (1998). The anatomy of the Perseus spiral arm: ^{12}CO and IRAS imaging observations of the W3-W4-W5 cloud complex. *Astrophysical Journal*, 502(1):265–277. 13

Hirano, S., Hosokawa, T., Yoshida, N., Omukai, K., and Yorke, H. W. (2015). Primordial star formation under the influence of far ultraviolet radiation: 1540 cosmological haloes and the stellar mass distribution. *Monthly Notices of the Royal Astronomical Society*, 448(1):568–587. 1

Hirota, T., Cesaroni, R., Moscadelli, L., Sugiyama, K., Burns, R. A., Kim, J., Sunada, K., and Yonekura, Y. (2021). Water maser variability in a high-mass YSO outburst. VERA and ALMA observations of S255 NIRS 3. *Astronomy and Astrophysics*, 647:A23. 20, 72, 75, 77

Hirota, T., Machida, M. N., Matsushita, Y., Motogi, K., Matsumoto, N., Kim, M. K., Burns, R. A., and Honma, M. (2017). Disk-driven rotating bipolar outflow in Orion Source I. *Nature Astronomy*, 1:0146. 16

Högbom, J. A. (1974). Aperture synthesis with a Non-Regular distribution of interferometer baselines. *Astronomy and Astrophysicss*, 15:417. 36

Hollenbach, D., Elitzur, M., and McKee, C. F. (2013). Interstellar H_2O masers from J shocks. *Astrophysical Journal*, 773(1):70. 8, 65, 70, 73

Hosokawa, T., Hirano, S., Kuiper, R., Yorke, H. W., Omukai, K., and Yoshida, N. (2016). Formation of massive primordial stars: Intermittent UV feedback with episodic mass accretion. *Astrophysical Journal*, 824(2):119. 22

Howard, E. M., Pipher, J. L., and Forrest, W. J. (1997). S255-2: The formation of a stellar cluster. *Astrophysical Journal*, 481(1):327–342. 19

Hunter, T. R., Brogan, C. L., De Buizer, J. M., Towner, A. P. M., Dowell, C. D., MacLeod, G. C., Stecklum, B., Cyganowski, C. J., El-Abd, S. J., and McGuire, B. A. (2021). The extraordinary outburst in the massive protostellar system NGC 6334 I-MM1: Strong increase in mid-infrared continuum emission. *Astrophysical Journal, Letters*, 912(1):L17. 2, 22, 27

Hunter, T. R., Brogan, C. L., MacLeod, G., Cyganowski, C. J., Chandler, C. J., Chibueze, J. O., Friesen, R., Indebetouw, R., Thesner, C., and Young, K. H. (2017). An extraordinary outburst in the massive protostellar System NGC6334I-MM1: Quadrupling of the millimeter continuum. *Astrophysical Journal, Letters*, 837(2):L29. 2, 26, 37

Hunter, T. R., Brogan, C. L., MacLeod, G. C., Cyganowski, C. J., Chibueze, J. O., Friesen, R., Hirota, T., Smits, D. P., Chandler, C. J., and Indebetouw, R. (2018). The extraordinary outburst in the massive protostellar system NGC 6334I-MM1: Emergence of strong 6.7 GHz methanol masers. *Astrophysical Journal*, 854(2):170. , 2, 3, 26, 45, 46, 66, 67, 68, 69, 72, 78, 79, 82

Hunter, T. R., Brogan, C. L., Megeath, S. T., Menten, K. M., Beuther, H., and Thorwirth, S. (2006). Millimeter multiplicity in NGC 6334 I and I(N). *Astrophysical Journal*, 649(2):888–893. 25, 26

Immer, K., Reid, M. J., Menten, K. M., Brunthaler, A., and Dame, T. M. (2013). Trigonometric parallaxes of massive star forming regions: G012.88+0.48 and W33. *Astronomy and Astrophysics*, 553:A117. 54

Jeans, J. H. (1902). The stability of a spherical nebula. *Philosophical Transactions of the Royal Society of London Series A*, 199:1–53. 14

Kobayashi, H., Sasao, T., Kawaguchi, N., Manabe, S., Omodaka, T., Kameya, O., Shibata, K. M., Miyaji, T., Honma, M., Tamura, Y., Hirota, T., Kuji, S., Horiai, K., Sakai, S., Sato, K., Iwadate, K., Kanya, Y., Ujihara, H., Jike, T., Fujii, T., Motiduki, N., Oyama, T., Kurayama, H., Kamohara, R., Suda, H., and Kasuga, T. (2003). VERA: A new VLBI instrument free from the atmosphere. In Minh, Y. C., editor, *New technologies in VLBI*, volume 306 of *Astronomical Society of the Pacific Conference Series*, page 367. 37

Kraus, J. D. (1966). *Radio astronomy*. 29

Krumholz, M. R., McKee, C. F., and Klein, R. I. (2005). The formation of stars by gravitational collapse rather than competitive accretion. *Nature*, 438(7066):332–334. 13

Kwan, J. and Tademaru, E. (1988). Jets from T Tauri stars: Spectroscopic evidence and collimation mechanism. *Astrophysical Journal, Letters*, 332:L41. 14

Kylafis, N. D. and Norman, C. A. (1991). Collisional pumping of H 2O Masers in star-forming regions. *Astrophysical Journal*, 373:525. 7

Lada, C. J. and Kylafis, N. D. (1991). The physics of star formation and early stellar evolution. In *The Physics of Star Formation and Early Stellar Evolution*, volume 342 of *NATO Advanced Study Institute (ASI) Series C*. 12

Ladeyschikov, D. A., Gong, Y., Sobolev, A. M., Menten, K. M., Urquhart, J. S., Breen, S. L., Shakhvorostova, N. N., Bayandina, O. S., and Tsivilev, A. P. (2022). Water masers as an early tracer of star formation. *Astrophysical Journal, Supplement*, 261(2):14. 70

Lankhaar, B. and Vlemmings, W. (2019). Characterizing maser polarization: effects of saturation, anisotropic pumping, and hyperfine structure. *Astronomy and Astrophysics*, 628:A14. 7

Larson, R. B. (1969). Numerical calculations of the dynamics of collapsing proto-star. *Monthly Notices of the Royal Astronomical Society*, 145:271. 14

Lee, C.-F., Ho, P. T. P., Li, Z.-Y., Hirano, N., Zhang, Q., and Shang, H. (2017). A rotating protostellar jet launched from the innermost disk of HH 212. *Nature Astronomy*, 1:0152. 16

Lee, S.-S., Oh, C. S., Roh, D.-G., Oh, S.-J., Kim, J., Yeom, J.-H., Kim, H. R., Jung, D.-G., Byun, D.-Y., Jung, T., Kawaguchi, N., Shibata, K. M., and Wajima, K. (2015). A new hardware correlator in Korea: Performance evaluation using KVN observations. *Journal of Korean Astronomical Society*, 48(2):125–137. 37

Leroy, A. K., Schinnerer, E., Hughes, A., Rosolowsky, E., Pety, J., Schruba, A., Usero, A., Blanc, G. A., Chevance, M., Emsellem, E., Faesi, C. M., Herrera, C. N., Liu, D., Meidt, S. E., Querejeta, M., Saito, T., Sandstrom, K. M., Sun, J., Williams, T. G., Anand, G. S., Barnes, A. T., Behrens, E. A., Belfiore, F., Benincasa, S. M., Bešlić, I., Bigiel, F., Bolatto, A. D., den Brok, J. S., Cao, Y., Chandar, R., Chastenet, J., Chiang, I. D., Congiu, E., Dale, D. A., Deger, S., Eibensteiner, C., Egorov, O. V., García-Rodríguez, A., Glover, S. C. O., Grasha, K., Henshaw, J. D., Ho, I. T., Kepley, A. A., Kim, J., Klessen, R. S., Kreckel, K., Koch, E. W., Kruijssen, J. M. D., Larson,

K. L., Lee, J. C., Lopez, L. A., Machado, J., Mayker, N., McElroy, R., Murphy, E. J., Ostriker, E. C., Pan, H.-A., Pessa, I., Puschnig, J., Razza, A., Sánchez-Blázquez, P., Santoro, F., Sardone, A., Scheuermann, F., Sliwa, K., Sormani, M. C., Stuber, S. K., Thilker, D. A., Turner, J. A., Utomo, D., Watkins, E. J., and Whitmore, B. (2021). PHANGS-ALMA: Arcsecond CO(2-1) imaging of nearby star-forming galaxies. *Astrophysical Journals*, 257(2):43. 1

Li, J. J., Moscadelli, L., Cesaroni, R., Furuya, R. S., Xu, Y., Usuda, T., Menten, K. M., Pestalozzi, M., Elia, D., and Schisano, E. (2012). Massive star formation toward G28.87+0.07 (IRAS 18411-0338) investigated by means of maser kinematics and radio to infrared continuum observations. *Astrophysical Journal*, 749(1):47. 74, 75, 77

Longair, M. S. (2011). *High energy astrophysics*. 9, 10

Longmore, S. N., Burton, M. G., Minier, V., and Walsh, A. J. (2006). Mid-infrared source multiplicity within hot molecular cores traced by methanol masers. *Monthly Notices of the Royal Astronomical Society*, 369(3):1196–1200. 19

Machida, M. N., Inutsuka, S.-i., and Matsumoto, T. (2011). Recurrent planet formation and intermittent protostellar outflows induced by episodic mass accretion. *Astrophysical Journal*, 729(1):42. 18

MacLeod, G. C., Chibueze, J. O., Sanna, A., Paulsen, J. D., Houde, M., van den Heever, S. P., and Goedhart, S. (2021). Systematic velocity drifts of methanol masers associated with G9.62+0.20E. *Monthly Notices of the Royal Astronomical Society*, 500(3):3425–3437. 65

MacLeod, G. C., Smits, D. P., Goedhart, S., Hunter, T. R., Brogan, C. L., Chibueze, J. O., van den Heever, S. P., Thesner, C. J., Banda, P. J., and Paulsen, J. D. (2018). A masing event in NGC 6334I: contemporaneous flaring of hydroxyl, methanol, and water masers. *Monthly Notices of the Royal Astronomical Society*, 478(1):1077–1092. 2, 5, 22, 25, 48, 50, 51, 72, 78

MacLeod, G. C., Sugiyama, K., Hunter, T. R., Quick, J., Baan, W., Breen, S. L., Brogan, C. L., Burns, R. A., Caratti o Garatti, A., Chen, X., Chibueze, J. O., Houde, M., Kaczmarek, J. F., Linz, H., Rajabi, F., Saito, Y., Schmidl, S., Sobolev, A. M., Stecklum, B., van den Heever, S. P., and Yonekura, Y. (2019). Detection of new methanol maser transitions associated with G358.93-0.03. *Monthly Notices of the Royal Astronomical Society*, 489(3):3981–3989. 21

Marvel, K. B., Wilking, B. A., Claussen, M. J., and Wootten, A. (2008). Time-resolved AU-scale jets traced by masers in the IRAS 4A/B regions of NGC 1333. *Astrophysical Journal*, 685(1):285–297. 51

Mathis, J. S. (1990). Interstellar dust and extinction. *Annual Review of Astronomy and Astrophysics*, 28:37–70. 4

Mathis, J. S., Rumpl, W., and Nordsieck, K. H. (1977). The size distribution of interstellar grains. *Astrophysical Journal*, 217:425–433. 10

Maud, L. T., Lumsden, S. L., Moore, T. J. T., Mottram, J. C., Urquhart, J. S., and Cicchini, A. (2015a). A distance-limited sample of massive star-forming cores from the RMS. *Monthly Notices of the Royal Astronomical Society*, 452(1):637–655. 75, 77

Maud, L. T., Moore, T. J. T., Lumsden, S. L., Mottram, J. C., Urquhart, J. S., and Hoare, M. G. (2015b). A distance-limited sample of massive molecular outflows. *Monthly Notices of the Royal Astronomical Society*, 453(1):645–665. 75

McBreen, B., Fazio, G. G., Stier, M., and Wright, E. L. (1979). Evidence for a variable far-infrared source in NGC 6334. *Astrophysical Journal, Letters*, 232:L183–L187. 24

Menten, K. M. (1991). The Discovery of a new, very strong, and widespread interstellar methanol maser line. *Astrophysical Journal, Letters*, 380:L75. 8

Menten, K. M., Reid, M. J., Pratap, P., Moran, J. M., and Wilson, T. L. (1992). VLBI observations of the 6.7 GHz methanol masers toward W3(OH). *Astrophysical Journal, Letters*, 401:L39. 9

Meyer, D. M. A., Haemmerlé, L., and Vorobyov, E. I. (2019a). On the episodic excursions of massive protostars in the Hertzsprung-Russell diagram. *Monthly Notices of the Royal Astronomical Society*, 484(2):2482–2498. 20

Meyer, D. M. A., Vorobyov, E. I., Elbakyan, V. G., Eislöffel, J., Sobolev, A. M., and Stöhr, M. (2021). Parameter study for the burst mode of accretion in massive star formation. *Monthly Notices of the Royal Astronomical Society*, 500(4):4448–4468. 23, 75, 77

Meyer, D. M. A., Vorobyov, E. I., Elbakyan, V. G., Stecklum, B., Eislöffel, J., and Sobolev, A. M. (2019b). Burst occurrence in young massive stellar objects. *Monthly Notices of the Royal Astronomical Society*, 482(4):5459–5476. 23

Meyer, D. M. A., Vorobyov, E. I., Kuiper, R., and Kley, W. (2017). On the existence of accretion-driven bursts in massive star formation. *Monthly Notices of the Royal Astronomical Society*, 464(1):L90–L94. 16, 22, 75

Minier, V., Booth, R. S., and Conway, J. E. (2000). VLBI observations of 6.7 and 12.2 GHz methanol masers toward high mass star-forming regions. I. Observational results: protostellar disks or outflows? *Astronomy and Astrophysics*, 362:1093–1108. 9

Minier, V., Ellingsen, S. P., Norris, R. P., and Booth, R. S. (2003). The protostellar mass limit for 6.7 GHz methanol masers. I. A low-mass YSO survey. *Astronomy and Astrophysics*, 403:1095–1100. 2, 8, 9, 19, 21

Moscadelli, L., Cesaroni, R., Rioja, M. J., Dodson, R., and Reid, M. J. (2011). Methanol and water masers in IRAS 20126+4104: the distance, the disk, and the jet. *Astronomy and Astrophysics*, 526:A66. 9

Moscadelli, L., Sanna, A., Goddi, C., Krishnan, V., Massi, F., and Bacciotti, F. (2020). Protostellar outflows at the EarliesT Stages (POETS). IV. Statistical properties of the 22 GHz H_2O masers. *Astronomy and Astrophysics*, 635:A118. 73

Moscadelli, L., Sanna, A., Goddi, C., Walmsley, M. C., Cesaroni, R., Caratti o Garatti, A., Stecklum, B., Menten, K. M., and Kraus, A. (2017). Extended CH_3OH maser flare excited by a bursting massive YSO. *Astronomy and Astrophysics*, 600:L8. 20

Muñoz, D. J., Mardones, D., Garay, G., Rebolledo, D., Brooks, K., and Bontemps, S. (2007). Massive clumps in the NGC 6334 star-forming region. *Astrophysical Journal*, 668(2):906–917. 24

Norris, R. P., Byleveld, S. E., Diamond, P. J., Ellingsen, S. P., Ferris, R. H., Gough, R. G., Kesteven, M. J., McCulloch, P. M., Phillips, C. J., Reynolds, J. E., Tzioumis, A. K., Takahashi, Y., Troup, E. R., and Wellington, K. J. (1998). Methanol masers as tracers of circumstellar disks. *Astrophysical Journal*, 508(1):275–285. 9, 80

Nyquist, H. (1928). Certain topics in telegraph transmission theory. *Transactions of the American Institute of Electrical Engineers*, 47(2):617–624. 29

Oliva, G. A. and Kuiper, R. (2020). Modeling disk fragmentation and multiplicity in massive star formation. *Astronomy and Astrophysics*, 644:A41. 23

Padoan, P., Pan, L., Juvela, M., Haugbølle, T., and Nordlund, Å. (2020). The origin of massive stars: The inertial-inflow model. *Astrophysical Journal*, 900(1):82. 13

Pfalzner, S., Tackenberg, J., and Steinhausen, M. (2008). Accretion bursts in young stars driven by the cluster environment. *Astronomy and Astrophysics*, 487(2):L45–L48. 19

Pospieszalski, M. W. (2012). Cryogenic amplifiers for Jansky Very Large Array receivers. In *19th International Conference on Microwave Radar and Wireless Communications (MIKON*, pages 748–752. 29

Proven-Adzri, E., MacLeod, G. C., Heever, S. P. v. d., Hoare, M. G., Kuditcher, A., and Goedhart, S. (2019). Discovery of periodic methanol masers associated with G323.46-0.08. *Monthly Notices of the Royal Astronomical Society*, 487(2):2407–2411. 22

Qiu, K., Wyrowski, F., Menten, K. M., Güsten, R., Leurini, S., and Leinz, C. (2011). APEX CO (9-8) mapping of an extremely high velocity and jet-like outflow in a high-mass star-forming region. *Astrophysical Journal, Letters*, 743(1):L25. 47, 70, 74, 79

Reid, M. J., Menten, K. M., Brunthaler, A., Zheng, X. W., Dame, T. M., Xu, Y., Wu, Y., Zhang, B., Sanna, A., Sato, M., Hachisuka, K., Choi, Y. K., Immer, K., Moscadelli, L., Rygl, K. L. J., and Bartkiewicz, A. (2014). Trigonometric parallaxes of high mass star forming regions: The structure and kinematics of the Milky Way. *Astrophysical Journal*, 783(2):130. 25, 58

Reid, M. J., Schneps, M. H., Moran, J. M., Gwinn, C. R., Genzel, R., Downes, D., and Roennaeng, B. (1988). The distance to the center of the galaxy: H 2O maser proper motions in Sagittarius B2(N). *Astrophysical Journal*, 330:809. 54

Richards, A. M. S., Sobolev, A., Baudry, A., Herpin, F., Decin, L., Gray, M. D., Etoka, S., Humphreys, E. M. L., and Vlemmings, W. (2020). Masers: Precision probes of molecular gas. *Advances in Space Research*, 65(2):780–789. 65

Robitaille, T. P. (2017). A modular set of synthetic spectral energy distributions for young stellar objects. *Astronomy and Astrophysics*, 600:A11. 22

Rodriguez, L. F., Canto, J., and Moran, J. M. (1982). Radio sources in NGC 6334. *Astrophysical Journal*, 255:103–110. 24

Rosen, A. L. and Krumholz, M. R. (2020). The role of outflows, radiation pressure, and magnetic fields in massive star formation. *Astronomical Journal*, 160(2):78. 75

Russeil, D., Schneider, N., Anderson, L. D., Zavagno, A., Molinari, S., Persi, P., Bontemps, S., Motte, F., Ossenkopf, V., André, P., Arzoumanian, D., Bernard, J. P., Deharveng, L., Didelon, P., Di Francesco, J., Elia, D., Hennemann, M., Hill, T., Könyves, V., Li, J. Z., Martin, P. G., Nguyen Luong, Q., Peretto, N., Pezzuto, S., Polychroni, D., Roussel, H., Rygl, K. L. J., Spinoglio, L., Testi, L., Tigé, J., Vavrek, R., Ward-Thompson, D., and White, G. (2013). The Herschel view of the massive star-forming region NGC 6334. *Astronomy and Astrophysics*, 554:A42. 24, 25

Russeil, D., Zavagno, A., Nguyen, A., Figueira, M., Adami, C., and Bouret, J. C. (2020). OB stars and YSO populations in the region of NGC 6334-NGC 6357 as seen with Gaia DR2. *Astronomy and Astrophysics*, 642:A21. 24

Rybicki, G. B. and Lightman, A. P. (1986). *Radiative processes in astrophysics*. 9, 10

Sabatini, G., Bovino, S., Giannetti, A., Grassi, T., Brand, J., Schisano, E., Wyrowski, F., Leurini, S., and Menten, K. M. (2021). Establishing the evolutionary timescales of the massive star formation process through chemistry. *Astronomy and Astrophysics*, 652:A71. 1

Sanna, A., Moscadelli, L., Cesaroni, R., Tarchi, A., Furuya, R. S., and Goddi, C. (2010a). VLBI study of maser kinematics in high-mass star-forming regions. I. G16.59-0.05. *Astronomy and Astrophysics*, 517:A71. 65, 77

Sanna, A., Moscadelli, L., Cesaroni, R., Tarchi, A., Furuya, R. S., and Goddi, C. (2010b). VLBI study of maser kinematics in high-mass star-forming regions. II. G23.01-0.41. *Astronomy and Astrophysics*, 517:A78. 77

Sault, R. J., Hamaker, J. P., and Bregman, J. D. (1996). Understanding radio polarimetry. II. Instrumental calibration of an interferometer array. *Astronomy and Astrophysicss*, 117:149–159. 34

Schulz, N. S. (2005). *From dust to stars studies of the formation and early evolution of stars*. 13

Schulz, N. S. (2012). *The formation and early evolution of stars*. 4

Shu, F. H., Adams, F. C., and Lizano, S. (1987). Star formation in molecular clouds: observation and theory. *Annual Review of Astronomy and Astrophysics*, 25:23–81. 10

Sobolev, A. M., Cragg, D. M., and Godfrey, P. D. (1997). Pumping of Class II methanol masers. II. The 5_1_-6_0_A$\hat{+}\hat{+}$transition. *Astronomy and Astrophysics*, 324:211–220. 9

Stacy, A., Greif, T. H., and Bromm, V. (2010). The first stars: formation of binaries and small multiple systems. *Monthly Notices of the Royal Astronomical Society*, 403(1):45–60. 22

Stecklum, B., Wolf, V., Linz, H., Caratti o Garatti, A., Schmidl, S., Klose, S., Eislöffel, J., Fischer, C., Brogan, C., Burns, R. A., Bayandina, O., Cyganowski, C., Gurwell, M., Hunter, T., Hirano, N., Kim, K. T., MacLeod, G., Menten, K. M., Olech, M., Orosz, G., Sobolev, A., Sridharan, T. K., Surcis, G., Sugiyama, K., van der Walt, J., Volvach, A., and Yonekura, Y. (2021). Infrared observations of the flaring maser source G358.93-0.03. SOFIA confirms an accretion burst from a massive young stellar object. *Astronomy and Astrophysics*, 646:A161. 2, 21

Sugiyama, K., Saito, Y., Yonekura, Y., and Momose, M. (2019). Bursting activity of the 6.668-GHz CH3OH maser detected in G 358.93-00.03 using the Hitachi 32-m. *The Astronomer's Telegram*, 12446:1. 21

THE CASA TEAM, Bean, B., Bhatnagar, S., Castro, S., Donovan Meyer, J., Emonts, B., Garcia, E., Garwood, R., Golap, K., Gonzalez Villalba, J., Harris, P., Hayashi, Y., Hoskins, J., Hsieh, M., Jagannathan, P., Kawasaki, W., Keimpema, A., Kettenis, M., Lopez, J., Marvil, J., Masters, J., McNichols, A., Mehringer, D., Miel, R., Moellenbrock, G., Montesino, F., Nakazato, T., Ott, J., Petry, D., Pokorny, M., Raba, R., Rau, U., Schiebel, D., Schweighart, N., Sekhar, S., Shimada, K., Small, D., Steeb, J.-W., Sugimoto, K., Suoranta, V., Tsutsumi, T., van Bemmel, I. M., Verkouter, M., Wells, A., Xiong, W., Szomoru, A., Griffith, M., Glendenning, B., and Kern, J. (2022). CASA, the Common Astronomy Software Applications for radio astronomy. *arXiv e-prints*, page arXiv:2210.02276. 39

Thompson, A. R., Moran, J. M., and Swenson, George W., J. (2017). *Interferometry and synthesis in radio astronomy, 3rd Edition*. 29, 30, 32, 36

Tigé, J., Motte, F., Russeil, D., Zavagno, A., Hennemann, M., Schneider, N., Hill, T., Nguyen Luong, Q., Di Francesco, J., Bontemps, S., Louvet, F., Didelon, P., Könyves, V., André, P., Leuleu, G., Bardagi, J., Anderson, L. D., Arzoumanian, D., Benedettini, M., Bernard, J. P., Elia, D., Figueira, M., Kirk, J., Martin, P. G., Minier, V., Molinari, S., Nony, T., Persi, P., Pezzuto, S., Polychroni, D., Rayner, T., Rivera-Ingraham, A., Roussel, H., Rygl, K., Spinoglio, L., and White, G. J. (2017). The earliest phases of high-mass star formation, as seen in NGC 6334 by Herschel-HOBYS. *Astronomy and Astrophysics*, 602:A77. 1, 13, 24, 83

Toomre, A. (1964). On the gravitational stability of a disk of stars. *Astrophysical Journal*, 139:1217–1238. 18

Torrelles, J. M., Patel, N. A., Curiel, S., Estalella, R., Gómez, J. F., Rodríguez, L. F., Cantó, J., Anglada, G., Vlemmings, W., Garay, G., Raga, A. C., and Ho, P. T. P. (2011). A wide-angle outflow with the simultaneous presence of a high-velocity jet in the high-mass Cepheus A HW2 system. *Monthly Notices of the Royal Astronomical Society*, 410(1):627–640. 16

Torrelles, J. M., Patel, N. A., Gómez, J. F., Ho, P. T. P., Rodríguez, L. F., Anglada, G., Garay, G., Greenhill, L., Curiel, S., and Cantó, J. (2001). Discovery of linear "building blocks" of water masers shaping linear/arcuate microstructures in Cepheus A. *Astrophysical Journal*, 560(2):853–864. 8, 51, 56

Trinidad, M. A., Imai, H., de la Fuente, E., Toledano-Juárez, I., Masqué, J. M., and Rodríguez-Esnard, T. (2021). Proper motions of water masers in the star-forming region IRAS 23139+5939. *Publications of the Astronomical Society of Japan*, 73(6):1669–1680. 53, 54

Tucker, J. R. (2009). The birth of SIS mixers. In Lis, D. C., Vaillancourt, J. E., Goldsmith, P. F., Bell, T. A., Scoville, N. Z., and Zmuidzinas, J., editors, *Submillimeter Astrophysics and Technology: a Symposium Honoring Thomas G. Phillips*, volume 417 of *Astronomical Society of the Pacific Conference Series*, page 355. 29

Uchiyama, M., Yamashita, T., Sugiyama, K., Nakaoka, T., Kawabata, M., Itoh, R., Yamanaka, M., Akitaya, H., Kawabata, K., Yonekura, Y., Saito, Y., Motogi, K., and Fujisawa, K. (2020). Near-infrared monitoring of the accretion outburst in the massive young stellar object S255-NIRS3. *Publications of the Astronomical Society of Japan*, 72(1):4. 20

Valdettaro, R., Palla, F., Brand, J., Cesaroni, R., Comoretto, G., Felli, M., and Palagi, F. (2002). Long-term study of water maser emission associated with young stellar objects. I. The database. *Astronomy and Astrophysics*, 383:244–266. 65

van Moorsel, G., Kemball, A., and Greisen, E. (1996). AIPS developments in the nineties. In Jacoby, G. H. and Barnes, J., editors, *Astronomical Data Analysis Software and Systems V*, volume 101 of *Astronomical Society of the Pacific Conference Series*, page 37. 37

VERA Collaboration, Hirota, T., Nagayama, T., Honma, M., Adachi, Y., Burns, R. A., Chibueze, J. O., Choi, Y. K., Hachisuka, K., Hada, K., Hagiwara, Y., Hamada, S., Handa, T., Hashimoto, M., Hirano, K., Hirata, Y., Ichikawa, T., Imai, H., Inenaga, D., Ishikawa, T., Jike, T., Kameya, O., Kaseda, D., Kim, J. S., Kim, J., Kim, M. K., Kobayashi, H., Kono, Y., Kurayama, T., Matsuno, M., Morita, A., Motogi, K., Murase, T., Nakagawa, A., Nakanishi, H., Niinuma, K., Nishi, J., Oh, C. S., Omodaka, T., Oyadomari, M., Oyama, T., Sakai, D., Sakai, N., Sawada-Satoh, S., Shibata, K. M., Shizugami, M., Sudo, J., Sugiyama, K., Sunada, K., Suzuki, S., Takahashi, K., Tamura, Y., Tazaki,

F., Ueno, Y., Uno, Y., Urago, R., Wada, K., Wu, Y. W., Yamashita, K., Yamashita, Y., Yamauchi, A., and Yuda, A. (2020). The first VERA astrometry catalog. *Publications of the Astronomical Society of Japan*, 72(4):50. 2, 37

Vorobyov, E. I. and Basu, S. (2006). The burst mode of protostellar accretion. *Astrophysical Journal*, 650(2):956–969. 18

Vorster, J. M., Okwe Chibueze, J., and Hirota, T. (2021). Spatio-kinematics of the massive star forming region NGC6334I during an episodic accretion event. In *South African Institute of Physics Conference at Potchefstroom*, page E1. 48

Walsh, A. J., Breen, S. L., Britton, T., Brooks, K. J., Burton, M. G., Cunningham, M. R., Green, J. A., Harvey-Smith, L., Hindson, L., Hoare, M. G., Indermuehle, B., Jones, P. A., Lo, N., Longmore, S. N., Lowe, V., Phillips, C. J., Purcell, C. R., Thompson, M. A., Urquhart, J. S., Voronkov, M. A., White, G. L., and Whiting, M. T. (2011). The H_2O Southern Galactic Plane Survey (HOPS) - I. Techniques and H_2O maser data. *Monthly Notices of the Royal Astronomical Society*, 416(3):1764–1821. 7

Wang, P., Li, Z.-Y., Abel, T., and Nakamura, F. (2010). Outflow feedback regulated massive star formation in parsec-scale cluster-forming clumps. *Astrophysical Journal*, 709(1):27–41. 16

Williams, D. A. (2005). Gas and dust in the interstellar medium. In *Journal of Physics Conference Series*, volume 6 of *Journal of Physics Conference Series*, pages 1–17. 10, 11

Williams, J. P., Blitz, L., and Stark, A. A. (1995). The density structure in the Rosette molecular cloud: Signposts of evolution. *Astrophysical Journal*, 451:252. 13

Williams, J. P. and McKee, C. F. (1997). The galactic distribution of OB associations in molecular clouds. *Astrophysical Journal*, 476(1):166–183. 13

Wilson, T. L., Rohlfs, K., and Hüttemeister, S. (2013). *Tools of radio astronomy*. 5, 28, 30, 32, 36

Winnewisser, G. and Herbst, E. (1993). Interstellar molecules. *Reports on Progress in Physics*, 56(10):1209–1273. 11

Yamamoto, S. (2017). *Introduction to astrochemistry: Chemical evolution from interstellar clouds to star and planet formation*. 4

Zernickel, A., Schilke, P., and Smith, R. J. (2013). The global velocity field of the filament in NGC 6334. *Astronomy and Astrophysics*, 554:L2. 25

Zinchenko, I., Liu, S. Y., Su, Y. N., Salii, S. V., Sobolev, A. M., Zemlyanukha, P., Beuther, H., Ojha, D. K., Samal, M. R., and Wang, Y. (2015). The disk-outflow system in the S255IR area of high-mass star formation. *Astrophysical Journal*, 810(1):10. 19, 20

Zinnecker, H. and Yorke, H. W. (2007). Toward understanding massive star formation. *Annual Review of Astronomy and Astrophysics*, 45(1):481–563. 1, 24